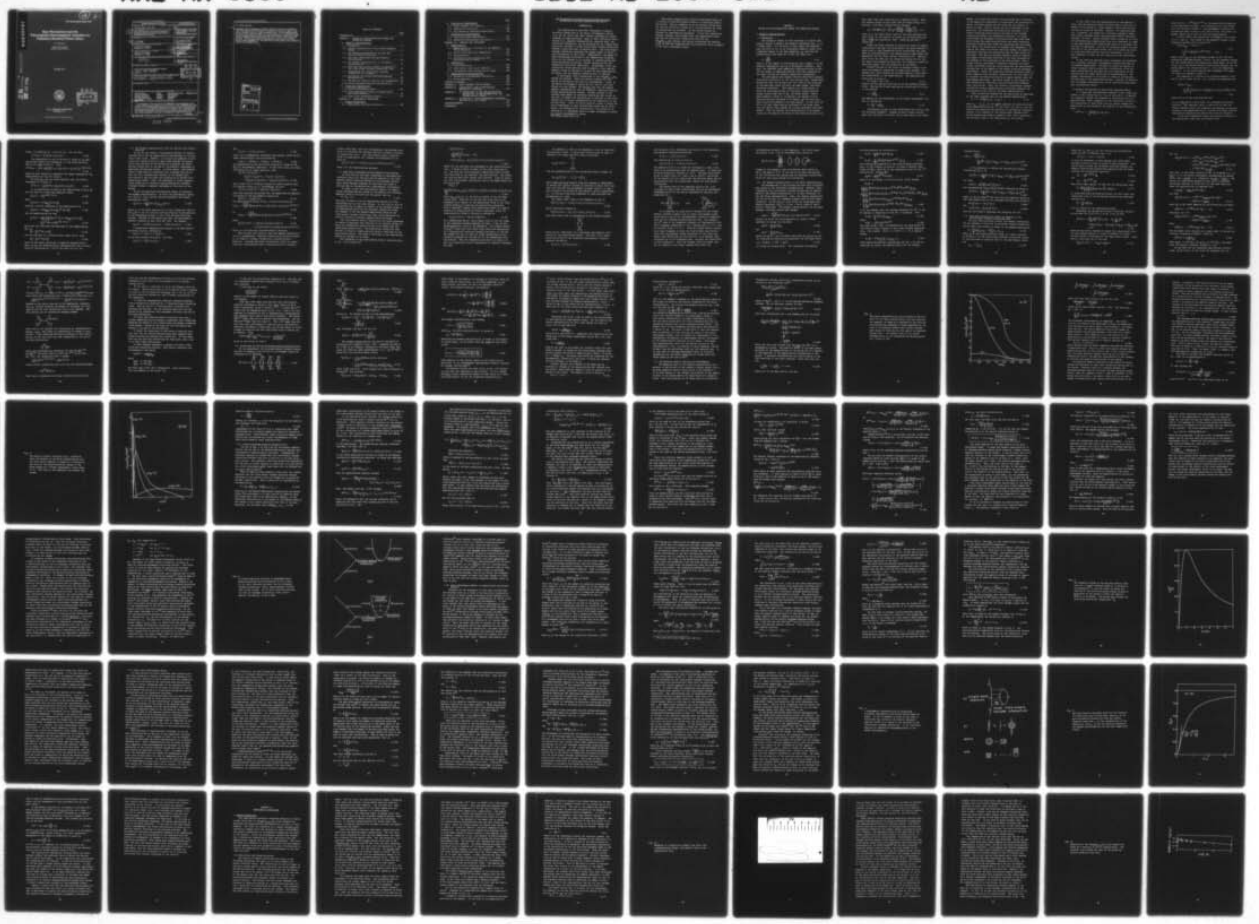
AD-A049 154 NAVAL RESEARCH LAB WASHINGTON D C F/G 20/3
SPIN FLUCTUATIONS AND THE PARAMAGNETIC-FERROMAGNETIC TRANSITION--ETC(U)
OCT 77 D J GILLESPIE

UNCLASSIFIED NRL-MR-3630 SBIE-AD-E000 056 NL

1 OF 3
AD A049 154



AD A049154

(12)

NRL Memorandum Report 3630

Spin Fluctuations and the Paramagnetic-Ferromagnetic Transition in Palladium-Rhodium-Nickel Alloys

D. J. GILLESPIE

Metal Physics Branch
Material Sciences Division

October 1977

AD No. ade00056
DDC FILE COPY



DDC
RECEIVED
JAN 31 1978
B

NAVAL RESEARCH LABORATORY
Washington, D.C.

Approved for public release; distribution unlimited.

SECURITY CLASSIFICATION OF THIS PAGE (When Data Entered)

REPORT DOCUMENTATION PAGE

READ INSTRUCTIONS BEFORE COMPLETING FORM

1. REPORT NUMBER: NRL Memorandum Report 3630
2. GOVT ACCESSION NO.
3. RECIPIENT'S CATALOG NUMBER

4. TITLE (and Subtitle): SPIN FLUCTUATIONS AND THE PARAMAGNETIC–FERROMAGNETIC TRANSITION IN PALLADIUM–RHODIUM–NICKEL ALLOYS.

5. TYPE OF REPORT & PERIOD COVERED: Interim report on a continuing NRL problem.

6. PERFORMING ORG. REPORT NUMBER

7. AUTHOR(s): D. J. Gillespie

8. CONTRACT OR GRANT NUMBER(s): RR022 01

9. PERFORMING ORGANIZATION NAME AND ADDRESS: Naval Research Laboratory, Washington, D. C. 20375

10. PROGRAM ELEMENT, PROJECT, TASK AREA & WORK UNIT NUMBERS: NRL Problem M01-19; Project RR022 01 46-5408

11. CONTROLLING OFFICE NAME AND ADDRESS: Office of Naval Research, Washington, D. C. 20360

12. REPORT DATE: October 1977

13. NUMBER OF PAGES: 285

14. MONITORING AGENCY NAME & ADDRESS (if different from Controlling Office): 287p.

15. SECURITY CLASS. (of this report): UNCLASSIFIED

15a. DECLASSIFICATION/DOWNGRADING SCHEDULE

16. DISTRIBUTION STATEMENT (of this Report)

Approved for public release; distribution unlimited.

NRL-MR-3630

17. DISTRIBUTION STATEMENT (of the abstract entered in Block 20, if different from Report)

SBIE AD-E000 056

DDC RECEIVED JAN 31 1978 B

18. SUPPLEMENTARY NOTES

19. KEY WORDS (Continue on reverse side if necessary and identify by block number)

Curie temperature	Nickel	Spectral density function	$(Pd_{95}Rh_5)_{1-x}Ni_x$
Dynamic susceptibility	Palladium	Spin fluctuations	
Exchange enhancement	Resistivity	Susceptibility	
Low temperature resistivity	Rhodium	$Pd_{95}Rh_5$	
Magnetization			

20. ABSTRACT (Continue on reverse side if necessary and identify by block number)

Low-temperature (1-20 K) low-field (½-4 kG) magnetization and low-temperature (1-20 K) zero-field electrical resistivity measurements have been made on a series of $(Pd_{95}Rh_5)_{1-x}Ni_x$ alloys ($x \leq 0.03$). At 4 K the magnetization measurements were extended to 56 kG, and in the case of the more dilute alloys the resistivity measurements were extended to 300 K. Curie temperatures and spontaneous magnetization obtained by an Arrott plot analysis of the magnetization data yield a critical concentration for the onset of ferromagnetism of 1.9±0.05 at% Ni. In the (Continues)

DD FORM 1 JAN 73 1473 EDITION OF 1 NOV 65 IS OBSOLETE S/N 0102-014-6601

SECURITY CLASSIFICATION OF THIS PAGE (When Data Entered)

251 950 LB

20. Abstract (Continued)

paramagnetic region the magnetization, susceptibility (dM/dH), and resistivity are well fitted by a model which considers local spin fluctuations to be associated with two types of magnetic center: a pair of interacting Ni atoms and a single noninteracting Ni atom. The local enhancement associated with a Ni pair is found to be roughly 3 to 4 times as large as that of a noninteracting Ni atom. The spin-fluctuation temperature and the characteristic-field parameter are, respectively, T_s = 59±4 K and H_s = 225±25 kG for the noninteracting Ni atom, and T_s = 18±8 K and H_s = 35±5 kG for the Ni pair. In the ferromagnetic alloys the magnetization of a large number of the Ni atoms appears to remain unsaturated at 4 K. The results for this system are compared with the corresponding results for the $Pd_{1-x}Ni_x$ system.

ACCESSION for
NTIS White Section ✓
DDC Buff Section ☐
UNANNOUNCED ☐
JUSTIFICATION
BY
DISTRIBUTION/AVAILABILITY CODES
Dist. AVAIL. and/or SPECIAL
A

TABLE OF CONTENTS

Page

INTRODUCTION..... 1

CHAPTER I: REVIEW OF SPIN-FLUCTUATION THEORY FOR TRANSITION METALS

A. Magnetic Susceptibility

1.1 Background..... 3

1.2 Dynamic Susceptibility from Linear Response Theory..... 6

1.3 The Dynamic Susceptibility and the two-particle Green's Function..... 11

1.4 Many-body Techniques and Spin-density Fluctuations..... 13

1.5 The Dynamic Susceptibility in the Bloch Representation..... 17

1.6 Many-body Perturbation Theory as Applied to the Intra-atomic Coulomb Interaction Term..... 19

1.7 Diagramming the Intra-atomic Coulomb Interaction in k, ω Space..... 23

1.8 Evaluating the Uniform Exchange-enhanced Susceptibility..... 26

1.9 The Spectral Density Function and Paramagnons.. 30

1.10 Locally-exchange-enhanced Susceptibility..... 40

B. Electrical Resistivity

1.11 Uniform Enhancement Model..... 50

1.12 Local Enhancement Models of Lederer-Mills and Kaiser-Doniach..... 56

1.13 Other Local Enhancement Models..... 67

CHAPTER II: EXPERIMENTAL PROCEDURES

A. Sample Preparation

2.1 Fabrication and Characterization..... 82

Page

B. Resistivity Measurements

2.2 Sample Chamber and Cryostat..... 97

2.3 Temperature Controller..... 102

2.4 High Precision Resistance Measurement..... 109

C. Magnetization Measurements

2.5 Vibrating Sample Magnetometer..... 114

2.6 Temperature Measurement and Control..... 118

CHAPTER III: RESULTS AND DISCUSSION

A. Magnetization

3.1 Magnetization as a Function of the Magnetic Field Intensity..... 120

3.2 Arrott Plots and Curie Temperature..... 155

3.3 Susceptibility..... 174

3.4 Contribution from Interacting and Noninteracting Ni Atoms..... 184

B. Resistivity

3.5 Total Resistivity..... 209

3.6 Contribution from the Ni Addition..... 224

3.7 Contribution from Interacting Ni Atoms..... 246

C. Magnetization and Resistivity

3.8 Estimation of Enhancement Parameters..... 259

3.9 Field Dependence..... 262

CONCLUDING REMARKS..... 267

APPENDIX A: LEAST SQUARES FITTING METHOD..... 269

APPENDIX B: EVALUATION OF THE KAISER-DONIACH RESISTIVITY FUNCTION..... 272

APPENDIX C: T^2 COEFFICIENT OF THE SPIN-FLUCTUATION *RESISTIVITY IN THE LEDERER-MILLS AND* KAISER-DONIACH MODELS..... 273

APPENDIX D: ESTIMATION OF LOCAL ENHANCEMENT PARAMETERS FOR THE Pd_{1-x} Ni_x SYSTEM..... 275

ACKNOWLEDGEMENTS..... 277

REFERENCES..... 278

SPIN FLUCTUATIONS AND THE PARAMAGNETIC–FERROMAGNETIC TRANSITION IN PALLADIUM–RHODIUM–NICKEL ALLOYS

INTRODUCTION

The application of many-body techniques to explain electronic properties of the nearly ferromagnetic metals (e.g. Rh, Pd, and Pt and their alloys) increased our understanding of these materials. Many of their electronic properties (e.g., magnetic susceptibility, specific heat, and electrical resistivity) can be accounted for by a model which explicitly includes a strong intra-atomic Coulomb interaction between d band electrons of opposite spin. The intra-atomic Coulomb interaction decreases the energy needed to excite a spin fluctuation in the d band. Consequently, the number of spin fluctuations occurring at low temperatures increases, which in turn results in an increase in conduction-electron spin-fluctuation scattering, thereby increasing the low-temperature electrical resistivity. Furthermore, since the interaction favors parallel spin alignment, a lower applied magnetic field is required to attain the same magnetization as before, and the magnetic susceptibility is enhanced.

In this paper, spin fluctuations in the $(Pd_{95}Rh_5)_{1-x}Ni_x$ system are studied. There are several reasons why this system is well-suited for such an investigation. First, of the nearly ferromagnetic metals Rh, Pd, and Pt, and their alloys with one another, the $Pd_{95}Rh_5$ host has the highest magnetic susceptibility and is, therefore, expected to exhibit strong spin-fluctuation effects. Second, because of the already large amount of potential scattering that occurs in the host, we expect the contribution of the host to the total resistivity to be well represented by the resistivity of the Ni-free alloy. Third, Ni can be used as a probe to study the local enhancement of spin fluctuations around the Ni sites. Lastly, by varying the Ni concentration, the system can be observed as it transforms from a strongly paramagnetic system to a weakly ferromagnetic system.

Note: Manuscript submitted October 3, 1977.

This report begins with a review of many-body theory as it relates to spin-fluctuation effects in transition metals and alloys. Special emphasis is on the dynamic susceptibility and the electrical resistivity; various models for these two properties are reviewed. In the second chapter we discuss the experimental procedures. In the last chapter we present, analyze, and discuss first the magnetization data and then the electrical resistivity data for the $(Pd_{95}Rh_5)_{1-x}Ni_x$ system, and finally we discuss the implications of both the magnetization and resistivity data in regard to the local enhancement model.

CHAPTER I

REVIEW OF SPIN-FLUCTUATION THEORY FOR TRANSITION METALS

A. Magnetic Susceptibility

1.1 Background

The classical theory of free electrons in a metal completely failed to explain the magnetic susceptibility, χ, of a normal metal. On the basis of this theory one expected each electron to act as an independent magnetic dipole with a magnetic moment of one Bohr magneton, μ_B, and thus the susceptibility was expected to obey the Curie law

$$\chi = \frac{n\mu_B^2}{k_B T} , \qquad (1.1)$$

where n is the number of electrons per unit volume, T is the absolute temperature, and k_B is Boltzmann's constant. However, the observed room temperature susceptibilities of metals are orders of magnitude smaller than that predicted by the Curie law and are largely temperature independent.

The discrepancy was largely resolved when Pauli applied Fermi-Dirac statistics to the free electron gas. Fermi-Dirac statistics take into account the fact that no two electrons in the same spin state can have the same energy (the Pauli exclusion principle). This results in a ground state in which the electrons occupy all available single-particle energy states from zero to E_F, the Fermi energy. When a small magnetic field, H, is applied, the energy of each spin-up electron increases by an amount $\mu_B H$ and each spin-down electron decreases by the same amount. In the limit as $H \to 0$ it is only those spin-up electrons at the Fermi level that can reduce their energy by filling unoccupied spin-down states. Thus one expects the susceptibility to be proportional to the density of states at the Fermi level and to be

much lower than that predicted on a classical model. When the thermal energy is much less than the Fermi energy (i.e., $k_B T \ll E_F$), this Pauli susceptibility becomes[1]

$$\chi_p = \tfrac{1}{2} g^2 \mu_B^2 D(E_F)\left[1 + \frac{\pi^2}{6}(k_B T)^2 \left\{\frac{D''(E_F)}{D(E_F)} - \left(\frac{D'(E_F)}{D(E_F)}\right)^2\right\}\right], \quad (1.2)$$

where g is the Lande factor (g=2 for the free electron system), $D(E_F)$ is the density of states at the Fermi level per unit volume per spin-state, $D'(E) \equiv dD(E)/dE$ and $D''(E) \equiv d^2D(E)/dE^2$.

Since the Fermi energies in metals are orders of magnitude greater than $k_B T$, one would expect the above formula to apply even at room temperature after corrections have been made for contributions to the susceptibility from Landau diamagnetism[2] and Van Vleck orbital susceptibility[3]. However, this is not the case for the transition metals Pd, Pt, and Rh, which have susceptibilities that are roughly an order of magnitude higher than the prediction of the model.

Stoner[4] was one of the first to develop a model to explain the magnetic properties of these metal systems. He assumed that there existed an internal magnetic field which was proportional to the magnetization. The magnetization would then be given by

$$M = \chi_p(H + \lambda M) = \chi H \quad , \quad (1.3)$$

where H is the applied field and λM is the induced internal field. Solving for M and equating the coefficient of H with χ, one obtains

$$\chi = \frac{\chi_p}{1-\lambda\chi_p} \quad . \quad (1.4)$$

The measure of the enhancement is the Stoner enhancement factor, S, defined as

$$S \equiv \frac{\chi}{\chi_p} = \frac{1}{1-\lambda\chi_p} \quad . \quad (1.5)$$

The physical origin of this enhancement can be seen from the following argument. Suppose we have a metal like Pd, where the electronic structure can be described by two bands,

namely, an s band with nearly free electrons and a relatively low density of states, and a d band where the electrons are mostly localized around the ion cores and the density of states is high. Since, except for the d electrons on the same site, the electrons are effectively screened, it is these d electrons which account for most of the Coulomb interaction between the conduction electrons. Of these d electrons the strongest interaction will come from those which occupy the same state, and since the Pauli exclusion principle dictates that these two electrons must have opposite spins, the interaction is strongly spin dependent. As long as the number of spin-up electrons equals the number of spin-down electrons the interaction has the same effect on each band. But when an external magnetic field is applied, the number of spin-down electrons in the band increases at the expense of the electrons in the spin-up band. Thus a single spin-up (spin-down) d-electron interacts with more (fewer) spin-down (spin-up) d-electrons and the electrostatic contribution to the energy of the single electron increases (decreases). Since the interaction between parallel spins is small compared with the above interaction, the net effect is to increase the band splitting by an amount greater than the $2\mu_B H$ Zeeman splitting. The total energy of the system is then minimized by additional spin-up d-electrons changing their spin states. Thus, the on-site (intra-atomic) Coulomb interaction between opposite-spin d-electrons enhances the susceptibility over that of the Pauli susceptibility.

This interaction between the two spin bands is described in the tight binding limit by the Hubbard Hamiltonian[5]

$$\mathcal{H} = T + \tfrac{1}{2}U\sum_i (n_{i\uparrow}n_{i\downarrow} + n_{i\downarrow}n_{i\uparrow}) \quad , \tag{1.6}$$

where $n_{i\uparrow} = c^{\dagger}_{i\uparrow}c_{i\uparrow}$ is the number operator for spin-up d-electrons associated with the ith unit cell, $c^{\dagger}_{i\uparrow}$ and $c_{i\uparrow}$ are the creation and annihilation operators in the Wannier representation, U is a measure of the intra-atomic Coulomb interaction between electrons of opposite spin, and T represents the one-body terms in the Hamiltonian of the system.

If one could find the eigenfunctions of this Hamiltonian, then perturbation theory could be used to find the response of the system to a small magnetic field and the susceptibility would be obtained. However, the eigenfunctions are, in general, not known and a different approach, based upon linear response theory and many-body Green's functions concepts, is used. Linear response theory allows us to write the perturbed-state expectation value of an operator in terms of the unperturbed-state expectation value of a suitable combination of operators. So it is not necessary to know the wave function of the perturbed system, and, as we shall see later, by using many-body Green's function techniques, it is not even necessary to know the wave function of the unperturbed system.

In the next few sections these techniques are developed for a uniform, isotropic, paramagnetic system described by the Hubbard Hamiltonian. We begin by using the results of linear response theory to motivate a definition of the dynamic susceptibility and show that this definition is consistent with the usual definition of susceptibility. The dynamic susceptibility is written in terms of spin-density fluctuations of the unperturbed system. Finally, we indicate how the dynamic susceptibility can be calculated using many-body perturbation theory.

1.2 Dynamic Susceptibility from Linear Response Theory

If a space and time dependent magnetic field, whose component in the μ-direction ($\mu = x,y,z$) is $H_\mu(\vec{r},t)$, is applied to a magnetic system, the response to this field will be a magnetization whose component in the ν-direction is $M_\nu(\vec{r},t)$. The interaction of this field with the system changes the Hamiltonian of the system by the addition of the interaction term,

$$\mathcal{H}^{ext}(t) = -\int_V d\vec{r} \sum_\mu \hat{M}_\mu(\vec{r},t) H_\mu(\vec{r},t) \quad , \tag{1.7}$$

where $\hat{M}_\mu(\vec{r},t) = e^{i\mathcal{H}t}\hat{M}_\mu(\vec{r})e^{-i\mathcal{H}t}$ is the magnetization operator in the Heisenberg picture. The integration is to be taken over the system of volume V. For paramagnetic systems the interaction goes to zero in the limit of $H \to 0$, and linear response theory can be used to find the magnetization.

In this theory the interaction is assumed to be turned on at a time t_o. The change in the ensemble average of any dynamical operator $\hat{O}(t)$ is given by[6]

$$\langle\langle \hat{O}(t) \rangle\rangle_{ext} - \langle\langle \hat{O}(t) \rangle\rangle = -i\int_{t_o}^{t} dt' \, \mathrm{Tr}\left\{\rho_G[\hat{O}(t), \mathcal{H}^{ext}(t')]\right\}, \quad t > t_o, \tag{1.8}$$

where $\langle\langle \hat{O}(t) \rangle\rangle_{ext}$ is the ensemble average of $\hat{O}(t)$ for the externally perturbed system, $\langle\langle \hat{O}(t) \rangle\rangle$ is the ensemble average for the system before the interaction takes place, Tr is the trace, ρ_G is the grand canonical statistical operator for the system before the interaction and [,] are the commutator brackets. In the above equation and throughout this paper the units are chosen so that $\hbar = 1$.

The response of a system to an external magnetic field $H(\vec{r},t)$ may be found via Eq. 1.8, yielding the magnetization

$$\langle\langle \hat{M}_\nu(\vec{r},t) \rangle\rangle_{ext} = i\sum_\mu \int_{-\infty}^{\infty} dt' \int_V d\vec{r}' \, \theta(t-t') \cdot \mathrm{Tr}\left\{\rho_G[\hat{M}_\nu(\vec{r},t), \hat{M}_\mu(\vec{r}',t')]\right\} H_\mu(\vec{r}',t'), \tag{1.9}$$

where $\theta(t-t')$ is the step function and

$\theta(t-t') \cdot \mathrm{Tr}\left\{\rho_G[\hat{M}_\nu(\vec{r},t), \hat{M}_\mu(\vec{r}',t')]\right\}$ is a retarded correlation function. The important point to note here is that the linear response result has connected the quantum statistical average of the magnetization of a system with space time correlations of magnetization before the field is turned on.

In the zero temperature limit this equation reduces to the expectation value over the ground state:

$$\langle \hat{M}_\nu(\vec{r},t)\rangle_{ext} =$$

$$i\sum_\mu \int_{-\infty}^{\infty} dt' \int_V d\vec{r}\,' \,\theta(t-t')\langle[\hat{M}_\nu(\vec{r},t),\hat{M}_\mu(\vec{r}',t')]\rangle H_\mu(\vec{r}',t') \quad , \tag{1.10}$$

where the expectation value of the magnetization is over the ground state of the externally perturbed system and the expectation value of the magnetization correlations is over the ground state of the unperturbed system. As a matter of convenience we will from now on use this zero temperature form.

For time independent systems such as the Hubbard Hamiltonian, we can explicitly display the time-translational invariance that results by first noting that

$$\langle[\hat{M}(\vec{r},t),\hat{M}(\vec{r}',t')]\rangle =$$

$$\langle e^{i\mathcal{H}t}\hat{M}(\vec{r})e^{-i\mathcal{H}t}e^{i\mathcal{H}t'}\hat{M}(\vec{r}')e^{-i\mathcal{H}t'}\rangle - \langle e^{i\mathcal{H}t'}\hat{M}(\vec{r}')e^{-i\mathcal{H}t'}e^{i\mathcal{H}t}\hat{M}(\vec{r})e^{-i\mathcal{H}t}\rangle$$

$$= \langle e^{i\mathcal{H}(t-t')}\hat{M}(\vec{r})e^{-i\mathcal{H}(t-t')}\hat{M}(\vec{r}')\rangle - \langle \hat{M}(\vec{r}')e^{i\mathcal{H}(t-t')}\hat{M}(\vec{r})e^{-i\mathcal{H}(t-t')}\rangle$$

and finally,

$$\langle[\hat{M}(\vec{r},t),\hat{M}(\vec{r}',t')]\rangle = \langle[\hat{M}(\vec{r},t-t'),\hat{M}(\vec{r}')]\rangle \quad .$$

Thus

$$M_\nu(\vec{r},t) = i\sum_\mu \int_{-\infty}^{\infty} dt' \int_V d\vec{r}\,'\langle[\hat{M}_\nu(\vec{r},t-t'),\hat{M}_\mu(\vec{r}')]\rangle H_\mu(\vec{r}',t') \quad , \tag{1.11}$$

where $M_\nu(\vec{r},t) \equiv \langle \hat{M}_\nu(\vec{r},t)\rangle_{ext}$ and $\hat{M}(\vec{r},t-t') \equiv 0$ for $t'>t$. This equation takes on a somewhat simpler form if we take the Fourier transform of $M_\nu(\vec{r},t)$ and write the other functions in terms of their transforms. After some algebra we have

$$M_\nu(\vec{q},\omega) = \frac{i}{V}\sum_\mu \sum_{\vec{q}'} \langle[\hat{M}_\nu(\vec{q},\omega),\hat{M}_\mu(-\vec{q}')]\rangle H_\mu(\vec{q}',\omega) \quad . \tag{1.12}$$

The form of the Fourier transform used throughout this paper is

$$F(\vec{r},t) = \frac{1}{2\pi V}\sum_{\vec{q}} \int d\omega\, F(\vec{q},\omega)e^{i(\vec{q}\cdot\vec{r}-\omega t)} \quad , \tag{1.13}$$

and

$$F(\vec{q},\omega) = \int d\vec{r}\, dt\, F(\vec{r},t)e^{-i(\vec{q}\cdot\vec{r}-\omega t)} \quad , \tag{1.14}$$

which lead to the following relations:

$$\frac{1}{V}\int d\vec{r}\; e^{i(\vec{q}-\vec{q}')\cdot\vec{r}} = \delta_{\vec{q}\vec{q}'} \quad , \quad \frac{1}{V}\sum_{\vec{q}} e^{i\vec{q}\cdot(\vec{r}-\vec{r}')} = \delta(\vec{r}-\vec{r}')$$

$$\frac{1}{2\pi}\int dt\; e^{i(\omega-\omega')t} = \delta(\omega-\omega') \quad , \quad \frac{1}{2\pi}\int d\omega\; e^{i\omega(t-t')} = \delta(t-t')$$

where $\delta_{\vec{q}\vec{q}'}$ is the Kronecker delta and $\delta(\vec{r}-\vec{r}')$ is the Dirac delta function.

By defining the generalized susceptibility as

$$\chi^{\nu\mu}(\vec{q},\vec{q}',\omega) \equiv \frac{i}{V}\langle[\hat{M}_\nu(\vec{q},\omega),\hat{M}_\mu(-\vec{q}')]\rangle \quad , \tag{1.15}$$

Eq. 1.12 takes on the simplified form

$$M_\nu(\vec{q},\omega) = \sum_\mu\sum_{\vec{q}'}\chi^{\nu\mu}(\vec{q},\vec{q}',\omega)H_\mu(\vec{q}',\omega) \quad . \tag{1.16}$$

This equation can be further simplified for the case of homogeneous systems. In the case of a homogeneous system, the application of the field $\vec{H}(\vec{r})$ translated by a distance $\vec{r}_o$ must produce the same response $\vec{M}(\vec{r})$ translated by the same distance $\vec{r}_o$. Since the Fourier transform of the translated field is given by $e^{-\vec{q}\cdot\vec{r}_o}\vec{H}(\vec{q})$ and the Fourier transform of the translated response is $e^{-\vec{q}\cdot\vec{r}_o}\vec{M}(\vec{q})$, we have then from the above equation,

$$e^{-\vec{q}\cdot\vec{r}_o}M_\nu(\vec{q},\omega) = \sum_\mu\sum_{\vec{q}'}\chi^{\nu\mu}(\vec{q},\vec{q}',\omega)e^{-iq'\cdot\vec{r}_o}H_\mu(\vec{q}',\omega) \quad ,$$

which we write as

$$M_\nu(\vec{q},\omega) = \sum_\mu\sum_{\vec{q}'}\chi^{\nu\mu}(\vec{q},\vec{q}',\omega)e^{-i(\vec{q}'-\vec{q})\cdot\vec{r}_o}H_\mu(\vec{q}',\omega) \quad . \tag{1.17}$$

Since the left hand side is independent of $\vec{r}_o$ for any arbitrary $\vec{r}_o$, the right hand side must also be independent of $\vec{r}_o$. This implies that for homogeneous systems

$$\chi^{\nu\mu}(\vec{q},\vec{q}',\omega) = \chi^{\nu\mu}(\vec{q},\omega)\delta_{\vec{q}\vec{q}'} \tag{1.18}$$

and consequently,

$$\boxed{M_\nu(\vec{q},\omega) = \sum_\mu\chi^{\nu\mu}(\vec{q},\omega)H_\mu(\vec{q},\omega)} \quad . \tag{1.19}$$

where, by comparing Eq. 1.15 with Eq. 1.18, we have

$$\chi^{\nu\mu}(\vec{q},\omega) = \frac{i}{V}\langle[\hat{M}_\nu(\vec{q},\omega),\hat{M}_\mu(-\vec{q})]\rangle \quad . \tag{1.20}$$

The susceptibility can be written in terms of the magnetization directly by expressing, in the above equation, $\hat{M}(\vec{q},\omega)$ in terms of $\hat{M}(\vec{r},t)$. Then

$$\chi^{\nu\mu}(\vec{q},\omega) = \int d\vec{r}\; dt\left\{\frac{i}{V}\int d\vec{r}'\,\theta(t)\langle[\hat{M}_\nu(\vec{r}+\vec{r}',t),\hat{M}_\mu(\vec{r}')]\rangle\right\}e^{-i(\vec{q}\cdot\vec{r}-\omega t)}, \tag{1.21}$$

where we have explicitly displayed the causal response of the magnetization by the $\theta(t)$ factor.

We also see from the above equation that the Fourier transform of $\chi^{\nu\mu}(\vec{q},\omega)$ is

$$\chi^{\nu\mu}(\vec{r},t) = \frac{i}{V}\int d\vec{r}'\,\theta(t)\langle[\hat{M}_\nu(\vec{r}+\vec{r}',t),\hat{M}_\mu(\vec{r}')]\rangle \quad . \tag{1.22}$$

It is instructive to look at the implications of Eq.1.19 for the case of a plane wave magnetic field,

$$H_\mu(\vec{r},t) = H_o^\mu e^{i(\vec{q}_o\cdot\vec{r}-\omega_o t)} \quad . \tag{1.23}$$

Then,

$$H_\mu(\vec{q},\omega) = 2\pi V\delta_{\vec{q}\vec{q}_o}\,\delta(\omega-\omega_o)H_o^\mu \quad . \tag{1.24}$$

From Eq. 1.19 the transform of the magnetization is

$$M_\nu(\vec{q},\omega) = 2\pi V\delta_{\vec{q}\vec{q}_o}\,\delta(\omega-\omega_o)\sum_\mu \chi^{\nu\mu}(\vec{q},\omega)H_o^\mu \tag{1.25}$$

and the magnetization is then

$$\begin{aligned} M_\nu(\vec{r},t) &= \frac{1}{2\pi V}\sum_\mu\sum_{\vec{q}}\int d\omega\;\chi^{\nu\mu}(\vec{q},\omega)\;2\pi V\delta_{\vec{q}\vec{q}_o}\,\delta(\omega-\omega_o)H_o^\mu \\ &= \sum_\mu \chi^{\nu\mu}(\vec{q}_o,\omega_o)H_o^\mu e^{i(\vec{q}_o\cdot\vec{r}-\omega_o t)} \end{aligned} \tag{1.26}$$

So we see for this case the amplitude of the magnetization, M_o^ν, is

$$M_o^\nu = \sum_\mu \chi^{\nu\mu}(\vec{q}_o,\omega_o)H_o^\mu \tag{1.27}$$

and for the case of a uniform static field ($\vec{q}_o=0$, $\omega_o=0$)

$$M_o^\nu = \sum_\mu \chi^{\nu\mu}(0,0)H_o^\mu \tag{1.28}$$

which is the usual definition of magnetic susceptibility. Thus, we see the measured static susceptibility can be calculated by evaluating Eq. 1.20 in the limit of $q\to 0$, $\omega\to 0$.

1.3 The Dynamic Susceptibility and the Two-particle Green's Function

So far we have shown a relationship between the dynamic susceptibility and the magnetization correlations in the system at zero field. However, it is still not possible to calculate the susceptibility in most cases because the ground state wave function of the system is in general not known. One way around this is the use of the powerful techniques of many-body perturbation theory. In this theory, time-ordered Green's functions are calculated and, although they do not have the full informational content of the ground state wave function, they do allow the calculation of ground state expectation values. Also, the extension to finite temperatures allows us to calculate quantum mechanical ensemble averages without a complete knowledge of the state of the system.

To use the many-body perturbation theory to calculate the dynamic susceptibility we write the spin-density operator, $\hat{S}_\nu(\vec{r},t)$, for a spin-$\frac{1}{2}$ electron system in the second quantization form[7]:

$$\hat{S}_\nu(\vec{r},t) = \tfrac{1}{2}\sum_{\alpha\beta}\psi_\alpha^\dagger(\vec{r},t)\left[\sigma_\nu\right]_{\alpha\beta}\psi_\beta(\vec{r},t) \qquad (1.29)$$

where σ_ν is the Pauli spin matrix in the ν direction; $\psi_\alpha^\dagger(\vec{r},t)$ and $\psi_\beta(\vec{r},t)$ are the creation and annihilation field operators in the Heisenberg picture; α and β are the spin direction indices. Because of the double spin sum, the spin-density operator consists of more than one term. For example,

$$\hat{S}_z(\vec{r},t) = \tfrac{1}{2}\{\psi_\uparrow^\dagger(\vec{r},t)\psi_\uparrow(\vec{r},t) - \psi_\downarrow^\dagger(\vec{r},t)\psi_\downarrow(\vec{r},t)\} \ . \qquad (1.30)$$

A significant simplification occurs if the spin-density operators, $\hat{S}_\pm(\vec{r},t)$, defined by

$$\hat{S}_\pm(\vec{r},t) = \hat{S}_x(\vec{r},t) \pm i\hat{S}_y(\vec{r},t), \qquad (1.31)$$

can be used instead of $\hat{S}_\nu(\vec{r},t)$, for then

$$\hat{S}_+(\vec{r},t) = \psi_\uparrow^\dagger(\vec{r},t)\psi_\downarrow(\vec{r},t) \qquad (1.32)$$

and

$$\hat{S}_-(\vec{r},t) = \psi_\downarrow^\dagger(\vec{r},t)\psi_\uparrow(\vec{r},t). \qquad (1.33)$$

Thus, for a homogeneous, isotropic spin system, where the dynamic susceptibility can be written as

$$\chi(\vec{q},\omega) = \chi^{xx}(\vec{q},\omega) = \chi^{yy}(\vec{q},\omega) = \chi^{zz}(\vec{q},\omega), \qquad (1.34)$$

the susceptibility can be written directly in terms of the $\hat{S}_\pm(\vec{r},t)$ spin-density operators. To see this, first note from the definition of these operators, that

$$[\hat{S}_-(\vec{r},t),\hat{S}_+(\vec{r}',t')] =$$
$$[\hat{S}_x(\vec{r},t),\hat{S}_x(\vec{r}',t')] + [\hat{S}_y(\vec{r},t),\hat{S}_y(\vec{r}',t')]$$
$$-i\{[\hat{S}_y(\vec{r},t),\hat{S}_x(\vec{r}',t')] - [\hat{S}_x(\vec{r},t),\hat{S}_y(\vec{r}',t')]\}. \qquad (1.35)$$

Then, since for an isotropic system the above equation must be invariant under an x,y interchange, we have

$$[\hat{S}_-(\vec{r},t),\hat{S}_+(\vec{r}',t')] = 2[\hat{S}_\nu(\vec{r},t),\hat{S}_\nu(\vec{r}',t')] \quad . \qquad (1.36)$$

From this equation and noting that the magnetization operator is related to the spin-density operator by

$$\hat{M}_\nu(\vec{r},t) = -g\mu_B\hat{S}_\nu(\vec{r},t), \qquad (1.37)$$

the susceptibility given by Eq. 1.21 can be written as

$$\chi(\vec{q},\omega) = \frac{ig^2\mu_B^2}{2V}\int d\vec{r}\,dt\,d\vec{r}'\,\theta(t-t')\langle[\hat{S}_-(\vec{r}+\vec{r}',t),\hat{S}_+(\vec{r})]\rangle e^{-i(\vec{q}\cdot\vec{r}-\omega t)} \qquad (1.38)$$

or

$$\chi(\vec{q},\omega) = \frac{ig^2\mu_B^2}{2V}\int d\vec{r}\,dt\,d\vec{r}'\,\chi_R^{-+}(\vec{r}+\vec{r}',t;\vec{r}',0)e^{-i(\vec{q}\cdot\vec{r}-\omega t)} \qquad (1.39)$$

where

$$\chi_R^{-+}(\vec{r},t;\vec{r}',t') = i\langle[\hat{S}_-(\vec{r},t),\hat{S}_+(\vec{r}',t')]\rangle\theta(t-t') \qquad (1.40)$$
$$= i\langle[\psi_\downarrow^\dagger(\vec{r},t)\psi_\uparrow(\vec{r},t),\psi_\uparrow^\dagger(\vec{r}',t')\psi_\downarrow(\vec{r}',t')]\rangle\theta(t-t'),$$

which is a two-particle retarded Green's function.

What we have just shown is that the dynamic susceptibility of a homogeneous, isotropic system can be written directly in terms of a single two-particle retarded Green's function. Although many-body perturbation theory is associated with time-ordered Green's functions and not retarded

Green's functions, once the corresponding time-ordered function is calculated the retarded function is easily obtained, as we shall see later. The time-ordered Green's function which is appppropriate for finding the susceptibility is given by

$$\chi_T^{-+}(\vec{r},t;\vec{r}',t') = i\langle T\,\psi_\downarrow^\dagger(\vec{r},t)\psi_\uparrow(\vec{r},t)\psi_\uparrow^\dagger(\vec{r}',t')\psi_\downarrow(\vec{r}',t')\rangle\ , \tag{1.41}$$

where T is the time-ordering operator.

1.4 Many-body techniques and Spin-density Fluctuations

In this section the basic techniques of many-body perturbation theory are outlined and are applied to the time-ordered Green's function defined in the previous section. Then, using Feynman diagrams, we show how this Green's function may be interpreted as a spin-density fluctuation.

In order to use this perturbation theory, the Hamiltonian representing the system in the absence of a external magnetic field is divided into two parts, that is,

$$\mathcal{H} = \mathcal{H}_o + \mathcal{H}'\ , \tag{1.42}$$

where $\mathcal{H}_o$ is taken to be the unperturbed system and $\mathcal{H}'$ the perturbing part of the total system. In the case we will be considering, $\mathcal{H}_o$ is taken to consist of the one-body terms in the Hamiltonian and $\mathcal{H}'$ all the two-body interaction terms. For example, $\mathcal{H}'$ for the Hubbard Hamiltonian would be the intra-atomic Coulomb interaction term, which describes the on-site interaction between opposite-spin electrons.

The time-ordered Green's function of the total system may be found by expanding this function in an infinite series in which all expectation values are now to be taken over the unperturbed ground state. The expectation values are then written in terms of single particle Green's functions of the unperturbed system. The Green's functions of the unperturbed system are assumed to be known.

The expansion of the time-ordered Green's function given in Eq. 1.41 is given by[8]

$$\chi_T^{-+}(\vec{r},t;\vec{r}',t') =$$

$$i\sum_{n=0}^{\infty}\frac{(-i)^n}{n!}\int_{-\infty}^{\infty} dt_1\, dt_2 \ldots dt_n$$

$$\times\langle T\mathcal{H}'(t_1)\mathcal{H}'(t_2)\ldots\mathcal{H}'(t_n)\psi_\downarrow^\dagger(\vec{r},t)\psi_\uparrow(\vec{r},t)\psi_\uparrow^\dagger(\vec{r}',t')\psi_\downarrow(\vec{r}',t')\rangle \ , \tag{1.43}$$

where all the operators are expressed in the interaction picture. A factor, which is equal to the right hand side of Eq. 1.43 with the field operators removed and which divides into this side of the equation, has been deleted. The reason for this deletion will become clear shortly. First we point out that the two-body interaction term of the Hamiltonian can be written as[9]

$$\mathcal{H}'(t_i) =$$

$$\tfrac{1}{2}\sum_{\substack{\alpha\alpha'\\ \beta\beta'}}\int d\vec{r}_i\, d\vec{r}_i'\, U_{\alpha\alpha',\beta\beta'}(\vec{r}_i,\vec{r}_i')\psi_\alpha^\dagger(\vec{r}_i,t_i)\psi_{\alpha'}^\dagger(\vec{r}_i',t_i')\psi_{\beta'}(\vec{r}_i',t_i')\psi_\beta(\vec{r}_i,t_i), \tag{1.44}$$

where $U_{\alpha\alpha',\beta\beta'}(\vec{r}_i,\vec{r}_i')$ is the matrix element of the two-body interaction. From this we can see that each term in the expansion will consist of the expectation value of the time-ordered product of creation and annihilation operators. Wick's theorem[10] reduces this expectation value to a sum of products of single particle Green's functions, where the single-particle Green's function is defined by

$$iG_{\alpha\beta}(\vec{r},t;\vec{r}',t') = \langle T\psi_\alpha(\vec{r},t)\psi_\beta^\dagger(\vec{r}',t')\rangle \ . \tag{1.45}$$

As a bookkeeping device, which keeps track of all the terms in the expansion, Feynman diagrams are used. A set of diagrams represents a term in the expansion. The linked Cluster theorem[11] shows that only those terms which are represented by a topologically connected diagram contribute to the sum. The reason for this is that the terms represented by disconnected diagrams are divided out by the denominator that was deleted. Thus the expansion given above is correct if only the terms which can be represented by connected diagrams are used.

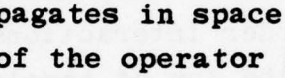
To represent a term in the expansion, a set of rules and definitions is used. A solid line with an arrow is used to represent the single-particle Green's function,

$G_{\alpha\beta}(\vec{r},t;\vec{r}',t') =$



and the representation of the interaction matrix element is

$U_{\alpha\alpha',\beta\beta'}(\vec{r}_i,\vec{r}_i') =$



This single-particle Green's function diagram is "described" by saying that $\psi_\beta^\dagger(\vec{r}',t')$ creates an electron at point $(\vec{r}',t')$ and that the electron then propagates in space until at a time t and at point $\vec{r}$ the action of the operator $\psi_\alpha(\vec{r},t)$ annihilates it. An electron traveling backwards in time describes the propagation of a hole.

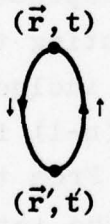
The lowest order term in the expansion of χ_T^{-+} is

$$^0\chi_T^{-+}(\vec{r},t;\vec{r}',t') = i\langle T\psi_\downarrow^\dagger(\vec{r},t)\psi_\uparrow(\vec{r},t)\psi_\uparrow^\dagger(\vec{r}',t')\psi_\downarrow(\vec{r}',t')\rangle \ , \tag{1.46}$$

which from Wick's theorm is

$$^0\chi_T^{-+}(\vec{r},t;\vec{r}',t') = iG_{\uparrow\uparrow}(\vec{r},t;\vec{r}',t')G_{\downarrow\downarrow}(\vec{r}',t';\vec{r},t) \ . \tag{1.47}$$

This zero order term is represented by the Feynman diagram,



which can be "described" as a transverse spin-density fluctuation of the unperturbed system. The point $(\vec{r}',t')$ represents the action of the transverse spin-density creation operator defined by,

$$\hat{S}_+(\vec{r}',t') = \psi_\uparrow^\dagger(\vec{r}',t')\psi_\downarrow(\vec{r}',t') \ , \tag{1.48}$$

and the point $(\vec{r},t)$ represents the action of the transverse spin-density annihilation operator,

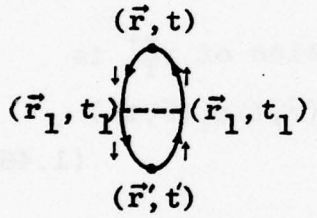
$$\hat{S}_-(\vec{r},t) = \psi_\downarrow^\dagger(\vec{r},t)\psi_\uparrow(\vec{r},t) \quad . \tag{1.49}$$

The fluctuation is then written as

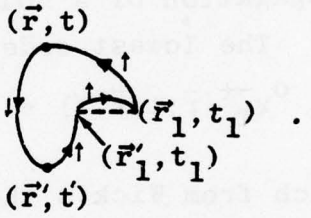
$$\chi_T^{-+}(\vec{r},t;\vec{r}',t') = i\langle T\,\hat{S}_-(\vec{r},t)\,\hat{S}_+(\vec{r}',t')\rangle \quad . \tag{1.50}$$

The operator $\hat{S}_+(\vec{r}',t')$ is viewed as creating at a time t' and point $\vec{r}'$ an electron-hole pair of opposite spin. It does this by spin-flipping an electron at $(\vec{r}',t')$. The pair then propagates in space until at a time t and at point $\vec{r}$ the action of the operator $\hat{S}_-(\vec{r},t)$ spin-flips the electron again and the electron-hole pair is annihilated, ending the spin-density fluctuation.

The second term in the expansion given by Eq. 1.43 includes all first order interactions and can be represented diagrammatically by the sum of topologically distinct diagrams such as,



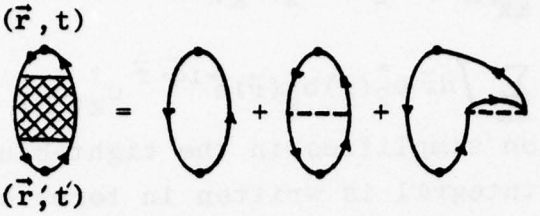
and



.

It is possible by using Wick's theorem and the Linked Cluster theorem to make a set of rules (the Feynman rules) which allow a one to one correspondence between an expansion term and the diagrams representing the term. For example, the nth term in the expansion includes all topologically distinct diagrams consisting of (n-1) interactions (-------) and 2n electron lines (——→——). From the Linked Cluster theorem, only those diagrams in which the interactions and electron lines are continuously linked contribute to the final sum. Other rules define how the vertices are to be labeled, what variables are to be integrated over, and what the coefficient of each diagram is. Once the Feynman rules are known, one can by looking at any single diagram write down the

corresponding integral in the expansion. The total expansion given in Eq. 1.43 is diagrammatically given by

$\chi_T^{-+}(\vec{r},t;\vec{r}',t') =$ 

Viewed in this manner a spin fluctuation which starts at $(\vec{r}',t')$ and ends at $(\vec{r},t)$ is the sum of the spin fluctuation in the noninteracting system plus all possible interactions which can take place during the fluctuation.

1.5 The Dynamic Susceptibility in the Bloch Representation

The expressions in the previous sections have in general been given in the coordinate representation. However, when considering the intra-atomic Coulomb interaction as approximated by the Hubbard Hamiltonian, it is more convenient to use the Bloch representation. Also, the dynamic susceptibility can be written in a somewhat simpler form in this representation. To see this we first write the transverse spin-density operators, $\hat{S}_{\pm}(\vec{r},t)$, in Eq. 1.38 in terms of their Fourier transforms. The dynamic susceptibility for the homogeneous, isotropic system then becomes

$$\chi(\vec{q},\omega) = \frac{ig^2\mu_B^2}{2V}\int dt\langle[\hat{S}_-(\vec{q},t),\hat{S}_+(-\vec{q})]\rangle\theta(t)e^{i\omega t}. \quad (1.51)$$

Second, we write the field operators in terms of Bloch operators by using the relations

$$\psi_\alpha^\dagger(\vec{r}) = \sum_{\vec{k}} b_{\vec{k}}^*(\vec{r})c_{\vec{k},\alpha}^\dagger \quad (1.52)$$

and

$$\psi_\alpha(\vec{r}) = \sum_{\vec{k}} b_{\vec{k}}(\vec{r})c_{\vec{k},\alpha} \quad , \quad (1.53)$$

where the $b_{\vec{k}}(\vec{r})$'s are the Bloch functions and $c_{\vec{k}}^\dagger$ and $c_{\vec{k}}$ are the creation and annihilation operators for the Bloch state,

e.g., $\langle\vec{r}|c_{\vec{k}}^\dagger|0\rangle = \langle\vec{r}|\vec{k}\rangle = b_{\vec{k}}(\vec{r})$, (1.53)

$|0\rangle$ being the vacuum state. The transverse spin-density

creation operator is then given by

$$\hat{S}_+(\vec{r}) = \sum_{\vec{k}\vec{k}'} b^*_{\vec{k}}(\vec{r})\, b_{\vec{k}'}(\vec{r})\, c^\dagger_{\vec{k}\uparrow} c_{\vec{k}'\downarrow} \qquad (1.55)$$

and

$$\hat{S}_+(\vec{q}) = \sum_{\vec{k}\vec{k}'} \int d\vec{r}\; b^*_{\vec{k}}(\vec{r})\, b_{\vec{k}'}(\vec{r})\, e^{-i\vec{q}\cdot\vec{r}}\, c^\dagger_{k\uparrow} c_{k\downarrow} \; . \qquad (1.56)$$

This expression simplifies in the tight-binding approximation, if the integral is written in terms of Wannier functions, $W(\vec{r}-\vec{R}_i)$, where $\vec{R}_i$ is the coordinate vector of the ith lattice site. Noting that

$$b_{\vec{k}}(\vec{r}) = \frac{1}{\sqrt{N}} \sum_i e^{i\vec{k}\cdot\vec{R}_i}\, W(\vec{r}-\vec{R}_i) \quad , \qquad (1.57)$$

where N is the number of lattice points, $\hat{S}_+(\vec{q})$ becomes

$$\hat{S}_+(\vec{q}) =$$

$$\frac{1}{N} \sum_{\vec{k}\vec{k}'} \sum_{ii'} \int d\vec{r}\; W^*(\vec{r}-\vec{R}_i) W(\vec{r}-\vec{R}_{i'})\, e^{-i\vec{k}\cdot\vec{R}_i} e^{i\vec{k}'\cdot\vec{R}_{i'}} e^{-i\vec{q}\cdot\vec{r}}\, c^\dagger_{\vec{k}\uparrow} c_{\vec{k}'\downarrow}$$

$$= \frac{1}{N} \sum_{\vec{k}\vec{k}'} \sum_{ii'} \int d\vec{r}\; W^*(\vec{r}) W(\vec{r}+\vec{R}_i-\vec{R}_{i'})\, e^{i(\vec{k}'-\vec{k}-\vec{q})\cdot\vec{R}_i} e^{-i\vec{k}'\cdot(\vec{R}_i-\vec{R}_{i'})} e^{-i\vec{q}\cdot\vec{r}}\, c^\dagger_{\vec{k}\uparrow} c_{\vec{k}'\downarrow}$$

$$= \sum_{\vec{k}\vec{k}'} \sum_{\Delta\vec{R}} \int d\vec{r}\; W^*(\vec{r}) W(\vec{r}+\Delta\vec{R})\, \delta_{\vec{k}',\vec{k}+\vec{q}}\, e^{-i\vec{k}'\cdot\Delta\vec{R}} e^{-i\vec{q}\cdot\vec{r}}\, c^\dagger_{\vec{k}\uparrow} c_{\vec{k}'\downarrow}$$

$$= \sum_{\vec{k}} \sum_{\Delta\vec{R}} \int d\vec{r}\; W^*(\vec{r}) W(\vec{r}+\Delta\vec{R})\, e^{-i(\vec{k}+\vec{q})\cdot\Delta\vec{R}} e^{-i\vec{q}\cdot\vec{r}}\, c^\dagger_{\vec{k}\uparrow} c_{\vec{k}+\vec{q},\downarrow} \; . \qquad (1.58)$$

It is now assumed that the overlap integrals for $\Delta\vec{R} \neq 0$ can be ignored in comparison to the $\Delta\vec{R} = 0$ integral. Then

$$\hat{S}_+(\vec{q}) = \sum_{\vec{k}} F^*(\vec{q})\, c^\dagger_{\vec{k}\uparrow} c_{\vec{k}+\vec{q},\downarrow} \quad , \qquad (1.59)$$

where

$$F(\vec{q}) = \int d\vec{r}\; |W(\vec{r})|^2 e^{i\vec{q}\cdot\vec{r}} \quad . \qquad (1.60)$$

The form factor, $F(\vec{q})$, is substantially the form factor of the d-state atomic orbital in this tight binding approximation. For $\vec{q}$ small, $|F(\vec{q})| \sim 1$; $|F(0)| = 1$. In a similar manner

$$\hat{S}_-(\vec{q}) = F^*(\vec{q}) \sum_{\vec{k}} c^\dagger_{\vec{k}\downarrow}(t)\, c_{\vec{k}+\vec{q},\uparrow}(t) \quad . \qquad (1.61)$$

After substituting these expressions into Eq. 1.51 and relabeling, we obtain the desired result for the dynamic

susceptibility,

$$\chi(\vec{q},\omega) = \frac{ig^2\mu_B^2}{2V}|F(\vec{q})| \times \sum_{\vec{k}\vec{k}'}\int dt\, \langle[c^\dagger_{\vec{k}\downarrow}(t)c_{\vec{k}+\vec{q},\uparrow}(t), c^\dagger_{\vec{k}'+\vec{q},\uparrow}c_{\vec{k}'\downarrow}]\rangle\theta(t)e^{i\omega t} \quad . \tag{1.62}$$

It is convenient to define the two-particle Green's function, $\chi_R^{-+}(\vec{q},\omega)$, as

$$\chi_R^{-+}(\vec{q},\omega) \equiv \frac{i}{V}\sum_{\vec{k}\vec{k}'}\int dt\, \langle[c^\dagger_{\vec{k}'\downarrow}(t)c_{\vec{k}+\vec{q},\uparrow}(t), c^\dagger_{\vec{k}'+\vec{q},\uparrow}c_{\vec{k}'\downarrow}]\rangle\theta(t)e^{i\omega t}, \tag{1.63}$$

for then

$$\chi(\vec{q},\omega) = \tfrac{1}{2}g^2\mu_B^2|F(\vec{q})|^2\,\chi_R^{-+}(\vec{q},\omega) \quad . \tag{1.64}$$

The corresponding time-ordered Green's function is given by

$$\chi_T^{-+}(\vec{q},\omega) = \frac{i}{V}\sum_{\vec{k}\vec{k}'}\int dt\, \langle T\, c^\dagger_{\vec{k}\downarrow}(t)c_{\vec{k}+\vec{q},\uparrow}(t)c^\dagger_{\vec{k}'+\vec{q},\uparrow}c_{\vec{k}'\downarrow}\rangle e^{i\omega t} \quad , \tag{1.65}$$

where it can be shown[12] that the real and imaginary parts of the time-ordered and of the retarded functions are related by

$$\mathrm{Re}\,\chi_R^{-+}(\vec{q},\omega) = \mathrm{Re}\,\chi_T^{-+}(\vec{q},\omega) \tag{1.66a}$$

and

$$\mathrm{Im}\,\chi_R^{-+}(\vec{q},\omega) = \frac{\omega}{|\omega|}\mathrm{Im}\,\chi_T^{-+}(\vec{q},\omega) \quad ; \tag{1.66b}$$

thus the two Green's functions are identical for $\omega>0$.

1.6 Many-body Perturbation Theory as Applied to the Intra-atomic Coulomb Interaction Term

The next three sections concern the dynamic susceptibility for systems in which the intra-atomic Coulomb interaction can be taken into account by means of the Hubbard Hamiltonian,

$$\mathcal{H} = \sum_{\vec{k}\alpha}\varepsilon_{\vec{k}}c^\dagger_{\vec{k},\alpha}c_{\vec{k},\alpha} + \frac{U}{2}\sum_{i\alpha}n_{i,\alpha}n_{i,-\alpha} \quad , \tag{1.67}$$

where $\varepsilon_{\vec{k}}$ is the single particle energy of a Bloch electron in $\vec{k}$ state, U is the intra-atomic Coulomb interaction energy of two electrons of opposite spin in the same Wannier state, and

$$n_{i,\alpha} = c^\dagger_{i\alpha}c_{i\alpha} \quad , \tag{1.68}$$

where the $c^{\dagger}_{i\alpha}$ and $c_{i\alpha}$ are the creation and annihilation operators for the Wannier state, e.g.

$$\langle \vec{r}|c^{\dagger}_{i}|0\rangle = \langle \vec{r}|i\rangle = W(\vec{r}-\vec{R}_i) \quad . \tag{1.69}$$

It will be convenient to also express the intra-atomic Coulomb interaction term in terms of Bloch operators. This can be done by using the following relations between the Wannier creation and annihilation operators and the Bloch creation and annihilation operators:

$$c^{\dagger}_{i\alpha} = \frac{1}{\sqrt{N}} e^{-i\vec{k}\cdot\vec{R}_i} c^{\dagger}_{\vec{k}\alpha} \tag{1.70a}$$

and

$$c_{i\alpha} = \frac{1}{\sqrt{N}} e^{i\vec{k}\cdot\vec{R}_i} c_{\vec{k}\alpha} \quad . \tag{1.70b}$$

Then after some algebra, we have for the interaction term

$$\mathcal{H}' = \frac{U}{2N} \sum_{\vec{k}} \sum_{\vec{k}'} \sum_{\vec{k}''} \sum_{\alpha} c^{\dagger}_{\vec{k}+\vec{k}'',\alpha} c_{\vec{k},\alpha} c^{\dagger}_{\vec{k}',-\alpha} c_{\vec{k}'+\vec{k}'',-\alpha} \quad . \tag{1.71}$$

In using many-body perturbation theory, we will treat this interaction term as the perturbing term, and the remaining term given by

$$\mathcal{H}_o = \sum_{\vec{k}\alpha} \varepsilon_{\vec{k}} c^{\dagger}_{\vec{k}\alpha} c_{\vec{k}\alpha} \tag{1.72}$$

will be treated as the unperturbed system.

Expanding the two-particle Green's function, $\chi_T^{-+}(\vec{q},\omega)$, as was done for $\chi_T^{-+}(\vec{r},t;\vec{r},t)$ in Eq. 1.43, we have

$$\chi_T^{-+}(\vec{q},\omega) = \frac{i}{V} \sum_{n=0}^{\infty} \frac{(-i)^n}{n!} \int dt_1\, dt_2 \ldots dt_n \sum_{\vec{k}\vec{k}'} \int dt \times \langle T\, \mathcal{H}'(t_1)\mathcal{H}'(t_2)\ldots\mathcal{H}'(t_n) c^{\dagger}_{\vec{k}\downarrow}(t) c_{\vec{k}+\vec{q},\uparrow}(t) c^{\dagger}_{\vec{k}'+\vec{q},\uparrow} c_{\vec{k}'\downarrow}\rangle \times e^{i\omega t} \quad . \tag{1.73}$$

Again we use Wick's theorem to reduce this expectation value of time-ordered product to a sum of products of single particle Green's functions for the unperturbed system. These Green's functions are of the form

$$iG^{o}_{\alpha\alpha'}(\vec{k},t;\vec{k}',t') = \langle T\, c_{\vec{k}\alpha}(t) c^{\dagger}_{\vec{k}'\alpha'}(t')\rangle \quad . \tag{1.74}$$

For $t>t'$,

$$iG^o_{\alpha\alpha}(\vec{k},t;\vec{k}',t') = \langle e^{i\mathcal{K}_o t} c_{\vec{k}\alpha} e^{-i\mathcal{K}_o t} e^{i\mathcal{K}_o t'} c^\dagger_{\vec{k}'\alpha'} e^{-i\mathcal{K}_o t'} \rangle$$
$$= e^{iE_o t} \langle c_{\vec{k}\alpha} e^{-i\mathcal{K}_o t} e^{i\mathcal{K}_o t'} c^\dagger_{\vec{k}'\alpha'} \rangle e^{-E_o t'}$$
$$= e^{iE_o t} e^{-i(E_o+\varepsilon_{\vec{k}})t} \langle c_{\vec{k}\alpha} c^\dagger_{\vec{k}'\alpha'} \rangle e^{i(E_o+\varepsilon_{\vec{k}'})t'} e^{-iE_o t'}$$
$$= e^{-i\varepsilon_{\vec{k}}t} e^{i\varepsilon_{\vec{k}'}t'} \langle c_{\vec{k}\alpha} c^\dagger_{\vec{k}'\alpha'} \rangle \quad . \tag{1.75}$$

Note that, if the state (labeled by $\vec{k}'\alpha'$) is occupied (i.e. if $b_{\vec{k}'\alpha'}(\vec{r})$ is in the Slater determinant representing the ground state) then $\langle c_{\vec{k}\alpha} c^\dagger_{\vec{k}'\alpha'} \rangle = 0$. Otherwise $\langle c_{\vec{k}\alpha} c^\dagger_{\vec{k}'\alpha'} \rangle = \delta_{\vec{k}\vec{k}'}\delta_{\alpha\alpha'}$. Now making the simplifying assumption that $\varepsilon_{\vec{k}}$ is a monotonic increasing function of $\vec{k}$ for all $\vec{k}$ in the same direction, these two equations can be combined into

$$\langle c_{\vec{k}\alpha} c^\dagger_{\vec{k}'\alpha'} \rangle = \delta_{\vec{k}\vec{k}'}\delta_{\alpha\alpha'}\theta(|\vec{k}|-|\vec{k}_F|) \quad , \tag{1.76}$$

and then

$$iG^o_{\alpha\alpha}(\vec{k},t;\vec{k}',t') = e^{-i\varepsilon_{\vec{k}}(t-t')}\delta_{\vec{k}\vec{k}'}\delta_{\alpha\alpha'}\theta(|\vec{k}|-|\vec{k}_F|)$$
$$= iG^o_\alpha(\vec{k},t-t')\delta_{\vec{k}\vec{k}'}\delta_{\alpha\alpha'} \quad , \tag{1.77}$$

where $\vec{k}_F$ is the Fermi momentum in the $\vec{k}$ direction and where

$$iG^o_\alpha(\vec{k},t) = e^{-i\varepsilon_{\vec{k}}t}\theta(|\vec{k}|-|\vec{k}_F|) \quad , \quad t>0 \quad . \tag{1.78}$$

Similarly, for $t<t'$,

$$iG^o_{\alpha\alpha}(\vec{k},t;\vec{k}',t') = -e^{i\varepsilon_{\vec{k}}t}\delta_{\vec{k}\vec{k}'}\delta_{\alpha\alpha'}\theta(|\vec{k}_F|-|\vec{k}|)$$
$$= iG^o_\alpha(\vec{k},t-t')\delta_{\vec{k}\vec{k}'}\delta_{\alpha\alpha'} \quad , \tag{1.79}$$

where

$$iG^o_\alpha(\vec{k},t) = -e^{i\varepsilon_{\vec{k}}t}\theta(|\vec{k}_F|-|\vec{k}|) \quad , \quad t<0 \quad . \tag{1.80}$$

The two cases can be written as a single case, if we use the ω Fourier transform of $G^o_\alpha(\vec{k},t)$, which is

$$G^o_\alpha(\vec{k},\omega) = \frac{1}{\omega-\varepsilon_{\vec{k}}-i\delta_{\vec{k}}} , \tag{1.81}$$

where $\delta_{\vec{k}}=\delta$, if $|\vec{k}|>|\vec{k}_F|$ and $\delta_{\vec{k}}=-\delta$, if $|\vec{k}|<|\vec{k}_F|$, and where, after the Fourier inversion to $G^o_\alpha(\vec{k},t)$, $\delta\to 0$.

As was done for the transverse spin-density fluctuations, $\chi^{-+}_T(\vec{r},t;\vec{r}',t')$, we can write the expansion for the

transverse susceptibility, $\chi_T^{-+}(\vec{q},\omega)$ in terms of Feynman diagrams. Each interaction factor is represented by a dashed line,

$$t_i \text{-------} t_i = U/2 \ ,$$

and each single particle Green's function is represented by the line,

$$t' \xrightarrow[\vec{k}\alpha]{} t = G_\alpha^o(\vec{k},t-t') = -i\langle T\, c_{\vec{k}\alpha}(t) c^\dagger_{\vec{k}\alpha}(t')\rangle$$

or

$$t' \xleftarrow[\vec{k}\alpha]{} t = G_\alpha^o(\vec{k},t'-t) = -i\langle T\, c_{\vec{k}\alpha}(t') c^\dagger_{\vec{k}\alpha}(t)\rangle \ ,$$

where the arrow points from creation to annihilation.

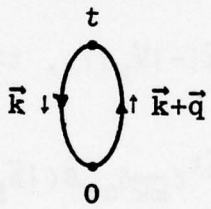
The lowest order term in the expansion of Eq. 1.73 is

$$^o\chi_T^{-+}(\vec{q},\omega) = \frac{i}{V}\sum_{\vec{k}\vec{k}'} \int dt\, \langle T\, c^\dagger_{\vec{k},\downarrow}(t) c_{\vec{k}+\vec{q},\uparrow}(t) c^\dagger_{\vec{k}'+\vec{q},\uparrow} c_{\vec{k}',\downarrow}\rangle e^{i\omega t} \ , \tag{1.82}$$

and, after applying Wick's theorem and the Linked Cluster theorem and summing over $\vec{k}'$,

$$^o\chi_T^{-+}(\vec{q},\omega) = \frac{i}{V}\sum_{\vec{k}} \int dt\, G^o_\downarrow(\vec{k},-t) G^o_\uparrow(\vec{k}+\vec{q},t) e^{i\omega t} \ . \tag{1.83}$$

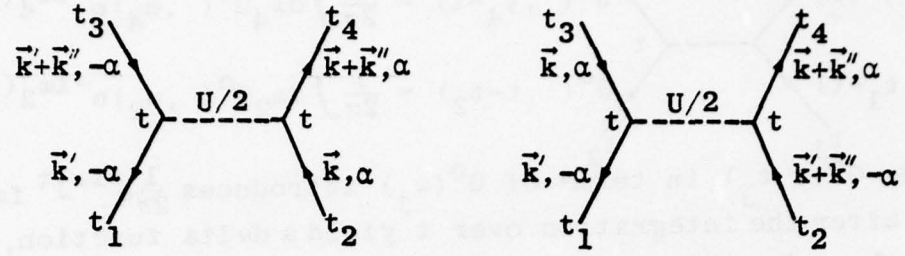
This can be represented graphically with the Feynman diagram



which can be described as a transverse spin-density fluctuation in $\vec{k}$ space of the unperturbed system. At time t=0 a spin-down electron in the Bloch state $\vec{k}$ is spin-flipped out of the Fermi sea into the spin-up state $\vec{k}+\vec{q}$, leaving a spin-down hole. The electron-hole pair propagates in time until at time t the electron-hole pair is annihilated.

Higher order terms in Eq. 1.73 (with $\mathcal{H}'(t)$ obtained from Eq. 1.71) are represented by diagrams which include interaction lines as well as particle lines. By applying Wick's theorem and the Linked Cluster theorem, one can show that only the following two combinations of interaction and

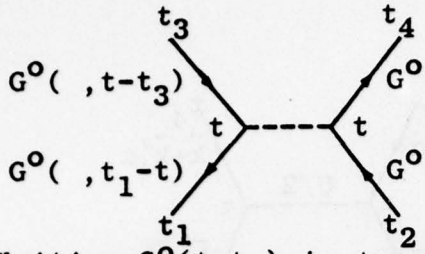
particle lines occur:



There are two points to note from the diagrams which will be useful later in constructing the Feynman rules for a diagrammatic analysis. First, in each diagram, the three parameters, $\vec{k}$, $\vec{k}'$, and $\vec{k}''$, can be viewed as crystal momenta which are conserved in the interaction. In this view, each single-particle Green's-function line is assigned, in the direction of the arrow, a momentum which is equal to the Bloch state parameter labeling the Green's function. Then as the interaction transfers momentum from one vertex to another there is conservation of momentum at each vertex. Second, the two particles which enter into the interaction have opposite spin states before and after the interaction. This will occur if the spin states of both particles either remain the same or if both change. A single spin flip is not allowed by the interaction, and only particles in opposite spin states interact.

1.7 Diagramming the Intra-atomic Coulomb Interaction in $\vec{k},\omega$ Space

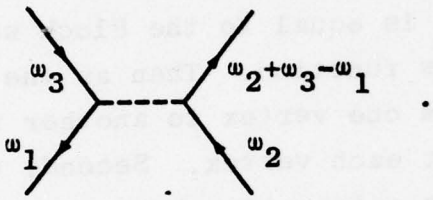
Although, in principle, we could now construct the Feynman rules, it turns out to be more convenient to first write all the time-ordered Green's functions, $G^o(\vec{k},t)$, in terms of their Fourier transforms, $G^o(\vec{k},\omega)$, and integrate over all time variables. The simplification that occurs by this change to ω space can be illustrated by changing a time dependent diagram into an ω dependent diagram. As seen from the previous section, an interaction diagram can be drawn in t space as follows:



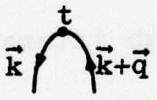
Writing $G^o(t,t_j)$ in terms of $G^o(\omega_j)$ introduces $\frac{1}{2\pi}e^{\pm i\omega_j t}$ factors which after the integration over t yield a delta function, i.e.,

$$\frac{1}{(2\pi)^4}\int dt\, e^{i(\omega_4-\omega_3-\omega_2+\omega_1)t} = \frac{1}{(2\pi)^3}\delta(\omega_4-\{\omega_3+\omega_2-\omega_1\}) .$$

Because of the delta function we can immediately integrate over ω_4, thereby reducing the number of variables in a diagram by one for each interaction line in the diagram. The new labeling for an interaction diagram becomes



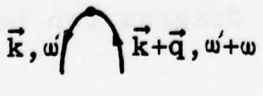
(Note that if we consider the interaction as transferring an energy, $\omega_3-\omega_1$, then there is conservation of energy at each vertex). After repeating the above procedure at each interaction, we are left with one time integration at the end of the spin-fluctuation,



Since the transformation introduces the factors $\frac{1}{2\pi}e^{-i\omega''t}$ and $\frac{1}{2\pi}e^{i\omega't}$ and since there is also the $e^{i\omega t}$ factor from Eq. 1.73, the integration over t yields

$$\frac{1}{(2\pi)^2}\int dt\, e^{-i(\omega''-\omega'-\omega)t} = \frac{1}{2\pi}\delta(\omega''-\omega'-\omega)$$

Finally after integrating over ω, we find the labeling becomes



Thus there is momentum and energy conservation associated

with the internal parameters, (k,ω'), but not with the external parameters, (q,ω), which are the arguments of the dynamic susceptibility.

We are now in a position to write the Feynman rules for $\vec{k},\omega$ space. These rules allow us to go directly from a diagram to a term in the perturbation expansion (Eq. 1.73) of $\chi_T^{-+}(\vec{q},\omega)$ and are listed as follows for the nth-order contribution to the expansion:

1) Draw all topologically distinct connected diagrams with n interaction lines and 2n + 2 directed Green's-function lines. Each of the 2n + 2 vertices has a directed line entering and leaving. The two vertices which are not connected to an interaction line represent the start and end of the spin-fluctuation.

2) Label each directed Green's function line with a crystal momentum $\vec{k}'$ and an energy ω' consistent with conserving momentum and energy at all interactions and assume a momentum q and energy ω enters at the start of the fluctuation and leaves at the end of the fluctuation.

3) Label the spin-state of each Green's function line such that the two interacting particles have opposite spin-states entering and leaving the interaction. If both spin-flip and non spin-flip scattering can take place, use α and $-\alpha$ to label these spin-states.

4) Each diagram represents a product of Green's functions and interaction factors. Each Green's function line corresponds to the factor

$$G_\alpha(\vec{k}',\omega') = \frac{1}{\omega'-\epsilon_{\vec{k}'}-i\delta_{\vec{k}'}},$$

where

$$\delta_{\vec{k}'}>0 \quad \text{if} \quad |\vec{k}'|>|\vec{k}_F| ,$$
$$\delta_{\vec{k}'}<0 \quad \text{if} \quad |\vec{k}'|<|\vec{k}_F| ,$$

and where $\delta_{\vec{k}'}\to 0$ after the ω' integration. Each interaction line corresponds to the factor U/2.

5) Sum over all spin-states labeled by $\pm\alpha$. Sum over the n+1 independent momenta and integrate over the n+1 independent energies.

6) Multiply by the factor

$$\frac{(-1)^F (i)^{n-1}}{2\pi V (2\pi N)^n}$$

where F is the number of closed loops of particle lines in the diagram.

This last rule comes from the fact that each Green's function introduces a factor i and, since there are 2n+2 Green's functions, we get a factor i^{2n+2}. A factor $\frac{1}{V}(-i)^{n-1}$ comes from the expansion given in Eq. 1.73. (The n! in this equation is cancelled by the n! topologically indistinguishable diagrams which result from Wick's theorem). The factor $(\frac{1}{2\pi})^{n+1}$ comes from the n+1 Fourier time-transforms, and the factor N^{-n} comes from the n $\mathcal{K}(t)$'s. The $(-1)^F$ comes from the fact that each interchange of creation and/or annihilation operators introduces a minus sign, and an odd number of interchanges is required for each loop before Wick's theorem can be applied. Thus,

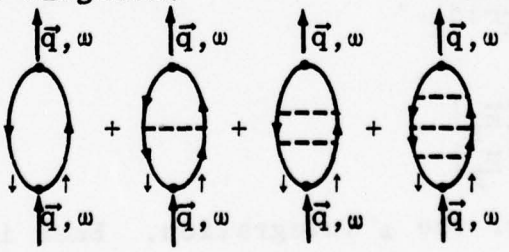
$$i^{2n+2}\frac{(-i)^{n-1}}{V}\left(\frac{1}{2\pi}\right)^{n+1} N^{-n}(-1)^F = \frac{(-1)^F (i)^{n-1}}{2\pi V (2\pi N)^n} ,$$

which is the factor of rule 6.

1.8 Evaluating the Uniform Exchange-enhanced Susceptibility

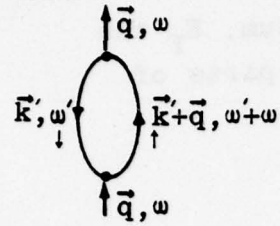
We can approximate the exchange-enhanced dynamic susceptibility by summing (with the aid of the Feynman rules) the following set of diagrams:

$$\chi_T^{-+}(\vec{q},\omega) \approx$$

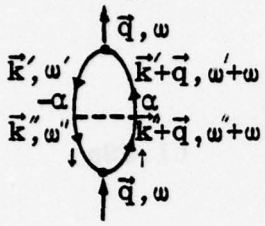


$$+ \ \ldots \ , \quad (1.84)$$

where



$$= \frac{-1}{2\pi V i}\sum_{\vec{k}'}\int d\omega' G_{\downarrow}(\vec{k}',\omega')G_{\uparrow}(\vec{k}'+\vec{q},\omega'+\omega) = {}^{o}\chi_{T}^{-+}(\vec{q},\omega) \ , \tag{1.84a}$$



$$= \frac{-1}{(2\pi)^2 V N}\sum_{\vec{k}'\vec{k}''}\sum_{\alpha}\int d\omega' d\omega'' G_{\downarrow}(\vec{k}',\omega')G_{\uparrow}(\vec{k}'+\vec{q},\omega'+\omega) \times \frac{U}{2} G_{-\alpha}(\vec{k}'',\omega')G_{\alpha}(\vec{k}''+\vec{q},\omega''+\omega)$$

$$= {}^{o}\chi_{T}^{-+}(\vec{q},\omega)\frac{V}{N}U\,{}^{o}\chi_{T}^{-+}(\vec{q},\omega) \ , \tag{1.84b}$$

and so on. So finally we have in this approximation,

$$\chi_{T}^{-+}(\vec{q},\omega) = {}^{o}\chi_{T}^{-+} + {}^{o}\chi_{T}^{-+}\frac{V}{N}U\,{}^{o}\chi_{T}^{-+} + {}^{o}\chi_{T}^{-+}\left(\frac{V}{N}U\,{}^{o}\chi_{T}^{-+}\right)^2 + \ldots$$

$$= \frac{{}^{o}\chi_{T}^{-+}}{1-\frac{V}{N}U\,{}^{o}\chi_{T}^{-+}} \ , \tag{1.85}$$

and, from Eqs. 1.64 and 1.65 for $\omega>0$,

$$\chi(\vec{q},\omega) = \tfrac{1}{2}g^2\mu_B^2|F(\vec{q})|^2\frac{{}^{o}\chi_{T}^{-+}}{1-\frac{V}{N}U\,{}^{o}\chi_{T}^{-+}} \ . \tag{1.86}$$

The dynamic susceptibility can now be calculated by evaluating the integral in Eq. 1.84a. Changing the sum in Eq. 1.84a to an integral, assuming an isotropic band, and using the effective mass approximation (i.e., $\varepsilon_{\vec{k}} = k^2/\{2m^*\}$, where m^* is the effective mass) yields

$${}^{o}\chi_{T}^{-+}(\vec{q},\omega) = \frac{i}{(2\pi)^4}\int d\vec{k}'d\omega' G_{\downarrow}(k',\omega')G_{\uparrow}(k'+q,\omega'+\omega)$$

$$= \frac{i}{(2\pi)^4}\int d\vec{k}'d\omega'\frac{1}{\omega'-\varepsilon_{k'}-i\delta_{k'}}\frac{1}{\omega+\omega'-\varepsilon_{k'+q}-i\delta_{k'+q}} \ , \tag{1.87}$$

where $k'=|\vec{k}'|$ and $q=|\vec{q}|$. This integral was first evaluated by Lindhard[13], who obtained

$${}^{o}\chi_{T}^{-+}(q,\omega) = D(E_F)u(\tilde{q},\tilde{\omega}) \ ; \ \tilde{q}=q/q_F \ , \ \tilde{\omega}=\omega/E_F \ , \tag{1.88}$$

where $D(E_F)$ is the density of d-states at the Fermi level per unit volume per spin-state, q_F the Fermi momentum, E_F the Fermi energy, and where the real and imaginary parts of $u(\tilde{q},\tilde{\omega})$, the Lindhard function, are given by

$$\mathrm{Re}\, u(\tilde{q},\tilde{\omega}) \equiv \frac{1}{2} + \frac{1}{4\tilde{q}}\left[\left\{1-\left(\frac{\tilde{\omega}}{2\tilde{q}} - \frac{\tilde{q}}{2}\right)^2\right\} \ell n \, \frac{1-\frac{\tilde{\omega}}{2\tilde{q}} + \frac{\tilde{q}}{2}}{1+\frac{\tilde{\omega}}{2q} - \frac{\tilde{q}}{2}}\right.$$

$$\left. - \left\{1-\left(\frac{\tilde{\omega}}{2\tilde{q}} + \frac{\tilde{q}}{2}\right)^2\right\} \ell n \, \frac{1-\frac{\tilde{\omega}}{2\tilde{q}} - \frac{\tilde{q}}{2}}{1+\frac{\tilde{\omega}}{2\tilde{q}} + \frac{\tilde{q}}{2}}\right] \qquad (1.89a)$$

and

$$\mathrm{Im}\, u(\tilde{q},\tilde{\omega}) \equiv \frac{\pi}{4\tilde{q}}\left[\left\{1-\left(\frac{\tilde{\omega}}{2\tilde{q}} - \frac{\tilde{q}}{2}\right)^2\right\}\theta\left(1-\left(\frac{\tilde{\omega}}{2\tilde{q}} - \frac{\tilde{q}}{2}\right)^2\right)\right.$$

$$\left. - \left\{1-\left(\frac{\tilde{\omega}}{2\tilde{q}} + \frac{\tilde{q}}{2}\right)^2\right\}\theta\left(1-\left(\frac{\tilde{\omega}}{2\tilde{q}} + \frac{\tilde{q}}{2}\right)^2\right)\right] . \qquad (1.89b)$$

The dynamic susceptibility then becomes

$$\chi(q,\omega) = \frac{\chi_o |F(q)|^2 u(\tilde{q},\tilde{\omega})}{1 - \frac{V}{N} U D(E_F) u(\tilde{q},\tilde{\omega})} \qquad (1.90)$$

where χ_o, the Pauli susceptibility, is given by

$$\chi_o = \tfrac{1}{2} g^2 \mu_B^2 D(E_F) . \qquad (1.91)$$

Rewriting the dynamic susceptibility in terms of the density of states, $N(E_F)$, at the Fermi level per <u>atom</u> per spin state yields

$$\boxed{\chi(q,\omega) = \frac{\chi_o |F(q)|^2 u(q/q_F, \omega/E_F)}{1 - UN(E_F) u(q/q_F, \omega/E_F)}} . \qquad (1.92)$$

This equation is the central result of the theory and is equivalent to the random-phase approximation formula obtained by Izuyama, Kim and Kubo[14].

We digress to point out that $\chi(q,\omega)$ of Eq. 1.92 differs in form from that employed by most authors. It is a common practice in most theoretical papers in this field to 1) drop the $g^2\mu_B^2$ factors, 2) use the transverse susceptibility,

$\chi^{-+}(q,\omega)$, which differs from the susceptibility $\chi^{zz}(q,\omega)$ by a factor of two, 3) use the atomic susceptibility rather than the volume susceptibility, and 4) use the reduced susceptibility (the susceptibility divided by the square of the absolute value of the form factor). In this paper none of the above have been used and consequently the susceptibility in this paper is closely related to the magnetization which is defined as the magnetic moment per unit volume (see Eq. 1.16). The relation between the dynamic susceptibility, $\chi(q,\omega)$, which we use in this paper and the susceptibility, $\chi'(q,\omega)$, in which all of the above conditions have been applied, is

$$\chi(q,\omega) = \tfrac{1}{2}g^2\mu_B^2\frac{N}{V}|F(q)|^2\chi'(q,\omega) = \frac{\chi_o}{N(E_F)}|F(q)|^2\chi'(q,\omega) \tag{1.93}$$

Returning now to Eq. 1.92, we look at the implications of the equation in some special cases. For the case of the static susceptibility we have, upon taking the limit of $\chi(q,\omega)$ as $\omega\to 0$ and then $q\to 0$,

$$\chi(0,0) = \frac{\chi_o}{1-UN(E_F)}\ , \tag{1.94}$$

since $F(0)=1$ and $u(0,0)=1$. Comparing this equation with the definition of the Stoner enhancement factor (Eq. 1.5), one finds that

$$S = \frac{1}{1-UN(E_F)}\ . \tag{1.95}$$

Thus, we see that in this model the internal field (λM) proposed by Stoner is caused by the intra-atomic Coulomb interaction between electrons of opposite spin, where λ is given by $\lambda = UN(E_F)/\chi_o$. The model also gives the condition for the ferromagnetic instability (the point at which the susceptibility diverges) to be $UN(E_F)=1$.

Further insight into results of the model may be obtained by looking at the magnetization that results when the static, delta-function magnetic field is applied to the system at the origin. The magnetic field is given by

$$H(r,t) = \delta(r)\ , \tag{1.96}$$

whose Fourier transform is

$$H(q,\omega) = 2\pi\delta(\omega) \quad . \tag{1.97}$$

Using Eq. 1.19, taking the Fourier transform, and integrating over ω, we find the magnetization,

$$M(r,t) = \frac{1}{V}\sum_{\vec{q}}\chi(q,0)e^{i\vec{q}\cdot\vec{r}} \quad , \tag{1.98}$$

that is, the magnetic response to the delta-function field at the origin is given by the Fourier transform of the static susceptibility. By writing the Lindhard function (Eq. 1.89) for the case of $\tilde{\omega}=0$, i.e.,

$$u(\tilde{q},0) = \frac{1}{2} + \frac{1}{2\tilde{q}}(1-\frac{\tilde{q}^2}{4})\ln\left|\frac{1-\tilde{q}/2}{1+\tilde{q}/2}\right| \quad , \tag{1.99}$$

and using this expression for $u(\tilde{q},\tilde{\omega})$ in Eq. 1.92, we can evaluate $\chi(q,0)$ for various values of the enhancement factor S. This static susceptibility is shown normalized in Fig. 1. The two solid curves give the static susceptibility for an unenhanced system (S=1) and an enhanced system (S=10). The dashed curve is the unenhanced susceptibility multiplied by a factor of 10. The point to note here is that the enhancement is greatest for q=0, falling off until at very short wavelengths ($q>2q_F$) there is hardly any enhancement at all; consequently the greater the enhancement factor, the narrower the susceptibility function is in q space. This means that magnetization, which is the Fourier inverse of the susceptibility, will, in addition to being enhanced, extend farther from the perturbing field for the enhanced case. It is this type of exchange-enhancement which is partially responsible for the giant magnetization clouds which are found around an Fe atom in Pd[15].

1.9 The Spectral Density Function and Paramagnons

The imaginary part of the dynamic susceptibility is a measure of the ability of the system to absorb energy from a periodic magnetic field of wave vector q and frequency ω. It is also related to the thermal fluctuations of the magnetization of the system before the application of a magnetic field. This relationship can be shown from the fluctuation

dissipation theorem, which for a homogeneous system can be written in the following form[16]:

$$\frac{\mathrm{Im}\{\chi_{\nu\mu}(\vec{q},\omega)+\chi_{\mu\nu}(\vec{q},\omega)\}}{1-e^{-\beta\omega}} =$$

$$\frac{1}{2V}\int dt \,\langle\!\langle\, \hat{M}_\nu(\vec{q},\omega)\hat{M}_\mu(-\vec{q}) + \hat{M}_\mu(\vec{q},\omega)\hat{M}_\nu(-\vec{q}) \,\rangle\!\rangle\, e^{i\omega t} \,, \tag{1.100}$$

where $\beta=(k_B T)^{-1}$, and $\langle\!\langle\ \rangle\!\rangle$ is the quantum mechanical ensemble average. For an isotropic system, we have

$$\frac{2\,\mathrm{Im}\,\chi(\vec{q},\omega)}{1-e^{-\beta\omega}} = \frac{1}{V}\int dt \,\langle\!\langle\, \hat{M}(\vec{q},\omega)\hat{M}(-\vec{q}) \,\rangle\!\rangle\, e^{i\omega t} \,, \tag{1.101}$$

and after integrating over ω and summing over $\vec{q}$, we obtain

$$\begin{aligned}\frac{1}{\pi V}\sum_{\vec{q}}\int d\omega \frac{\mathrm{Im}\,\chi(\vec{q},\omega)}{1-e^{-\beta\omega}} &= \frac{1}{V^2}\sum_{\vec{q}}\int dt \,\langle\!\langle\, \hat{M}(\vec{q},\omega)\hat{M}(-\vec{q}) \,\rangle\!\rangle \int \frac{d\omega}{2\pi}\, e^{i\omega t} \\ &= \frac{1}{V^2}\sum_{\vec{q}} \langle\!\langle\, \hat{M}(\vec{q})\hat{M}(-\vec{q}) \,\rangle\!\rangle \\ &= \frac{1}{V}\int d\vec{r}\ \ \langle\!\langle\, \hat{M}(\vec{r})^2 \,\rangle\!\rangle \\ &= \overline{M^2} \\ &= \overline{(M-\bar{M})^2} \,, \end{aligned} \tag{1.102}$$

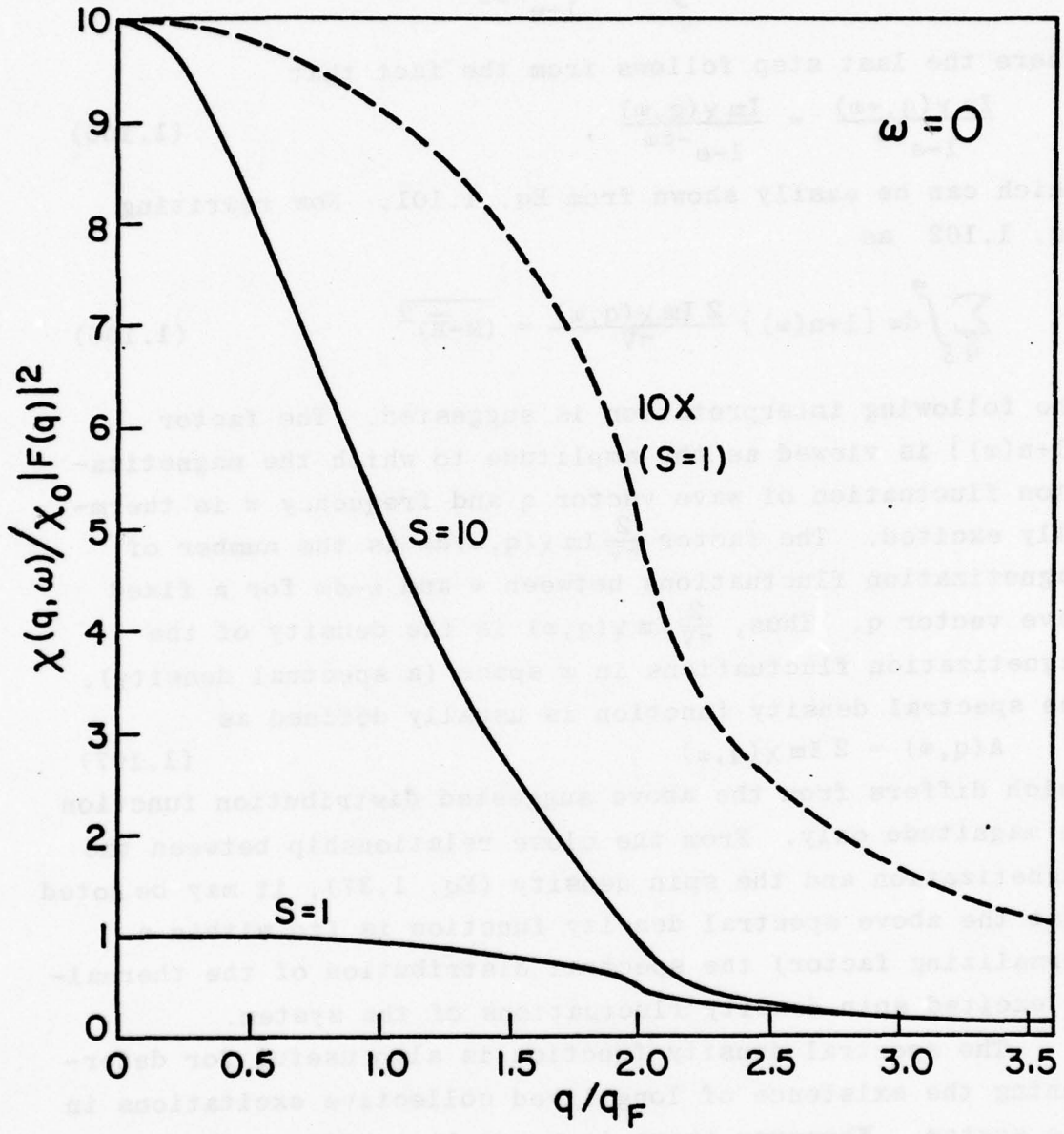
where the last step follows from the fact that $\bar{M}=0$ for a paramagnetic system. The quantity $\overline{(M-\bar{M})^2}$ is the mean square deviation of the magnetization of the system and is a measure of the magnitude of the magnetization fluctuations of the system. A physical interpretation can also be given to the left hand side of the above equation. First note that for $\omega>0$,

$$\frac{1}{1-e^{-\beta\omega}} = 1+\frac{1}{e^{\beta\omega}-1} = 1+n(\omega) \,, \tag{1.103}$$

where $n(\omega)$ is the Bose factor, and that

Fig. 1.

The static susceptibility $\chi(q,0)$, scaled by the product, of the Pauli susceptibility and the form factor squared, is shown as a function of the ratio of spin-fluctuation momentum to Fermi momentum for the case of an enhanced system with a Stoner enhancement factor of S=10 and for the case of an enhanced system (S=1). The dashed curve is the scaled susceptibility of the unenhanced system multiplied by a factor of ten.


ω = 0
10X
(S=1)
S=10
S=1
χ(q,ω)/χ₀|F(q)|²
q/q_F
0
0.5
1.0
1.5
2.0
2.5
3.0
3.5
0
1
2
3
4
5
6
7
8
9
10

$$\int_{-\infty}^{\infty} d\omega \frac{\text{Im}\,\chi(q,\omega)}{1-e^{-\beta\omega}} = \int_{0}^{\infty} d\omega \frac{\text{Im}\,\chi(q,\omega)}{1-e^{-\beta\omega}} + \int_{0}^{\infty} d\omega \frac{\text{Im}\,\chi(q,-\omega)}{1-e^{\beta\omega}}$$

$$= \int_{0}^{\infty} d\omega \frac{2\,\text{Im}\,\chi(q,\omega)}{1-e^{-\beta\omega}} , \qquad (1.104)$$

where the last step follows from the fact that

$$\frac{\text{Im}\,\chi(q,-\omega)}{1-e^{\beta\omega}} = \frac{\text{Im}\,\chi(q,\omega)}{1-e^{-\beta\omega}} , \qquad (1.105)$$

which can be easily shown from Eq. 1.101. Now rewriting Eq. 1.102 as

$$\sum_{\vec{q}} \int_{0}^{\infty} d\omega \{1+n(\omega)\} \frac{2\,\text{Im}\,\chi(q,\omega)}{\pi V} = \overline{(M-\bar{M})^2} \qquad (1.106)$$

the following interpretation is suggested. The factor $\{1+n(\omega)\}$ is viewed as the amplitude to which the magnetization fluctuation of wave vector q and frequency ω is thermally excited. The factor $\frac{2}{\pi V}\,\text{Im}\,\chi(q,\omega)d\omega$ is the number of magnetization fluctuations between ω and $\omega+d\omega$ for a fixed wave vector q. Thus, $\frac{2}{\pi V}\,\text{Im}\,\chi(q,\omega)$ is the density of the magnetization fluctuations in ω space (a spectral density). The spectral density function is usually defined as

$$A(q,\omega) = 2\,\text{Im}\,\chi(q,\omega) , \qquad (1.107)$$

which differs from the above suggested distribution function in magnitude only. From the close relationship between the magnetization and the spin density (Eq. 1.37), it may be noted that the above spectral density function is (to within a normalizing factor) the spectral distribution of the thermally excited spin density fluctuations of the system.

The spectral density function is also useful for determining the existence of long lived collective excitations in the system. Whenever there is a coupling between the exchange-enhanced band of electrons and some external energy source, such as a magnetic field, a beam of neutrons, or the conduction electrons in the metal, there will be an interchange of energy which will excite spin-fluctuations in the

system. In general, this excited state is not an energy eigenstate of the system and will therefore yield energy eigenvalues which spread over some range of energies. If the spread is small compared with the average excitation energy, then the excitation can be treated for some purposes as a particle with a finite lifetime (a quasiparticle). The energy distribution for a spin-fluctuation excitation of wave vector q is given by the spectral density function. The inverse of the half-width of the spectral density function defines the lifetime (τ) of a quasiparticle. For the quasiparticle picture to hold, the average energy, ω, must be much greater than $1/\tau$, i.e.

$$\omega\tau >> 1 \ . \tag{1.108}$$

For exchange-enhanced systems whose susceptibility can be represented by Eq. 1.92, Doniach[17] showed that the spectral density function develops a peak which becomes larger and sharper as the Stoner enhancement factor increases. In Fig. 2 the spectral density function is shown as a function of ω/E_F. As the enhancement increases from the unenhanced case, S=1, the peak becomes sharper and moves closer to zero. For a given enhancement factor, the peak in the spectral density function becomes larger and sharper as q approaches zero. This is seen in Fig. 3 where the spectral density function is shown as a function of ω/E_F for various values of q/q_F and for S=10. Thus, for small q and ω it appears that the quasiparticle concept may be valid.

For $\tilde{\omega}/\tilde{q} << 2$ and $\tilde{q}<2$, the Lindhard function (given by Eq. 1.89) can be approximated by

$$u(\tilde{q},\tilde{\omega}) \approx 1 - \frac{\tilde{q}^2}{12} + i\frac{\pi\tilde{\omega}}{4\tilde{q}} \ . \tag{1.109}$$

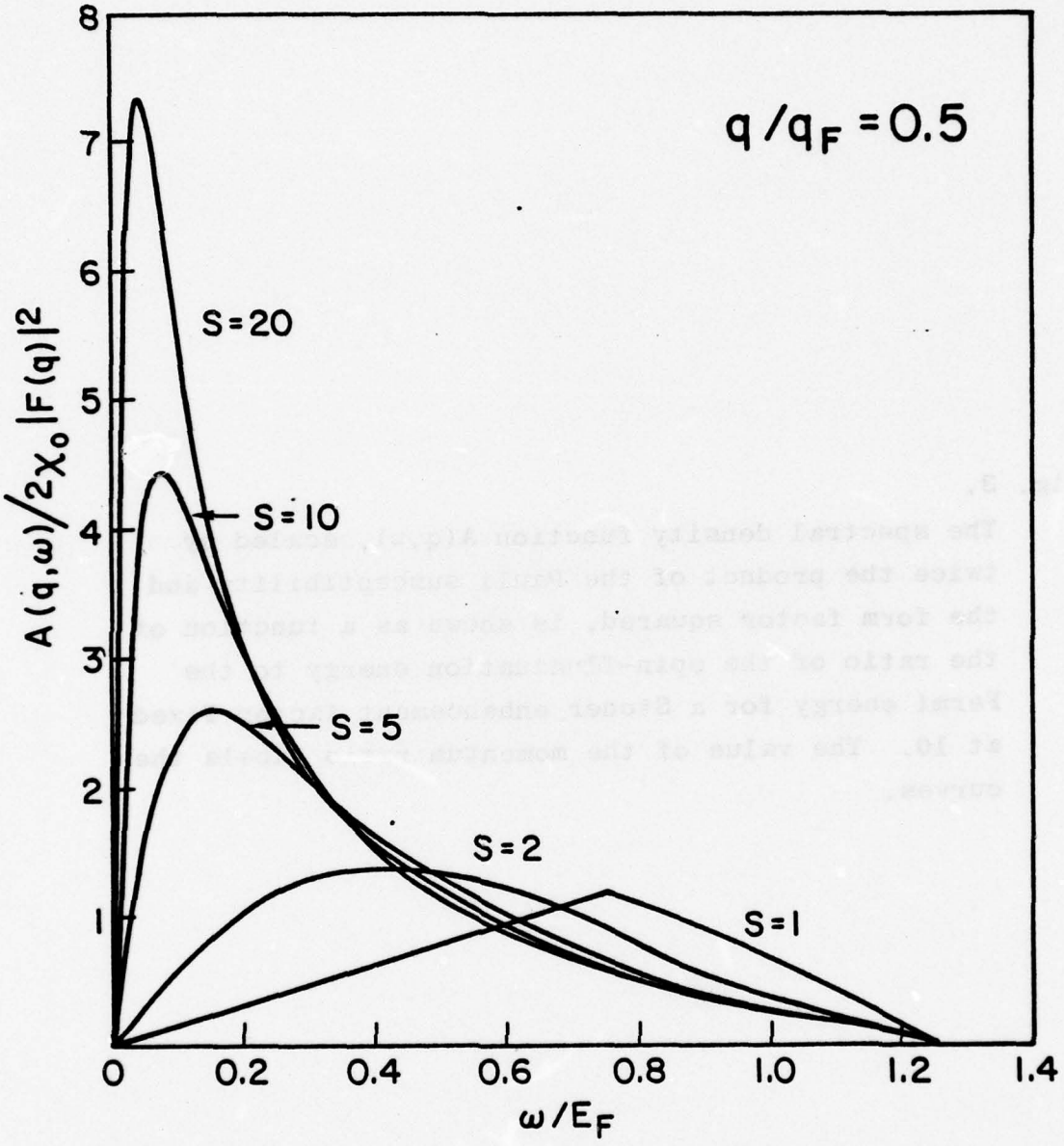
It then follows that

$$\mathrm{Im}\,\chi(\tilde{q},\tilde{\omega}) \approx \chi_o \frac{\frac{\pi\tilde{\omega}}{4\tilde{q}}}{\left(1-\bar{I}+\bar{I}\frac{\tilde{q}^2}{12}\right)^2 + \left(\frac{\pi\bar{I}\tilde{\omega}}{4\tilde{q}}\right)^2} \ , \tag{1.110}$$

where $\bar{I}=1-S^{-1}$. For $S >> 1$ the enhancement peak in the

Fig. 2.

The spectral density function $A(q,\omega)$, scaled by twice the product of the Pauli susceptibility and the form factor squared, is shown as a function of the ratio of the spin-fluctuation energy to the Fermi energy for a momentum ratio fixed at 0.5. The value of the Stoner enhancement factor labels the curves.


$q/q_F = 0.5$
S=20
S=10
S=5
S=2
S=1
$A(q,\omega)/2\chi_0|F(q)|^2$
ω/E_F
0
0.2
0.4
0.6
0.8
1.0
1.2
1.4
1
2
3
4
5
6
7
8

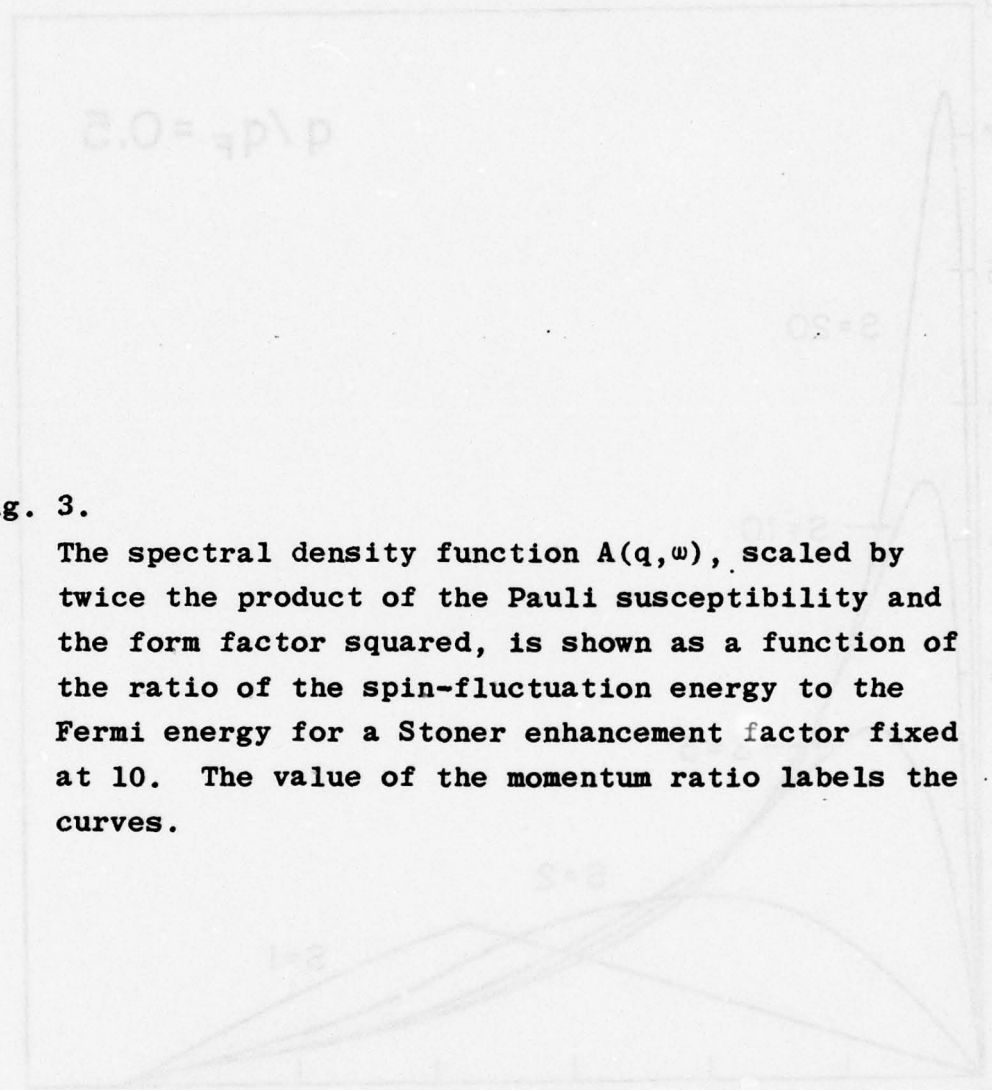
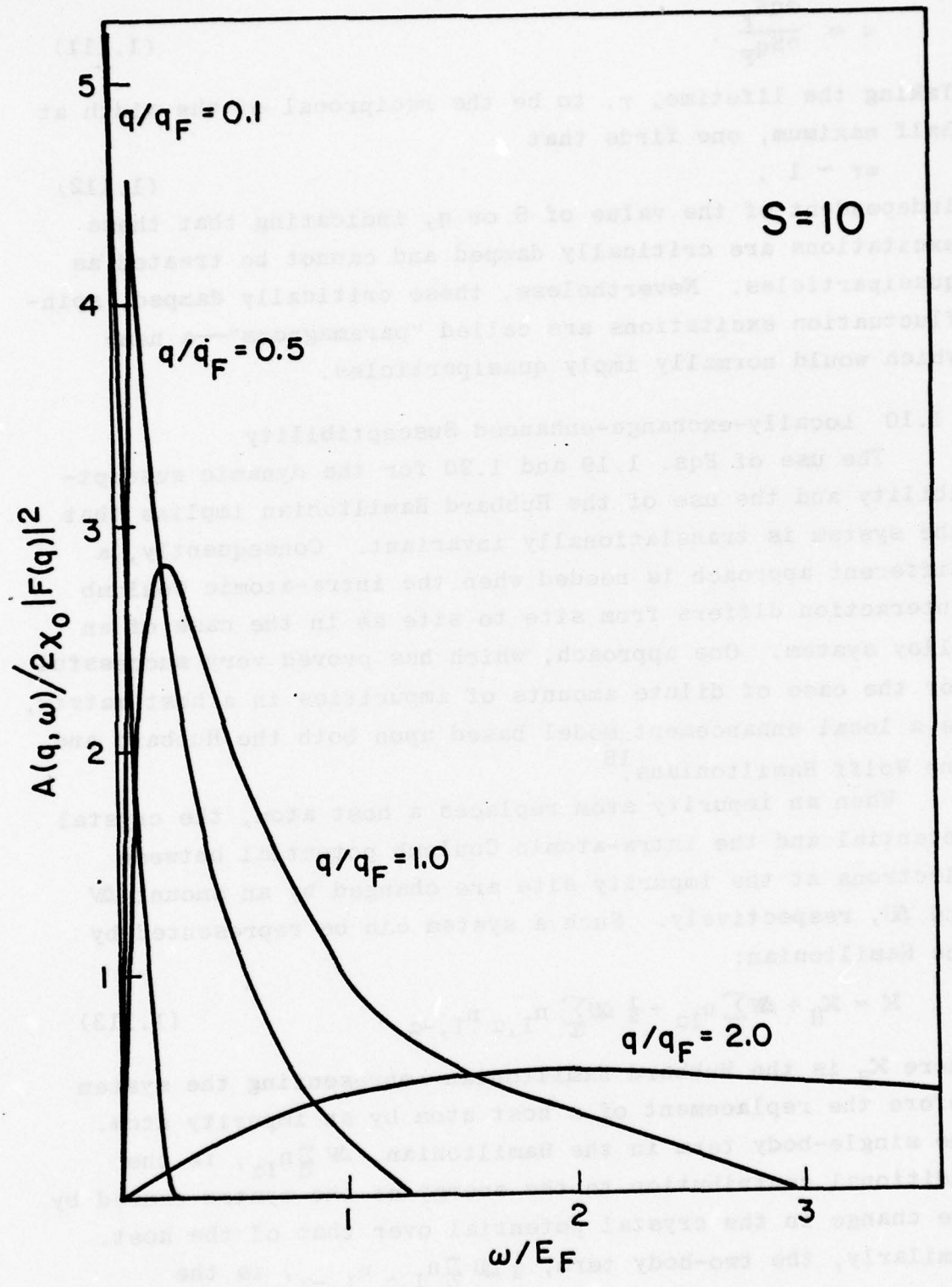


Fig. 3.

The spectral density function $A(q,\omega)$, scaled by twice the product of the Pauli susceptibility and the form factor squared, is shown as a function of the ratio of the spin-fluctuation energy to the Fermi energy for a Stoner enhancement factor fixed at 10. The value of the momentum ratio labels the curves.


S=10
q/q_F = 0.1
q/q_F = 0.5
q/q_F = 1.0
q/q_F = 2.0
A(q, ω)/2χ_o |F(q)|^2
ω/E_F
1
2
3
4
5

spectral density function occurs at

$$\omega \approx \frac{4qE_F}{\pi S q_F} . \qquad (1.111)$$

Taking the lifetime, τ, to be the reciprocal of the width at half maximum, one finds that

$$\omega\tau \sim 1 , \qquad (1.112)$$

independent of the value of S or q, indicating that these excitations are critically damped and cannot be treated as quasiparticles. Nevertheless, these critically damped, spin-fluctuation excitations are called "paramagnons"—a name which would normally imply quasiparticles.

1.10 Locally-exchange-enhanced Susceptibility

The use of Eqs. 1.19 and 1.20 for the dynamic susceptibility and the use of the Hubbard Hamiltonian implies that the system is translationally invariant. Consequently, a different approach is needed when the intra-atomic Coulomb interaction differs from site to site as in the case of an alloy system. One approach, which has proved very successful for the case of dilute amounts of impurities in a host matrix, is a local enhancement model based upon both the Hubbard and the Wolff Hamiltonians.[18]

When an impurity atom replaces a host atom, the crystal potential and the intra-atomic Coulomb potential between electrons at the impurity site are changed by an amount ΔV and ΔU, respectively. Such a system can be represented by the Hamiltonian:

$$\mathcal{H} = \mathcal{H}_H + \Delta V \sum_\alpha n_{I\alpha} + \tfrac{1}{2}\Delta U \sum_\alpha n_{I,\alpha}\, n_{I,-\alpha} , \qquad (1.113)$$

where $\mathcal{H}_H$ is the Hubbard Hamiltonian representing the system before the replacement of a host atom by an impurity atom. The single-body term in the Hamiltonian, $\Delta V \sum_\alpha n_{I\alpha}$, is the additional contribution to the energy of the system caused by the change in the crystal potential over that of the host. Similarly, the two-body term, $\frac{1}{2}\Delta U \sum_\alpha n_{I,\alpha}\, n_{I,-\alpha}$, is the

additional contribution to the energy caused by the change in the intra-atomic Coulomb interaction over that of the host.

In the discussion which follows, the dynamic-effective-field approximation used by Lederer and Mills[19] will be presented. (This approach yields a solution for the susceptibility which is equivalent to the random phase approximation.[20]) We begin by applying a magnetic field, $he^{i(\vec{q}_o\cdot\vec{r}-\omega_o t)}$, in the z direction to a system whose Hamiltonian is given by Eq. 1.113. The interaction of this field with the system results in the addition of a Zeeman term,

$$\mathcal{H}^{ext}(t) = -\int d\vec{r}\,\hat{M}_z(\vec{r},t)he^{i(\vec{q}_o\cdot\vec{r}-\omega_o t)} , \qquad (1.114)$$

to the Hamiltonian. The magnetization operator (obtained from Eqs. 1.37 and 1.30) is

$$\hat{M}_z(\vec{r},t) = -\frac{g\mu_B}{2}\{\psi_\uparrow^\dagger(\vec{r},t)\psi_\uparrow(\vec{r},t) - \psi_\downarrow^\dagger(\vec{r},t)\psi_\downarrow(\vec{r},t)\}. \qquad (1.115)$$

If the field operators are written in terms of the Wannier creation and annihilation operators by using the relations

$$\psi_\alpha^\dagger(\vec{r},t) = \sum_i W^*(\vec{r}-\vec{R}_i)c_{i\alpha}^\dagger(t) \qquad (1.116)$$

and

$$\psi_\alpha(\vec{r},t) = \sum_i W(\vec{r}-\vec{R}_i)c_{i\alpha}(t) , \qquad (1.117)$$

then the magnetization operator becomes

$$\hat{M}_z(\vec{r},t) = -\frac{g\mu_B}{2}\sum_{ii'} W^*(\vec{r}-\vec{R}_i)W(\vec{r}-\vec{R}_{i'}) \times \{c_{i\uparrow}^\dagger(t)c_{i'\uparrow}(t) - c_{i\downarrow}^\dagger(t)c_{i'\downarrow}(t)\} . \qquad (1.118)$$

Thus, the Zeeman term (Eq. 1.114) becomes

$$\mathcal{H}^{ext}(t) = \frac{g\mu_B}{2}F(\vec{q}_o)\sum_i\{n_{i\uparrow}(t) - n_{i\downarrow}(t)\}e^{i(\vec{q}_o\cdot\vec{R}_i-\omega_o t)} \qquad (1.119)$$

where the assumption that the overlap integrals can be neglected has been used when integrating over $\vec{r}$ (see the derivation of Eq. 1.59).

The effective-field approximation consists in replacing the two-body operator $\frac{1}{2}\sum_{\alpha} n_{i,\alpha} n_{i,-\alpha}$ in the Hamiltonian by the single-body operator, $\sum_{\alpha} \langle n_{i,\alpha} \rangle n_{i,-\alpha}$, where $\langle n_{i,\alpha} \rangle$ is the average number of particles with spin α in the cell i and is to be calculated in a self-consistent manner. (Since the external field is time dependent, $\langle n_{i,\alpha} \rangle$ will also be time dependent. We display this time dependence as $\langle n_{i,\alpha}(t) \rangle$.) After the above approximation is made, the total Hamiltonian (given by Eq. 1.113 plus the Zeeman term, Eq. 1.114) becomes

$$\mathcal{H} = \sum_{k\alpha} \varepsilon_k c^{\dagger}_{k\alpha} c_{k\alpha} + U\sum_{i\alpha} \langle n_{i,\alpha}(t) \rangle n_{i,-\alpha}(t) + \Delta U \sum_{\alpha} \langle n_{I,\alpha}(t) \rangle n_{I,-\alpha}(t) + \Delta V \sum_{\alpha} n_{I,\alpha}(t) + \tfrac{1}{2} g \mu_B F(q_o) \sum_{i} \{n_{i\uparrow}(t) - n_{i\downarrow}(t)\} . \tag{1.120}$$

Defining the operator,

$$S^z_i(t) \equiv \tfrac{1}{2}\{n_{i\uparrow}(t) - n_{i\downarrow}(t)\} , \tag{1.121}$$

which is related to the spin-density at the i site, we note that

$$\langle S^z_i(t) \rangle = \tfrac{1}{2}\{\langle n_{i\uparrow}(t) \rangle - \langle n_{i\downarrow}(t) \rangle\} \tag{1.122}$$

is the value of the spin associated with the i site. We also define

$$\bar{n}_i \equiv \tfrac{1}{2}\{\langle n_{i\uparrow}(t) \rangle + \langle n_{i\downarrow}(t) \rangle\} = \tfrac{1}{2}\sum_{\alpha} \langle n_{i,\alpha}(t) \rangle , \tag{1.123}$$

which, since the total number of electrons on each site remains the same, is the time average of the number of electrons associated with the i site and associated with a given spin state. It then follows from the above two definitions that the expectation value of the spin-up-electron density associated with the i site is

$$\langle n_{i\uparrow}(t) \rangle = \bar{n}_i + \langle S^z_i(t) \rangle \tag{1.124}$$

and for the spin-down case is

$$\langle n_{i\downarrow}(t) \rangle = \bar{n}_i - \langle S^z_i(t) \rangle . \tag{1.125}$$

Using these results in the Hamiltonian given by Eq. 1.120 and

rearranging terms results in

$$\mathcal{H}(t) = \sum_{\vec{k}} \epsilon_k c_k^\dagger c_k + U\sum_i \bar{n}_i \sum_\alpha n_{i,\alpha}(t) + (\Delta U \bar{n}_I + \Delta V)\sum_\alpha n_{I,\alpha}(t)$$
$$+ \sum_i \Big[\tfrac{1}{2}\{n_{i\uparrow}(t) - n_{i\downarrow}(t)\}$$
$$\times \{g\mu_B h F(q_o) e^{i(\vec{q}_o\cdot\vec{R} - \omega t)} - 2U\langle S_i^z(t)\rangle - 2\Delta U\langle S_I^z(t)\rangle\}\Big] \quad . \tag{1.126}$$

The last summation in this equation is very similar to the Zeeman term given by Eq. 1.119 and, as we shall see later, it is possible to express this term as the magnetization times an effective field.

Solutions for the susceptibility of a system represented by the above Hamiltonian have been given for two limiting cases: 1) for the case[21] when U=0, and 2) for the case[19] when $\Delta U n_I + \Delta V = 0$. It is the latter case that is of interest here, for this is the case that is most likely to apply to the isoelectronic exchange-enhanced alloys.

The result of neglecting the effective change in potential at the impurity site ($\Delta U n_I + \Delta V$) greatly simplifies the problem, for then it is possible to treat the application of a magnetic field to the inhomogeneous system as equivalent to applying a new field, H^{eff}, to a homogeneous system. To see this we first note that the Hamiltonian in Eq. 1.126 reduces to

$$\mathcal{H}_o = \sum_{\vec{k}} \epsilon_k c_k^\dagger c_k + U\sum_i \bar{n}_i \sum_\alpha n_{i\alpha} \tag{1.127}$$

when $(\Delta U n_I + \Delta V)$ and h are taken to be zero. That this Hamiltonian represents a uniform system is seen by solving for $\bar{n}_i$ in a self-consistent manner and showing that $\bar{n}_i$ is independent of the site i. This homogeneity can also be seen from the Friedel sum rule[22]. This rule directly relates the excess charge density at the impurity site to the phase shifts which occur in the wave function as a result of the impurity changing the potential at the site. Since for the above case the potential is assumed not to change upon the addition of the impurity, the Friedel sum rule says that the electron density

at the impurity will be the same as at a host site.

The dynamic susceptibility of the above system is

$$\chi_o(\vec{q},\omega) = \chi_o |F(q)|^2 u(q/k_F, \omega/E_F) \ , \tag{1.128}$$

which is the same as that for an unenhanced system (see Eq. 1.92 for U=0). To see this we use the independence of $\bar{n}_i$ upon location to write the interaction term as

$$U\sum_i \bar{n}_i \sum_\alpha n_{i\alpha} = U\bar{n}\left\{\sum_{i\alpha} n_{i\alpha}\right\} \ , \tag{1.129}$$

where we then note that $\Sigma n_{i\alpha}$ is the operator which gives the number of electrons in the d band. Since this number remains fixed, the interaction term will act as a constant and, although it will change the energy of the system by a constant amount, it will not change any of the dynamic properties of the system. Therefore the susceptibility of this system is the same as the system represented by Eq. 1.67 with U=0.

Since the effective magnetic field intensity is that field which when applied to the homogeneous system will yield the same magnetization as the actual field when applied to the inhomogeneous system, the magnetization in both systems can be found from the relation

$$M(q,\omega) = \chi_o(q,\omega) H^{eff}(q,\omega) \ . \tag{1.130}$$

To find $H^{eff}(q,\omega)$, first note that the Zeeman term for an isotropic homogeneous system can be written as

$$\mathcal{H}^{ext}(t) = -\int d\vec{r}\, \hat{M}_z(r,t) H_z(r,t) \ , \tag{1.131}$$

for a field in the z direction. This equation becomes

$$\mathcal{H}^{ext}(t) = -\frac{1}{V}\sum_{\vec{q}} \hat{M}_z(-q,t) H_z(q,t) \tag{1.132}$$

after the magnetization and the field have been written in terms of their spatial Fourier transforms and after the $\vec{r}$ integration has been performed. Then $H^{eff}(q,\omega)$ can be found by comparing this equation with the Zeeman term for the homogeneous system. This term (the last summation in Eq. 1.126) may be written as

$$\mathcal{H}^{ext}(t) =$$

$$\sum_i \left[S_i^z(t) \{ g\mu_B F(q_o) h e^{i(\vec{q}_o \cdot \vec{R}_i - \omega_o t)} + 2U\langle S_i^z(t)\rangle + 2\Delta U \langle S_I^z(t)\rangle \} \right] . \tag{1.133}$$

To make the comparison it is convenient to define

$$S_q^z(t) \equiv \sum_i S_i^z(t) e^{-i\vec{q}\cdot\vec{R}_i} \tag{1.134}$$

which, when inverted, yields

$$S_i^z(t) = \frac{1}{N}\sum_{\vec{q}} S_q^z(t) e^{i\vec{q}\cdot\vec{R}_i} . \tag{1.135}$$

Substituting the above expression for $S_i^z(t)$ into the Zeeman term and summing over i yields

$$\mathcal{H}^{ext}(t) = \sum_{\vec{q}} \left[S_q^z(t) \{ g\mu_B F(q_o) h \delta_{\vec{q}\vec{q}_o} e^{-i\omega_o t} - \frac{2U}{N} \sum_{\vec{q}'} \langle S_{q'}^z(t)\rangle \delta_{\vec{q}',-\vec{q}} - \frac{2\Delta U}{N^2} \sum_{\vec{q}'} \langle S_{q'}^z(t)\rangle e^{i(\vec{q}'+\vec{q})\cdot\vec{R}_I} \} \right] . \tag{1.136}$$

The spatial Fourier transform of the magnetization operator (given by Eq. 1.118) is

$$\hat{M}_z(q,t) = -g\mu_B F^*(t) \sum_i S_i^z(t) e^{-i\vec{q}\cdot\vec{R}_i}$$

$$= -g\mu_B F^*(q) S_q^z(t) , \tag{1.137}$$

where again we have neglected the contribution from the overlap integrals. If this equation is used to write S_q^z in terms of $\hat{M}_z(q,t)$ and if the impurity is taken to be at the origin, then the Zeeman term becomes

$$\mathcal{H}^{ext}(t) =$$

$$-\frac{1}{V}\sum_{\vec{q}} \left[\hat{M}_z(-q,t) \{ Vh\delta_{\vec{q}\vec{q}_o} e^{-i\omega_o t} + \frac{2VUM(q,t)}{Ng^2\mu_B^2 |F(q)|^2} - \frac{2V\Delta U}{N^2 g\mu_B F(q)} \sum_{\vec{q}'} \langle S_{q'}^z(t)\rangle \} \right] . \tag{1.138}$$

By comparing this equation with the Zeeman term given in Eq. 1.132, we see that the Fourier transform of the effective field can be written as

$$H^{eff}(q,t) = Vh\delta_{qq_o}e^{-i\omega_o t} + \frac{2VUM(q,t)}{Ng^2\mu_B^2|F(q)|^2} - \frac{2V\Delta U}{N^2 g\mu_B F(q)}\sum_{\vec{q}'}\langle S^z_{q'}(t)\rangle$$

or

$$H^{eff}(q,\omega) = H_o(q,\omega) + \frac{2VUM(q,\omega)}{Ng^2\mu_B^2|F(q)|^2} - \frac{2V\Delta U}{N^2 g\mu_B F(q)}\sum_{\vec{q}'}\langle S^z_{q'}(\omega)\rangle \ , \tag{1.139}$$

where $H_o(q,\omega)=2\pi V\delta_{qq_o}\delta(\omega-\omega_o)h$ is the Fourier transform of the applied field, h.

Substituting $H^{eff}(q,\omega)$ given above into Eq. 1.130, solving for $M(q,\omega)$, and using Eq. 1.92 to simplify the relation yields

$$M(q,\omega) = \chi(q,\omega)H_o(q,\omega) - \chi(q,\omega)\frac{2V\Delta U}{N^2 g\mu_B F(q)}\sum_{\vec{q}'}\langle S^z_{q'}(\omega)\rangle \ , \tag{1.140}$$

where $\chi(q,\omega)$ is the exchange-enhanced susceptibility of the host.

We can find the dynamic susceptibility of the locally enhanced system by first writing $\langle S^z_q(\omega)\rangle$ in terms of the magnetization (see Eq. 1.137) and subsituting the result into Eq. 1.140. This yields

$$M(q,\omega) = \chi(q,\omega)H_o(q,\omega) - \chi(q,\omega)\frac{2V\Delta U}{N^2 g^2\mu_B^2 F(q)}\sum_{\vec{q}'}\frac{M(q',\omega)}{F^*(q')}$$

and after repeated iteration yields

$$\begin{aligned} M(q,\omega) &= \chi(q,\omega)H_o(q,\omega) + \chi(q,\omega)\frac{2V\Delta U}{N^2 g^2\mu_B^2 F(q)}\left[\sum_{\vec{q}'}\frac{\chi(q',\omega)}{F^*(q')}H_o(q',\omega)\right] \\ &\quad\times\left\{1 + \sum_{\vec{q}'}\frac{\chi(q',\omega)2V\Delta U}{N^2 g^2\mu_B^2|F(q')|^2} + \left[\sum_{\vec{q}'}\frac{\chi(q',\omega)2V\Delta U}{N^2 g^2\mu_B^2|F(q')|^2}\right]^2 + \ldots\right\} \\ &= \chi(q,\omega)H_o(q,\omega) + \frac{\chi(q,\omega)2V\Delta U}{N^2 g^2\mu_B^2 F(q)}\left[\sum_{\vec{q}'}\frac{\chi(q',\omega)}{F^*(q')}H_o(q',\omega)\right] \\ &\quad\times\left[1 + \sum_{\vec{q}'}\frac{\chi(q',\omega)2V\Delta U}{N^2 g^2\mu_B^2|F(q')|^2}\right]^{-1} \\ &= \sum_{\vec{q}'}\left\{\left[\chi(q,\omega)\delta_{\vec{q}\vec{q}'} + \frac{\Delta U\, N(E_F)\chi(q,\omega)\chi(q',\omega)}{N\chi_o F(q)F^*(q)\{1-\Delta U\bar{\chi}(\omega)\}}\right]H_o(q',\omega)\right\} \ , \end{aligned} \tag{1.141}$$

where χ_o, the Pauli susceptibility,

$$\chi_o = \tfrac{1}{2} g^2 \mu_B^2 \frac{N}{V} N(E_F) \ , \tag{1.142}$$

has been used, and where $\bar{\chi}(\omega)$ has been defined by

$$\bar{\chi}(\omega) \equiv \frac{N(E_F)}{\chi_o N} \sum_{\vec{q}} \frac{\chi(q,\omega)}{|F(q)|^2} \ . \tag{1.143}$$

Comparing Eq. 1.141 with Eq. 1.16, we see that the dynamic susceptibility of the locally enhanced system is

$$\boxed{\chi(\vec{q},\vec{q}',\omega) = \chi(q,\omega)\delta_{\vec{q}\vec{q}'} + \frac{\Delta U\, N(E_F)\chi(q,\omega)\chi(q',\omega)}{N\chi_o F(q)F^*(q)\{1-\Delta U\bar{\chi}(\omega)\}}} \tag{1.144}$$

The above equation is the main result of the local enhancement model. It gives the dynamic susceptibility of an exchange-enhanced system which contains a single locally enhanced impurity at the origin. It may be noted that if we take the increase in the intra-atomic Coulomb interaction energy at the impurity site to be zero (i.e., $\Delta U=0$), then the model yields, as it must, the uniform exchange-enhanced susceptibility. Thus, the first term on the right in Eq. 1.144 is the contribution of the host to the susceptibility of the system and the last term is the contribution of the impurity to the susceptibility. Note that, in the susceptibility given by this model, all the parameters are dependent only on the nature of the host except for ΔU, which depends upon the properties of the impurity in the host.

This local enhancement model should apply to the case of a localized impurity which does not form a local moment but exhibits a strong intra-atomic Coulomb interaction and which does not significantly change the crystal potential from that of the host. The condition for the formation of a local moment is that the impurity contribution to the susceptibility diverge, i.e. $\Delta U\bar{\chi}(0) \to 1$.

It is of interest to examine the implications of this formula for the case of a uniform static applied magnetic field, h. The Fourier transform of this field is

$$H_o(q,\omega) = 2\pi V\delta_{q,0}\delta(\omega) \quad . \tag{1.145}$$

The Fourier transform of the magnetization is from Eq.1.141

$$M(q,\omega) = \left[\chi(0,\omega)\delta_{q,0} + \frac{\Delta U\, N(E_F)\chi(q,\omega)\chi(0,\omega)}{N\chi_o F(q)\{1-\Delta U\bar{\chi}(\omega)\}}\right] 2\pi Vh\delta(\omega) \ , \tag{1.146}$$

where the sum over $\vec{q}'$ has been performed and it has been noted that $F^*(0)=1$. The magnetization then becomes

$$M(r,t) = \chi(0,0)\left[1 + \frac{\Delta U\, N(E_F)}{N\chi_o\{1-\Delta U\bar{\chi}(0)\}}\sum_{\vec{q}}\frac{\chi(q,0)}{F(q)}e^{i\vec{q}\cdot\vec{r}}\right]h \tag{1.147}$$

after the integration over ω has been performed. It is of interest to note that when $F(q)$ can be taken to be unity in Eqs. 1.143 and 1.147 (as in the case of a narrow band and a large enhancement) the magnetization at the impurity site is given by

$$\begin{aligned} M(0,t) &= \chi(0,0)\left[1 + \frac{\Delta U\bar{\chi}(0)}{\{1-\Delta U\bar{\chi}(0)\}}\right]h \\ &= \alpha\chi(0,0)h \ , \end{aligned} \tag{1.148}$$

where

$$\alpha = \{1-\Delta U\bar{\chi}(0)\}^{-1} \ . \tag{1.149}$$

Thus, we see that for a homogeneous static field the magnetization at the impurity site is a factor, α (the local enhancement factor), times the magnetization of the host at a distance far from the impurity.

Finally, we exhibit for this system the static susceptibility that one would measure experimentally. This susceptibility will be the total magnetic moment of the system per unit volume divided by the uniform applied magnetic field, that is,

$$\chi = \frac{1}{hV}\int d\vec{r}\, M(\vec{r}) \ . \tag{1.150}$$

The magnetization of the system is from Eq. 1.147

$$M(r) = \chi(0,0)\left[1 + c\alpha N(E_F)\Delta U\sum_{\vec{q}}\frac{\chi(q,0)}{\chi_o F(q)}\, e^{i\vec{q}\cdot\vec{r}}\right]h \tag{1.151}$$

where we have changed the system from a single impurity system to a dilute alloy system. This was done by multiplying

the term which represents the contribution of the single impurity to the magnetization by the number of impurity atoms, N_I, and then writing the impurity concentration as $c=N_I/N$. In changing to a dilute alloy system the impurity concentration is assumed to be low enough that the impurities do not interact. The alloy susceptibility is then

$$\chi_A = \chi(0,0) + c\alpha SN(E_F)\Delta U\chi(0,0) \ , \qquad (1.152)$$

where we have used Eqs. 1.150 and 1.151, integrated over $\vec{r}$, summed over $\vec{q}$, and have used the definition of the Stoner enhancement factor. Rewriting this equation in a dimensionless form and taking the limit as $c\to 0$ yields

$$\boxed{\frac{1}{\chi}\frac{d\chi_A}{dc}\bigg|_{c\to 0} = \alpha SN(E_F)\Delta U} \ . \qquad (1.153)$$

That is, for a system which becomes locally exchange-enhanced upon the addition of small amounts of an impurity, the fractional rate of change of the static susceptibility of the system with increasing impurity concentration will be directly proportional to the product of the local enhancement factor, the Stoner enhancement factor of the host, the density of states per atom per spin-state of the host, and the change in the intra-atomic Coulomb interaction energy over that of the host.

B. Spin-fluctuction Resistivity

Besides enhancing the susceptibility, the intra-atomic Coulomb interaction, U, is expected to affect other properties of the exchange-enhanced metals. For example, it has been calculated[23] that, as a result of this interaction, the tendency for parallel spin alignment in Pd is sufficient to completely suppress the Cooper pairing (of opposite-spin electrons) which is necessary for superconductivity. Also it has been shown[23,24] that, by including these paramagnon interactions in single-particle self-energy corrections, there is a significant enhancement in the effective d-electron mass and consequently a corresponding increase in the low-temperature electronic heat capacity coefficient. Lastly, several theoretical calculations[25,26,27,28,29,30,31] have been made predicting the effect of spin-density fluctuations on electron transport properties. It is the effect of the spin-fluctuations upon the electrical resistivity that we now consider.

1.11 Uniform Enhancement Model

If a metal were perfectly periodic there would be no scattering of the electrons and the electrical resistivity would be zero. However, impurities, strains, thermal motion of the ion cores, and thermally excited charge-density and spin-density fluctuations all destroy the periodicity of the crystal to some degree. The resistivity that results from this scattering can be written as the sum of the individual scattering contributions

$$\rho = \rho_o + \rho_p + \rho_e \tag{1.154}$$

where ρ_o is the contribution to the resistivity from the electrons scattering from impurities and strains, ρ_p is the contribution from electron-phonon scattering and ρ_e is the contribution from electron-electron scattering. In general, these three terms are not independent. Since for scattering to take place the initial state must be occupied and the

final state unoccupied, the resistivity depends not only on the intrinsic probability that an electron will scatter from one state to another but also on the electron distribution. Thus, if two different scattering processes yield different electron distributions, then it is not possible to calculate the contribution to the resistivity of one process without considering the other. If, however, a given scattering process is a small perturbation upon the dominant scattering, then the contributions to the resistivity can be considered to be independent, for in this case the electron distribution is not changed to first order. In the following discussion, the electron-electron scattering contribution to the resistivity is considered to be independent of the other contributions.

When considering the electrical and thermal resistivities of transition metals, one generally assumes that the electrons are in two bands: 1) an s-like band (nearly-free-electron in character) and 2) a d band, with a high density of states at the Fermi level and with electrons whose effective mass is large compared to that of the s electrons. Because of the high effective mass of the d electrons, the current is largely carried by the s electrons. The transport current of the d electrons is usually neglected and the electron-electron scattering is taken to be the result of the s electrons interacting with the d electrons by either direct screened-Coulomb interaction (Baber[32] scattering) and/or by an s-d exchange interaction of the form discussed by Thompson[33]

$$\mathcal{H}_{s-d} = V_c J \sum_{\nu} \int d\vec{r}\, \hat{s}_{\nu}(\vec{r})\, \hat{S}_{\nu}(\vec{r}) , \qquad (1.155)$$

where V_c is the volume of the unit cell, J is the s-d interaction parameter, $\hat{s}(\vec{r})$ is the spin density operator of the electrons in the s band, and $\hat{S}(\vec{r})$ is the spin density operator of the electrons in the d band.

Baber scattering may be regarded[27,34] as a scattering process by which the conduction electrons of the s-band scatter via the screened-Coulomb interaction from the

charge-density fluctuations of the d-band. This scattering is illustrated in Fig. 4a. Here the incoming s-electron scatters from a $\vec{k}$ state to a $\vec{k}'$ state by creating a particle-hole pair in the d-band, via the screened Coulomb interaction. Since the screened Coulomb interaction is spin independent, the spin states of both the s electron and the d electron do not change.

In contrast to Baber scattering, spin-fluctuation scattering is the result of the conduction electrons of the s band scattering via the s-d exchange interaction from the spin-density fluctuations of the d band. The simplest type of spin-fluctuation scattering is spin-flip scattering, which comprises two-thirds of the spin-fluctuation scattering in paramagnetic materials. An example of spin-flip scattering is shown in Fig. 4b. Here, as a result of the s-d exchange interaction, the incoming s-electron spin-flips to another state by creating an electron-hole pair of opposite spin in the d band. Unlike Baber scattering where the electron and hole have the same spin-state, the electron and hole have opposite spin states in the spin-flip case. As a result, the spin fluctuation becomes enhanced by the intra-atomic Coulomb interaction. One can easily imagine for the case of a nearly ferromagnetic metal like Pd, where spin-fluctuations are easily formed and where the intra-atomic Coulomb interaction is large, that spin-fluctuation scattering might well be the dominant electron-electron scattering mechanism.

Mills and Lederer[35] were the first to calculate the electrical resistivity arising from spin-flip scattering from enhanced spin fluctuations in a uniform material. This work has been extended by a number of authors[25,28,30,31] and a qualitative discription of the temperature dependence of the resistivity found by these investigators will now be given. If the spin-fluctuation temperature is defined by $T_{SF} \equiv T_F/S$, where T_F is the d-band degeneracy temperature and S is the Stoner enhancement factor, then the temperature dependence of the resistivity, ρ, depends upon the relative magnitudes of

T_F, T_{SF}, and temperature T:

$\rho \propto (T/T_{SF})^2$, for $T_{SF} >> T$;

$\rho \propto T/T_{SF}$, for $T_F >> T >> T_{SF}$;

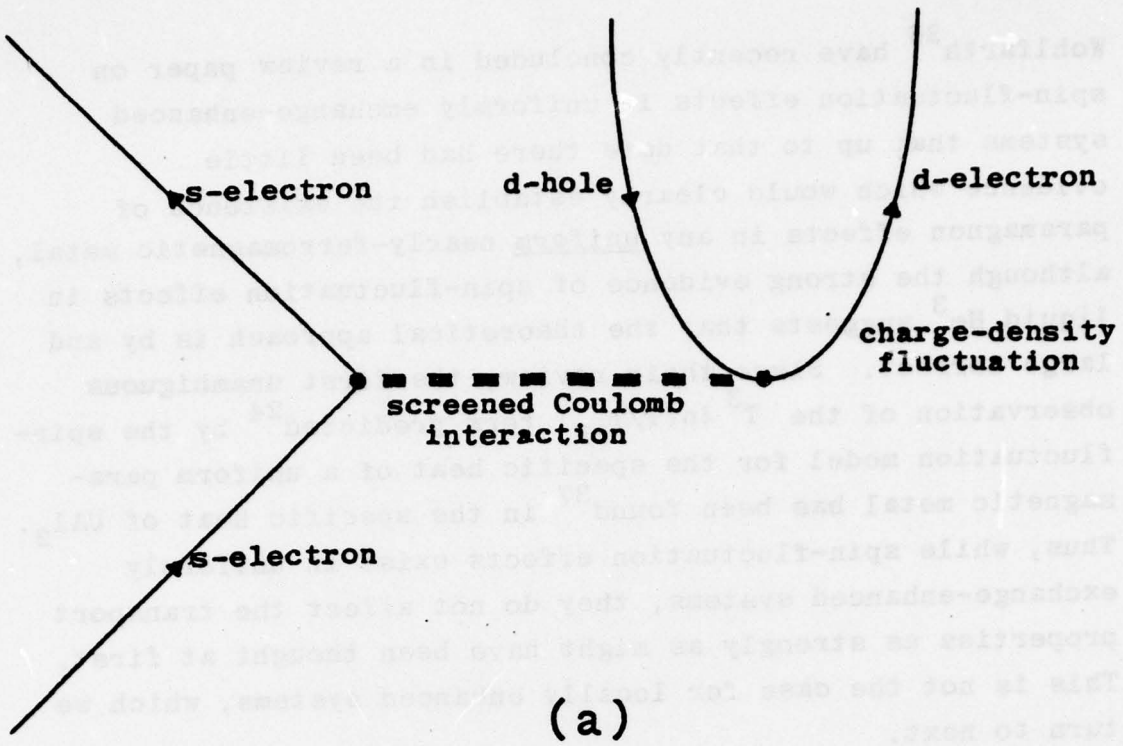
$\rho \rightarrow$ const. , for $T >> T_F$;

$\rho \propto T^{5/3}$, for $T_{SF}=0$ and $T << T_F$.

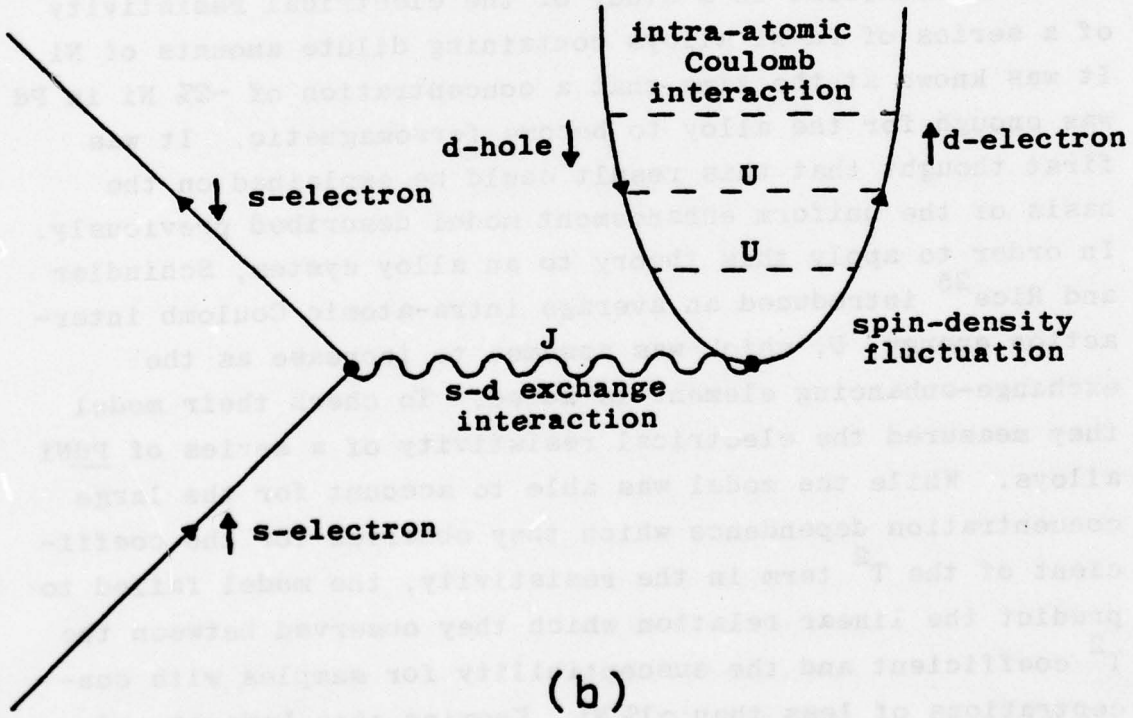
Because of the high Stoner enhancement factor (S=10) of Pd, this metal is a good choice of material in which to look for electron-paramagnon scattering effects. The resistivity of pure Pd does display the qualitative features predicted by the theory, namely a T^2 dependence at low temperatures, a linear region, and then a turning over at high T. The fact that a spin-fluctuation model[31] could be made to fit the data with reasonable values of the parameters is suggestive of electron-paramagnon scattering. However, the neglect of Baber scattering and s-d phonon induced scattering makes it far from certain that the main effect is spin-flip scattering. Stronger evidence comes from the data of Schindler and Rice[25]. In a series of Pd alloys containing dilute amounts of Ni, they measured the dependence of the T^2 term in the resistivity upon Ni concentration. Lederer and Mills[19] then showed, using a local spin-fluctuation model, that their model would give excellent quantitative agreement at low temperatures if the T^2 term in pure Pd originated almost entirely from spin-fluctuation scattering. On the other hand, Schriempf et al.[25] have measured in Pd-Ni both the electron-electron scattering contribution to the electrical resistivity, ρ_e, and the contribution to the thermal resistivity, w_e. The best fit to their results for the Lorenz number, $L_e=\rho_e/(w_eT)$, in these alloys was obtained when it was assumed the electron scattering in pure Pd was largely Baber scattering and not spin-fluctuation scattering. This result agrees with an earlier calculation of Rice[26] which indicated that the Lorenz number found for Pd was largely a result of Baber scattering. Finally, de Chatel and

Fig. 4.

A s-band conduction electron is diagrammatically shown scattering from fluctuations in the d band. In (a) the s electron scatters, via the screened-Coulomb interaction, from a charge-density fluctuation in the d band. In (b) the s electron scatters, via the s-d exchange interaction, from a spin-density fluctuation in the d band.


s-electron
d-hole
d-electron
charge-density
fluctuation
screened Coulomb
interaction
s-electron

(a)


intra-atomic
Coulomb
interaction
d-hole
d-electron
U
s-electron
U
spin-density
fluctuation
J
s-d exchange
interaction
s-electron

(b)

Wohlfarth[36] have recently concluded in a review paper on spin-fluctuation effects in uniformly exchange-enhanced systems that up to that date there had been little evidence which would clearly establish the existence of paramagnon effects in any uniform nearly-ferromagnetic metal, although the strong evidence of spin-fluctuation effects in liquid He^3 suggests that the theoretical approach is by and large correct. Since their review, the first unambiguous observation of the $T^3 \ln(T/T_{SF})$ term predicted[24] by the spin-fluctuation model for the specific heat of a uniform paramagnetic metal has been found[37] in the specific heat of UAl_2. Thus, while spin-fluctuation effects exist in uniformly exchange-enhanced systems, they do not affect the transport properties as strongly as might have been thought at first. This is not the case for locally enhanced systems, which we turn to next.

1.12 Local Enhancement Models of Lederer-Mills and Kaiser-Doniach

Evidence for the existence of local spin fluctuations was obtained first in a study of the electrical resistivity of a series of Pd-Ni alloys containing dilute amounts of Ni. It was known at the time that a concentration of ~2% Ni in Pd was enough for the alloy to become ferromagnetic. It was first thought that this result could be explained on the basis of the uniform enhancement model described previously. In order to apply this theory to an alloy system, Schindler and Rice[25] introduced an average intra-atomic Coulomb interaction energy, U, which was assumed to increase as the exchange-enhancing element is added. To check their model they measured the electrical resistivity of a series of PdNi alloys. While the model was able to account for the large concentration dependence which they observed for the coefficient of the T^2 term in the resistivity, the model failed to predict the linear relation which they observed between the T^2 coefficient and the susceptibility for samples with concentrations of less than ~1% Ni. Knowing this, Lederer and

Mills[19] showed that a resistivity model based on scattering of conduction electrons from local spin fluctuations (see section 1.10) would be in good quantitative agreement with the PdNi data. It is this resistivity model of Lederer and Mills and the later extension of the model by Kaiser and Doniach[38] which we now outline.

The electrical resistivity that results from conduction electrons scattering inelastically from the d-band spin-fluctuations is calculated by using a variation technique[39] to solve the Boltzmann transport equation. Such a calculation for a single isotropic parabolic band of conduction electrons yields

$$\rho = \frac{\beta}{(2\pi)^2 2n_c e^2 k_F} \iint d\vec{k}\, d\vec{k}' \int_0^{2k_F} dq\, q^3 P(\vec{k}\to\vec{k}') \quad , \qquad (1.156)$$

where $\beta=1/(k_B T)$, n_c is the number of conduction electrons per unit volume, e is the electronic charge, k_F is the magnitude of the Fermi wave vector of the conduction electrons, $q\equiv|\vec{k}-\vec{k}'|$, and $P(\vec{k}\to\vec{k}')$ is the probability that a conduction electron in a state $\vec{k}$ will be scattered into a state $\vec{k}'$ via the s-d exchange interaction (Eq. 1.155).

The transition probability (found by using the Fermi Golden Rule) can be written as the sum of two parts: 1) the probability that a conduction electron in a state $\vec{k}$ will scatter from a spin fluctuation by the absorption of a paramagnon and will go into a final state $\vec{k}'$ of higher energy ($\varepsilon_{\vec{k}'}>\varepsilon_{\vec{k}}$), 2) the probability that a conduction electron in a state $\vec{k}'$ will scatter from a spin fluctuation by the emission of a paramagnon and will go into a final state $\vec{k}$ of lower energy. The transition probability for absorption of a paramagnon is given by[38]

$$P_{abs}(\vec{k}\to\vec{k}') = \frac{3(V_c J)^2}{4g^2\mu_B^2} f(\varepsilon_{\vec{k}})\{1-f(\varepsilon_{\vec{k}'})\}n(\omega)A(q,\omega) \quad , \qquad (1.157)$$

where ε_k is the energy of the conduction electrons; $q\equiv|\vec{k}-\vec{k}'|$

and $\omega \equiv \varepsilon_{\vec{k}'} - \varepsilon_{\vec{k}}$ are respectively the momentum† and energy† change that occurs when the conduction electrons are scattered from the spin fluctuation via the s-d exchange interaction, $A(q,\omega)$ is the spectral density function giving the momentum and energy distribution of the spin fluctuations, $n(\omega)$ is the Bose factor and is a measure of the excitation level of the fluctuation, and $f(\varepsilon_{\vec{k}})$ is the Fermi-Dirac function. Since $f(\varepsilon_{\vec{k}})$ gives the probability that the state $\vec{k}$ will be occupied, the factor $1-f(\varepsilon_{\vec{k}'})$ gives the probability that the state $\vec{k}'$ will be unoccupied. The transition probability for a conduction electron to scatter from $\vec{k}'$ to $\vec{k}$ by the emission $(\varepsilon_{\vec{k}'} > \varepsilon_{\vec{k}})$ of a paramagnon is given by[38]

$$P_{em}(k' \to k) = \frac{3(V_c J)^2}{4g^2 \mu_B^2} f(\varepsilon_{\vec{k}'})\{1-f(\varepsilon_{\vec{k}})\}\{1+n(\omega)\}A(q,\omega) \ , \tag{1.158}$$

where again $\omega \equiv \varepsilon_{\vec{k}'} - \varepsilon_{\vec{k}}$. Since it can be shown from the definitions of $f(\varepsilon_{\vec{k}})$ and $n(\omega)$ that

$$f(\varepsilon_{\vec{k}})\{1-f(\varepsilon_{\vec{k}'})\}n(\omega) = f(\varepsilon_{\vec{k}'})\{1-f(\varepsilon_{\vec{k}})\}\{1+n(\omega)\} \ , \tag{1.159}$$

the contribution to the resistivity from the emission of paramagnons will equal the contribution from the absorption of paramagnons. Thus, we need to consider only the scattering by the absorption of paramagnons and multiply by a factor of two to obtain the total resistivity.

The total spin fluctuation resistivity is then given by

$$\rho = \frac{b_o V_c^{\beta}}{k_{F_c}^4} \int d\omega \int d\varepsilon_{\vec{k}} f(\varepsilon_{\vec{k}})\{1-f(\varepsilon_{\vec{k}+\omega})\}n(\omega) \int_0^{2k_F} dq \, q^3 \frac{A(q,\omega)}{\frac{1}{2}g^2\mu_B^2} \ , \tag{1.160}$$

where

$$b_o = \left[\frac{JN_c(E_F)}{2}\right]^2 \frac{1}{n_c V_c} \frac{mE_F}{n_c e^2} \ , \quad N_c(E_F) = \frac{mk_F V_c}{2\pi^2} \ , \quad E_F = \frac{k_F^2}{2m} \ ,$$

and $k_F = 3\pi n_c$ are, respectivly, the density of states per atom

---

† The units have been chosen such that $\hbar = 1$.

per spin state at the Fermi level of the isotropic parabolic band of conduction electrons, the Fermi energy, and the Fermi momentum of the band, with m being the effective mass of the conduction electrons. The resistivity can now be written as

$$\rho = b_o \beta \int_0^\infty d\omega \, \frac{\omega \bar{A}(\omega)}{(e^{\beta\omega}-1)(1-e^{-\beta\omega})} \quad , \tag{1.161}$$

where

$$\int_{-\infty}^{\infty} d\varepsilon_k \, f(\varepsilon_k)\{1-f(\varepsilon_k+\omega)\} = \frac{\omega}{1-e^{-\beta\omega}} \tag{1.162}$$

has been used and where $\bar{A}(\omega)$ is defined as a weighted average of the spectral density function over the wave vector q:

$$\bar{A}(\omega) = \frac{N(E_F)}{\chi_o k_F^4} \int_0^{2k_F} dq \, q^3 A(q,\omega) \quad . \tag{1.163}$$

The resistivity in Eq. 1.161 is the total contribution to the resistivity that results from conduction electrons scattering from spin fluctuations. At this point the equation could apply either to a uniformly exchange-enhanced system or to a locally exchange-enhanced system. The distinction between the two systems lies in the spectral density function, $A(q,\omega)$. In the following discussion we shall obtain the contribution to the spin fluctuation resistivity from locally enhanced spin fluctuations.

As in the case of a uniformly enhanced system, the spectral density function for a locally enhanced system is found from the dynamic susceptibility of the system. We use the single impurity model of Lederer and Mills for the dynamic susceptibility of the locally exchange-enhanced system (Eq. 1.144) and use the relation[19] $A(q,\omega)=2 \operatorname{Im} \chi(q,q'=q,\omega)$ to obtain the spectral density function. This yields the spectral density function

$$A(q,\omega) = A_U(q,\omega) + A_I(q,\omega) \quad , \tag{1.164}$$

where

$$A_U(q,\omega) = 2 \operatorname{Im} \chi(q,\omega) \quad , \tag{1.165}$$

$$A_I(q,\omega) = \frac{2c\Delta U\, N(E_F)}{\chi_o |F(q)|^2} \, \mathrm{Im}\left(\frac{\chi^2(q,\omega)}{1-\Delta U\bar{\chi}(\omega)}\right), \qquad (1.166)$$

and c is the impurity concentration. Noting that $\chi(q,\omega)$ is the susceptibility of the host (c=0), we see that $A_I(q,\omega)$ is the additional contribution to the spectral density function that results from the addition of the locally exchange-enhancing impurities to the host.

The total spin-fluctuation resistivity for the locally enhanced system can correspondingly be divided into a contribution from the host and from the locally enhancing impurities. From Eqs. 1.161, 1.163, and 1.164 we have that the impurity contribution is

$$\rho_I = b_o \beta \int_o^\infty d\omega \, \frac{\omega \bar{A}_I(\omega)}{(e^{\beta\omega}-1)(1-e^{-\beta\omega})} \, . \qquad (1.167)$$

Kaiser and Doniach[38] have shown that, when Eq. 1.92 is used to describe the exchange-enhanced host, the weighted average of $A_I(q,\omega)$ can be written as

$$\bar{A}_I(\omega) = a \frac{\tilde{\omega}}{1+\tilde{\omega}^2} \, , \qquad (1.168)$$

where

$$\tilde{\omega} \equiv \alpha \Delta U \, \mathrm{Im}\chi(\omega) \, , \qquad (1.169)$$

and a is a parameter which depends upon the properties of both the host and the impurity but is to a good approximation independent of ω.

For the case of strongly locally-enhanced systems, the peak in $\bar{A}_I(\omega)$ will occur at a value of ω low enough that taking $\mathrm{Im}\bar{\chi}(\omega)$ to be linear in ω will yield a good approximation for $\bar{A}_I(\omega)$. Since $\tilde{\omega}$ will then be directly proportional to ω, we can define a parameter

$$T_s \equiv \frac{\omega}{k_B \tilde{\omega}} \, , \qquad (1.170)$$

which will be largely independent of ω. If one considers the characteristic energy of the local spin-fluctuation to be given by the value of ω at the peak of the spectral density

function, $\bar{A}_I(\omega)$, then $k_B T_s$ is this characteristic energy and T_s is the spin-fluctuation temperature.

The general form of the spectral density function $\bar{A}_I(\omega)$ is shown in Fig. 5, where $\bar{A}_I(\omega)/a$ is shown as a function of $\omega/k_B T_s$. At small ω ($\omega << k_B T_s$) this spectral density function increases linearly with ω, then peaks at $k_B T_s$ and falls off as $1/\omega$ as $\omega \to \infty$. The form shown here is similar[30] to the weighted average of the spectral density function of a uniform exchange-enhanced system, and consequently the two systems will show qualitatively similar resistivity behavior.

The contribution to the resistivity that results when the conduction electrons scatter from the enhanced spin fluctuation around the impurity sites is obtained by inserting $\bar{A}_I(\omega)$ for the spectral density function in Eq. 1.167. This yields

$$\rho_I = \frac{c\rho_s}{\tilde{T}} \int_0^\infty d\tilde{\omega} \, \frac{\tilde{\omega}^2}{(e^{\tilde{\omega}/\tilde{T}}-1)(1-e^{-\tilde{\omega}/\tilde{T}})(1+\tilde{\omega}^2)} \tag{1.171}$$

after $\tilde{T} \equiv T/T_s$ and $\rho_s \equiv b_o a k_B T_s$ have been introduced.

This equation is the central result of the Kaiser and Doniach model. In Fig. 6 we show $\rho_I/c\rho_s$ as a function of T/T_s. At high temperatures the curve becomes linear and the resistivity reduces to

$$\rho_I = c\rho_s \{\frac{\pi T}{2T_s} - \frac{1}{2}\} \quad , \text{ for } T >> T_s \; . \tag{1.172}$$

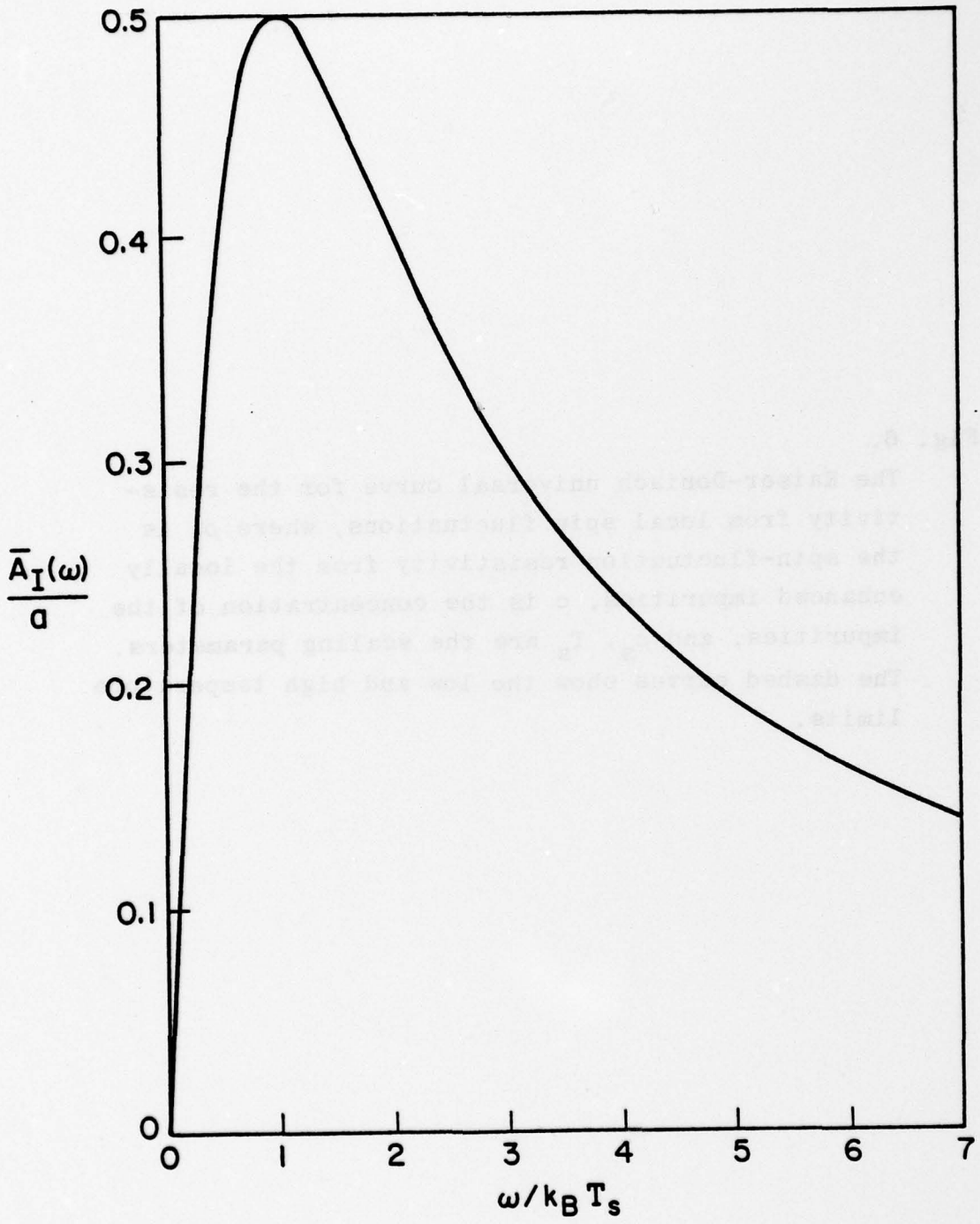
This limit is shown by the dashed straight line in Fig. 6. At low temperatures the resistivity reduces to

$$\rho_I = \frac{c\rho_s \pi^2}{3T_s^2} T^2 \quad , \text{ for } T << T_s \; , \tag{1.173}$$

which is shown by the dashed parabola in Fig. 6. The spin-fluctuation temperature acts as a dividing point between the two regions. The actual shape of the resistivity curve that will be observed depends upon the spin-fluctuation

Fig. 5.

The weighted average of the spectral density function for a locally enhanced impurity is divided by the parameter[38] a, and the result is shown as a function of the spin-fluctuation energy divided by $k_B T_s$, which is the energy at which the spectral density is a maximum. The energy $k_B T_s$ defines the local spin-fluctuation temperature, T_s.


0.5
0.4
0.3
0.2
0.1
0
$\frac{\bar{A}_I(\omega)}{a}$
0
1
2
3
4
5
6
7
$\omega / k_B T_s$

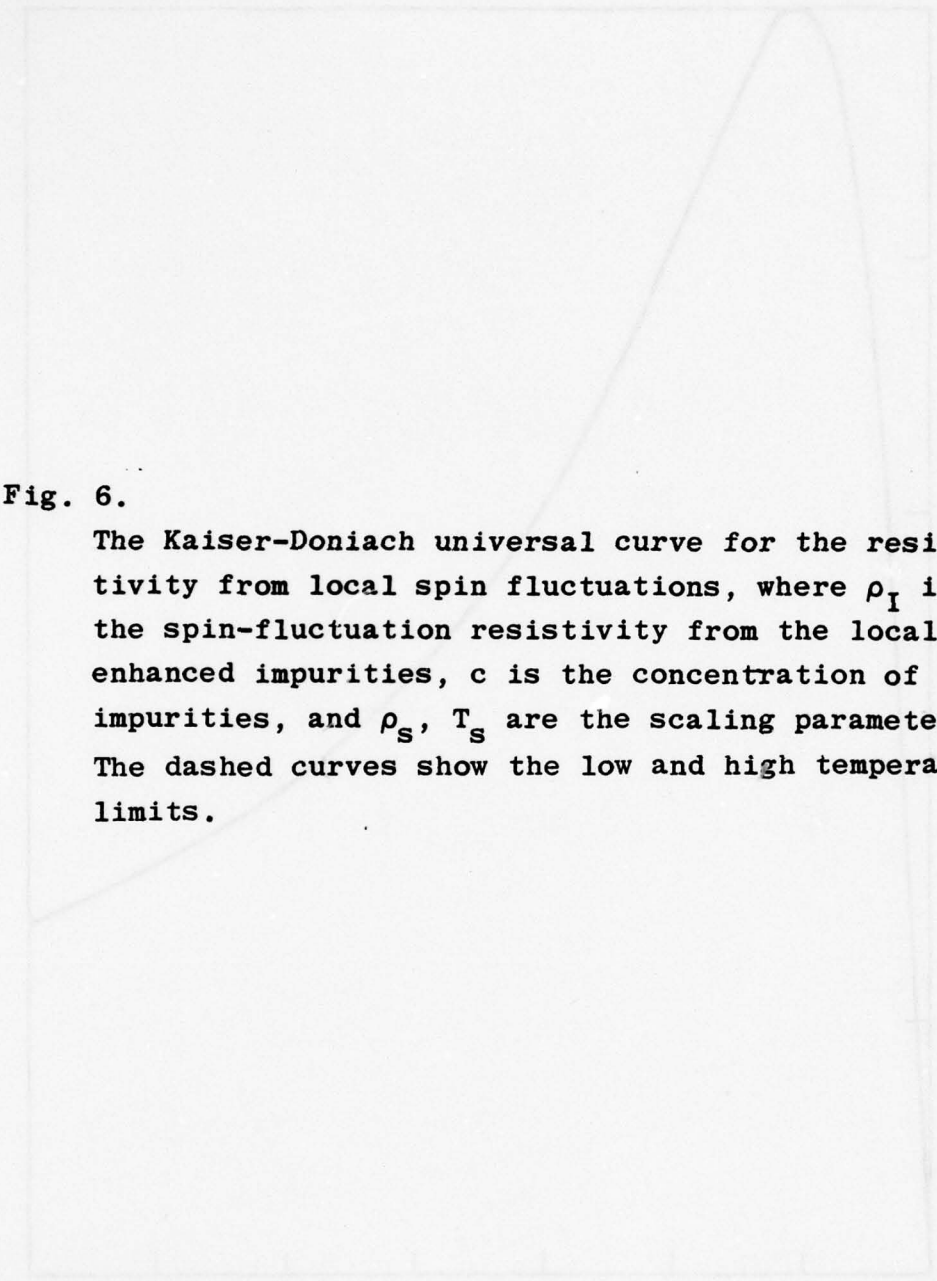
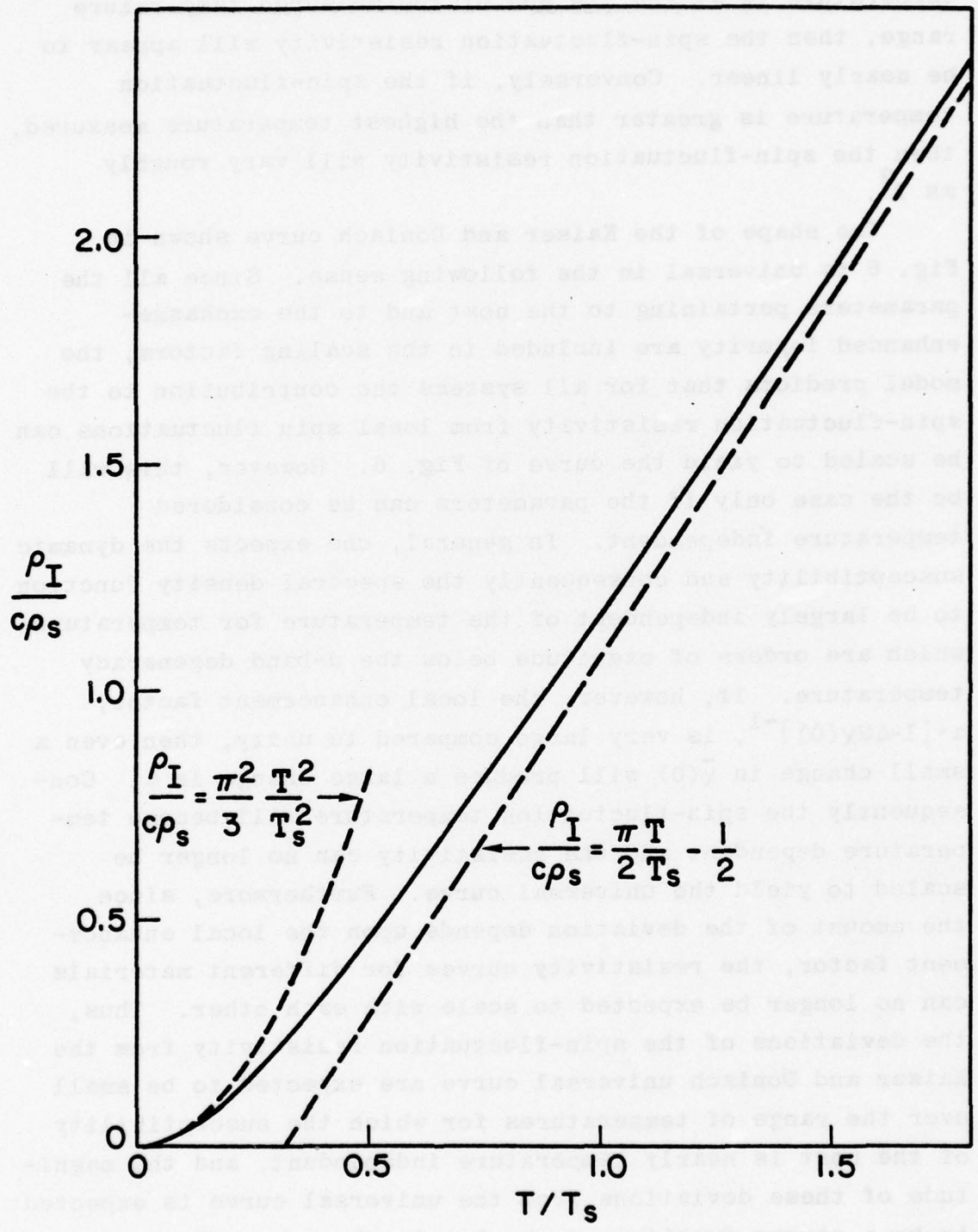


Fig. 6.

The Kaiser-Doniach universal curve for the resistivity from local spin fluctuations, where ρ_I is the spin-fluctuation resistivity from the locally enhanced impurities, c is the concentration of the impurities, and ρ_s, T_s are the scaling parameters. The dashed curves show the low and high temperature limits.


2.0
1.5
1.0
0.5
0
$\frac{\rho_I}{c\rho_s}$
$\frac{\rho_I}{c\rho_s} = \frac{\pi^2}{3}\frac{T^2}{T_s^2}$
$\frac{\rho_I}{c\rho_s} = \frac{\pi}{2}\frac{T}{T_s} - \frac{1}{2}$
0
0.5
1.0
1.5
T/T_s

temperature and upon the temperature range over which the measurements are made. For example, if the spin-fluctuation temperature is at the low end of the measured temperature range, then the spin-fluctuation resistivity will appear to be nearly linear. Conversely, if the spin-fluctuation temperature is greater than the highest temperature measured, then the spin-fluctuation resistivity will vary roughly as T^2.

The shape of the Kaiser and Doniach curve shown in Fig. 6 is universal in the following sense. Since all the parameters pertaining to the host and to the exchange-enhanced impurity are included in the scaling factors, the model predicts that for all systems the contribution to the spin-fluctuation resistivity from local spin fluctuations can be scaled to yield the curve of Fig. 6. However, this will be the case only if the parameters can be considered temperature independent. In general, one expects the dynamic susceptibility and consequently the spectral density function to be largely independent of the temperature for temperatures which are orders of magnitude below the d-band degeneracy temperature. If, however, the local enhancement factor, $\alpha=\{1-\Delta U\chi(0)\}^{-1}$, is very large compared to unity, then even a small change in $\bar{\chi}(0)$ will produce a large change in α. Consequently the spin-fluctuation temperature will become temperature dependent and the resistivity can no longer be scaled to yield the universal curve. Furthermore, since the amount of the deviation depends upon the local enhancement factor, the resistivity curves for different materials can no longer be expected to scale with each other. Thus, the deviations of the spin-fluctuation resistivity from the Kaiser and Doniach universal curve are expected to be small over the range of temperatures for which the susceptibility of the host is nearly temperature independent, and the magnitude of these deviations from the universal curve is expected to be a strong function of the local enhancement factor.

1.13 Other Local Enhancement Models

In this section we briefly describe other models which have been proposed to explain the temperature dependence of the electrical resistivity which results when the conduction electrons are scattered by the localized spin-fluctuations. In order to better understand some of the concepts which go into these models, it will be of value to review in a qualitative manner the nature of a local spin-fluctuation and its interaction with the conduction electrons.

We have seen in previous sections that the spin-fluctuations are characterized by their spectral density functions. The lifetime (τ) of the spin fluctuation is generally taken to be the reciprocal of the width of the spectral density function at half maximum, and the characteristic frequency (energy) is generally taken to be the value of the frequency at which the peak in the spectral density function occurs. As was the case for spin fluctuations in a uniformly enhanced system, the local spin fluctuations have a characteristic energy spread which is of the same order of magnitude as the characteristic energy itself (see Fig. 5), that is, $\omega\tau \approx 1$ ($\hbar=1$) and consequently the lifetime of the spin-fluctuation is $\tau \approx (k_B T_s)^{-1}$.

This intrinsic or characteristic lifetime (τ) of the spin fluctuation may or may not be the significant lifetime in the experiment. As an example of this, let us consider the case of measuring the static susceptibility at a locally enhanced site. Such a susceptibility can be found by applying a magnetic field and measuring the increase in the magnetization of the locally enhanced system over that of the host system (as described in Sect. 1.10). In order to simplify the discussion we will assume the measurement takes place over periods which are long in comparison with the spin-fluctuation lifetime. In practice this will be the case if the measurement occurs over a time $\Delta t \gg 10^{-11} T_s^{-1}$ seconds. This leaves two lifetimes which are of interest: 1) the lifetime $(k_B T)^{-1}$ of a thermal fluctuation of the system, and

2) the lifetime of the spin fluctuation. When $T \ll T_s$, the lifetime of a thermal fluctuation will be much longer than that of the spin fluctuation. In this case we would expect the magnetic properties of the system to resemble those of the locally enhanced system described in Sect. 1.10. However, once the temperature becomes much greater than the spin-fluctuation temperature ($T \gg T_s$), the lifetime of the thermal fluctuations becomes much shorter than the lifetime of the spin fluctuation and there is a high probability that the electron-hole pair of the spin fluctuation will be thermally scattered before the spin fluctuation has decayed. Thus, for temperatures larger than T_s, one would expect that as the temperature increases the temperature dependence of the system would approach that of a local-moment system.

Consider next the case of a conduction electron scattering from a spin fluctuation. For low temperatures ($T \ll T_s$) the lifetime of the conduction electron in a given state is much longer than the lifetime of the spin-fluctuation, and the conduction electron "sees" a time average of the properties of the spin fluctuation. However, at high temperature ($T \gg T_s$) the electron no longer sees the complete temporal nature of the spin fluctuation before it is thermally scattered. Thus, we expect the electron to react more to the local-moment nature of the spin fluctuation that results once the electron-hole pair of the spin-fluctuation is created. Also, on the basis of this intuitive argument we would expect the scattering of the conduction electron to eventually reach the spin-disorder limit, that is, the maximum spin-scattering possible from a single local moment.

A phenomonological model[40,41,42] of the electrical resistivity can be formed in which the above mentioned concepts are taken into account. In this model one assumes the following: 1) There is a single conduction band. 2) The local spin fluctuation takes place in this conduction band and is screened by the conduction electrons. 3) The local spin fluctuation is represented by an effective magnetic moment

which reflects the average moment the conduction electron "sees" as a result of the spin fluctuation. Thus as the temperature increases, the effective moment is assumed to increase from zero at T=0 to the maximum value of the moment for a electron-hole pair. 4) The value of the effective moment is found from susceptibility data by using the Curie law,

$$\chi_{imp} = \frac{ng^2 S(S+1)\mu_B^2}{3k_B T} , \tag{1.174}$$

where S is the effective spin and n is the number of locally enhanced impurity atoms per unit volume.

The spin-fluctuation resistivity is calculated by using the Friedel sum rule[22] to obtain the phase shifts for the scattering cross section. The sum rule is generally written as

$$Z = \frac{2}{\pi} \sum_{\ell=0}^{\infty} (2\ell+1)\eta_\ell , \tag{1.175}$$

where Z is the number of conduction electrons associated with an impurity site minus the number of conduction electrons associated with a host site, and η_ℓ is the phase shift of the ℓth partial wave of the conduction electron. Since the sum rule assumes that the number of spin-up electrons equals the number of spin-down electrons, we must modify the rule in the case of local spin fluctuations. This is done by using the rule to describe each spin band separately, that is,

$$Z_\uparrow = \frac{1}{\pi} \sum_{\ell=0}^{\infty} (2\ell+1)\eta_{\ell\uparrow} \tag{1.176}$$

and

$$Z_\downarrow = \frac{1}{\pi} \sum_{\ell=0}^{\infty} (2\ell+1)\eta_{\ell\downarrow} . \tag{1.177}$$

The total charge difference is given by

$$Z = Z_\uparrow + Z_\downarrow , \tag{1.178}$$

and the effective spin on the impurity site is

$$S = \frac{Z_\uparrow - Z_\downarrow}{2} . \tag{1.179}$$

For simplicity, one assumes that the d-band spin fluctuation is screened entirely by the ℓ=2 partial wave. Then the sum rule reduces to

$$Z_{\uparrow} = \frac{5}{\pi}\eta_{2\uparrow} \tag{1.180}$$

and

$$Z_{\downarrow} = \frac{5}{\pi}\eta_{2\downarrow} . \tag{1.181}$$

The resistivity that results from the scattering is in this case given by[43]

$$\rho_I = \frac{c\rho_m}{2}\{\sin^2\eta_{2\uparrow} + \sin^2\eta_{2\downarrow}\} , \tag{1.182}$$

where c is the impurity concentration and ρ_m is the maximum possible resistivity per atomic percent. After solving for the phase shifts in terms of Z and S and reducing the equation to factors in Z and S, we have the final result:

$$\boxed{\rho_I = c\rho_m \sin^2(\frac{\pi}{10}Z) + c\rho_m \cos(\frac{\pi}{5}Z)\sin^2(\frac{\pi}{5}S)} \quad . \tag{1.183}$$

There are two features to note from the model. First, since the effective spin of the fluctuation is zero at T=0 and since the net charge at the impurity site is independent of the excitation level of the spin fluctuation, the first term is the temperature independent residual resistivity. For an isoelectronic impurity (Z=0), the residual resistivity is zero. The residual resistivity is a maximum for impurities where the charge difference corresponds to Z=5. Second, the temperature dependence is the result of the spin fluctuations changing the effective spin at the impurity site and is given by the second term. The temperature dependence of the resistivity will be positive for $|Z| < \frac{5}{2}$ and negative for $\frac{5}{2} < |Z| < \frac{15}{2}$.

Experimental tests of the model have been carried out for some alloy systems. The model is fitted to the resistivity data after the Curie law (Eq. 1.174) has been used to obtain the effective spin from susceptibility data. Souletie[42] found good agreement between the model and experiment in dilute alloy systems with a Cu or Au host, Nagasawa[41] found good

agreement for dilute Fe or Mn in Rh, and Loram et al.[40] were able to account qualitatively for the temperature dependent resistivity in Pt and Pd hosts using the model.

Another model for the electrical resistivity of locally exchange-enhanced systems is the single band model developed by Rivier and Zlatic[44] and extended by Fischer[45]. In the Rivier and Zlatic calculation, as in the Lederer-Mills and Kaiser-Doniach model, potential scattering from the locally enhanced impurities was neglected and therefore their calculation is expected to apply only to impurities which are nearly isoelectronic (Z~0) with the host. Fischer has extended the calculation by including the potential scattering from the impurity ($\Delta V \neq 0$) and by allowing for an exchange-enhanced host ($U \neq 0$).

Although in both this model and the Lederer-Mills and Kaiser-Doniach model the system is described by the Hubbard and Wolff Hamiltonians (see Eq. 1.113),

$$\mathcal{H} = \mathcal{H}_H + \mathcal{H}_W \ , \tag{1.184}$$

where

$$\mathcal{H}_H = \sum_\alpha \sum_{ij} T_{ij} c^\dagger_{i\alpha} c_{j\alpha} + \tfrac{1}{2} U \sum_\alpha \sum_i n_{i,\alpha} n_{i,-\alpha} \tag{1.185}$$

and

$$\mathcal{H}_W = \Delta V \sum_\alpha n_{I\alpha} + \tfrac{1}{2} \Delta U \sum_\alpha n_{I,\alpha} n_{I,-\alpha} \ , \tag{1.186}$$

the philosophy in calculating the resistivity is quite different. In the two-band model of Lederer-Mills and of Kaiser-Doniach, one uses the first Born approximation to calculate the resistivity that results from s-band conduction electrons scattering (via the s-d exchange interaction) from spin-fluctuations in the d band. In the single-band model of Rivier-Zlatic and of Fischer, one assumes that the spin-fluctuation resistivity is the result of conduction electrons scattering (via the intra-atomic Coulomb interaction) from spin fluctuations within the conduction band. One finds the spin-fluctuation resistivity by using many-body perturbation techniques to calculate the relaxation time for a conduction electron scattering from the local spin fluctuation.

The calculation can be outlined in terms of Feynman diagrams. An example of the type of scattering considered is given by the diagram in Fig. 7a. Here a conduction electron is scattered via the intra-atomic Coulomb interaction, ΔU, creating an electron-hole pair where both the electron and hole have spin states opposite to that of the conduction electron. At later times the conduction electron and the newly created hole interact via the intra-atomic Coulomb interaction. The electron-hole pair is annihilated and the conduction electron is again scattered. Each line (——►——) represents a single particle Green's function of the unperturbed system, which in this case is the exchange-enhanced host. The dashed line represents the local interaction factor, $\Delta U/2$. The single particle Green's function for the perturbed system (═══►═══) is given by the Dyson equation which is represented diagrammatically in Fig. 7b. The shaded circle is the sum of all possible diagrams which can be connected to an incoming and an outgoing electron line but can not be separated into two pieces by cutting only one particle line. This sum is the "proper" self-energy. In the Rivier-Zlatic model one calculates the self-energy by using the "ladder" approximation (represented diagramatically at the bottom of Fig. 7b). Once the self energy is found it is relatively straightforward to calculate[44,45] the relaxation time, $\tau(\omega)$. The spin-fluctuation resistivity is then obtained from the relation[44,45,46]

$$\rho_I = \rho_o' \left\{ \int d\omega \left[-\frac{\partial f(\omega)}{\partial \omega} \right] \tau(\omega) \right\}^{-1} , \qquad (1.187)$$

where ρ_o is a constant which is to be chosen so as to give the unitary limit at $T \to \infty$.

After replacing the Fermi window $(-\frac{\partial f(\omega)}{\partial \omega})$ in the above equation by the delta function, Rivier and Zlatic finally obtain the spin-fluctuation resistivity,

$$\boxed{\rho_I = c\rho_s \left[1 - \{ 1 + \pi\tilde{T} + \psi(\tfrac{1}{2} + \frac{1}{2\pi\tilde{T}}) - \psi(1 + \frac{1}{2\pi\tilde{T}}) \}^{-1} \right]} , \qquad (1.188)$$

where $\psi(x)$ is the digamma function, $\tilde{T} \equiv T/T_s$ (as in the Kaiser

and Doniach formula), and $c\rho_s$ is the unitary limit. As in the Kaiser and Doniach case, the Rivier and Zlatic calculation yields a universal curve. This curve is shown in Fig. 8, where the scaled resistivity is shown as a function of the scaled temperature. At temperature $T \leq 0.1\, T_s$ the resistivity follows a T^2 behavior,

$$\rho_I = c\rho_s \frac{\pi^2}{2} \left(\frac{T}{T_s}\right)^2 \quad , \; T \leq 0.1\, T_s \; . \tag{1.189}$$

At $T=0.14\, T_s$ there is an inflection point and consequently a linear region around this point. Just above T_s there is a logarithmic region and beyond that the curve approaches the unitary limit. This is to be contrasted with the Kaiser and Doniach universal curve which is T^2 below $\sim 0.1\, T_s$, but does not become linear until $T > T_s$ (see Sect. 1.12).

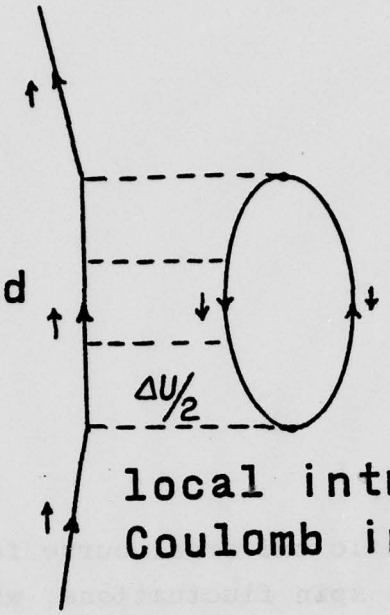
In the Rivier and Zlatic model several approximations have been made which quantitatively affect the results. For example, the delta function approximation for the Fermi window results in an error which affects the temperature behavior of the universal curve at low temperatures. If this approximation is not made, one finds[44] that the T^2 term is 50% larger and the linear region moves to a lower temperature (the unitary limit does not change, of course).

Fischer[45] has calculated the transport properties of an exchange-enhanced system using a model similar to that of Rivier and Zlatic. In this model he allowed for the changes that occur in the electron hopping term T_{ij} and the potential term V as a result of the introduction of the impurity (i.e., $\Delta V \neq 0$ and $T_{I,j} \neq T_{i,j}$, where I refers to the impurity site with the impurity present and i refers to the impurity site with the impurity replaced by the host atom). He finds that the universality of the spin-fluctuation resistivity is lost; that is, scaling ρ_I by $c\rho_s$ and T by T_s no longer results in a single curve, but a family of curves which depend upon the values of T_s, ΔV and the change in the hopping term. When fitting our 1-300 K resistivity data, we shall qualitatively include the results of these extensions of the model.

Fig. 7.

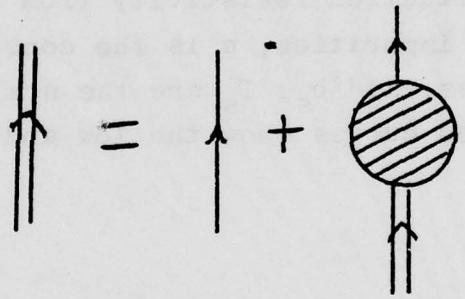
A diagrammatic representation of scattering processes considered in the Rivier-Zlatic model is shown. In (a) an example is given of the type of scattering that occurs at the locally enhanced impurity center as a result of the increase in the intra-atomic Coulomb interaction. In (b) the Dyson equation is represented diagrammatically in the ladder approximation.

a) single-band electron



local intra-atomic Coulomb interaction

b)



where

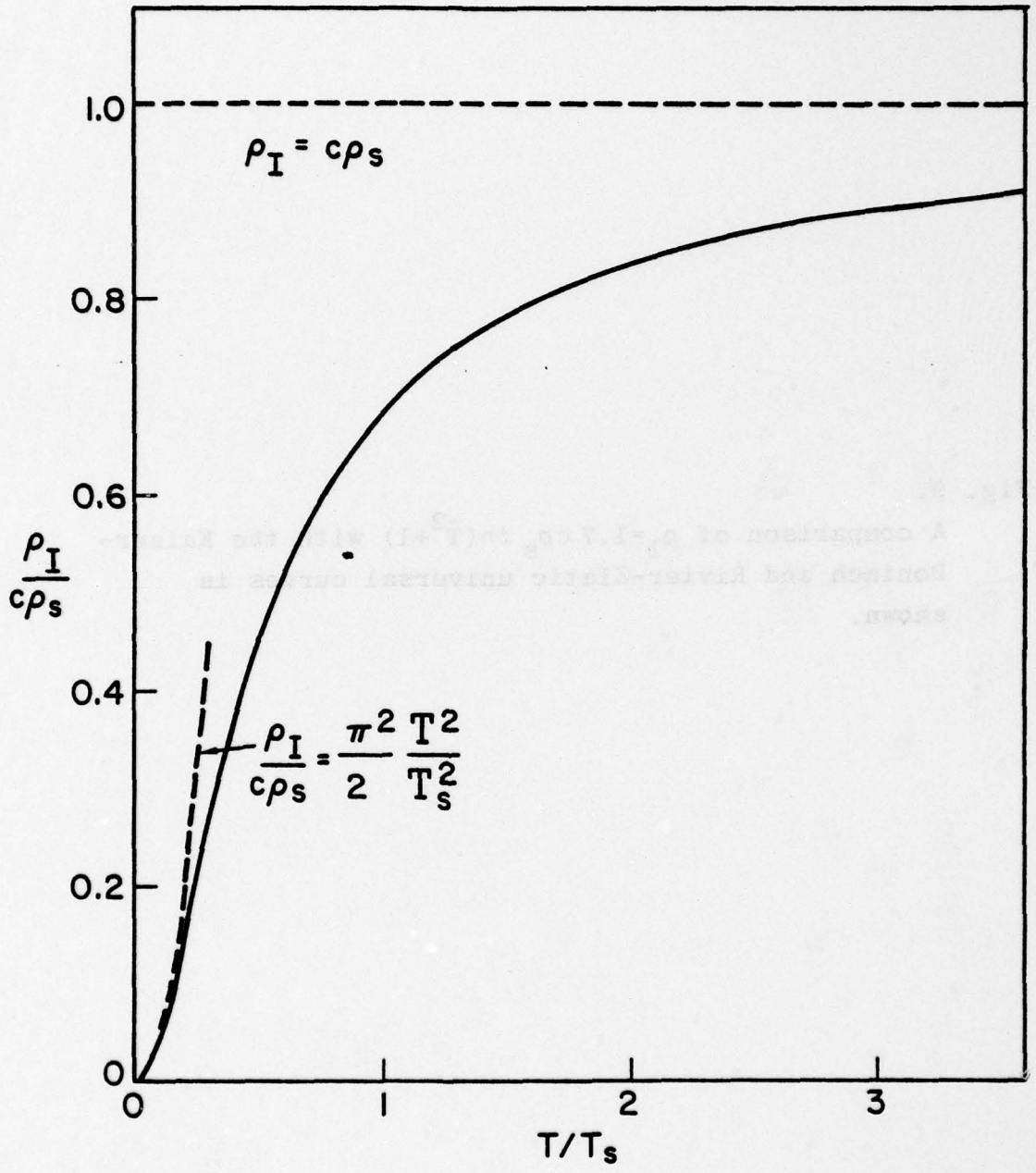


and



Fig. 8.

The Rivier-Zlatic universal curve for the resistivity from local spin fluctuations, where ρ_I is the spin-fluctuation resistivity from the locally enhanced impurities, c is the concentration of the impurities, and ρ_s, T_s are the scaling parameters. The dashed curves show the low and high temperature limits.


1.0
0.8
0.6
0.4
0.2
0
$\rho_I = c\rho_s$
$\frac{\rho_I}{c\rho_s}$
$\frac{\rho_I}{c\rho_s} = \frac{\pi^2}{2}\frac{T^2}{T_s^2}$
0
1
2
3
T/T_s

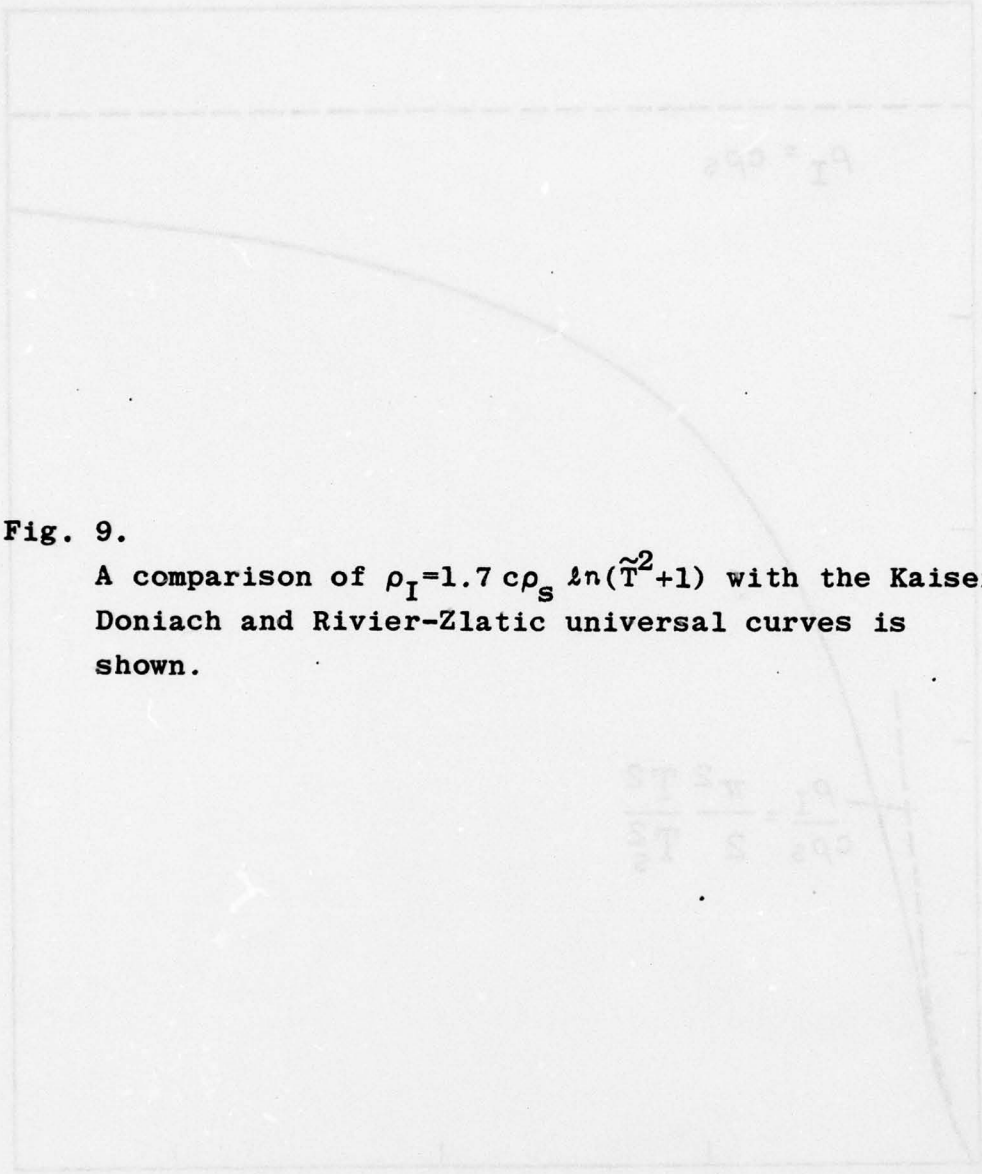
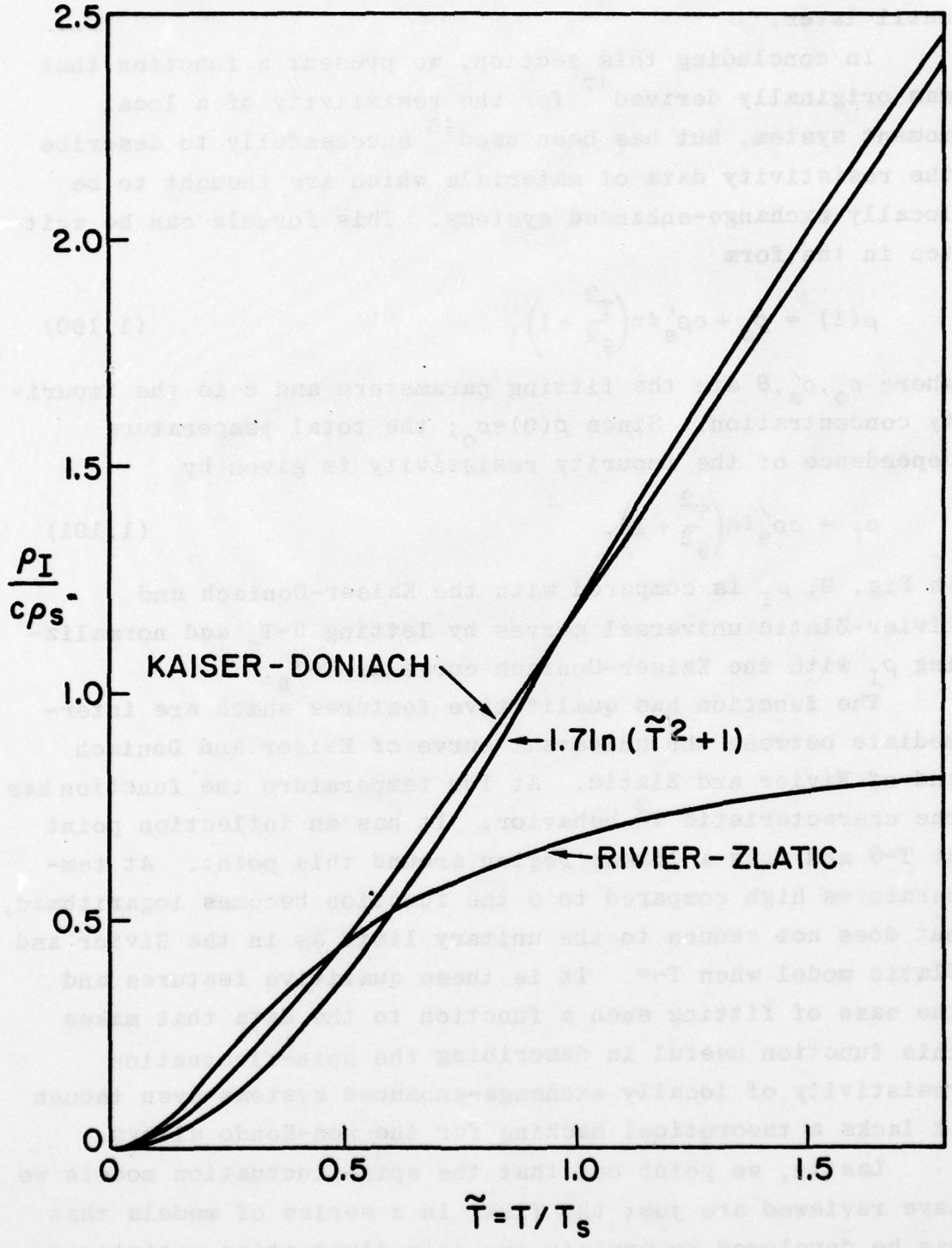


Fig. 9.
A comparison of $\rho_I = 1.7\, c\rho_s \ln(\tilde{T}^2+1)$ with the Kaiser-Doniach and Rivier-Zlatic universal curves is shown.


2.5
2.0
1.5
1.0
0.5
0
0
0.5
1.0
1.5
$\frac{\rho_I}{c\rho_s}$
KAISER - DONIACH
$1.71 \ln (\tilde{T}^2 + 1)$
RIVIER - ZLATIC
$\tilde{T} = T/T_s$

This is done by parameterizing the Rivier-Zlatic universal curve, and the discussion of this procedure will be left until later.

In concluding this section, we present a function that was originally derived[47] for the resistivity of a local moment system, but has been used[40] successfully to describe the resistivity data of materials which are thought to be locally exchange-enhanced systems. This formula can be written in the form

$$\rho(T) = \rho_o + c\rho_s' \ell n\left(\frac{T^2}{\theta^2} + 1\right), \tag{1.190}$$

where ρ_o, ρ_s', θ are the fitting parameters and c is the impurity concentration. Since $\rho(0)=\rho_o$, the total temperature dependence of the impurity resistivity is given by

$$\rho_I = c\rho_s' \ell n\left(\frac{T^2}{\theta^2} + 1\right). \tag{1.191}$$

In Fig. 9, ρ_I is compared with the Kaiser-Doniach and Rivier-Zlatic universal curves by letting $\theta=T_s$ and normalizing ρ_I with the Kaiser-Doniach curve at $T=T_s$.

The function has qualitative features which are intermediate between the universal curve of Kaiser and Doniach and of Rivier and Zlatic. At low temperature the function has the characteristic T^2 behavior. It has an inflection point at $T=\theta$ and thus a linear region around this point. At temperatures high compared to θ the function becomes logarithmic, but does not reduce to the unitary limit as in the Rivier and Zlatic model when $T\to\infty$. It is these qualitive features and the ease of fitting such a function to the data that makes this function useful in describing the spin-fluctuation resistivity of locally exchange-enhanced systems even though it lacks a theoretical backing for the non-Kondo alloys.

Lastly, we point out that the spin-fluctuation models we have reviewed are just the first in a series of models that may be developed to explain the spin-fluctuation resistivity. The present situation is somewhat analogous to having the

Bloch-Grüneisen model to explain the electrical resistivity that results when the electrons are scattered from thermal vibrations of the lattice. In both cases one neglects details of the band structure by assuming spherically symmetric, parabolic bands (i.e., the electrons are assumed to be free but to have an effective mass different from the free electron mass), and the crystal momentum is assumed to be conserved (Umklapp processes are neglected). In the case of the lattice vibrations (phonons), the energy distribution is given by the Debye spectrum. In the case of the spin-fluctuations (paramagnons), the energy distribution is given by the spectral density functions of the previous sections. The distribution functions are generally assumed to be temperature independent, and the interaction of the electrons with the phonons or paramagnons is assumed to be independent of other scattering processes. Even though many simplifications were made, the spin-fluctuation models have increased our understanding of the spin-fluctuation resistivity, somewhat in the same manner that the Bloch-Grüneisen model increased our understanding of the resistance in metal due to electrons scattering from thermal vibrations of the lattice.

CHAPTER II
EXPERIMENTAL PROCEDURES

A. Sample Preparation

The experimental procedure consisted basically of fabricating three sets of $(Pd_{95}Rh_5)_{100-x}Ni_x$ alloy samples and measuring the magnetization and resistivity of each of these samples. The first set consisted of a single $(Pd_{95}Rh_5)_{99}Ni_1$ resistivity sample which was measured in order to determine the overall feasibility of successfully completing the goals of the project. Since the preliminary results were promising, a second set consisting of four resistivity and four magnetization samples was fabricated and measured. The third and final set consisted of seven resistivity and five magnetization samples which were prepared in order to extend and to clarify the experimental results of measurements on the previous two sets.

2.1 Fabrication and Characterization

The details of sample fabrication are given in the following discussion and apply to all three sample sets unless otherwise noted. The fabrication of each set began by melting a single master alloy from which the other members of the set were derived. The starting materials for the master alloys were 5-9's Pd powder, 4-9's Rh powder and, in the case of the master alloy for the first set, 5-9's Ni rod. The starting materials were weighed, mixed, and placed in a quartz crucible. The mixture was then slowly degassed and sintered by induction heating in a vacuum which was kept below ~1 millitorr by controlling the heating. This procedure continued until a sintered compact was formed. The compact was then melted in a gas-cooled quartz crucible filled with

argon. For the first two sets, each melted compact (weighing ~10 g each) was removed, turned upside down, and remelted. This procedure was then repeated. For the last set, there were several melted compacts of the same composition and these were arc melted together in a water-cooled copper crucible. The resulting ingot (weighing 147 g) was turned over, melted, and the procedure repeated several times. This large amount of master alloy served two functions. First, it provided enough material for future work, and, second, it greatly improved the accuracy to which the sample composition was known.

Once the master alloys had been made, ingots were prepared with the desired sample compositions. For the first set, which consisted of just the one composition, the ingot was a portion of the master alloy. For the second set, appropriate amounts of the $Pd_{95}Rh_5$ master alloy and of the $(Pd_{95}Rh_5)_{99}Ni_1$ master alloy of the first set were induction melted to form ingots (~2 g each) with the desired $\frac{1}{4}$, $\frac{1}{2}$, and $\frac{3}{4}$ at% Ni compositions. For the third set, the $Pd_{95}Rh_5$ master alloy of this set was divided roughly in half. One of the halves was arc melted with the appropriate amount of Ni to form a $(Pd_{95}Rh_5)_{97}Ni_3$ secondary master alloy. Then the appropriate amounts of material from each of these two master alloys were combined and arc melted to form ingots (~4 g each) with Ni concentrations of 0.1, 0.2, 1.5, 2.0, and 2.5 at%. Portions (~4 g each) of the master alloy and of the 3% Ni secondary master alloy complete the ingots of this final set.

All samples were made from the above ingots using the procedures to be described below. The procedures used in fabricating the single sample of the first set differ slightly from those used for the rest of the samples. These differences will be described later. The ingots (roughly cylindrical in shape) were first reduced in diameter by swaging. Once the diameter had been reduced by 20 to 25% the ingot was cleaned and given a strain relieving anneal by heating

the ingot in vacuum (~10^{-5} torr) to ≈1000°C for a few seconds with an induction heater. This procedure was repeated until the ingots reached diameters of ~3.7 mm and ~5.5 mm for the second and the third sample sets, respectively. The ingots were then cleaned, etched and annealed for 20 h at 1200°C in a sealed quartz tube which was filled with argon to a pressure of 1/3 bar. The purpose of the anneal was to remove any nonequilibrium microstructure that may have formed during the melt. After the 1200°C anneal the ingots were cooled to ~800°C at a rate of ~200°C/h and water quenched to room temperature. The magnetization samples were machined directly from these ingots by spark erosion to form spheres ~3.0 mm in diameter, weighing ~0.17 g, and spheres ~4.6 mm in diameter, weighing ~0.61 g, in the case of the second and third sample sets respectively. The material that remained was then fabricated into wire samples. The above swaging procedure was continued until a diameter of ~0.7 mm was reached. Then, instead of further swaging to reduce the diameter, we pulled the wires through drawing dies until the final sample diameter of ~0.51 mm was reached. A small section was taken from each wire and further reduced to a diameter of ~0.25 mm. These finer wires were spot welded onto the corresponding sample wires to form the potential leads. The samples were then given a final strain relieving anneal for 1 h @ 800°C and water quenched to room temperature.

The single $(Pd_{95}Rh_5)_{99}Ni_1$ sample of the first set was made in a manner similar to the above samples with the following exceptions: 1) No spherical magnetization sample was made. 2) The final wire sample was 0.42 mm in diameter. 3) The final sample anneal was 1200°C for 20 h and the 1200°C anneal midway in the procedure was not performed.

All of the resistivity samples were roughly 20 cm in length. Examples of a magnetization sample and a resistivity sample are shown in Fig. 10.

A number of factors were considered in choosing the shape and size of the samples. In the case of the magnetization

samples, a spherical geometry was chosen because of the ease with which such a geometry allows for the correction of the demagnetizing field. The size of the sample was dictated by either the amount of material available or the maximum diameter the magnetometer would accommodate. In the case of the resistivity samples, there were several factors to consider in choosing the length and diameter of samples. The important parameter in this choice is the form factor (A/ℓ), where A is the cross sectional area of the wire sample, and ℓ is the distance between the potential probes. Since the resistivity is

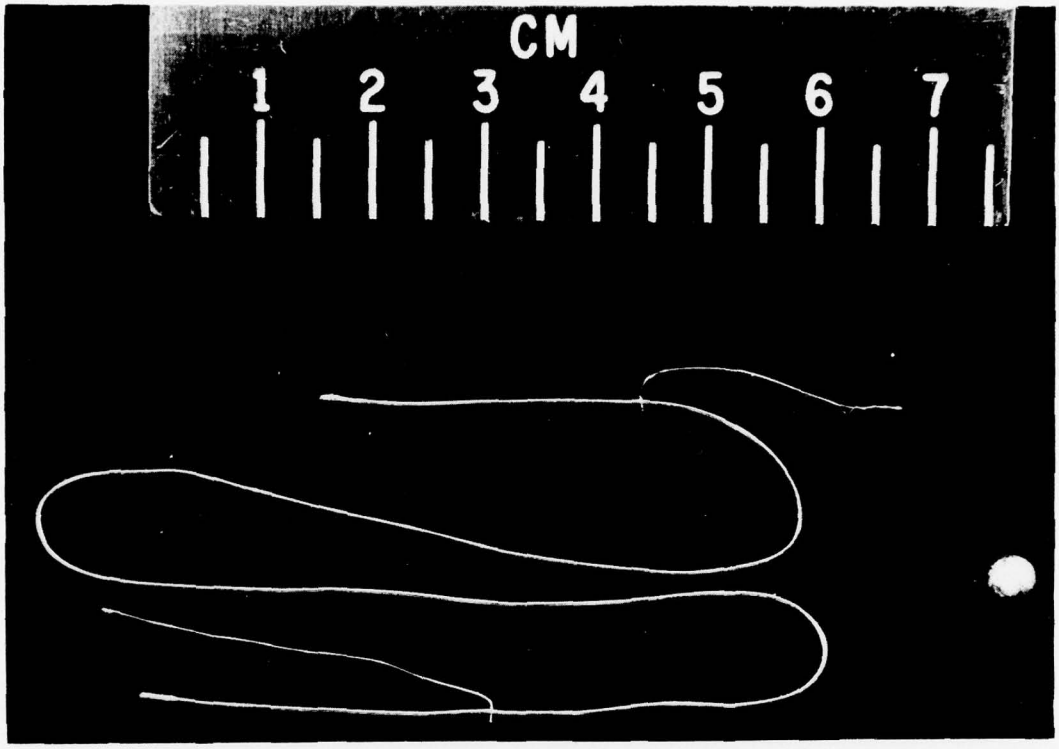
$$\rho = \left(\frac{A}{\ell}\right) \cdot R \ , \qquad (2.1)$$

where R is the resistance between the potential probes, the uncertainty in the resistivity depends on the uncertainty in the form factor. In fact, because of the high accuracy to which the resistance is measured, the fractional uncertainty in the resistivity is for all practical purposes equal to the fractional uncertainty in the form factor. Thus, we would want to choose a sample geometry in which the form factor could be easily and accurately measured. Another consideration is that we would like a sample geometry which produces a minimum amount of Joule heating for a given voltage (V) between the probes. This is desirable in order to minimize the error that occurs in the measurement of the sample temperature as a result of the self heating. It is also desirable, for reasons which will become clear when we discuss the method used for measuring the sample resistance, to have samples whose resistances are approximately equal to that of the standard resistor used in measuring the sample current. Finally, there is the consideration that as the wire becomes longer and finer the fabrication becomes more difficult.

The above factors are, of course, not all independent. For example, we can see from the relation between the Joule heating (V^2/R) and the form factor,

$$V^2/R = (V^2/\rho) \cdot (A/\ell) \ , \qquad (2.2)$$

Fig. 10.
Examples of a resistivity sample (the wire) and a magnetization sample (the sphere) used in the experimental work.


CM
1 2 3 4 5 6 7

that we would like the form factor to be as small as possible in order to minimize the Joule heating while maintaining a constant voltage. However, the more we reduce the diameter of the wire the more difficult it becomes to directly measure the average diameter, and the accuracy of the form factor decreases.

This conflict between improved form-factor accuracy and reduced Joule heating can be greatly alleviated by measuring the cross sectional area in an indirect manner. The procedure we used was to calculate the average cross section from the measured values for the length, weight, and density of the wire samples. The measured values of the densities of the sample ingots after the 1200°C anneal are shown in Fig. 11 as a function of the Ni concentration. The straight line through the data points is the density we calculated for this alloy system using X-ray lattice-parameter data obtained from measurements of the Pd-Rh system[48] and the Pd-Ni system.[49] Using the density from the graph, the total length of the wire sample, and the weight of the wire sample before attaching the potential probes, we calculate the average cross section of the wire. In this manner we are able to determine the form factor to an estimated accuracy of $\frac{1}{4}$%. This accuracy is much greater than that which would normally be obtained for wires of this size by measuring the diameter directly.

Another parameter which is necessary to characterize the samples is the sample composition. In a study such as this, where we are mainly interested in the contribution of the Ni to the spin-fluctuation properties of the system, it is the Ni concentration that will be the most important. The best way to control the Ni concentration to a high accuracy in an alloy with a fixed Rh to Pd ratio is to use the procedure we used in making the third sample set. Here the master alloy (the host) was large enough so that the error in weighing was negligible compared to the total weight loss of $\sim\frac{1}{2}$% that occurred as a result of the numerous meltings. Since it is reasonable to assume that the material lost had a composition

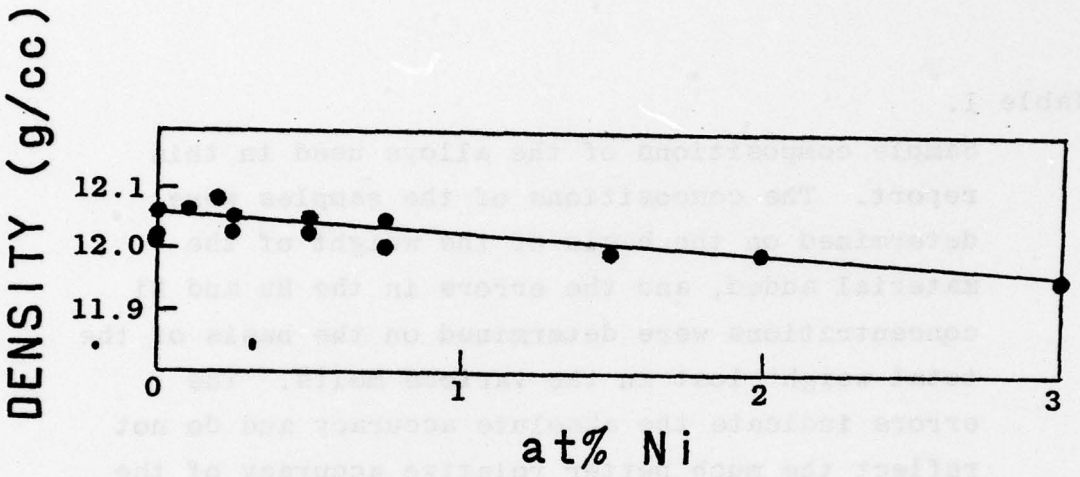
roughly that of the final alloy (say to within 20%), we estimate that the 5 at% Rh concentration in the host is accurate to better than ±0.05 at%. In adding the Ni to the host material to make the 3% Ni alloy we recorded a loss of only 0.004%. However, this may be somewhat misleading since there may have been a small amount of host material picked up as a result of melting in the same crucible that had been used for the host. In any case we would estimate that the Ni concentration for this alloy is accurate to better than 0.01 at% Ni. The amount of material lost (~0.1%) while making the alloys of this set indicates that the relative accuracy of the compositions of the members of each set will be much better than the absolute accuracy (stated above).

The composition of the earlier alloy sets was not as well controlled as for the set just described. Since the two master alloys from which these samples are derived were made independently of each other, the Rh to Pd ratios were unavoidably somewhat different. This problem was further compounded by an algebraic error which resulted in a master alloy with a concentration of 5.2 at% Rh instead of the 5.0 at% that was intended. This error was not discovered until after samples in the second set had been fabricated and their spin-fluctuation properties measured. Because of the error, we considered fabricating and measuring a new set of samples with the same Ni concentration as in the first two sets, but based on the master alloy of the third set. However, the consistency between the spin fluctuation results obtained from the three different sets convinced us that these results were largely independent of the small variation in the Pd to Rh ratio and therefore a new alloy set was not necessary. The compositions of all the alloys are given in table 1.

The high degree of consistency between members of the same set is reflected in the residual resistivities of the samples. In Fig. 12 we show the residual resistivity of the samples as a function of Ni concentration. The error bars shown represent the estimated form factor error of $\frac{1}{4}$%. The

Fig. 11.

Densities of the $(Pd_{95}Rh_5)_{1-x}Ni_x$ alloy ingots are shown as a function of the Ni concentration. The straight line through the data is the predicted density based on X-ray data.


DENSITY (g/cc)
12.1
12.0
11.9
0
1
2
3
at% Ni

AD-A049 154 NAVAL RESEARCH LAB WASHINGTON D C F/G 20/3
SPIN FLUCTUATIONS AND THE PARAMAGNETIC-FERROMAGNETIC TRANSITION--ETC(U)
OCT 77 D J GILLESPIE

UNCLASSIFIED NRL-MR-3630 SBIE-AD-E000 056 NL

2 OF 3
AD A049154

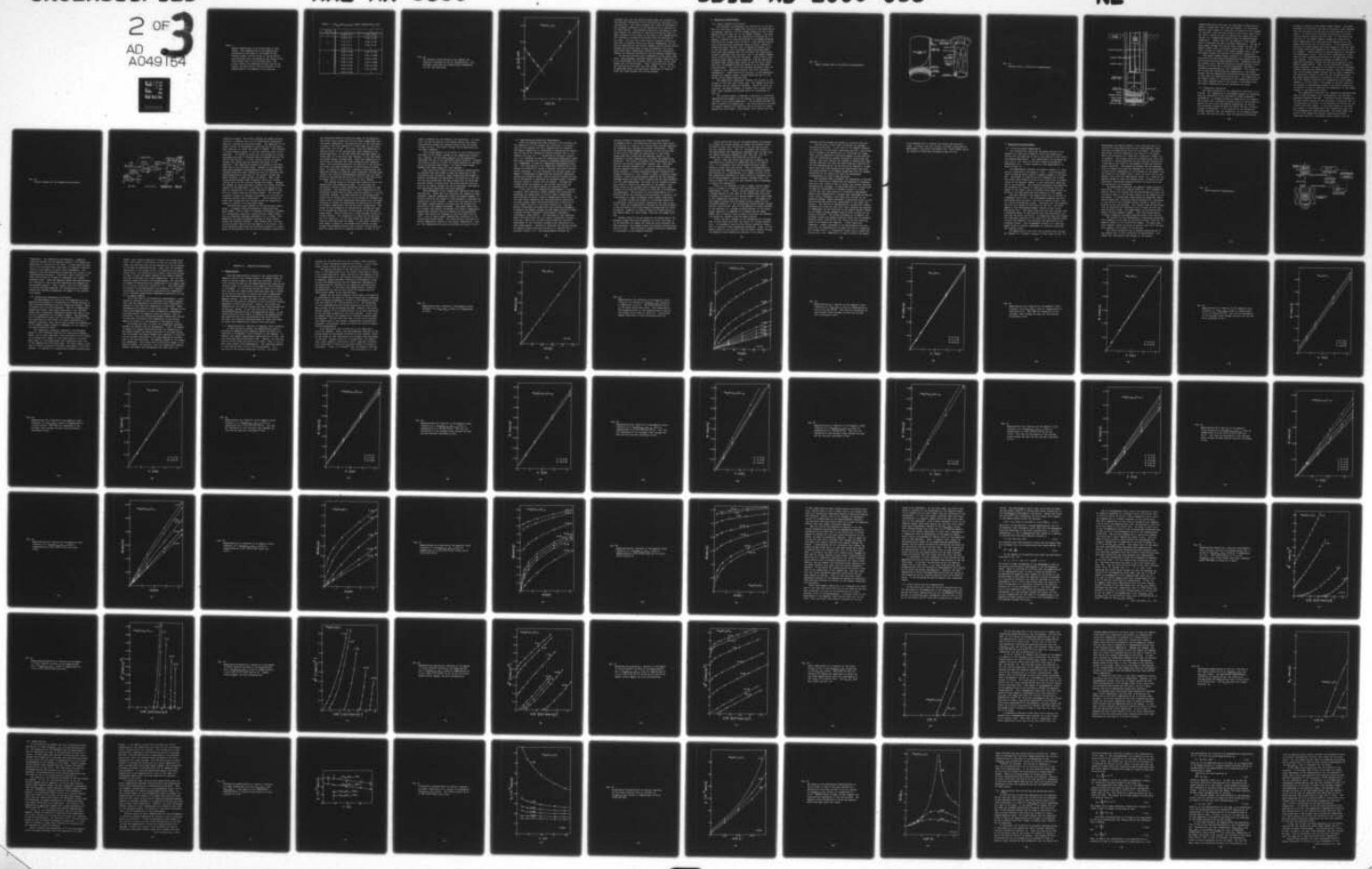


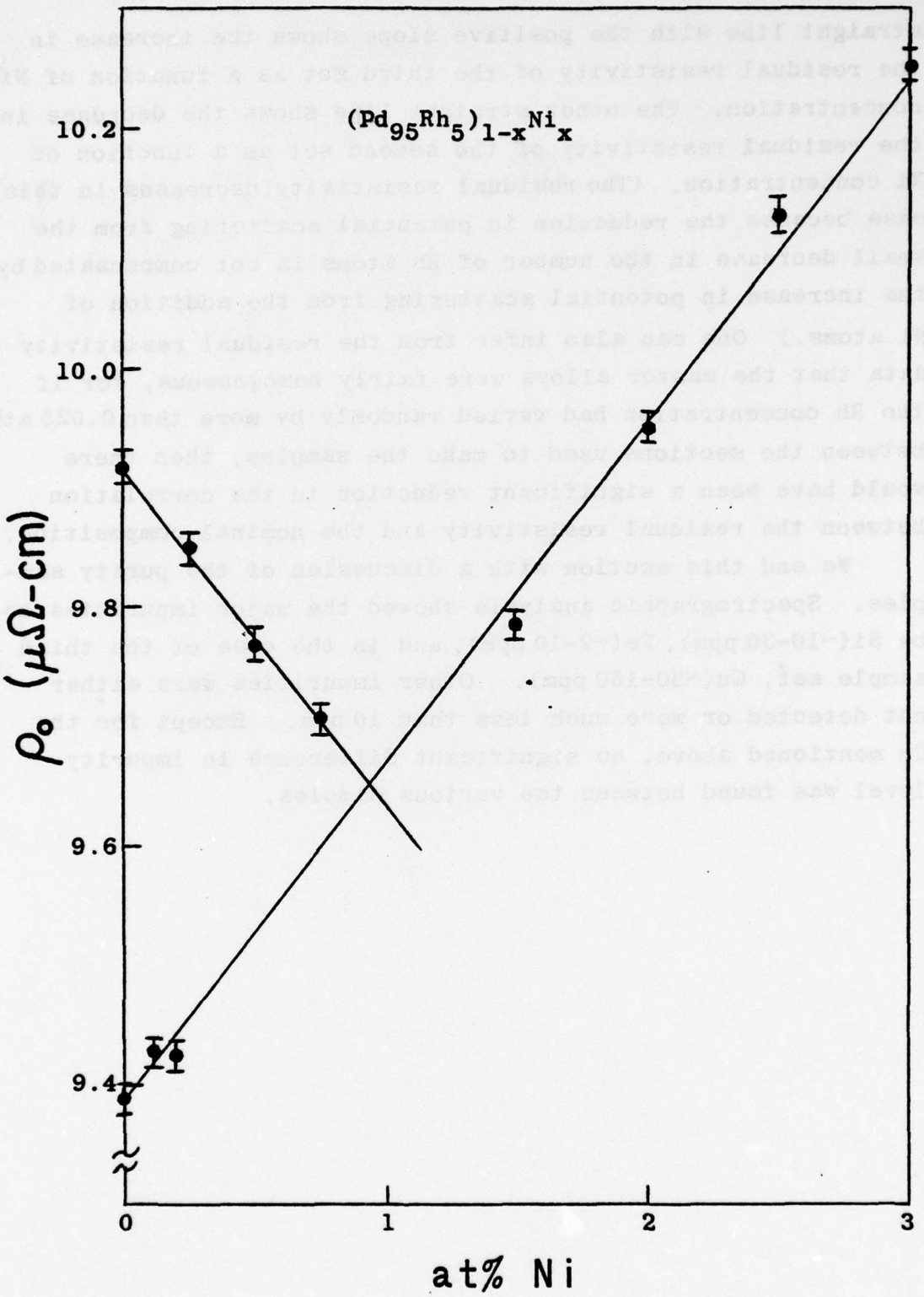
Table 1.

Sample compositions of the alloys used in this report. The compositions of the samples were determined on the basis of the weight of the material added, and the errors in the Rh and Ni concentrations were determined on the basis of the total weight lost in the various melts. The errors indicate the absolute accuracy and do not reflect the much better relative accuracy of the compositions of the members of the same set.

TABLE 1: $(Pd_{100-y}Rh_y)_{100-x}Ni_x$ SAMPLE COMPOSITIONS (at%)

Set No.	y	x
1	5.00 ± 0.1	1.00 ± 0.04
2	5.05 ± 0.1	0.75 ± 0.03
	5.10 ± 0.1	0.50 ± 0.02
	5.15 ± 0.1	0.25 ± 0.01
	5.20 ± 0.1	0
3	5.00 ± 0.05	3.00 ± 0.010
	5.00 ± 0.05	2.50 ± 0.008
	5.00 ± 0.05	2.00 ± 0.007
	5.00 ± 0.05	1.50 ± 0.005
	5.00 ± 0.05	0.20 ± 0.003
	5.00 ± 0.05	0.10 ± 0.003
	5.00 ± 0.05	0

Fig. 12.
The residual resistivities of the samples are shown as a function of the Ni concentration. The straight lines show the concentration dependence for the two alloy sets.


$(Pd_{95}Rh_5)_{1-x}Ni_x$
10.2
10.0
9.8
9.6
9.4
ρ_o ($\mu\Omega$-cm)
0
1
2
3
at% Ni

straight line with the positive slope shows the increase in the residual resistivity of the third set as a function of Ni concentration. The other straight line shows the decrease in the residual resistivity of the second set as a function of Ni concentration. (The residual resistivity decreases in this case because the reduction in potential scattering from the small decrease in the number of Rh atoms is not compensated by the increase in potential scattering from the addition of Ni atoms.) One can also infer from the residual resistivity data that the master alloys were fairly homogeneous, for if the Rh concentration had varied randomly by more than 0.025 at% between the sections used to make the samples, then there would have been a significant reduction in the correlation between the residual resistivity and the nominal composition.

We end this section with a discussion of the purity samples. Spectrographic analysis showed the major impurities to be Si(~10-30 ppm), Fe(~2-10 ppm), and in the case of the third sample set, Cu(~80-150 ppm). Other impurities were either not detected or were much less than 10 ppm. Except for the Cu mentioned above, no significant difference in impurity level was found between the various samples.

B. Resistivity Measurements

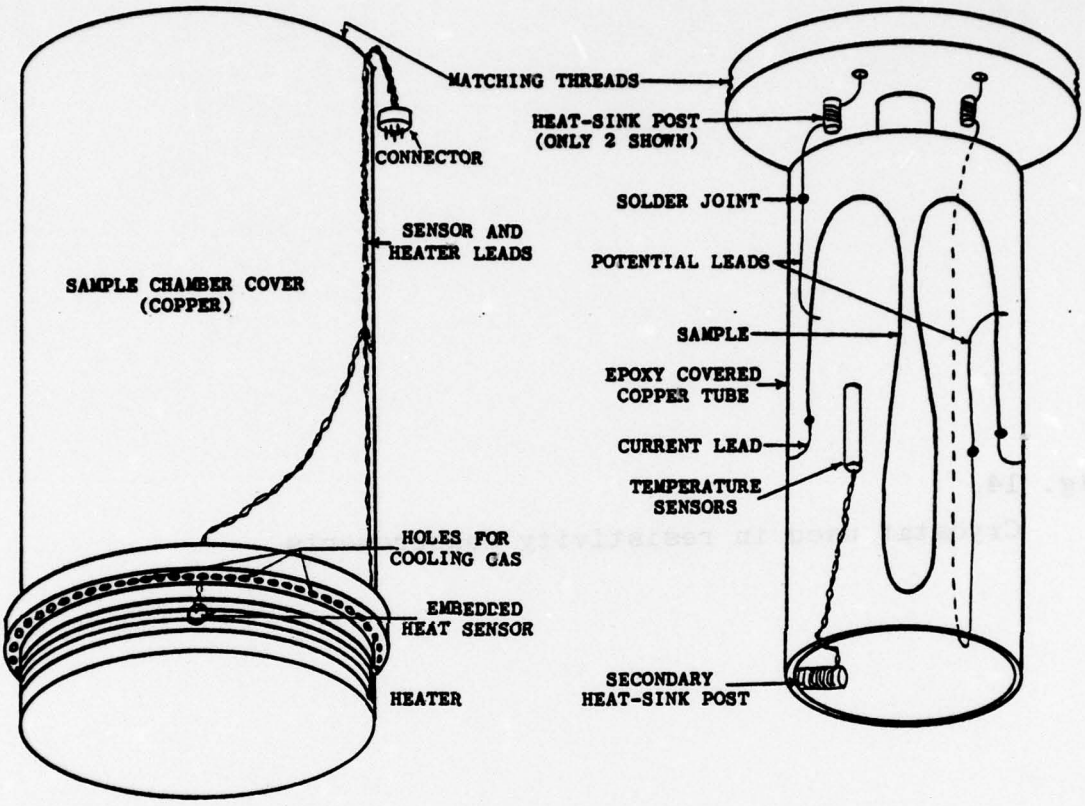
2.2 Sample Chamber and Cryostat

The procedure for measuring the resistivity of the samples as a function of temperature starts with the mounting of the samples (usually a Ni-free sample along with one or more samples from the same set) in the sample chamber. The chamber (Fig. 13), which has the capability of holding up to 5 samples, consists of three main parts: 1) the sample mounting tube which is a copper tube (~3 cm O.D.) that has been coated with an electrically insulating layer of highly thermally-conducting epoxy (Stycast; mfd. by Emerson & Cuming, Inc.), 2) the top plate, with individual copper heat-sink posts which have been epoxyed into the top plate and remain electrically insulated from the plate, and 3) the sample chamber cover, which screws onto the top plate. Twenty wires (thermocouple grade copper ~$\frac{1}{4}$ mm in diameter) from the measuring equipment pass through small holes in the top plate, where each wire is wrapped around and soldered to an individual heat-sink post. The wires then continue unbroken either to a sample or to a temperature sensor (Ge or Pt resistance thermometer). Those wires which continue to the temperature sensors are wrapped around a second heat-sink post at the bottom of the sample mounting tube.

The samples and temperature sensors are secured to the surface of the tube with teflon tape. The samples are wired in series, and all leads are soldered. After the cover is attached, the sample chamber is lowered into a Janus "Vari-Temp" dewar forming the cryostat which is illustrated in Fig. 14.

The cryostat makes it possible to maintain a controlled temperature environment for the samples at temperatures ranging from 1.3 K to room temperature. Two different methods are used to control the temperature. The first method is to flood the sample chamber with liquid He and to control the vapor pressure of the liquid. This method, while useful only for

Fig. 13.
Sample chamber used in resistivity measurements.


MATCHING THREADS
HEAT-SINK POST
(ONLY 2 SHOWN)
CONNECTOR
SOLDER JOINT
SENSOR AND
HEATER LEADS
POTENTIAL LEADS
SAMPLE CHAMBER COVER
(COPPER)
SAMPLE
EPOXY COVERED
COPPER TUBE
CURRENT LEAD
TEMPERATURE
SENSORS
HOLES FOR
COOLING GAS
EMBEDDED
HEAT SENSOR
HEATER
SECONDARY
HEAT-SINK POST

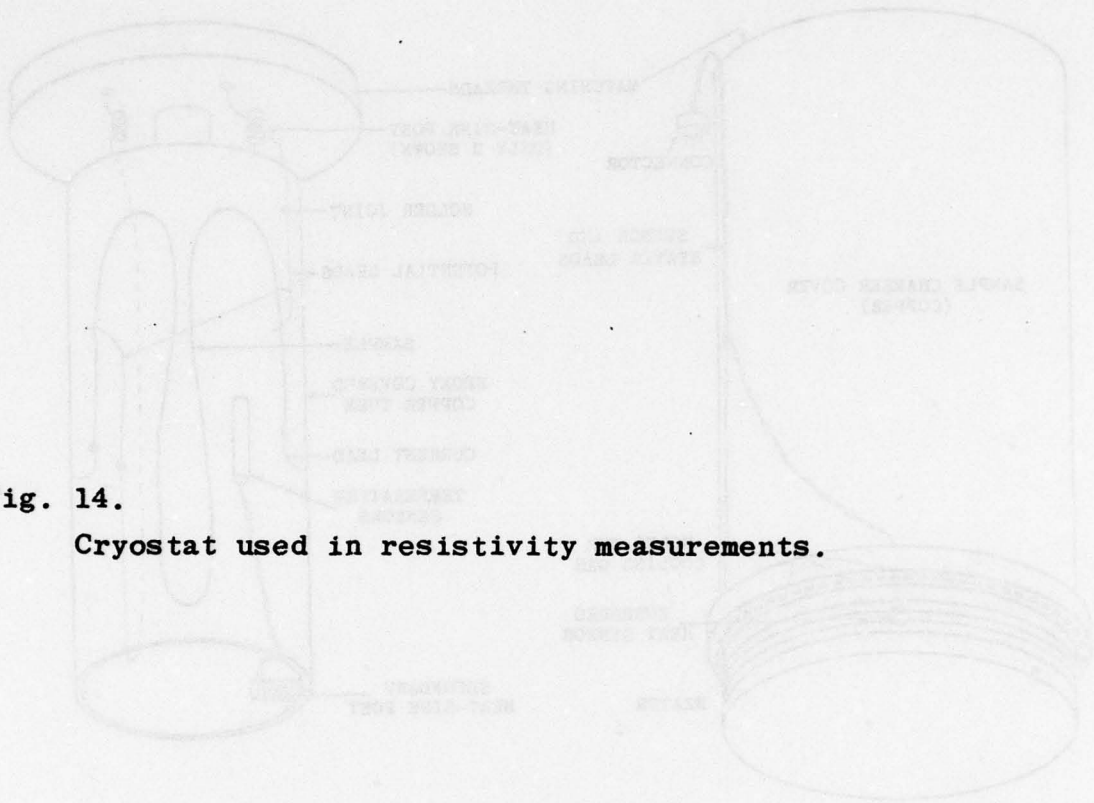
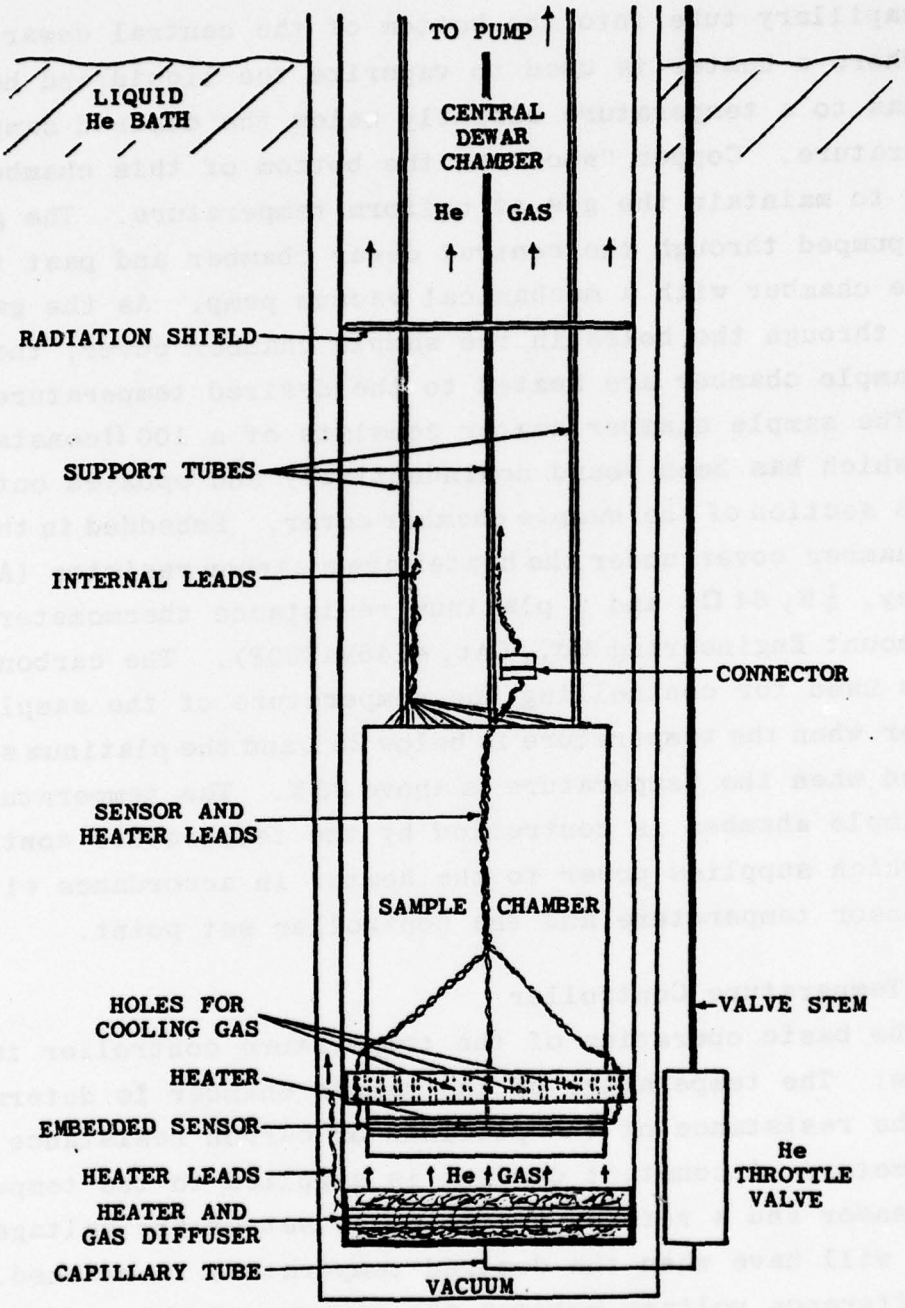


Fig. 14.
Cryostat used in resistivity measurements.


TO PUMP
LIQUID
He BATH
CENTRAL
DEWAR
CHAMBER
He
GAS
RADIATION SHIELD
SUPPORT TUBES
INTERNAL LEADS
CONNECTOR
SENSOR AND
HEATER LEADS
SAMPLE
CHAMBER
VALVE STEM
HOLES FOR
COOLING GAS
HEATER
EMBEDDED SENSOR
HEATER LEADS
He GAS
He
THROTTLE
VALVE
HEATER AND
GAS DIFFUSER
CAPILLARY TUBE
VACUUM

temperatures below 4.2 K, has the advantage of being able to handle a larger heat load from the samples. In the second method a small amount of liquid He is allowed to flow through the capillary tube into the bottom of the central dewar chamber where a heater is used to vaporize the liquid and heat the gas to a temperature slightly below the desired sample temperature. Copper "wool" at the bottom of this chamber helps to maintain the gas at uniform temperature. The gas is then pumped through the central dewar chamber and past the sample chamber with a mechanical vacuum pump. As the gas flows through the holes in the sample chamber cover, the gas and sample chamber are heated to the desired temperature.

The sample chamber heater consists of a 100 Ω constantan wire which has been wound noninductively and epoxyed onto the bottom section of the sample chamber cover. Embedded in the sample chamber cover under the heater are a carbon resistor (Allen Bradley, $\frac{1}{4}$ W, 64 Ω) and a platinum resistance thermometer (Rosemount Engineering Co., Cat. #146MA200F). The carbon sensor is used for controlling the temperature of the sample chamber when the temperature is below 25 K and the platinum sensor is used when the temperature is above 25 K. The temperature of the sample chamber is controlled by the temperature controller, which supplies power to the heater in accordance with the sensor temperature and the controller set point.

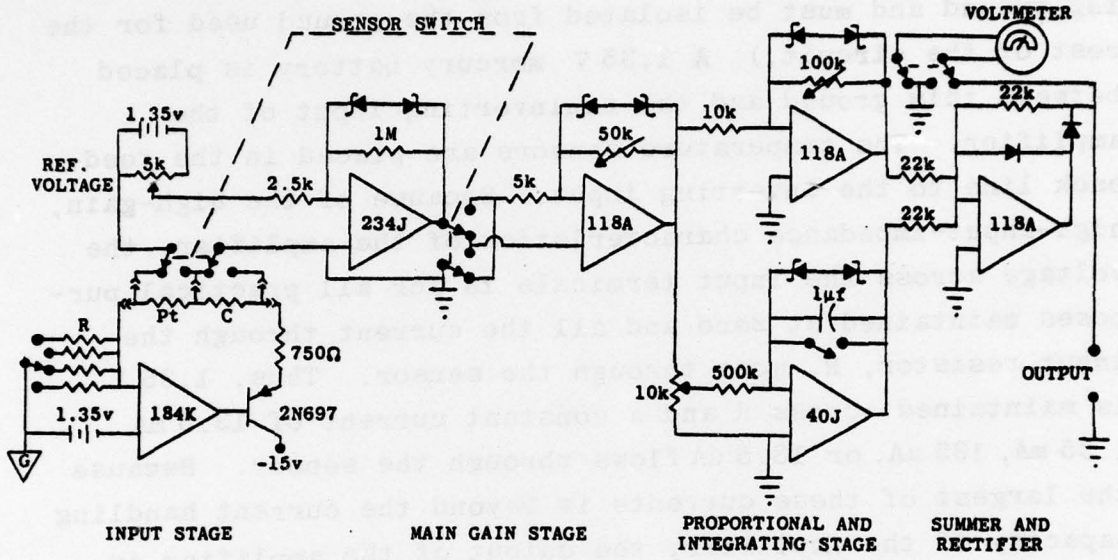
2.3 Temperature Controller

The basic operation of the temperature controller is as follows: The temperature of the sample chamber is determined from the resistance of the platinum or carbon resistance thermometer. A constant current is supplied to the temperature sensor and a reference voltage is set at the voltage the sensor will have when the desired temperature is reached. The difference voltage between the sensor and the reference voltage is amplified. If the polarity of the difference voltage indicates that the temperature of the sample chamber is lower than the set point, then the amplified difference

voltage is applied to the sample chamber heater. The power developed in the heater then heats the sensor, thus lowering both the difference voltage and the power supplied to the heater. A steady state condition is reached as the power from the heater balances the heat loss. At this point the deviation of the sample chamber temperature from the set point temperature is a function of the sensitivity of the sensor and the gain of the controller. If the sensitivity and gain are high enough then large changes in the heat load will cause only small changes in the temperature of the sample chamber. These changes are further reduced by turning on an integrating circuit. This circuit integrates as a function of time an adjustable fraction of the amplified difference voltage. The integrated voltage is added to the amplified difference voltage and the sum is applied to the sample chamber heater. Thus, as the difference voltage is being integrated, the power to the heater is being increased, thereby reducing the difference voltage. Once the temperature of the sample chamber reaches the set point temperature, the difference voltage is zero and the integration stops. The power being supplied to the heater by the integrator is just that needed to maintain the temperature of the sample chamber at the set point. Any change in the heat load will now produce a corresponding change in the power supplied to the heater in order to maintain the temperature of the sample chamber at the desired set point.

The temperature controller was changed and upgraded from time to time throughout this investigation, but the basic operation remained the same. A detailed circuit diagram for the most recent version of the controller is given in Fig. 15. In explaining the circuit it is convenient to divide the controller into four stages: 1) the input stage, 2) the main gain stage, 3) the proportional and integrating stage, and 4) the summing and rectifying stage. The input stage consists of the carbon and platinum temperature sensors (described earlier), the sensor current supply, and the

Fig. 15.
Circuit diagram of the temperature controller.


SENSOR SWITCH
VOLTMETER
1.35v
REF. VOLTAGE
5k
1M
2.5k
234J
5k
50k
118A
10k
100k
118A
22k
22k
22k
118A
1µf
Pt
C
R
750Ω
1.35v
184K
2N697
-15v
G
10k
500k
40J
OUTPUT
INPUT STAGE
MAIN GAIN STAGE
PROPORTIONAL AND INTEGRATING STAGE
SUMMER AND RECTIFIER

reference voltage. The current through the sensor is maintained at a constant level by the differential operational amplifier (Analog Devices model #184K). The magnitude of the sensor current is determined by selecting one of the precision resistors, R (100Ω, 1kΩ, 10kΩ, or 100kΩ). This resistor is placed between ground, G, and the inverting input of the amplifier. (It should be noted that this ground is a floating ground and must be isolated from the ground used for the rest of the circuit.) A 1.35 V mercury battery is placed between this ground and the noninverting input of the amplifier. The temperature sensors are placed in the feedback line to the inverting input. Because of the high-gain, high-input-impedance characteristics of the amplifier, the voltage across the input terminals is for all practical purposes maintained at zero and all the current through the input resistor, R, goes through the sensor. Thus, 1.35 V is maintained across R and a constant current of 13.5 mA 1.35 mA, 135 μA, or 13.5 μA flows through the sensor. Because the largest of these currents is beyond the current handling capacity of the amplifier, the output of the amplifier is used in conjunction with a power transistor (2N697) to control the current from the 15 V power supply. The variable reference voltage is obtained by dividing the 1.35 volts of a mercury battery with a 5 kΩ helipot. The difference between this voltage and the voltage across the temperature sensor is applied to the main gain stage.

The main gain stage consists of two operational amplifiers: a chopper stabilized amplifier (Analog Devices, model #234J), with a fixed 1 M feedback resistance, followed by a differential amplifier (Analog Devices, Model #118A), with an adjustable feedback resistance of 0 to 50 kΩ. Each amplifier is protected against overload by Zener diodes across the feedback resistor. These diodes limit the gain so that no more than 8 volts can appear at the output. The first amplifier amplifies the difference voltage by a factor which is determined by the raio of the feedback resistance to

the resistance directly across the input of the amplifier. Since this ratio varies with the set point temperature and the sensor temperature, the amplification of the difference voltage by the first amplifier of this stage can vary anywhere from ~100 to 400. The output from this amplifier is applied either to the noninverting input terminal of the second amplifier, in the case where the platinum sensor is being used, or to the inverting terminal, in the case where the carbon sensor is being used. Since the temperature coefficients of platinum and carbon resistors have opposite signs, this switching maintains the polarity of the controller output the same irrespective of which sensor is being used. It should be noted that, because of switching of the amplified voltage to different input terminals, the main gain control (the variable 50 kΩ feedback resistor) has the capability of multiplying the gain by 1 to 11 in the case of the Pt sensor and by 0 to 10 in the case of the C sensor.

The voltage output of the main gain stage is fed to the proportional and integrating stage. In this stage the difference voltage is both integrated and amplified to form two outputs: one proportional to a time integration of the difference voltage and the other directly proportional to the difference voltage. The amplification of the proportional output can be varied from 0 to 10 by varying the feedback resistor from 0 to 100 kΩ. Monitoring this output with the panel voltmeter is useful in determining the deviation of the sample chamber temperature from the set point temperature. The output of the integrator is controlled by varying the input of the integrator from zero to full value of the main gain stage output. This is done with a 10 kΩ heliopot wired as a voltage divider. The integrator is turned off by shorting the 1 μf capacitor. In the last stage the output voltages from the previous stage are added. If the input voltage to this stage is negative, the diodes allow current to pass through the feedback resistor and an output voltage which is equal in magnitude but of opposite polarity to that of the

input is supplied to the output of the controller. If, however, the sum is positive, the diodes prevent the current from passing through the feedback resistor and the output voltage is zero. The output voltage can be monitored with the panel voltmeter.

The voltage applied to the heater is to be directly proportional to the output voltage of the temperature controller. However, the low power capacity of the controller precludes the use of the controller output directly. Instead, the output is used to control the power supplied to the heater by an external power supply. We used a Kepco (model #BOP36-1.5M) power supply for this purpose.

This controller differs from the earlier version mainly in features that were added to make the operation of the controller more convenient: Zener diodes have been added to prevent overloading the amplifiers, the polarity of the output has been maintained the same irrespective of which temperature sensor is being used, deviation from set point as well as the output voltage can now be monitored, and some of the operational amplifiers have been upgraded.

The performance of the temperature controller was quite satisfactory. Below 20 K, the controller was capable of maintaining a constant temperature inside the sample chamber to within 0.001 K for the length of time necessary to measure the resistivity (a few minutes). Above 20 K, the specific heat of the sample chamber greatly increases and the thermal conductivity of the chamber decreases. This means there will be a longer time before the sensors will sense a temperature change some distance from the sensors and correspondingly longer time before the response of the controller will be felt. Also at these higher temperatures, gradients in the cooling gas become larger. All these factors contribute to poorer temperature control at the higher temperatures. Even so, the temperature was always controlled to within $\pm$0.1 K.

2.4 High Precision Resistance Measurements

After the samples have been mounted in the cryostat and the temperature of the samples has stabilized, the resistances of the samples and their temperatures are measured. The sample temperature is determined by measuring the resistance of one of the temperature sensors mounted next to the samples (see Fig. 13). A calibrated Ge resistor (Cryocal Inc., Cat. #CR1000) is used for temperature measurement below 20 K, and a calibrated Pt resistor (Rosemount Engineering Co., Cat. #146MA200F) is used for temperature measurements above 20 K. The resistances of the temperature sensors and of the samples are measured by using a standard four-probe potentiometric technique. In this technique the voltage across the sample is determined by measuring the potential difference between the potential leads, and the current through the sample is determined by measuring the voltage across a standard resistor placed in series with the sample. Dividing the voltage across the sample by the current then gives the resistance of the sample between the potential leads.

In the case of the temperature measurements, a digital voltmeter (Data Precision, Model #2540A1) was sufficient to determine the temperature to within ~1 mK at temperatures below 20 K and to within ~10 mK at temperatures above 20 K. On the other hand, measuring the spin-fluctuation resistivity of these alloys, where the spin-fluctuation resistivity is only a small fraction of the total resistivity, requires special techniques and especially high precision equipment. To measure the sample voltage and the sample current we used a Double Six-Dial Thermofree Potentiometer (Honeywell Instruments, Model #2773). The advantage of this potentiometer over most others lies in a nearly thermofree construction and a double set of dials which allows for the fast measurement of two different voltages with essentially the same potentiometer. Instead of obtaining the nulling voltage by tapping across different sections of a resistor with a constant current in it, this potentiometer obtains the

nulling voltage by varying the current in the resistor (a manganin wire), thus shifting the dials with their sliding contacts to a part of the circuit which is less sensitive to thermoelectric voltages and contact resistances. There are only two copper-manganin junctions in the critical part of the circuit and these are placed next to each other. These junctions, along with the manganin resistor, are enclosed in a heavy aluminum can to reduce the temperature gradients. The current to operate the potentiometer is supplied by two battery substitutes (Dynage, Inc.; Batt-Sub) and one internal standard cell. Each of these current sources supplies current to a particular section of the manganin resistor. A single unsaturated Eppley Standard Cell (Leads & Northrup Co., Cat. #7308) is used to calibrate these currents. Since the potentiometer measures the two unknown voltages using the same current sources and the same standard cell for each measurement, and since the two unknown voltages are divided to obtain the resistance of the sample, first order errors in the standard cell voltage and first order changes in the Batt-Sub voltage are cancelled in determining the resistance. The accuracy of this potentiometer is to within 0.01% of the reading or 10 nV whichever is greater, and a precision of ~1 ppm is possible under proper conditions.

In order to push the system to its maximum capability in precision, there are several conditions that must be met. First, since the thermoelectric voltages in the potentiometer can be as high as 10 nV, both unknown voltages must be ~10 mV or greater. However, in order to keep the Joule heating in the sample small, we would choose ~10 mV for the sample voltage.

Second, since on the low range of the potentiometer the maximum voltage that can be measured is ~11 mV, and since it is not practical to change the range and still maintain the high precision, the voltage across the standard resistor must also be ~10 mV. This dictates a sample resistance comparable in resistance to the standard resistor.

Third, since each dial on the potentiometer is accurate to ~10 ppm, the voltage across the sample and standard resistor must be such that the setting of the top knob on each dial set remains fixed. That is, throughout the course of the measurements the temperature dependence must be such that the sample resistance changes by less than 10%. For the present set of alloys this condition is easily met.

Fourth, since the total time required to measure the resistance as a function of temperature may be as long as 10 h, it is necessary that the standard resistor remain stable to 1 ppm over this period. This is accomplished by controlling the temperature of the standard resistor (Leeds and Northrup Co., 0.1Ω resistor, Cat. #4221) to 25 C ± 0.5 C. The temperature dependence of other pieces of equipment such as the potentiometer, current sources, standard cell, etc. tend to cancel as a result of the division that is necessary to obtain the resistivity.

Fifth, it is necessary to have a sample current supply which is stable to ~1 ppm over the time period of a single measurement (~1 min). Such a current supply was built using a design similar to that used in the temperature controller to supply the current to the control sensors (see input stage of the temperature controller in Fig. 15). The sample current supply differs from the sensor current supply in the following respects: 1) the controlling voltage between ground and the noninverting input of the amplifier is made variable by the addition of a voltage dividing network, 2) the operational amplifier is upgraded to an Analog Devices model #260J, and, 3) special care is taken to insulate the temperature sensitive elements from the power sources.

Sixth, and last, changes in the thermoelectric voltages must be kept below 10 nV over the course of a single measurement. To accomplish this we avoid having dissimilar conductors in regions of high temperature gradients. Thus, all the sample leads are led directly from the sample chamber through the sample-to-room temperature gradient to the sample

selector switch without any breaks or joints in the wire.

We were able to meet these conditions for maximum precision quite well. In the case of the samples immersed in liquid He, all the above conditions were met, and we were able to measure the resistivity to a precision of ~1 ppm. Above 4.2 K we observed a noticeable amount of self heating with the 100 ma current needed to maintain 10 mV across the sample. Once this current was reduced to 20 mA,no self heating was observed, but then the 10 mV condition could not be met and consequentially the precision was reduced to ~5 ppm. Above 20 K, such high precision was superfluous since both the uncertainties in the sample temperature and the thermal hysteresis in the resistivity made the measurement irreproducible to such a high precision.

The procedure used to measure the resistance of the samples as a function of temperature was designed to eliminate the error that results from not taking into account existing thermoelectric voltages. As mentioned earlier, we were able to keep the thermoelectric voltages constant to within ~0.01 μV over the time period of a resistance measurement. However the thermoelectric voltages were sometimes as high as 0.2 μV which, although a very small part (0.01%) of the measured voltage, would contribute a significant error to the spin-fluctuation resistivity measurement if not taken into account. The effects of thermoelectric voltages are largely eliminated by using the fact that these voltages are generally independent of the direction of the sample current, whereas the sample voltage changes polarity upon reversal of the current direction. The actual procedure is to measure the voltages between the sample potential leads and the standard resistor leads, reverse both the current and the potential leads of the sample and remeasure, reverse again and remeasure. Proper averaging of the measurements will subtract out the thermoelectric voltages and tend to compensate for voltage drifts. A 12-position 4-pole switch (Leeds and Northrup Co., Cat. #8256-4A-3) is used to select the sample

to be measured and to reverse the current and potential leads. To detect the null voltage, we used a photoelectric galvanometer (Guildline Instruments Ltd., Model #9460) which was capable of detecting voltages as small as 5nV.

C. Magnetization Measurements

2.5 Vibrating Sample Magnetometer

The procedure for measuring the magnetization of the samples as a function of magnetic field and temperature starts with the mounting of one of the samples in the vibrating sample magnetometer. This magnetometer was designed and built by Dr. N.C. Koon of the Naval Research Laboratory, Washington, D.C. A block diagram of this magnetometer is shown in Fig. 16.

The magnetometer measures the magnetic moment of a sample as a function of the magnetic field. A uniform magnetic field is applied which induces a magnetic moment in the sample. The sample is vibrated and the changing flux through the pickup coils induces an emf in the coils which is proportional to the magnetic moment, to the vibrational amplitude, and to the frequency. The unwanted dependence upon amplitude and frequency is removed by comparing the signal from the sample to the signal from a calibrated fixed moment which is driven at the same amplitude and frequency as the sample.

The basic design of the sample drive unit is similar to a Mössbauer drive unit. Two loud-speaker magnets and their associated coils are used. One coil is used to drive a rod in a vertical sinusoidal motion. The other coil (the monitoring coil is attached to and driven by the rod. The fixed moment of the loud-speaker magnet induces an emf in the monitoring coil. The signal from this coil and a signal from a reference source (a very stable sine wave oscillator) are fed into the drive controller. By comparing these two signals the controller supplies to the drive coil the necessary power to drive the sample at the frequency and amplitude of the reference source. This arrangement results in a vibrating sample which is largely independent of external vibrations and changing loads.

The sample end of the drive rod is placed into the sample chamber of a cryostat (similar to that shown in Fig. 14).

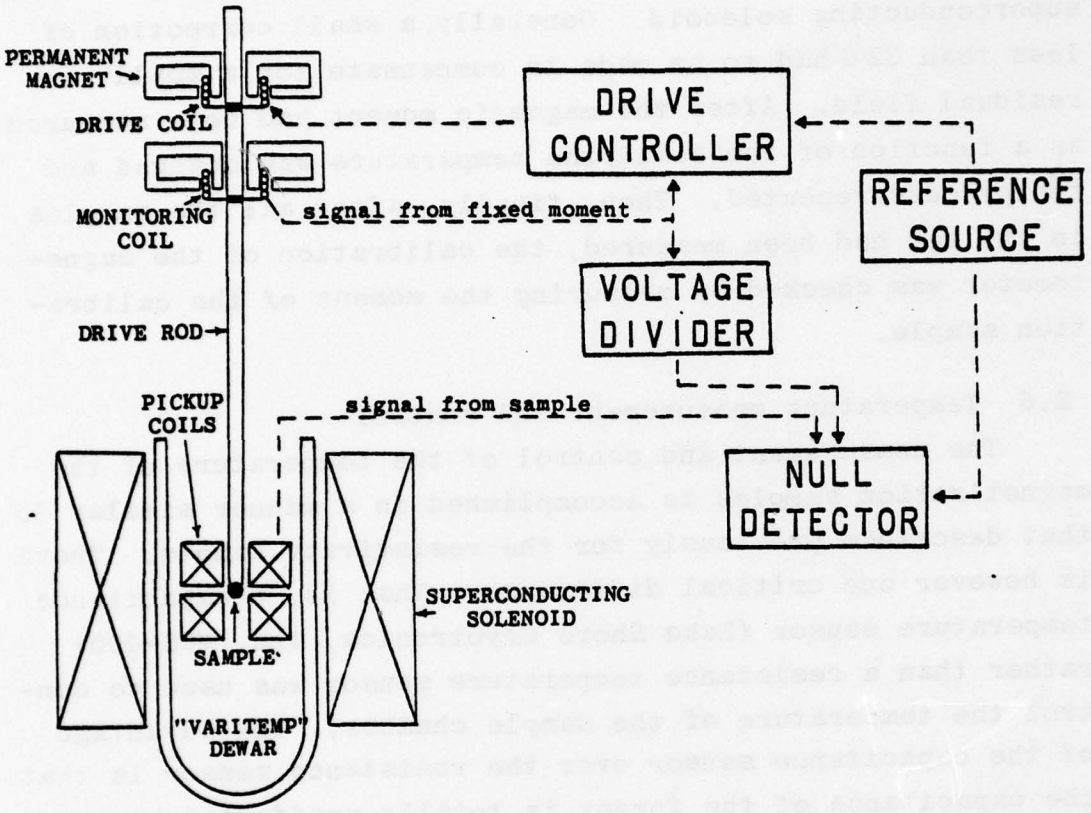
Surrounding the sample chamber in the liquid He bath is a 60 kG, Nb-Ti superconducting solenoid (Westinghouse) which provides the magnetizing field for the sample. The sample and pickup coils are mounted at the center of the magnet, where the uniformity is 0.005% over a spherical volume 1 cm in diameter. The pickup coils are a balanced pair which are connected in series opposition so that spurious signals due to motions of the coils in the magnetic fields are approximately cancelled. The separation between the two opposing coils is chosen such that the response to a vibrating sample is most nearly independent of the distance of the sample from the center of the pickup coils. Since the drive rod is suspended freely from the loud-speaker coils (i.e., does not rub against guides or touch the pickup coils), virtually all the mechanical vibrational-coupling between the drive unit and the pickup unit is eliminated.

The magnetometer measures the magnetic moment potentiometrically. A volt box (General Radio Co., Cat. #1455-B) is used to divide the voltage from the monitoring coil until the voltage is equal to the voltage induced in the pickup coil by the sample. A narrow-band, phase-sensitive amplifier (HR-8 Lock-In Amplifier, Princeton Applied Research Co.) operating at the 20 Hz of the reference source is used to detect the nulling of the two voltages. The voltage from the monitoring coil is adjusted and calibrated so as to make the volt box read directly in emu. The magnetometer is calibrated with a sphere of known magnetic moment. This calibration sphere (3.2 mm in diameter) was spark machined from a 5-9's Ni rod.

The accuracy of the magnetometer in measuring large magnetic moments is the same as the known accuracy (~1%) for the magnetic moment of the calibration sample. For small magnetic moments, where the noise is greater than 1% of the magnetic moment, the accuracy is ±0.0001 emu.

The actual procedure used to measure magnetization of the samples was to first calibrate the magnetometer. The sample was then mounted and brought to the desired

Fig. 16.
Block diagram of magnetometer.


PERMANENT MAGNET
DRIVE COIL
MONITORING COIL
DRIVE ROD
PICKUP COILS
SAMPLE
"VARITEMP" DEWAR
SUPERCONDUCTING SOLENOID
DRIVE CONTROLLER
signal from fixed moment
VOLTAGE DIVIDER
REFERENCE SOURCE
signal from sample
NULL DETECTOR

temperature. The temperature was measured. A magnetic field was applied and the magnetic moment of the sample was measured as a function of the field. In most cases the magnetic field was kept below 5 kG, where the magnetic susceptibility of the samples is nearly field independent. The magnetic field was determined by measuring the current in the superconducting solenoid. Generally, a small correction of less than 32 G had to be made to compensate for a small residual field. After the magnetic moment had been measured as a function of the field, the temperature was changed and the process repeated. Then, finally, after all the samples in the set had been measured, the calibration of the magnetometer was checked by measuring the moment of the calibration sample.

2.6 Temperature measurement and control

The measurement and control of the temperature of the magnetization samples is accomplished in a manner similar to that described previously for the resistivity sample. There is however one critical difference. That is, a capacitance temperature sensor (Lake Shore Cryotronics, Inc. #CS-400) rather than a resistance temperature sensor was used to control the temperature of the sample chamber. The advantage of the capacitance sensor over the resistance sensor is that the capacitance of the former is totally uneffected by a magnetic field and, thus, may be used to keep the temperature of the sample chamber constant independent of the value of the applied magnetic field.

The temperature controller operates in an analogous manner to the controller used for the resistivity measurements. As in that controller, this controller can be thought of as having four stages: 1) the input stage, 2) the main gain stage, 3) the proportional and integrating stage, and 4) the summing and rectifying stage. The input stage in this case is totally external to the main electronics of the controller. It consists of a capacitance bridge, the capacitance

sensor, and a lock-in amplifier to detect the bridge unbalance. The output of the lock-in is fed into the main gain stage and from this point on the operation of the controller is the same as described earlier. Thus, once the standard capacitance of the bridge circuit is adjusted to the appropriate value, the controller will supply a sufficient amount of power to heat the sample chamber to the desired temperature and to maintain it at that temperature. Over the temperature range (2 to 25 K) of the measurements, the controller is capable of maintaining the temperature of the sample chamber to within 0.01 K over a period of ~1 h. This high degree of control is also maintained in the presence of a complete field sweep, as was verified by monitoring the temperature with a constant-volume He-gas thermometer mounted on the top of the sample chamber.

As in the case of the resistivity measurements, a calibrated Ge resistor is used to determine the sample temperature when the temperature is below 20 K, and a calibrated Pt resistor is used when the temperature is above 20 K. These thermometers are mounted on the pickup coils. Because of the large field-dependence of these thermometers, measurements are taken before the magnetic field is applied. This is sufficient, since the capacitance-sensor temperature controller was able to maintain this temperature to the stated degree of accuracy in the presence of the magnetic field.

An attempt was made to detect any temperature gradient between the samples and the thermometers. First, the magnetic moment of a sample was measured when the temperature of the sample chamber was being controlled in the usual manner. Then the sample and sample chamber were immersed in liquid He and the He bath controlled at the same temperature as measured in the previous case. The magnetic moment of the sample was remeasured. Since there was no detectable change in the magnetic moment, we calculate that the temperature gradient between the sample and thermometers was less than 0.1 K.

CHAPTER III: RESULTS AND DISCUSSION

A. Magnetization

From the magnetization results we can characterize the magnetic state of the various alloys. We present these results in various forms in the next four sections. In the first section we show all the magnetization data taken on the various alloys as a function of the magnetic field intensity in the sample. In the second section we replot on an Arrott plot the data for those alloys containing more than 1 at% Ni. By the use of this plot, we extract the Curie temperatures and the spontaneous magnetizations for the various ferromagnetic alloys. We then use these results to estimate the minimum Ni concentration necessary for the occurrence of ferromagnetism in this alloy system. Finally, the results are compared with the similar results that have been obtained for the $Pd_{1-x}Ni_x$ system. In the third section we obtain the differential susceptibility from magnetization data. In the fourth section we use a model to separate the magnetization and susceptibility into contributions from three sources: the host, the isolated (noninteracting) Ni atoms, and those Ni atoms which magnetically interact with each other.

3.1 Magnetization as a Function of Magnetic Field Intensity

In this section we present the magnetization data by plotting the magnetization (magnetic moment per gram) as a function of the magnetic field intensity in the samples. In general, the sample temperatures ranged from 2 K to 20 K and the field was varied from $\frac{1}{2}$ kG to 4 kG. However, for the samples at 4 K the field was varied up to 56 kG. Figs. 17 and 18 show these higher field measurements. The remaining figures in this section show the low field measurements. For the case of the alloys containing $\leq$1 at% Ni, the curves

through the low field data are the straight lines obtained from a linear regression analysis of the data. In all other cases, french curves were used in drawing the curves.

The general features of the data can be listed as follows: 1) The magnetization of the alloys containing ≤1 at% Ni is an increasing, nearly linear function of the magnetic field. 2) The magnetization of the alloys containing ≥1½ at% Ni is an increasing, highly nonlinear function of the magnetic field. 3) Both the magnetization and the temperature dependence of the magnetization increase as the higher Ni concentrations are approached. 4) The zero field magnetization (found by extrapolating the data to zero field) is nonzero even for those alloys lowest in Ni concentration.

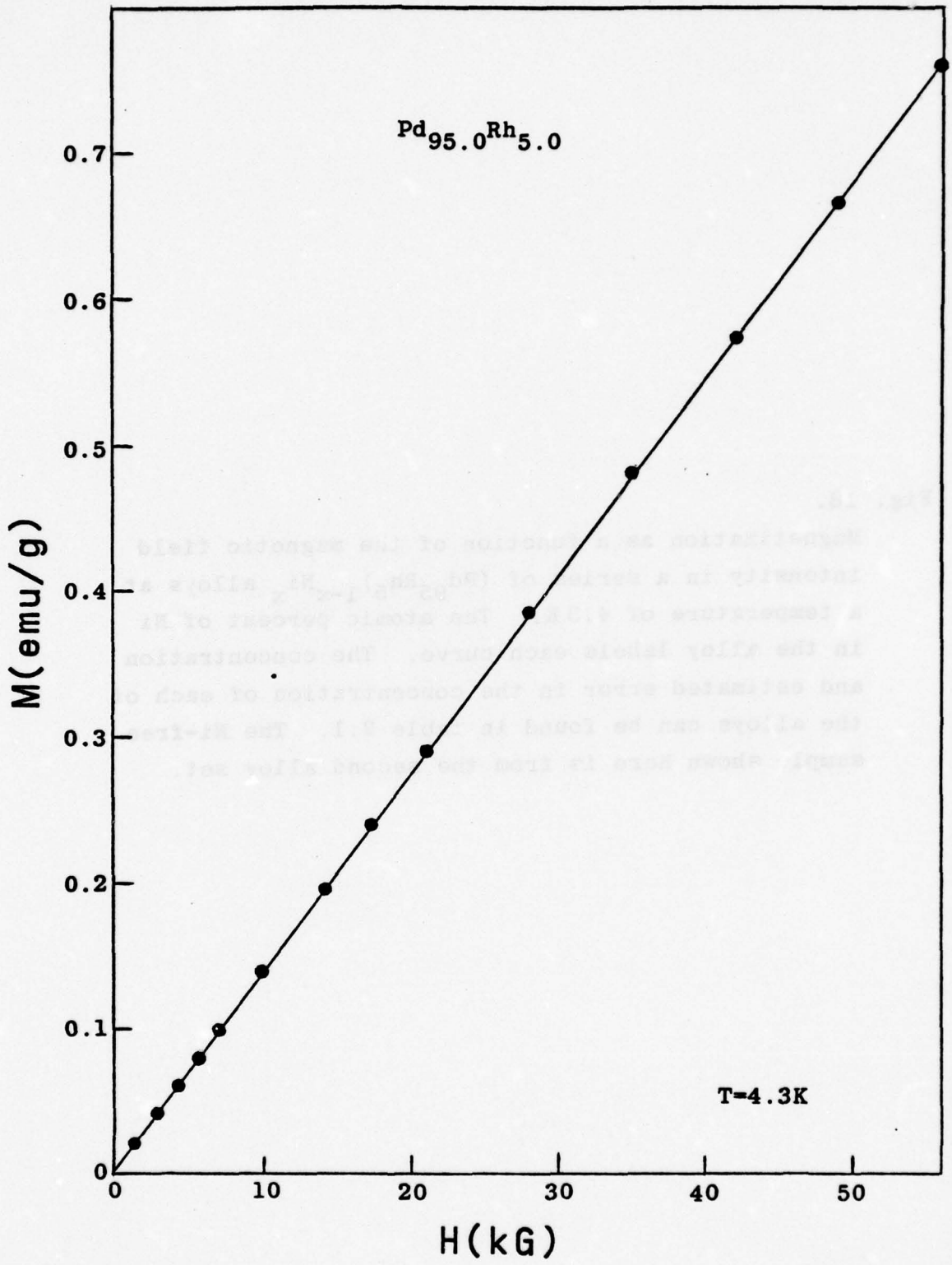
Except for the fourth feature listed above, the data can be explained on the basis of an alloy system which transforms from a strongly paramagnetic system to a ferromagnetic system with the addition of a dilute amount of Ni. The mechanisms of the transformation will become clearer as we analyze the data further in the following sections. However, the fourth feature appears to be a characteristic of the data taking and not an intrinsic property of the alloy systems. To see this we examine some of the reasons why a nonzero intercept might be expected. Obvious ones that come to mind are as follows: iron impurtities in the alloys, inappropriate extrapolation procedure, and systemic errors in either the field or magnetization measurements.

Iron impurities can be ruled out as the cause for a varity of reasons. First, the spectrographic analysis of the alloys showed no detectable variation in iron content, whereas the values of the intercepts vary strongly from one sample to the next. Second, since it is obvious that iron impurities (local moments) could never yield a negative intercept, this cause must be ruled out for those alloys with negative intercepts. Third, it is known[50] that the magnetic behavior

(text continues on p. 154)

Fig. 17.

Magnetization as a function of the magnetic field intensity in a $Pd_{95.0}Rh_{5.0}$ alloy at a temperature of 4.3 K.


$Pd_{95.0}Rh_{5.0}$
M(emu/g)
0.7
0.6
0.5
0.4
0.3
0.2
0.1
0
0
10
20
30
40
50
H(kG)
T=4.3K

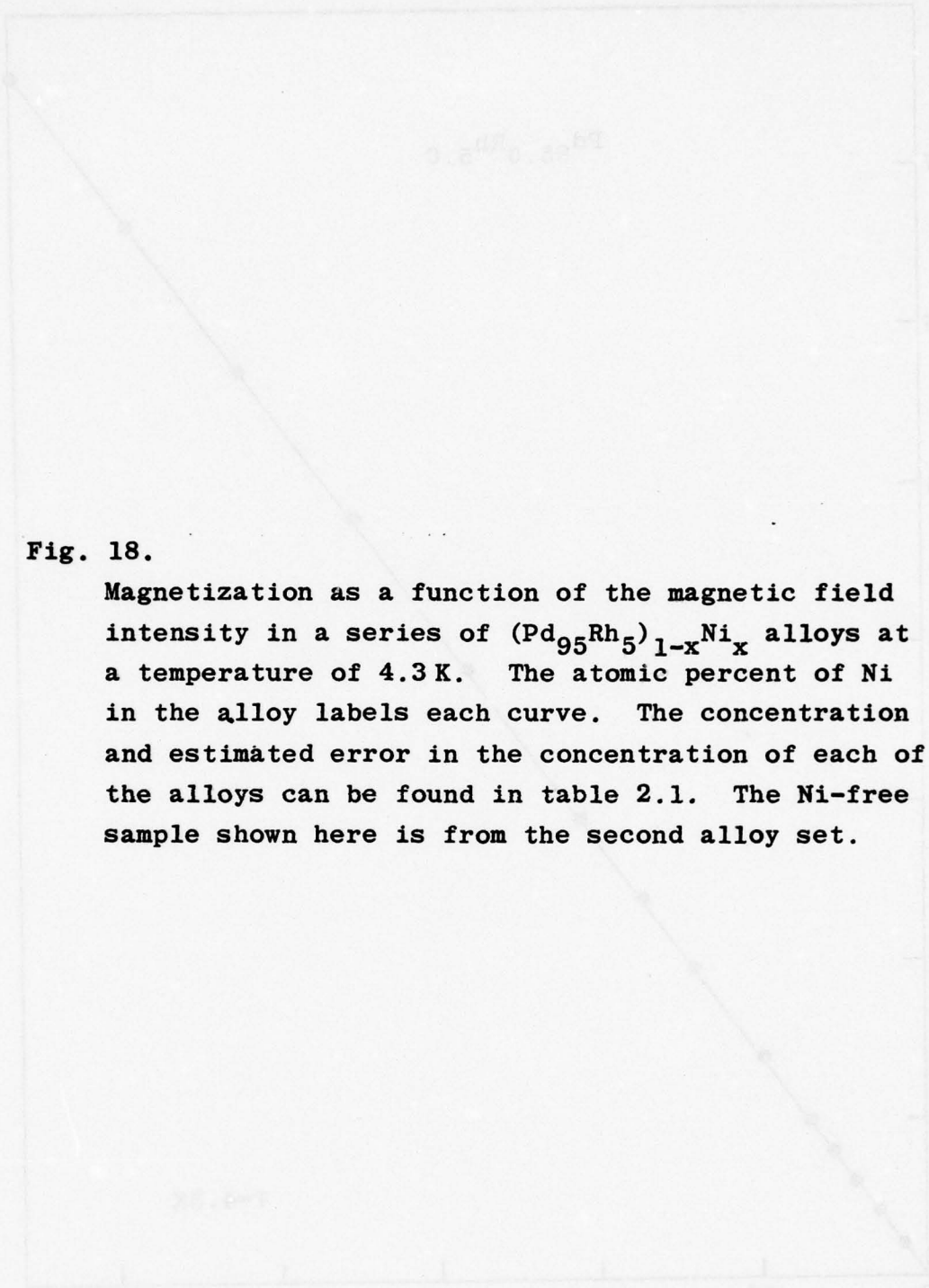
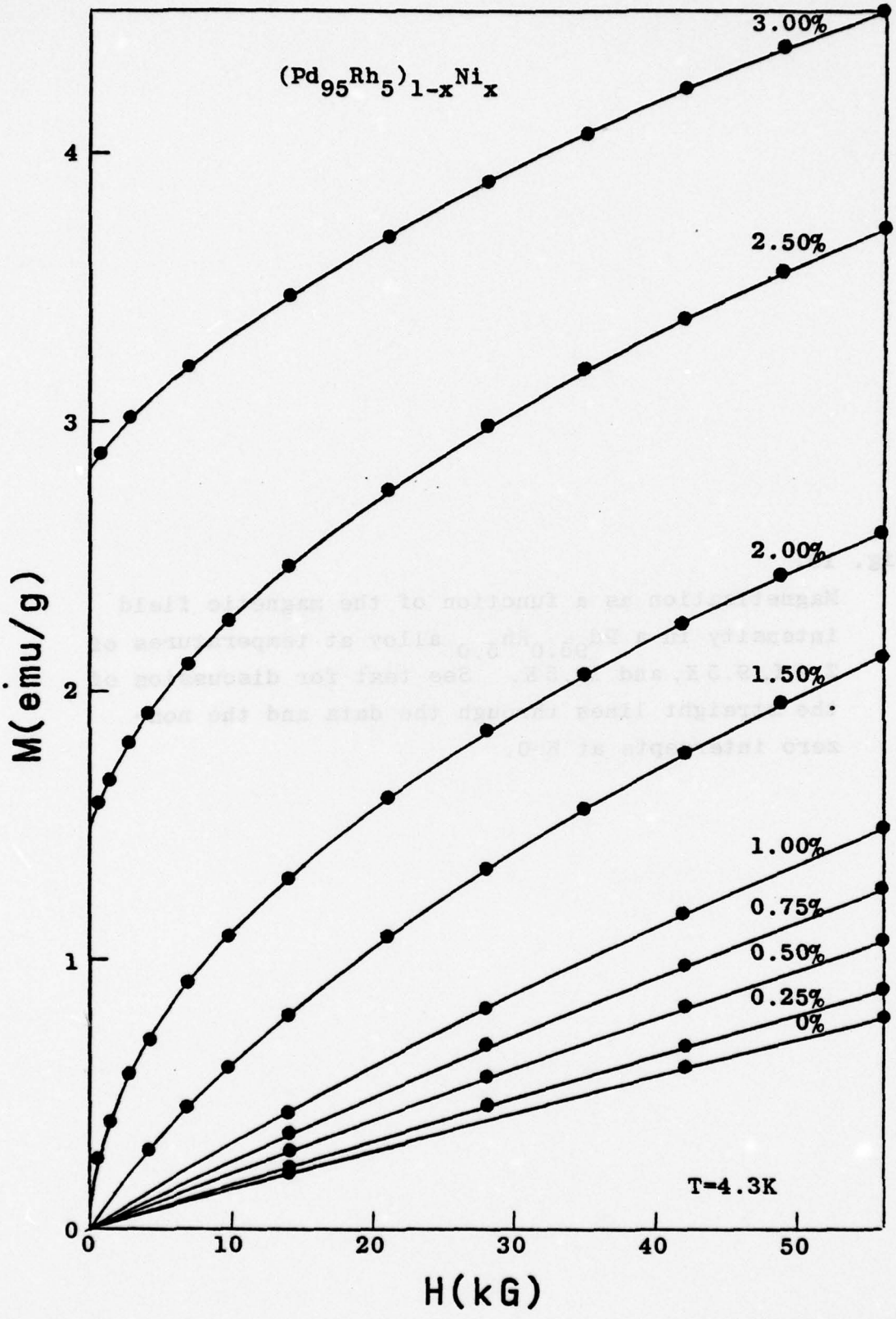


Fig. 18.

Magnetization as a function of the magnetic field intensity in a series of $(Pd_{95}Rh_5)_{1-x}Ni_x$ alloys at a temperature of 4.3 K. The atomic percent of Ni in the alloy labels each curve. The concentration and estimated error in the concentration of each of the alloys can be found in table 2.1. The Ni-free sample shown here is from the second alloy set.


$(Pd_{95}Rh_5)_{1-x}Ni_x$
3.00%
2.50%
2.00%
1.50%
1.00%
0.75%
0.50%
0.25%
0%
T=4.3K
M(emu/g)
H(kG)
0
1
2
3
4
0
10
20
30
40
50

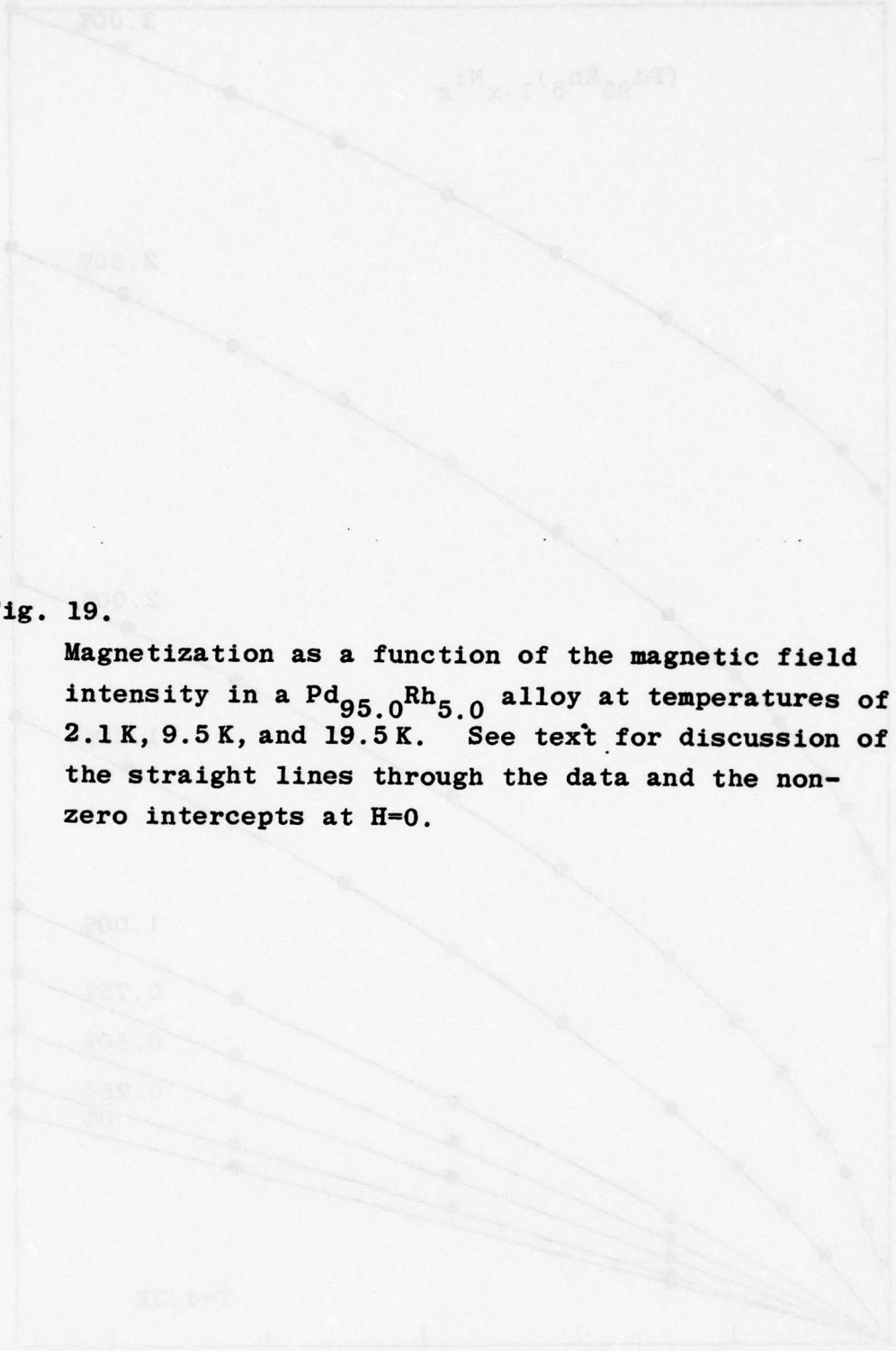
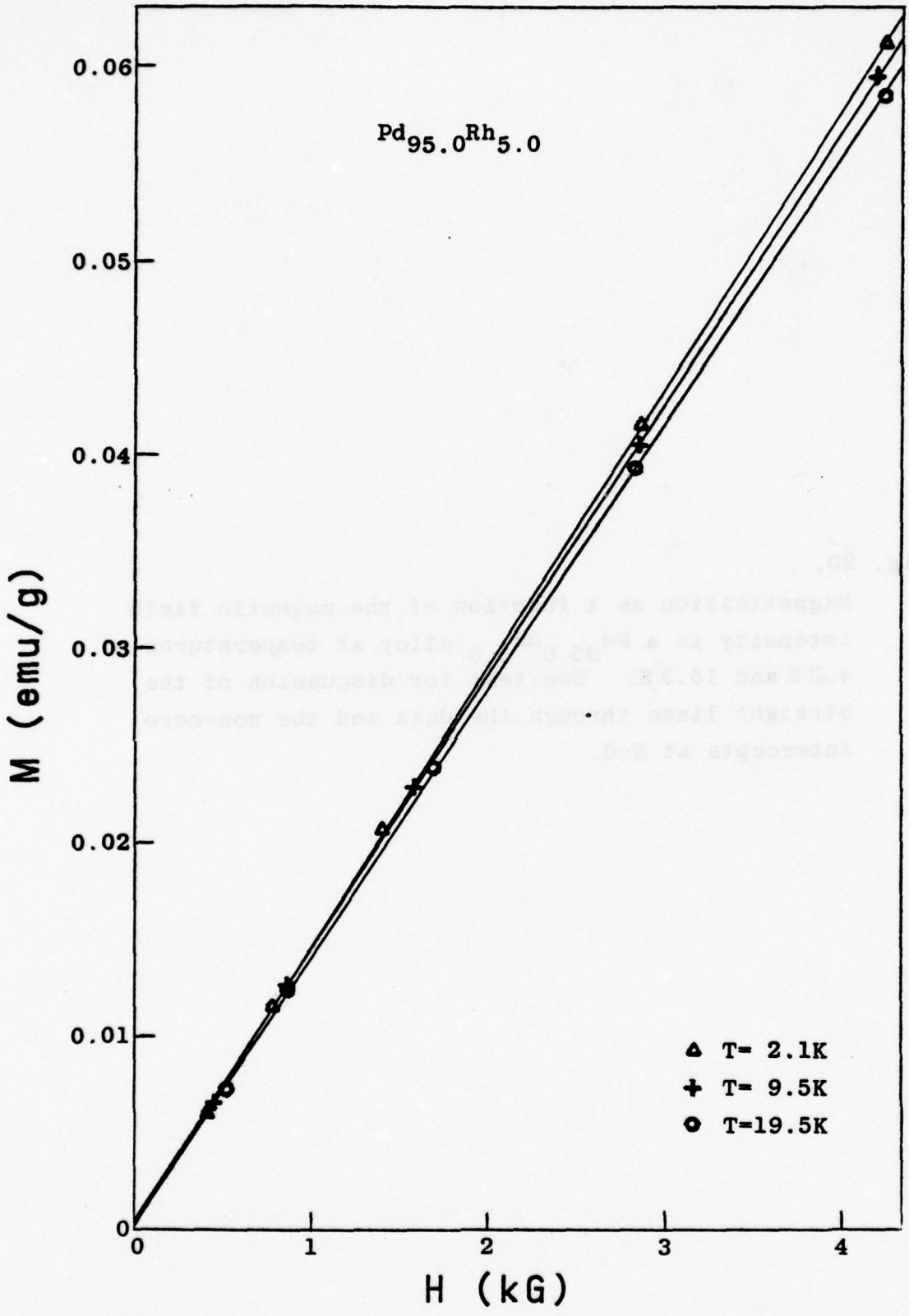


Fig. 19.

Magnetization as a function of the magnetic field intensity in a $Pd_{95.0}Rh_{5.0}$ alloy at temperatures of 2.1 K, 9.5 K, and 19.5 K. See text for discussion of the straight lines through the data and the non-zero intercepts at H=0.


$Pd_{95.0}Rh_{5.0}$
0.06
0.05
0.04
0.03
0.02
0.01
0
M (emu/g)
0
1
2
3
4
H (kG)
T= 2.1K
T= 9.5K
T=19.5K

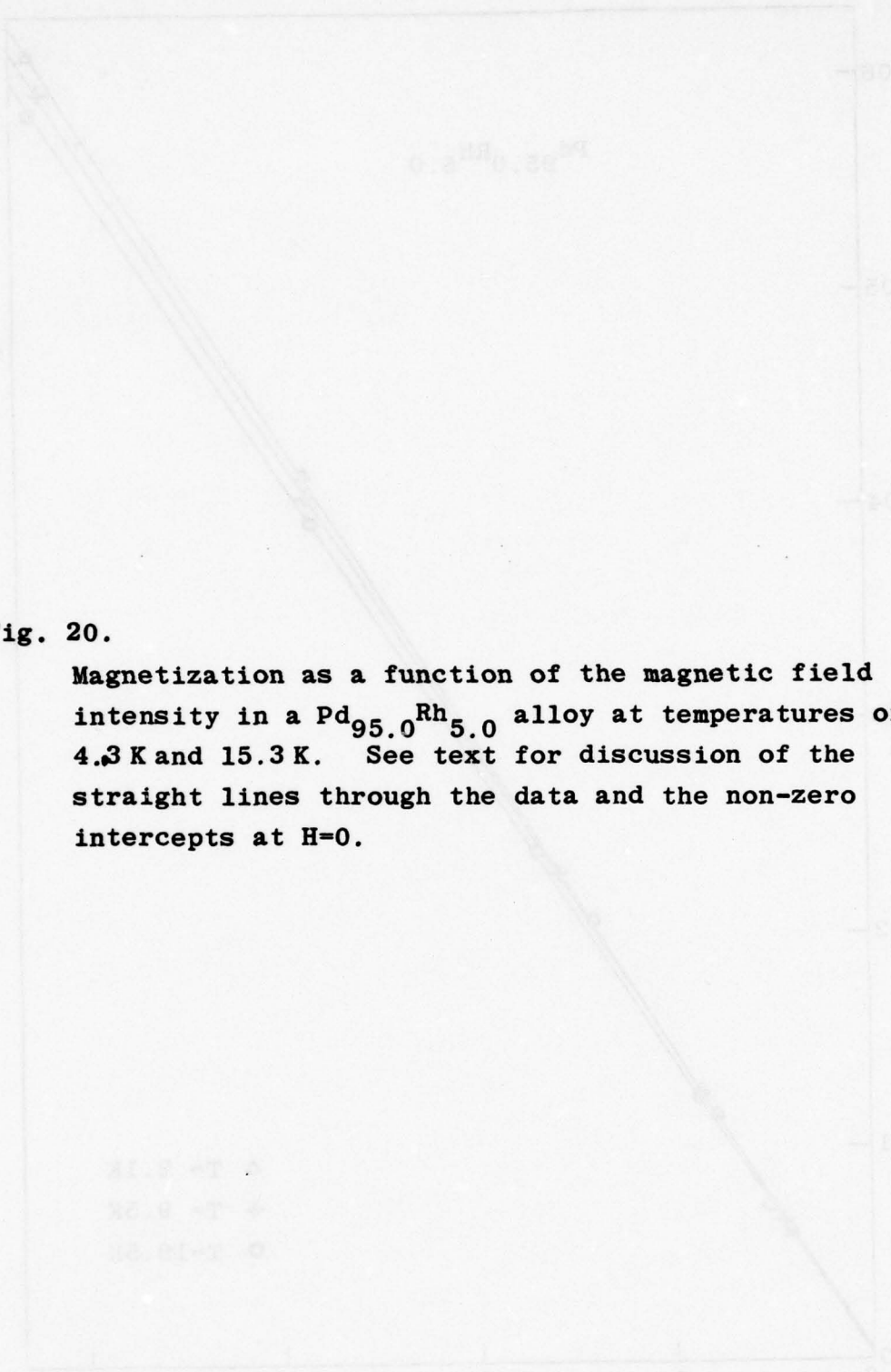


Fig. 20.

Magnetization as a function of the magnetic field intensity in a $Pd_{95.0}Rh_{5.0}$ alloy at temperatures of 4.3 K and 15.3 K. See text for discussion of the straight lines through the data and the non-zero intercepts at H=0.

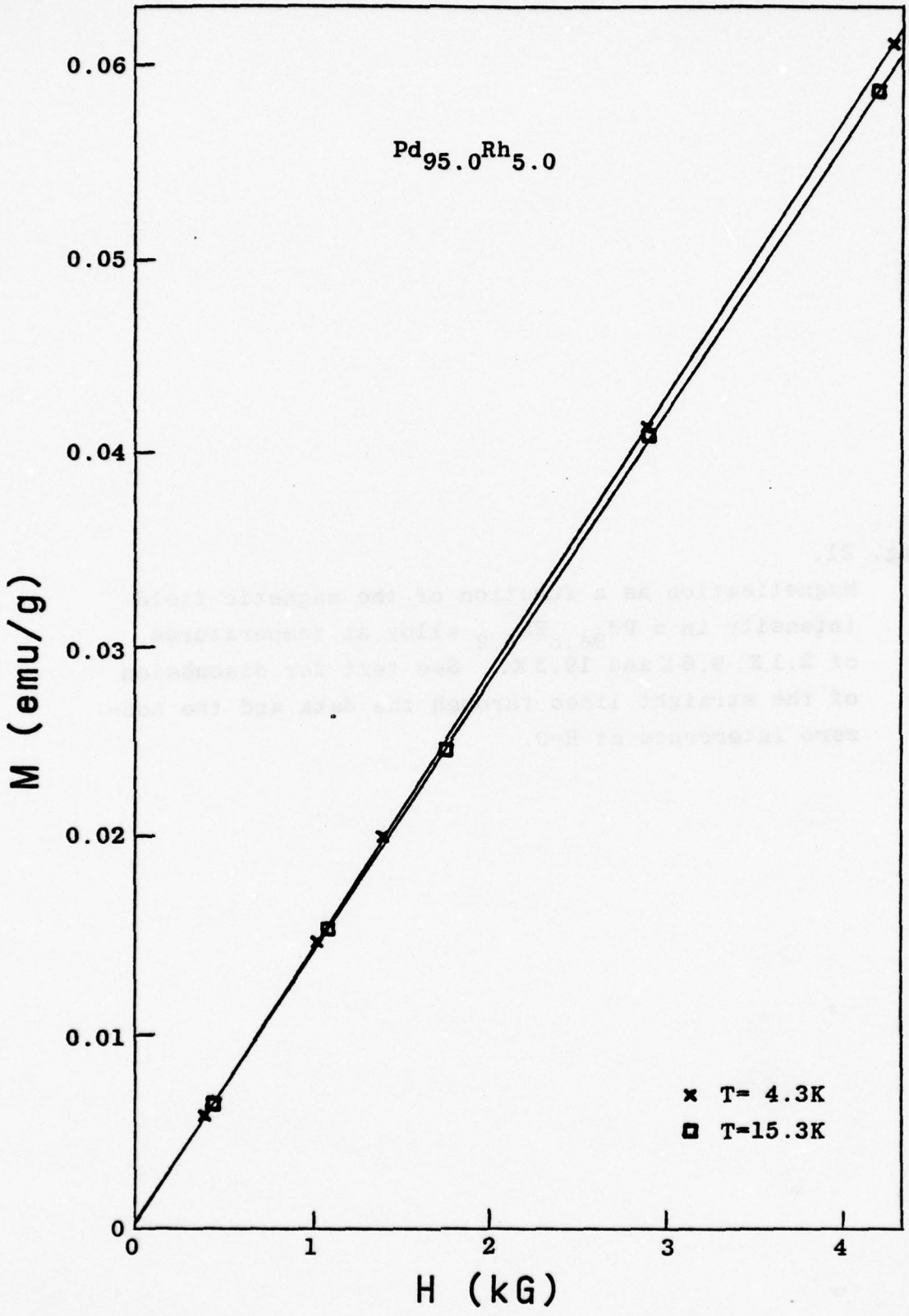
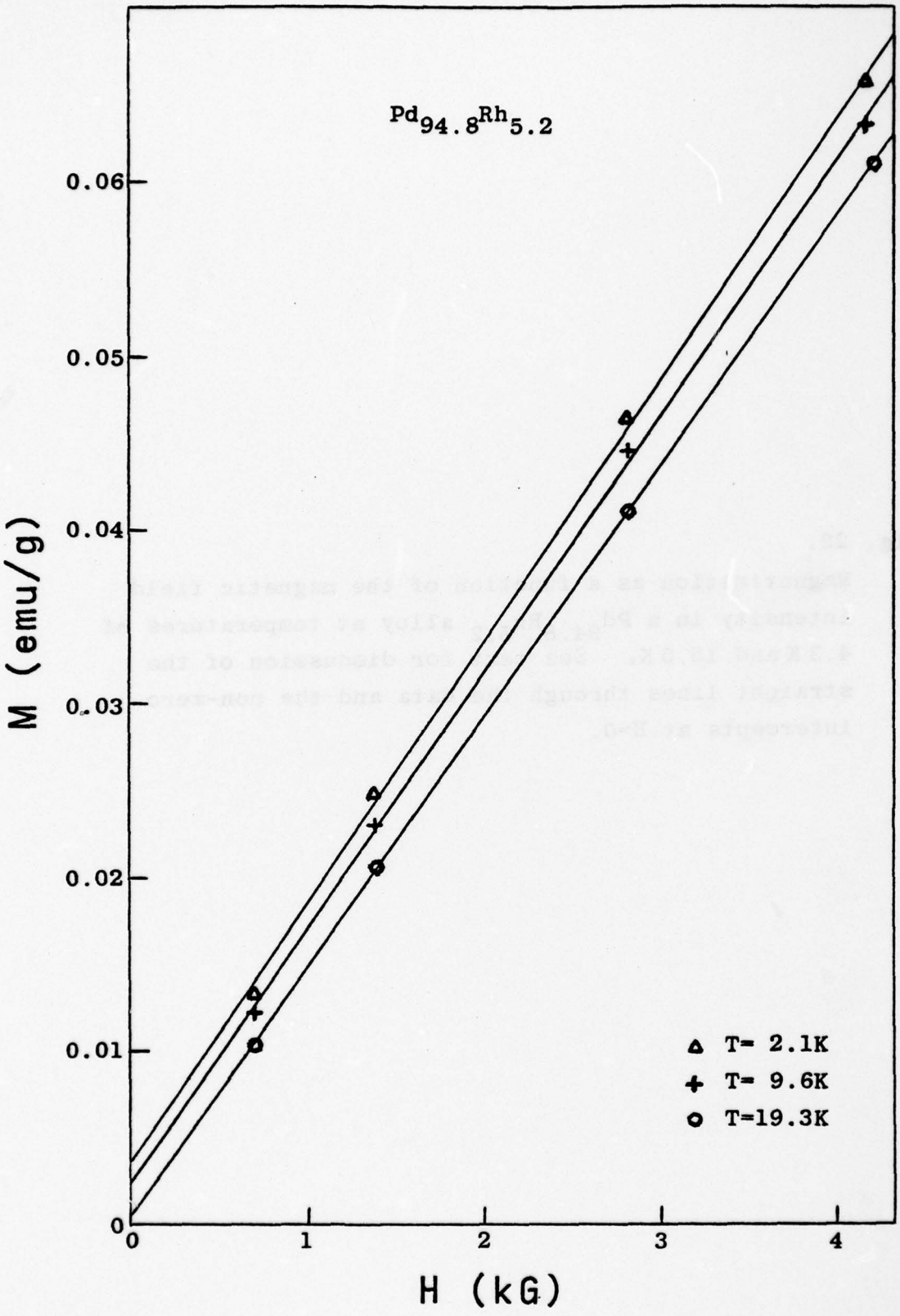

$Pd_{95.0}Rh_{5.0}$
0.06
0.05
0.04
0.03
0.02
0.01
0
M (emu/g)
0
1
2
3
4
H (kG)
× T= 4.3K
□ T=15.3K

Fig. 21.

Magnetization as a function of the magnetic field intensity in a $Pd_{94.8}Rh_{5.2}$ alloy at temperatures of 2.1 K, 9.6 K and 19.3 K. See text for discussion of the straight lines through the data and the non-zero intercepts at H=0.


$Pd_{94.8}Rh_{5.2}$
M (emu/g)
0.06
0.05
0.04
0.03
0.02
0.01
0
0
1
2
3
4
H (kG)
T= 2.1K
T= 9.6K
T=19.3K

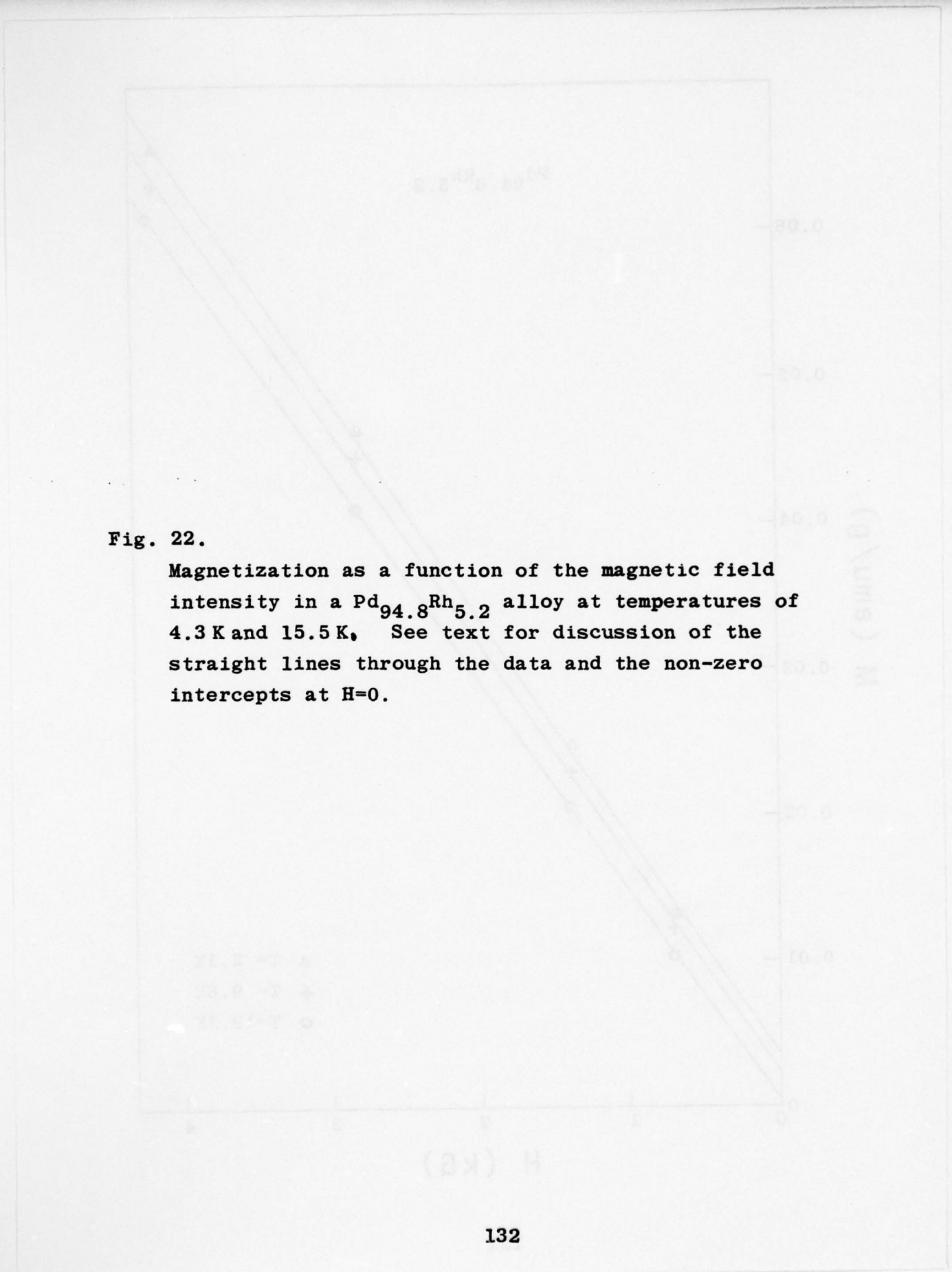


Fig. 22.

Magnetization as a function of the magnetic field intensity in a $Pd_{94.8}Rh_{5.2}$ alloy at temperatures of 4.3 K and 15.5 K. See text for discussion of the straight lines through the data and the non-zero intercepts at H=0.

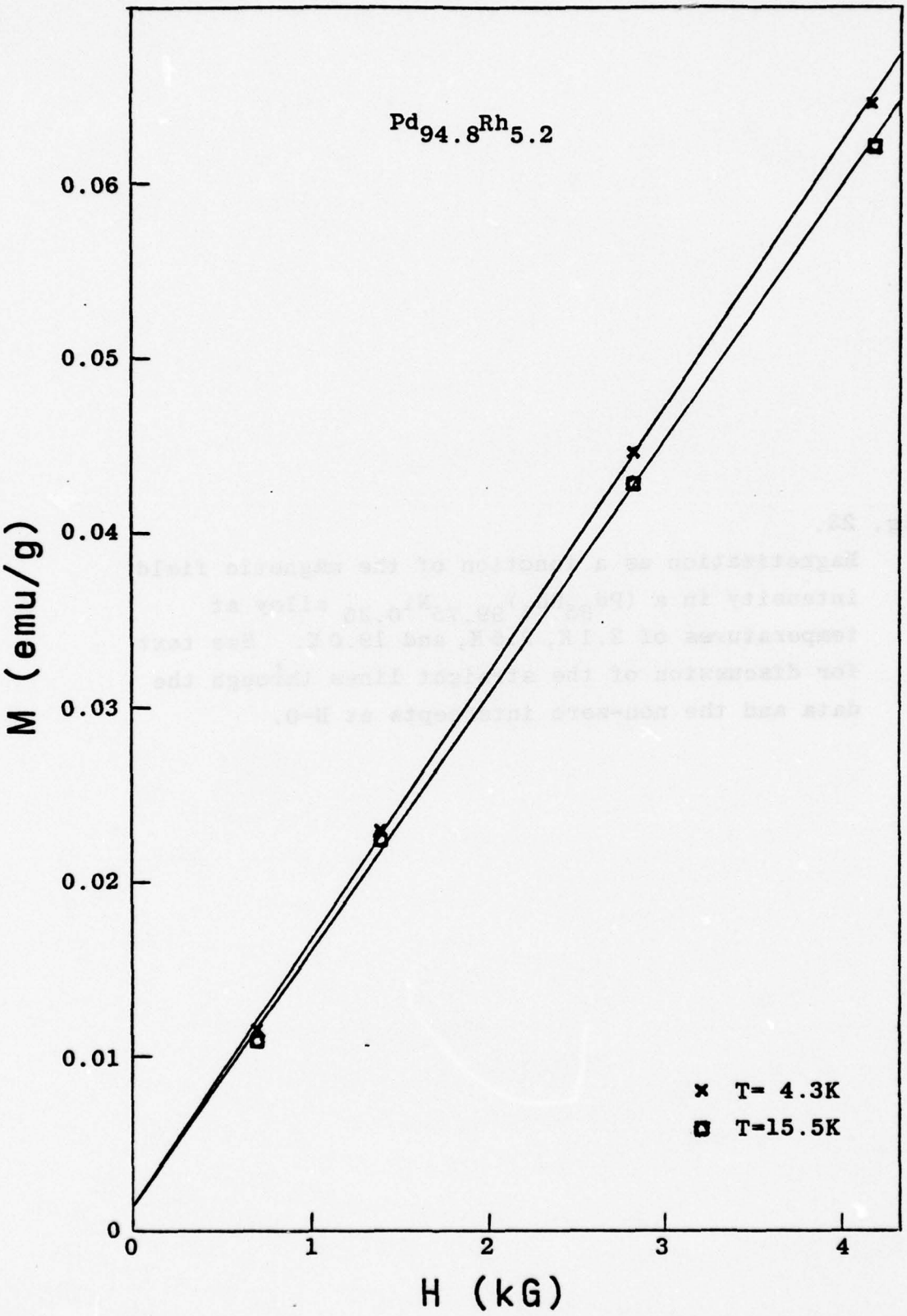
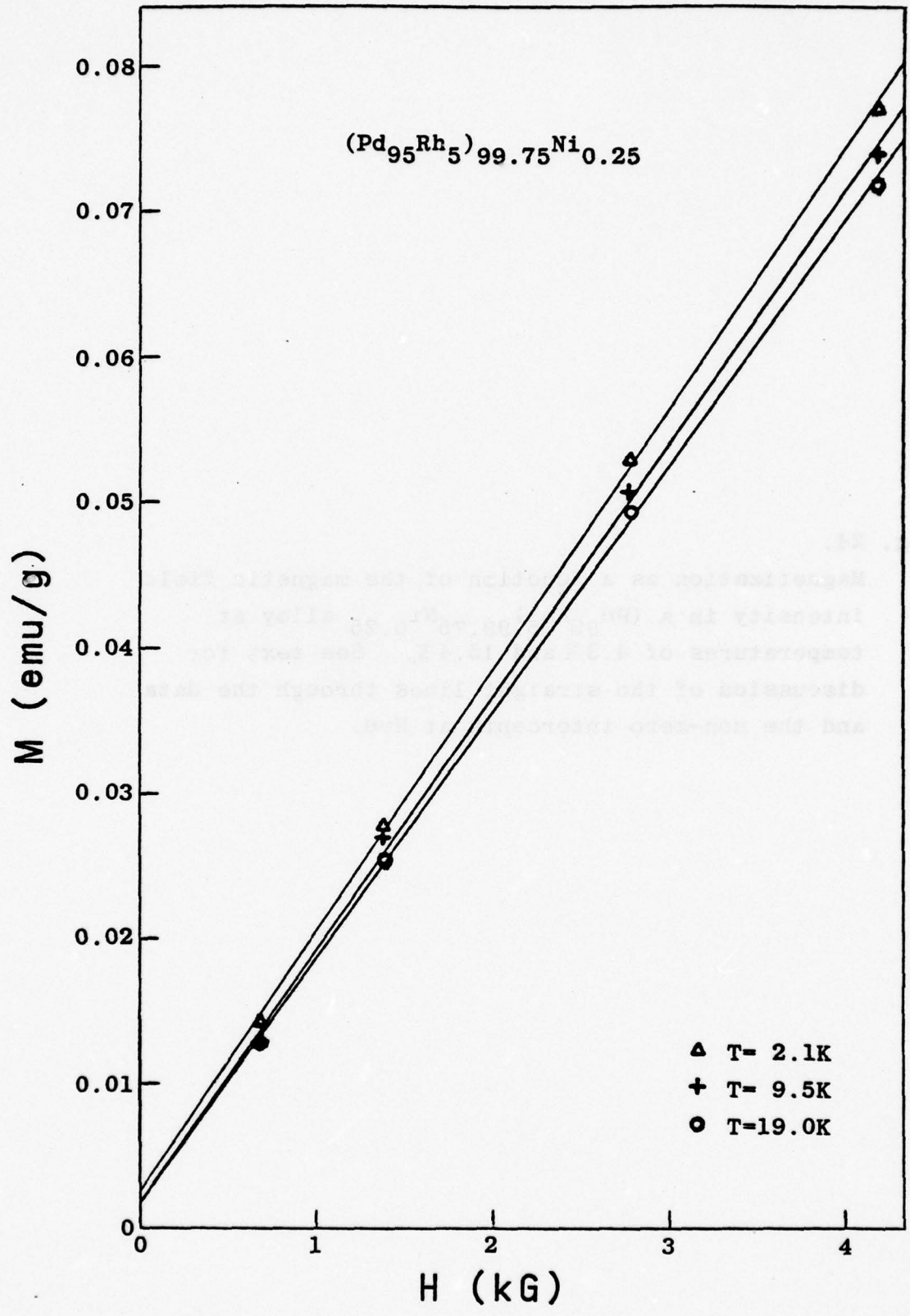

$Pd_{94.8}Rh_{5.2}$
M (emu/g)
0.06
0.05
0.04
0.03
0.02
0.01
0
0
1
2
3
4
H (kG)
T= 4.3K
T=15.5K

Fig. 23.

Magnetization as a function of the magnetic field intensity in a $(Pd_{95}Rh_5)_{99.75}Ni_{0.25}$ alloy at temperatures of 2.1 K, 9.5 K, and 19.0 K. See text for discussion of the straight lines through the data and the non-zero intercepts at H=0.


$(Pd_{95}Rh_5)_{99.75}Ni_{0.25}$
M (emu/g)
H (kG)
0.08
0.07
0.06
0.05
0.04
0.03
0.02
0.01
0
0
1
2
3
4
T= 2.1K
T= 9.5K
T=19.0K

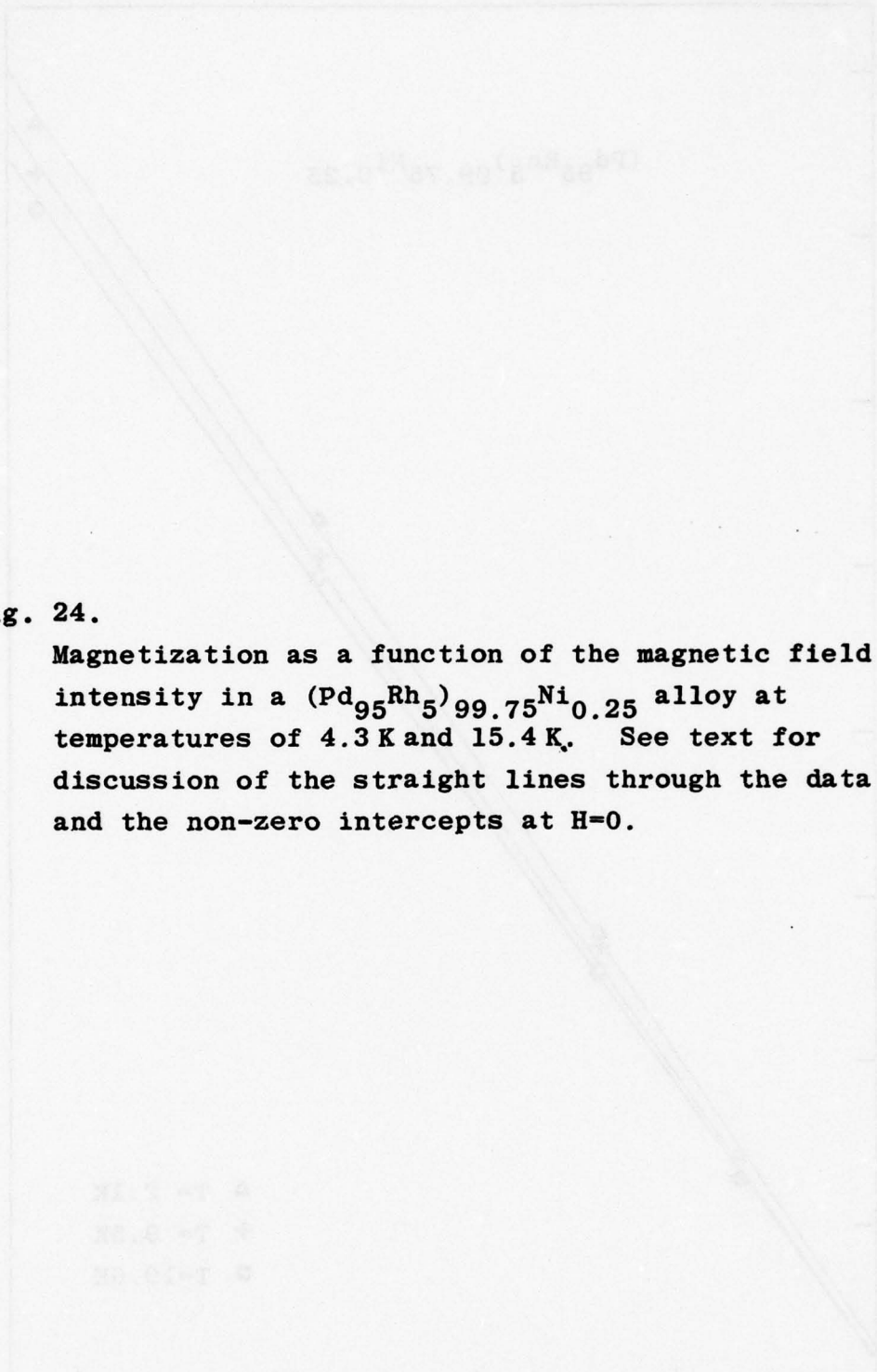


Fig. 24.

Magnetization as a function of the magnetic field intensity in a $(Pd_{95}Rh_5)_{99.75}Ni_{0.25}$ alloy at temperatures of 4.3 K and 15.4 K. See text for discussion of the straight lines through the data and the non-zero intercepts at H=0.

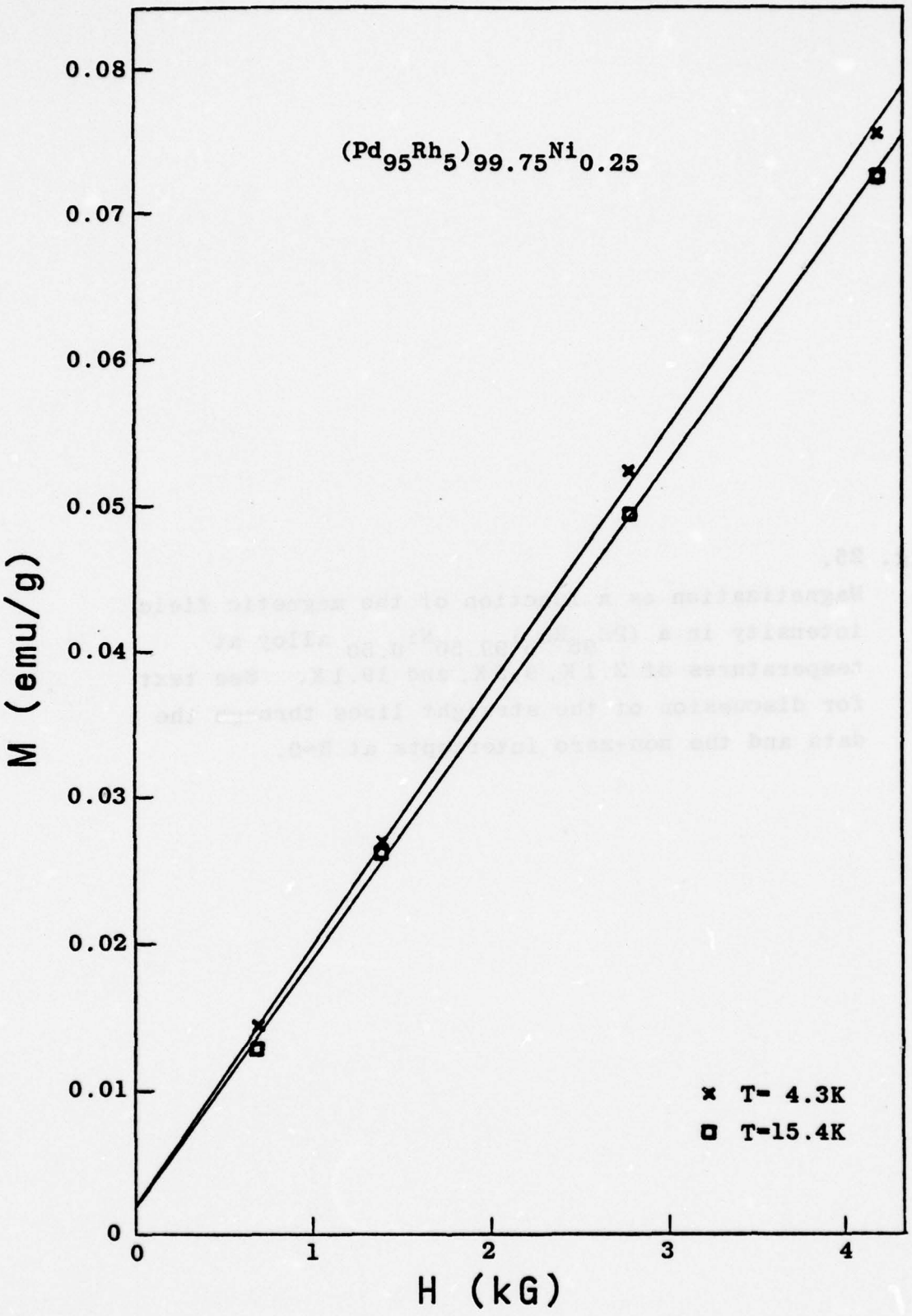
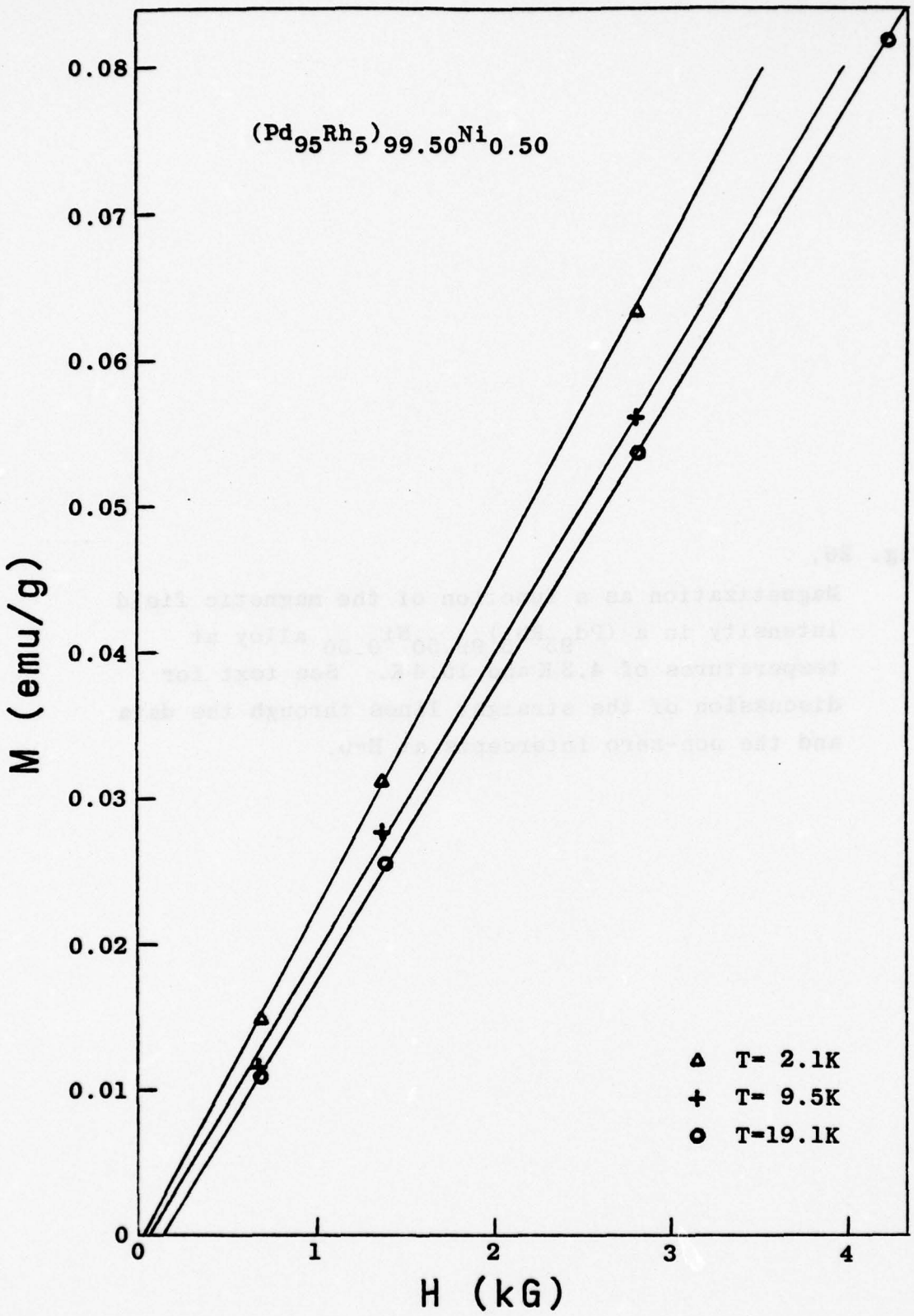

$(Pd_{95}Rh_5)_{99.75}Ni_{0.25}$
M (emu/g)
0.08
0.07
0.06
0.05
0.04
0.03
0.02
0.01
0
0
1
2
3
4
H (kG)
× T= 4.3K
□ T=15.4K

Fig. 25.

Magnetization as a function of the magnetic field intensity in a $(Pd_{95}Rh_5)_{99.50}Ni_{0.50}$ alloy at temperatures of 2.1 K, 9.5 K, and 19.1 K. See text for discussion of the straight lines through the data and the non-zero intercepts at H=0.


$(Pd_{95}Rh_5)_{99.50}Ni_{0.50}$
M (emu/g)
H (kG)
0.08
0.07
0.06
0.05
0.04
0.03
0.02
0.01
0
0
1
2
3
4
T= 2.1K
T= 9.5K
T=19.1K

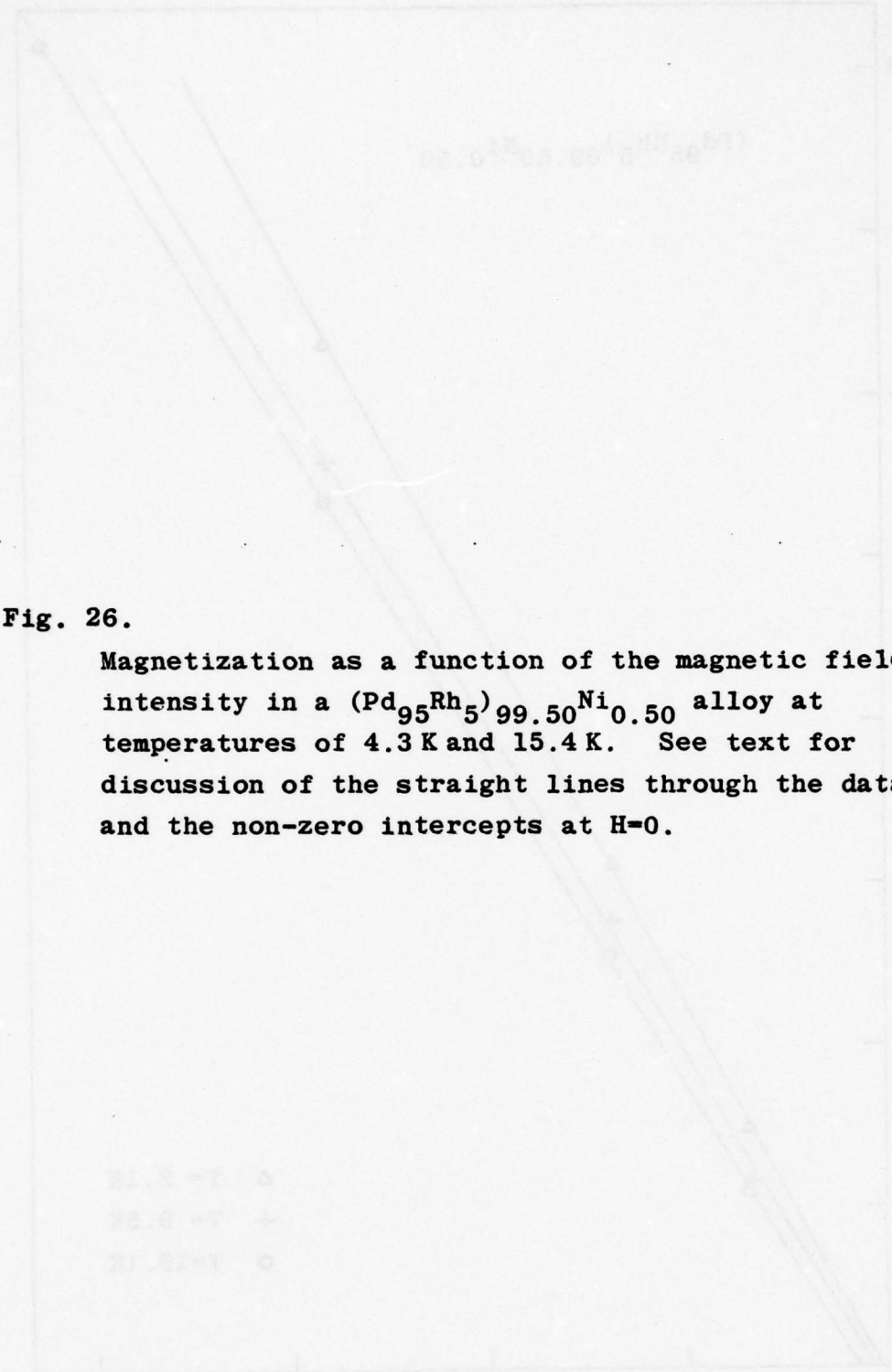
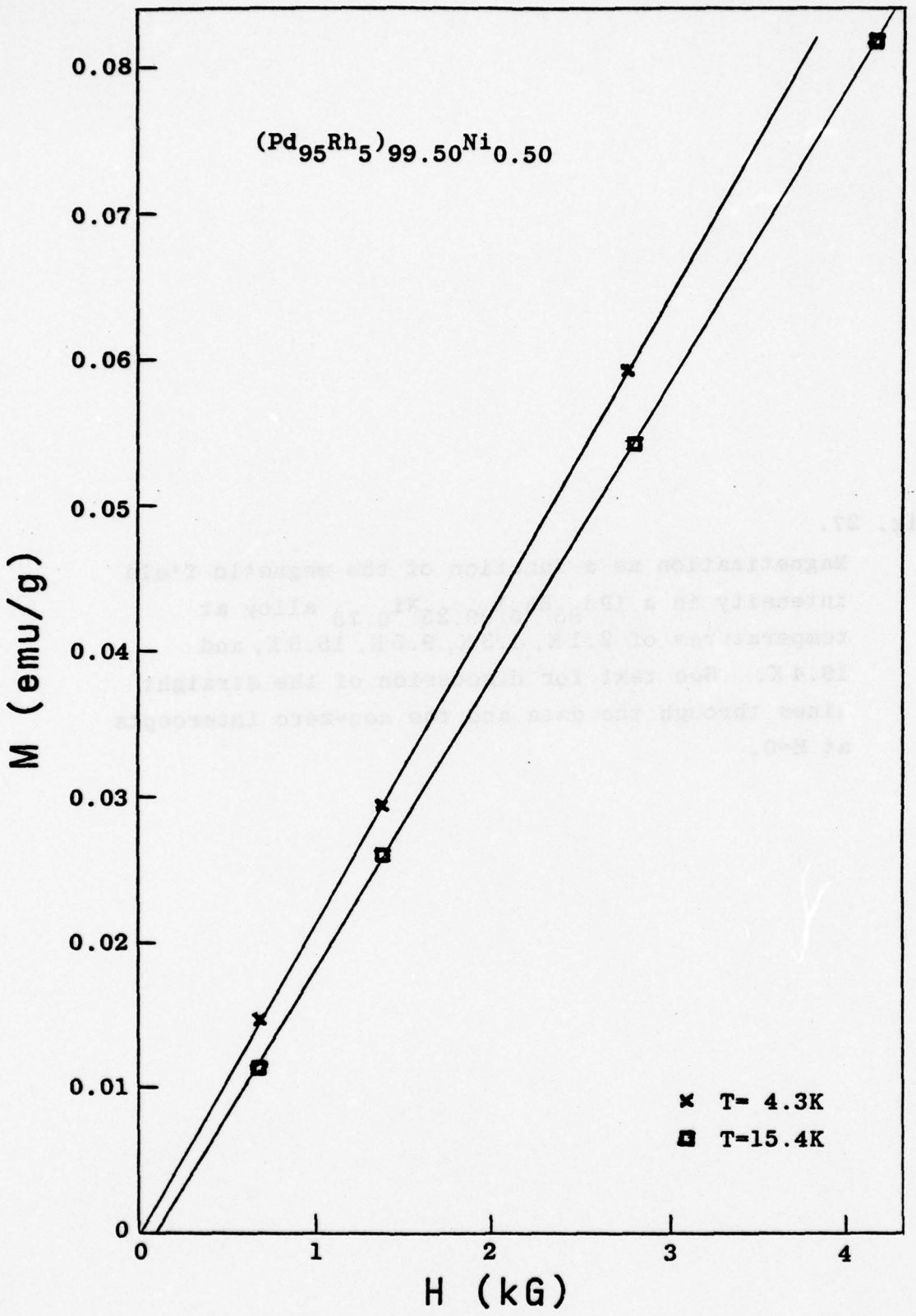


Fig. 26.

Magnetization as a function of the magnetic field intensity in a $(Pd_{95}Rh_5)_{99.50}Ni_{0.50}$ alloy at temperatures of 4.3 K and 15.4 K. See text for discussion of the straight lines through the data and the non-zero intercepts at H=0.


$(Pd_{95}Rh_5)_{99.50}Ni_{0.50}$
M (emu/g)
H (kG)
0.08
0.07
0.06
0.05
0.04
0.03
0.02
0.01
0
0
1
2
3
4
T= 4.3K
T=15.4K

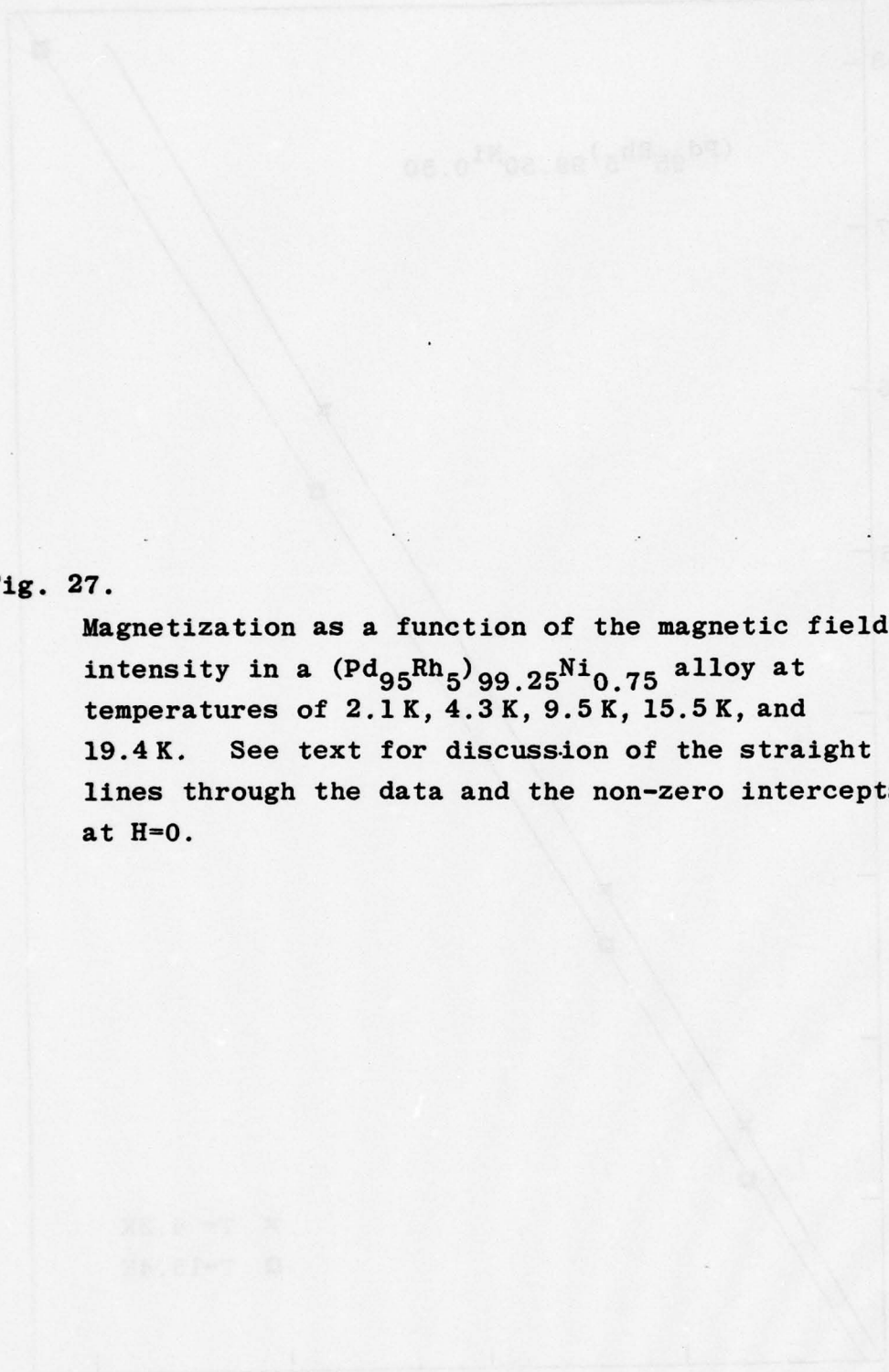


Fig. 27.

Magnetization as a function of the magnetic field intensity in a $(Pd_{95}Rh_5)_{99.25}Ni_{0.75}$ alloy at temperatures of 2.1 K, 4.3 K, 9.5 K, 15.5 K, and 19.4 K. See text for discussion of the straight lines through the data and the non-zero intercepts at H=0.

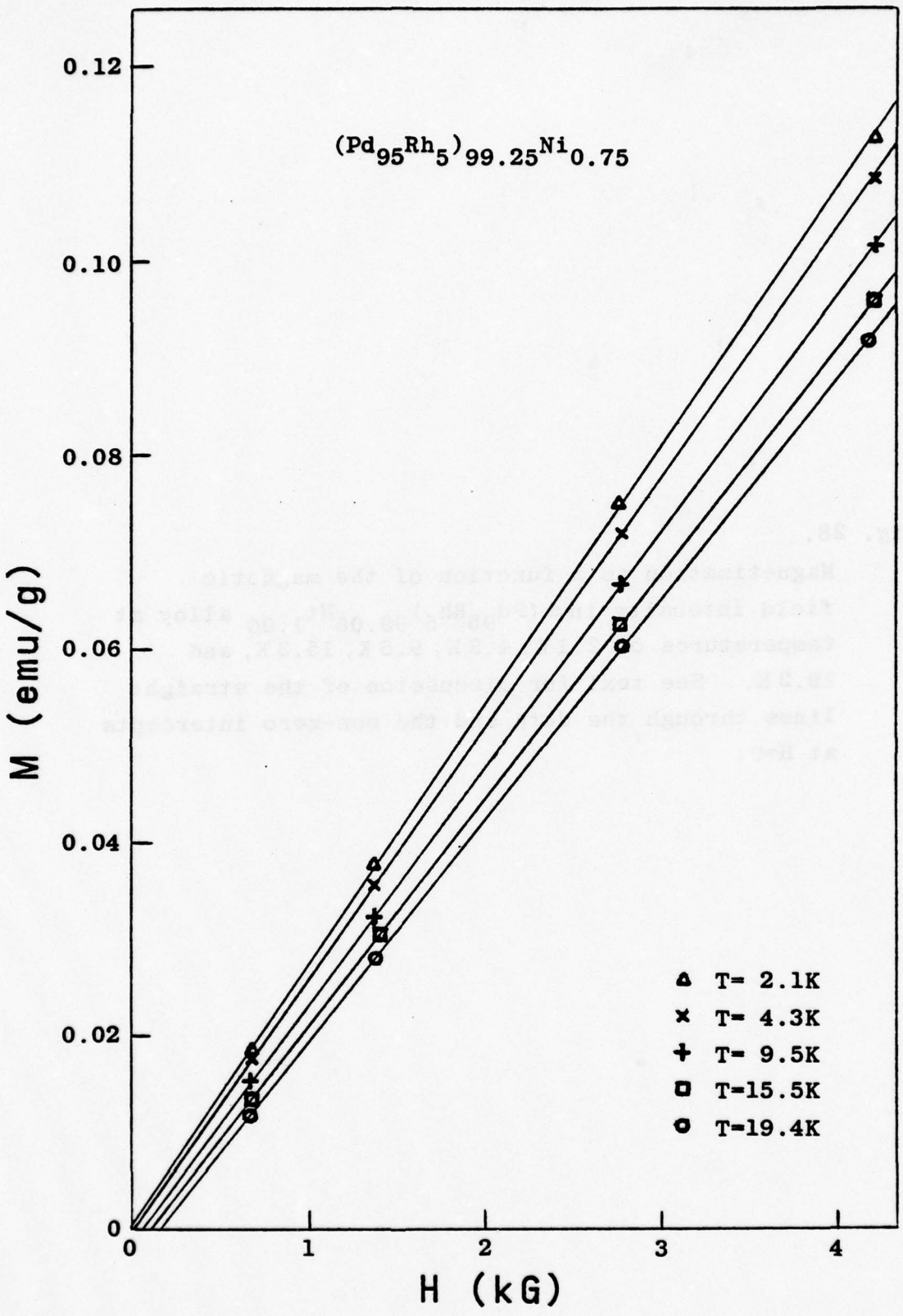
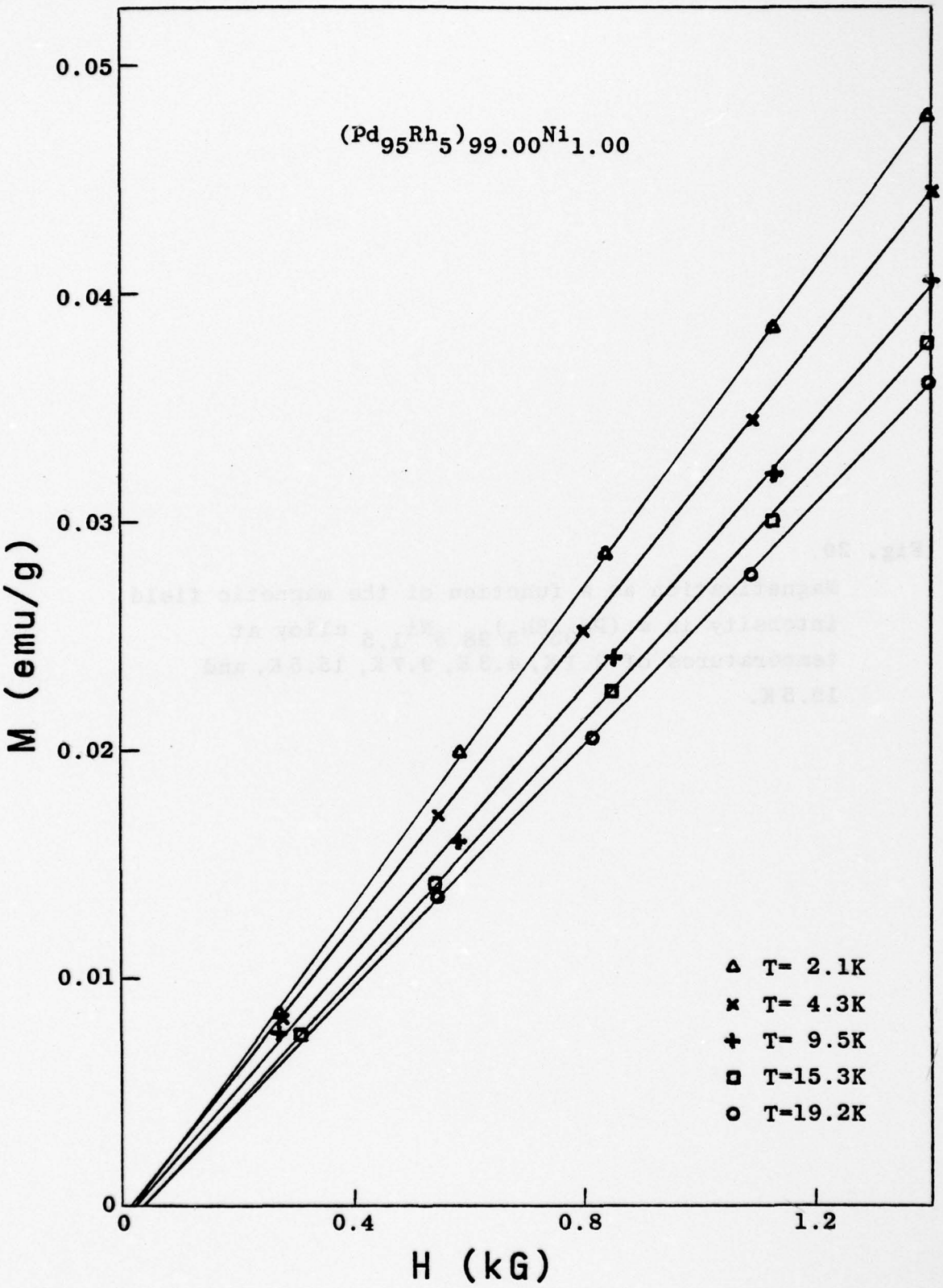

$(Pd_{95}Rh_5)_{99.25}Ni_{0.75}$
M (emu/g)
H (kG)
0.12
0.10
0.08
0.06
0.04
0.02
0
0
1
2
3
4
T= 2.1K
T= 4.3K
T= 9.5K
T=15.5K
T=19.4K

Fig. 28.

Magnetization as a function of the magnetic field intensity in a $(Pd_{95}Rh_5)_{99.00}Ni_{1.00}$ alloy at temperatures of 2.1 K, 4.3 K, 9.5 K, 15.3 K, and 19.2 K. See text for discussion of the straight lines through the data and the non-zero intercepts at H=0.


$(Pd_{95}Rh_5)_{99.00}Ni_{1.00}$
M (emu/g)
H (kG)
0.05
0.04
0.03
0.02
0.01
0
0.4
0.8
1.2
T= 2.1K
T= 4.3K
T= 9.5K
T=15.3K
T=19.2K

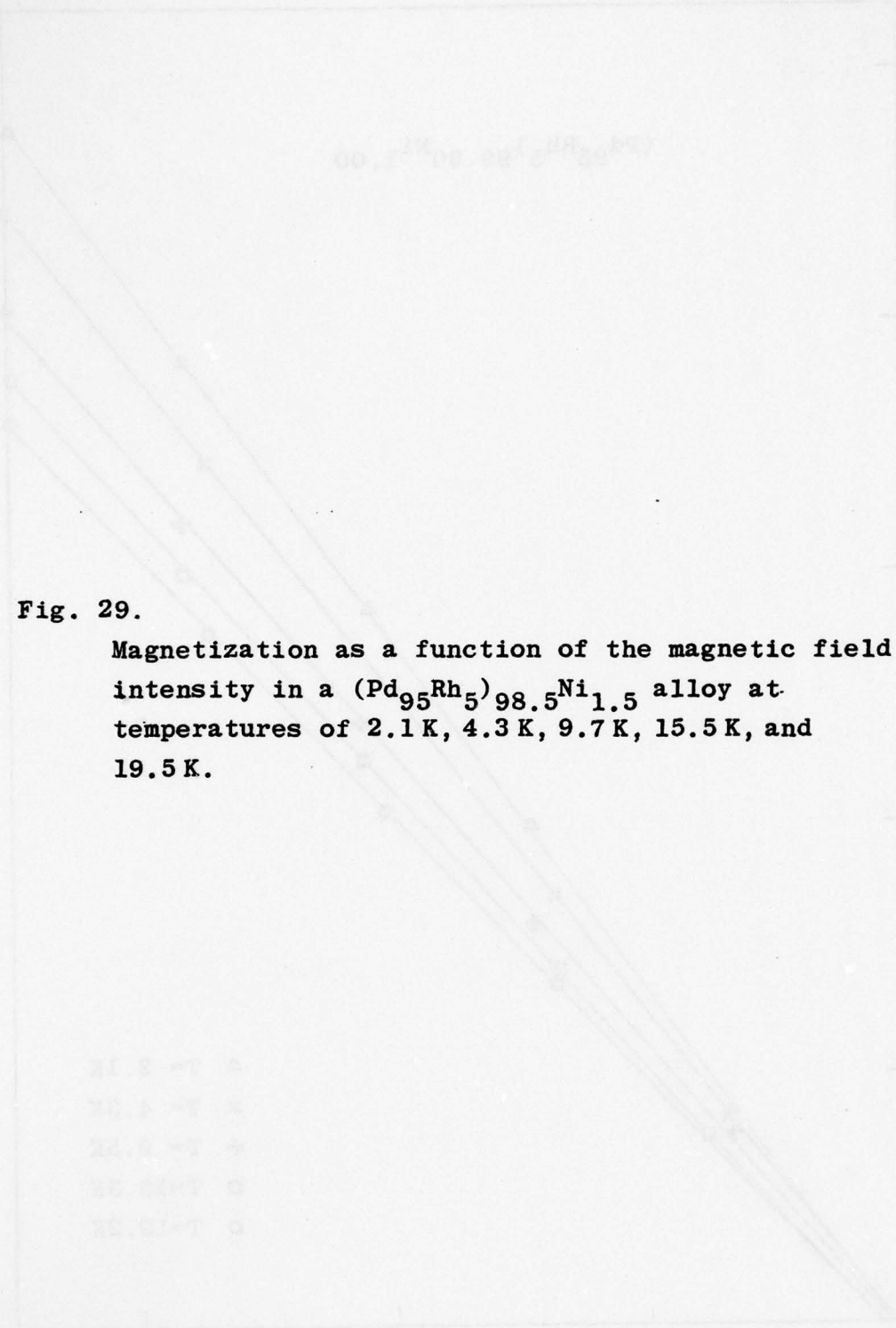
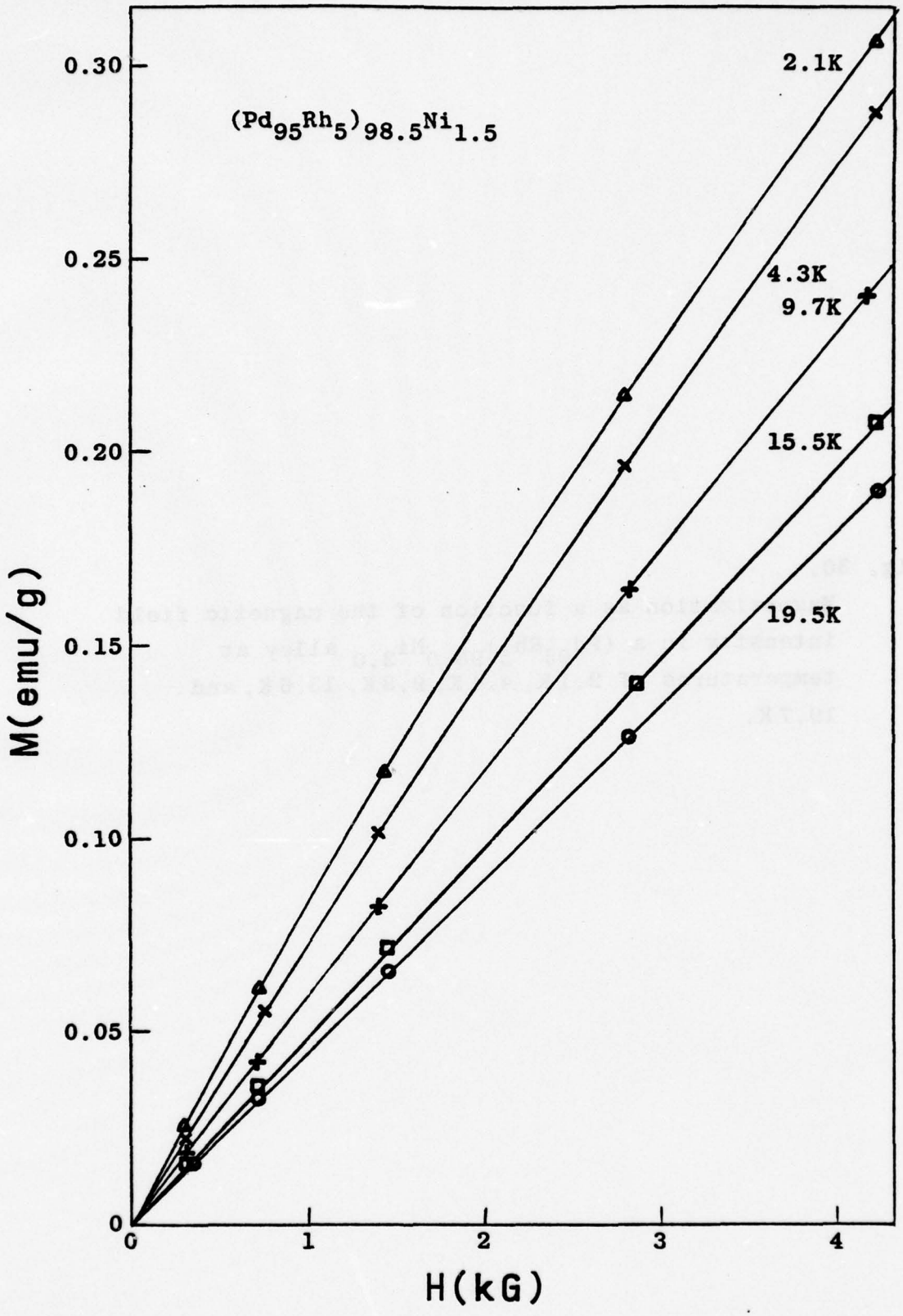


Fig. 29.

Magnetization as a function of the magnetic field intensity in a $(Pd_{95}Rh_5)_{98.5}Ni_{1.5}$ alloy at temperatures of 2.1 K, 4.3 K, 9.7 K, 15.5 K, and 19.5 K.


0.30
0.25
0.20
0.15
0.10
0.05
0
M(emu/g)
$(Pd_{95}Rh_5)_{98.5}Ni_{1.5}$
2.1K
4.3K
9.7K
15.5K
19.5K
0
1
2
3
4
H(kG)

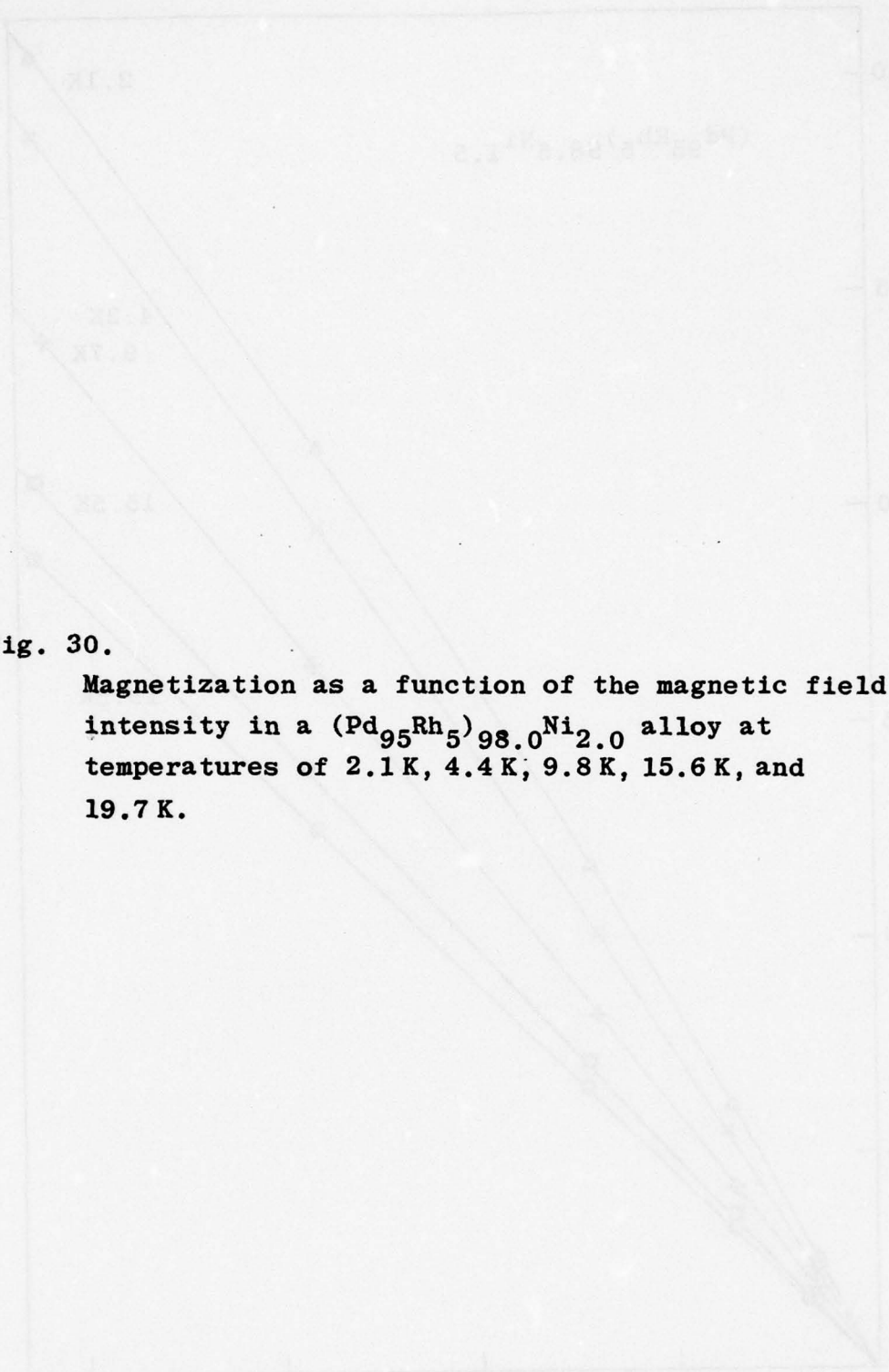
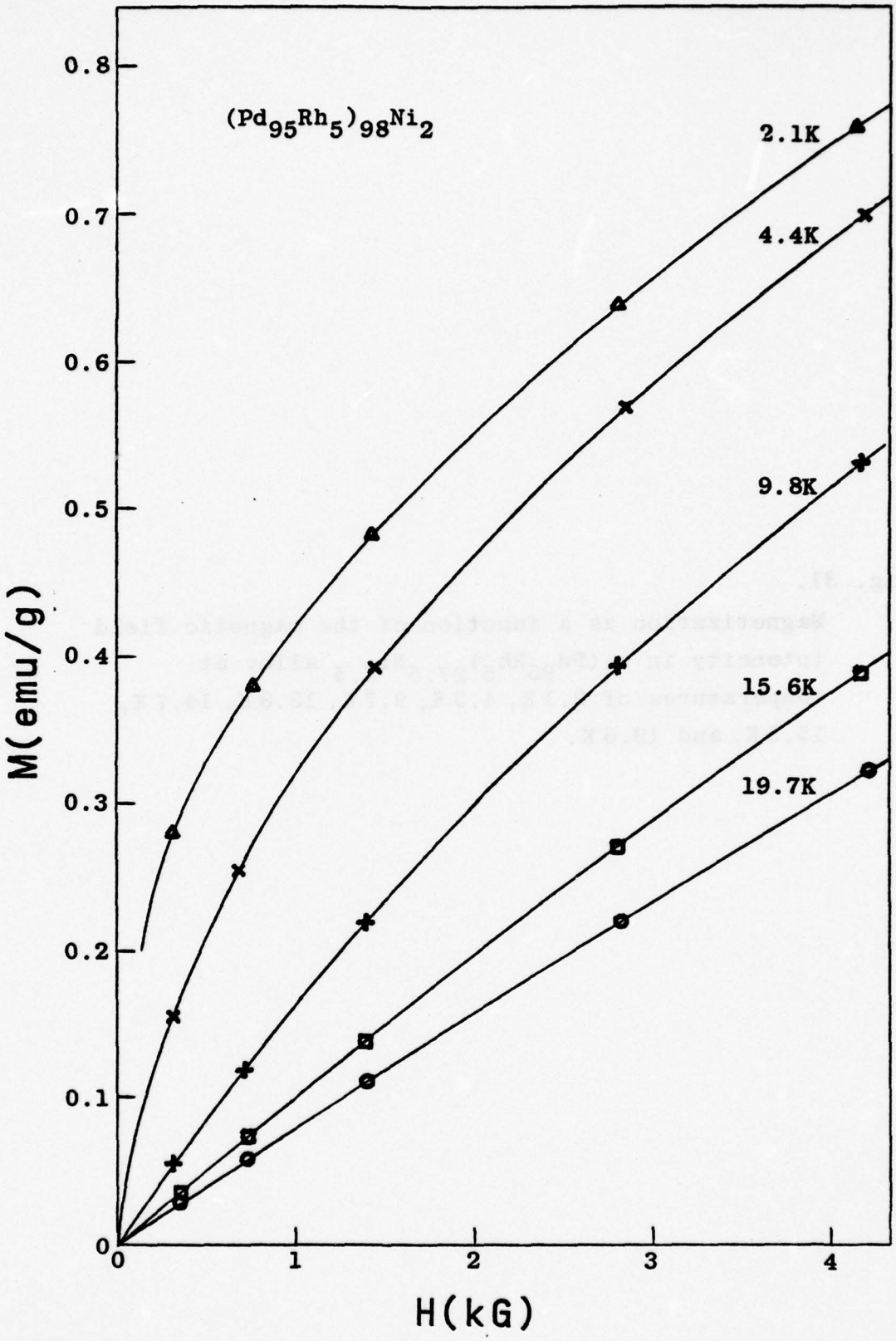


Fig. 30.

Magnetization as a function of the magnetic field intensity in a $(Pd_{95}Rh_5)_{98.0}Ni_{2.0}$ alloy at temperatures of 2.1 K, 4.4 K, 9.8 K, 15.6 K, and 19.7 K.


$(Pd_{95}Rh_5)_{98}Ni_2$
2.1K
4.4K
9.8K
15.6K
19.7K
M(emu/g)
H(kG)
0.8
0.7
0.6
0.5
0.4
0.3
0.2
0.1
0
0
1
2
3
4

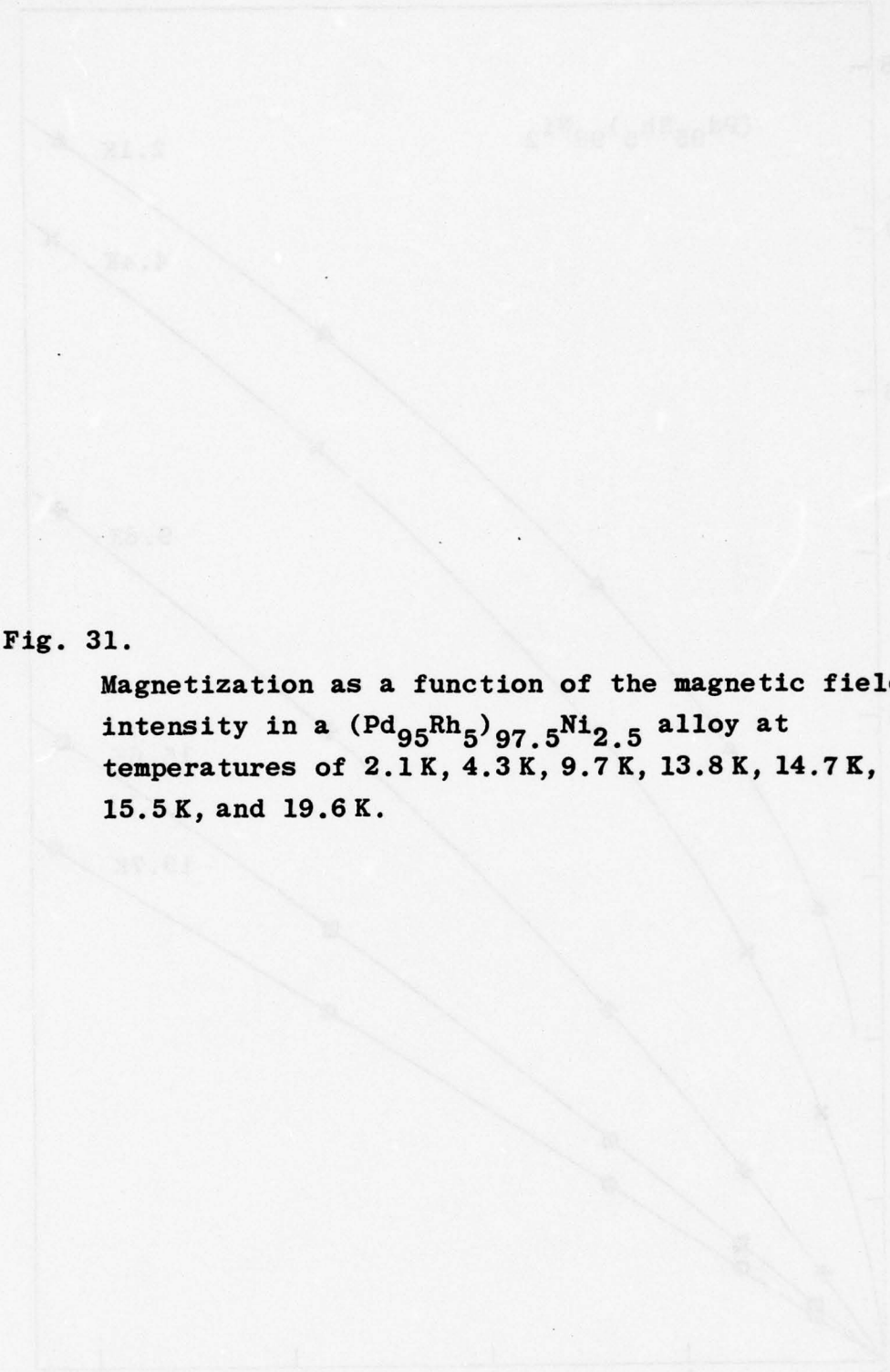
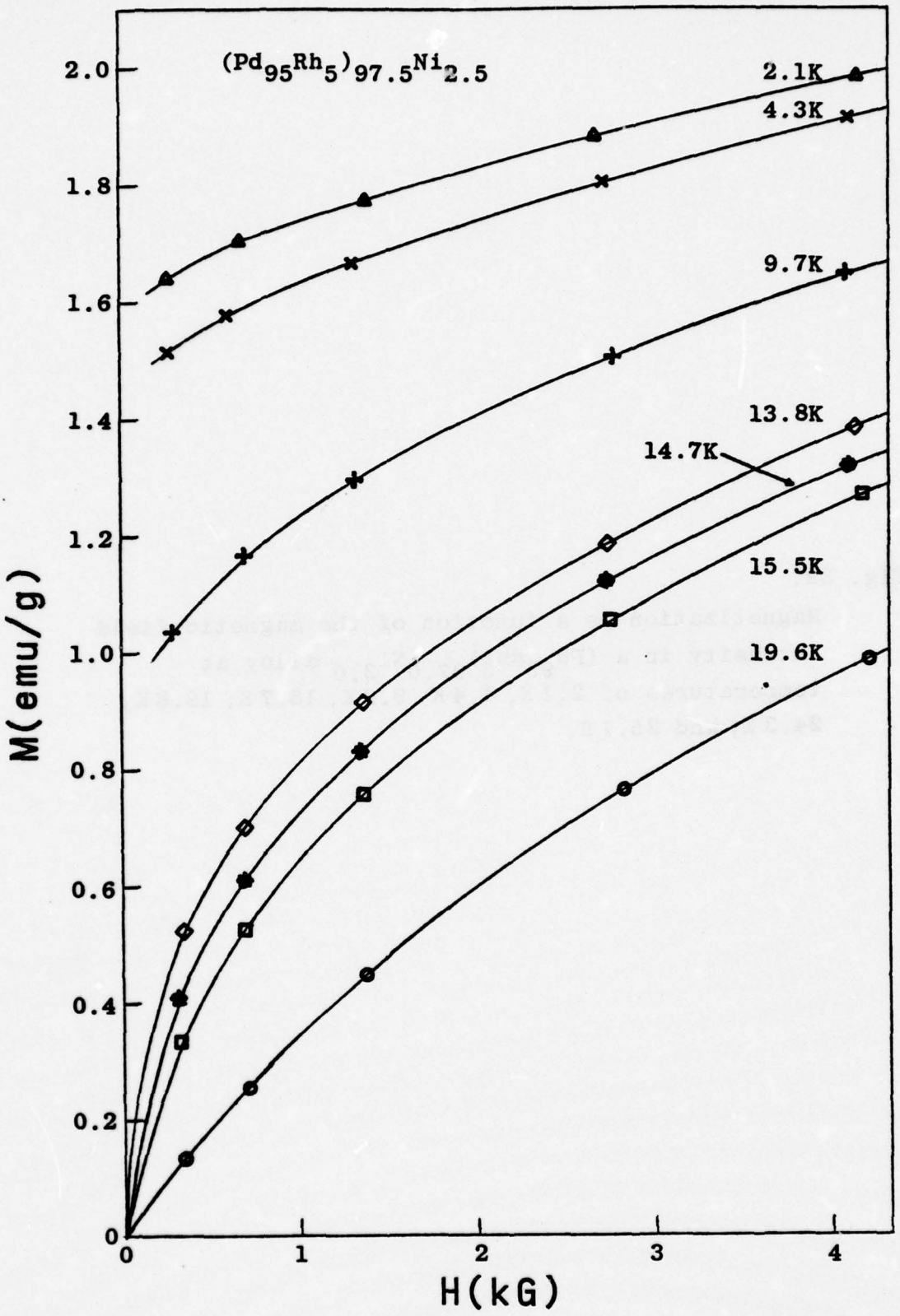


Fig. 31.

Magnetization as a function of the magnetic field intensity in a $(Pd_{95}Rh_5)_{97.5}Ni_{2.5}$ alloy at temperatures of 2.1 K, 4.3 K, 9.7 K, 13.8 K, 14.7 K, 15.5 K, and 19.6 K.


$(Pd_{95}Rh_5)_{97.5}Ni_{2.5}$
2.1K
4.3K
9.7K
13.8K
14.7K
15.5K
19.6K
M(emu/g)
H(kG)
0
0.2
0.4
0.6
0.8
1.0
1.2
1.4
1.6
1.8
2.0
0
1
2
3
4

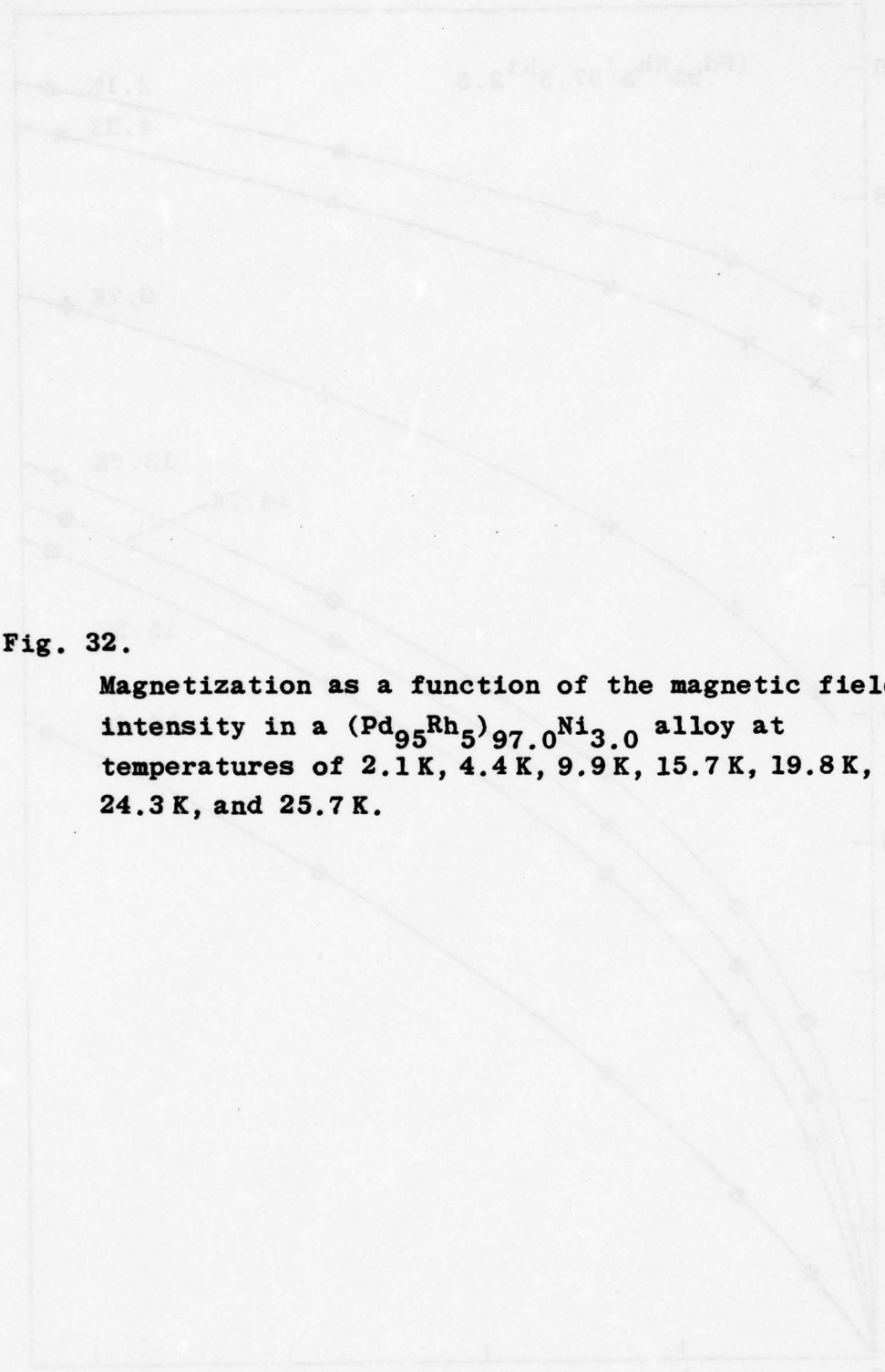
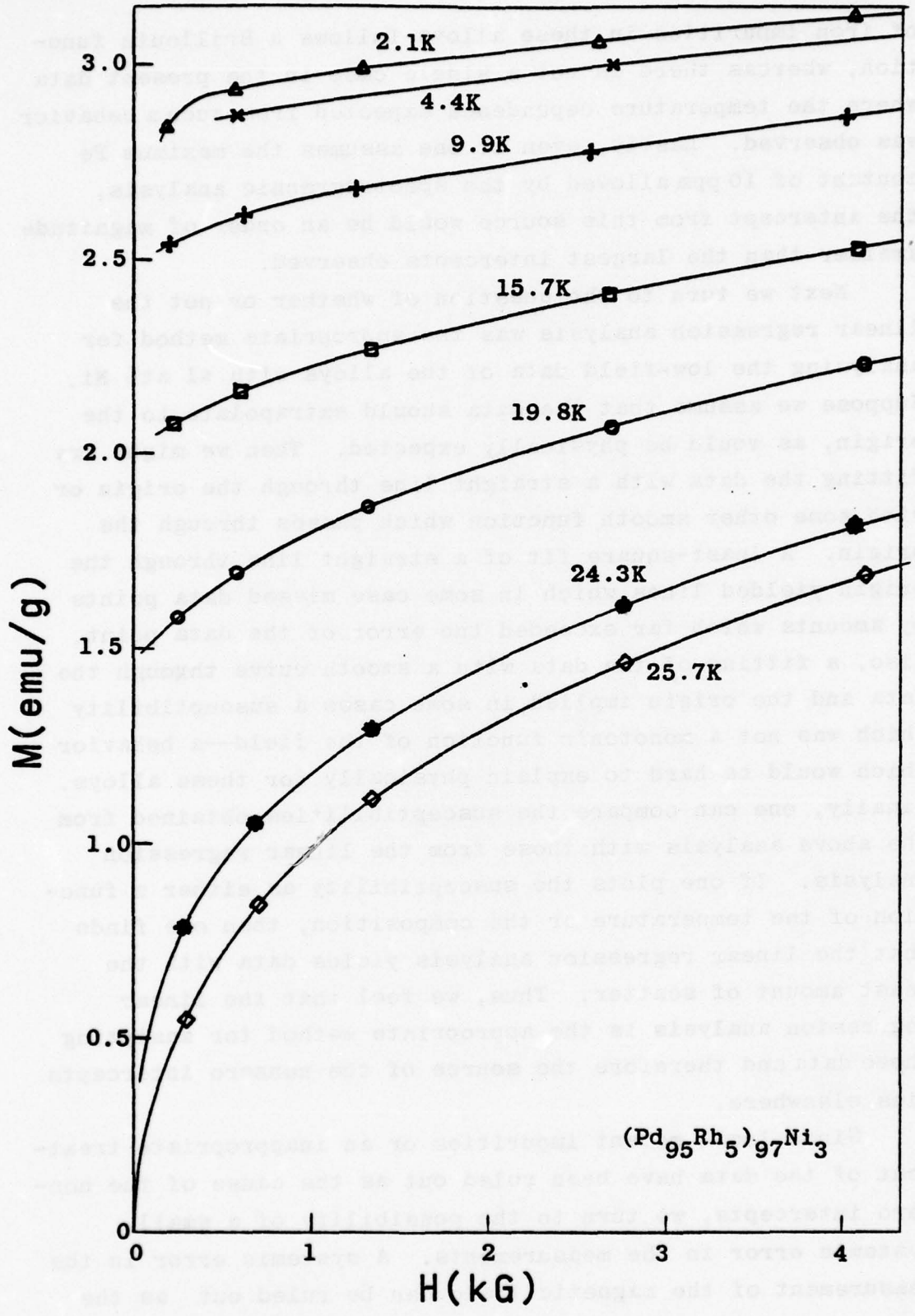


Fig. 32.

Magnetization as a function of the magnetic field intensity in a $(Pd_{95}Rh_5)_{97.0}Ni_{3.0}$ alloy at temperatures of 2.1 K, 4.4 K, 9.9 K, 15.7 K, 19.8 K, 24.3 K, and 25.7 K.


2.1K
4.4K
9.9K
15.7K
19.8K
24.3K
25.7K
3.0
2.5
2.0
1.5
1.0
0.5
0
0
1
2
3
4
M(emu/g)
H(kG)
(Pd95Rh5)97Ni3

of iron impurities in these alloys follows a Brillouin function, whereas there is not a single case in the present data where the temperature dependence expected from such a behavior was observed. Lastly, even if one assumes the maximum Fe content of 10 ppm allowed by the spectrographic analysis, the intercept from this source would be an order of magnitude smaller than the largest intercepts observed.

Next we turn to the question of whether or not the linear regression analysis was the appropriate method for analyzing the low-field data of the alloys with ≤1 at% Ni. Suppose we assume that the data should extrapolate to the origin, as would be physically expected. Then we might try fitting the data with a straight line through the origin or with some other smooth function which passes through the origin. A least-square fit of a straight line through the origin yielded lines which in some case missed data points by amounts which far exceeded the error of the data point. Also, a fitting of the data with a smooth curve through the data and the origin implied in some cases a susceptibility which was not a monotonic function of the field—a behavior which would be hard to explain physically for these alloys. Finally, one can compare the susceptibilities obtained from the above analysis with those from the linear regression analysis. If one plots the susceptibility as either a function of the temperature or the composition, then one finds that the linear regression analysis yields data with the least amount of scatter. Thus, we feel that the linear regression analysis is the appropriate method for analyzing these data and therefore the source of the nonzero intercepts lies elsewhere.

Since local moment impurities or an inappropriate treatment of the data have been ruled out as the cause of the nonzero intercepts, we turn to the possibility of a small systemic error in the measurements. A systemic error in the measurement of the magnetic field can be ruled out as the cause, since the error that would be required is far too

large to be reasonable. On the other hand, the errors that would be required in the measurement of the magnetic moment of the samples are not much larger than the resolution in the measurement. In fact the largest intercept which was found corresponded to a magnetic moment which was only five times that of the resolution. Such a small systematic error in the magnetic moment would also explain why the zero field intercepts were consistently smaller in the $Pd_{95.0}Rh_{5.0}$ alloy. This follows because this alloy was 3 to 4 times as massive as any of the alloys containing ≤1 at% Ni, and, consequently, a comparable error in measurement of the magnetic moment would yield a correspondently smaller error in the magnetization of this specimen. Thus, it appears that a small but detectable error exists in the magnetization measurement; however this is easily corrected by subtracting the value of the zero-field intercept from the data. For the alloys with Ni concentration >1 at%, the above error is even less significant since both the magnetization and the mass of these alloys are greater than the alloys from the first two sets.

In conclusion, we have presented in this section all the magnetization data and have discussed some aspects of the low field data. In the next few sections we will be taking a closer look at this data. It is clear from the data just presented that with the addition of approximately $1\frac{1}{2}$ to $2\frac{1}{2}$ at% Ni the alloy has become ferromagnetic. However, the exact composition at which ferromagnetism occurs and the nature of the transition are not readily apparent from the M versus H plots. In the following section we explore this transition region.

3.2 Arrott Plots and Curie Temperatures

In this section we find the critical concentration for the occurrence of ferromagnetism in the $(Pd_{95}Rh_5)_{1-x}Ni_x$ system and the Curie temperatures for the ferromagnetic alloys. The key to extracting this information from the data is the use of the Arrott plot[51], where M^2 is plotted as a function

of H/M. The usefulness of such a plot can be seen by applying the Landau theory[52] of second order phase transitions to the paramagnetic-ferromagnetic transition. Using this theory one can show[28] that minimizing the free energy with respect to the magnetization yields the equation,

$$H(r) = A(c,T)M(r) + B(c,T)M^3(r) - C(c,T)\nabla^2 M(r) \quad , \quad (3.1)$$

where M(r) is the spatially varying magnetization, H(r) is the magnetic field intensity, and A, B>0, C>0, are parameters which are functions of the alloy concentration, c, and the temperature, T. For a homogeneous alloy system in a spatially unifrom field the above equation reduces to

$$H = A(c,T)M + B(c,T)M^3 \quad . \quad (3.2)$$

On an Arrott plot this equation of state has the simple form of a straight line, as is easily seen upon rewriting Eq. 3.2 as

$$M^2 = -\frac{A}{B} + \frac{1}{B}\frac{H}{M} \quad . \quad (3.3)$$

In the absence of an applied field there are two relevant solutions to Eq. 3.2:

$$M = 0 \ , \ A > 0 \ , \text{ and } \ M = (-A/B)^{\frac{1}{2}} \ , \ A < 0 \ .$$

The first of these corresponds to the paramagnetic state of the system and the second corresponds to the ferromagnetic state. Thus, by plotting on an Arrott plot the magnetization of the homogeneous alloy, we have a clear-cut method for determining the magnetic state (phase) of the alloys in the system—those alloys where the equation of state corresponds to a line which intersects the positive abscissa are in the paramagnetic state, while those alloys where the equation of state corresponds to a line which intersects the positive ordinate are in the ferromagnetic state. The Curie temperature is the temperature for which the equation of state corresponds to a line passing through the origin, and the critical composition for the onset of ferromagnetism is the composition whose equation of state at T=0 corresponds to a line passing through the origin.

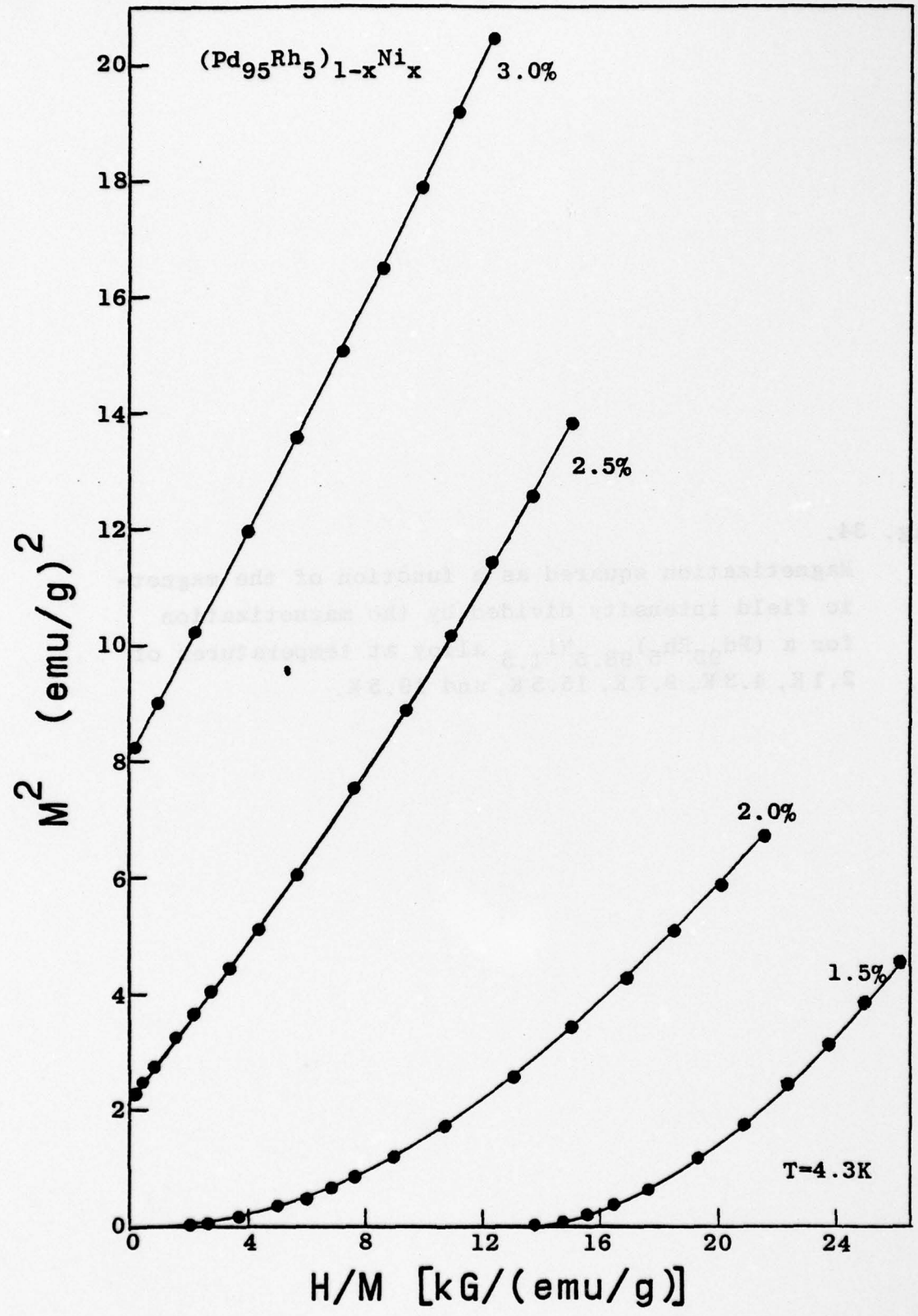
For an inhomogeneous alloy, where the equation of state no longer corresponds to a straight line on the Arrott plot, it is still useful to define a Curie temperature and a critical composition in a manner analogous to that given above. The Curie temperature in this case is defined as the temperature at which the magnetization, when extrapolated to H=0,will go to the origin of the Arrott plot. An alloy is said to be in the ferromagnetic state if the extrapolation yields M>0 and is said to be in the paramagnetic state if the extrapolation yields M=0. The critical composition is that alloy composition which has a Curie temperature equal to zero. That the above criteria yields a useful method for determining the critical composition is supported by the work of Murani et al.[53] on the $Pd_{1-x}Ni_x$ system. They found, that if they apply the above definition when analyzing their magnetization results, then the critical concentration they obtained would be in excellent agreement with the critical concentration found both from resistivity and from specific heat measurements.

With this background in mind, we re-examine the magnetization data (Sect. 3.1) for those alloys containing $\geq 1\frac{1}{2}$ at% Ni. The high field data are shown in the first Arrott plot (Fig. 33). The low field data are shown in the four following plots (Fig. 35 through Fig. 37). It is clear from examining the curves drawn through the data and applying the criteria for ferromagnetism given above that the 1.5 at% Ni sample is paramagnetic at all temperatures, while the 2.0, 2.5, and 3.0 at% Ni samples have Curie temperatures of 2.0± 0.5 K, 13.0±0.5 K, and 24.5±0.5 K, respectively. In Fig. 38 we compare these Curie temperatures with the Curie temperatures[53] obtained in the same manner for the $Pd_{1-x}Ni_x$ system. Extrapolating the Curie temperature data to a zero Curie temperature, we obtain a critical concentration of 1.9±0.05 at% Ni for the onset of ferromagnetism in the $(Pd_{95}Rh_5)_{1-x}Ni_x$ system, which is significantly lower than the 2.3±0.05 at% Ni value[53] found for the $Pd_{1-x}Ni_x$ system.

(text continues on p. 170)

Fig. 33.

Magnetization squared as a function of the magnetic field intensity divided by the magnetization for a series of $(Pd_{95}Rh_5)_{1-x}Ni_x$ alloys at a temperature of 4.3 K. The atomic percent of Ni in the $(Pd_{95}Rh_5)_{1-x}Ni_x$ alloys labels each curve. Measurements were made in fields up to 56 kG.


$(Pd_{95}Rh_5)_{1-x}Ni_x$
3.0%
2.5%
2.0%
1.5%
T=4.3K
M^2 (emu/g)^2
H/M [kG/(emu/g)]
0
2
4
6
8
10
12
14
16
18
20
0
4
8
12
16
20
24

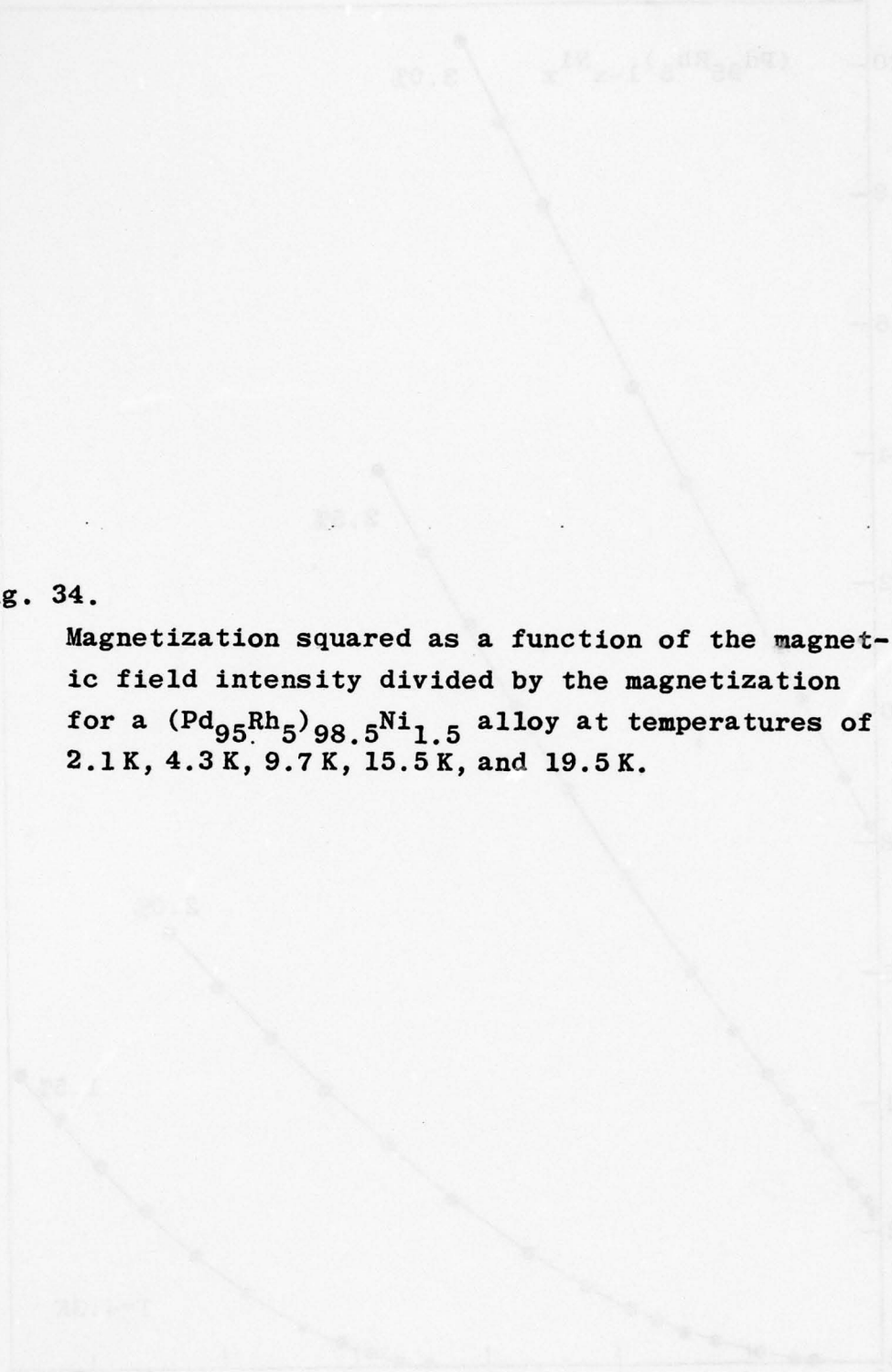


Fig. 34.

Magnetization squared as a function of the magnetic field intensity divided by the magnetization for a $(Pd_{95}Rh_5)_{98.5}Ni_{1.5}$ alloy at temperatures of 2.1 K, 4.3 K, 9.7 K, 15.5 K, and 19.5 K.

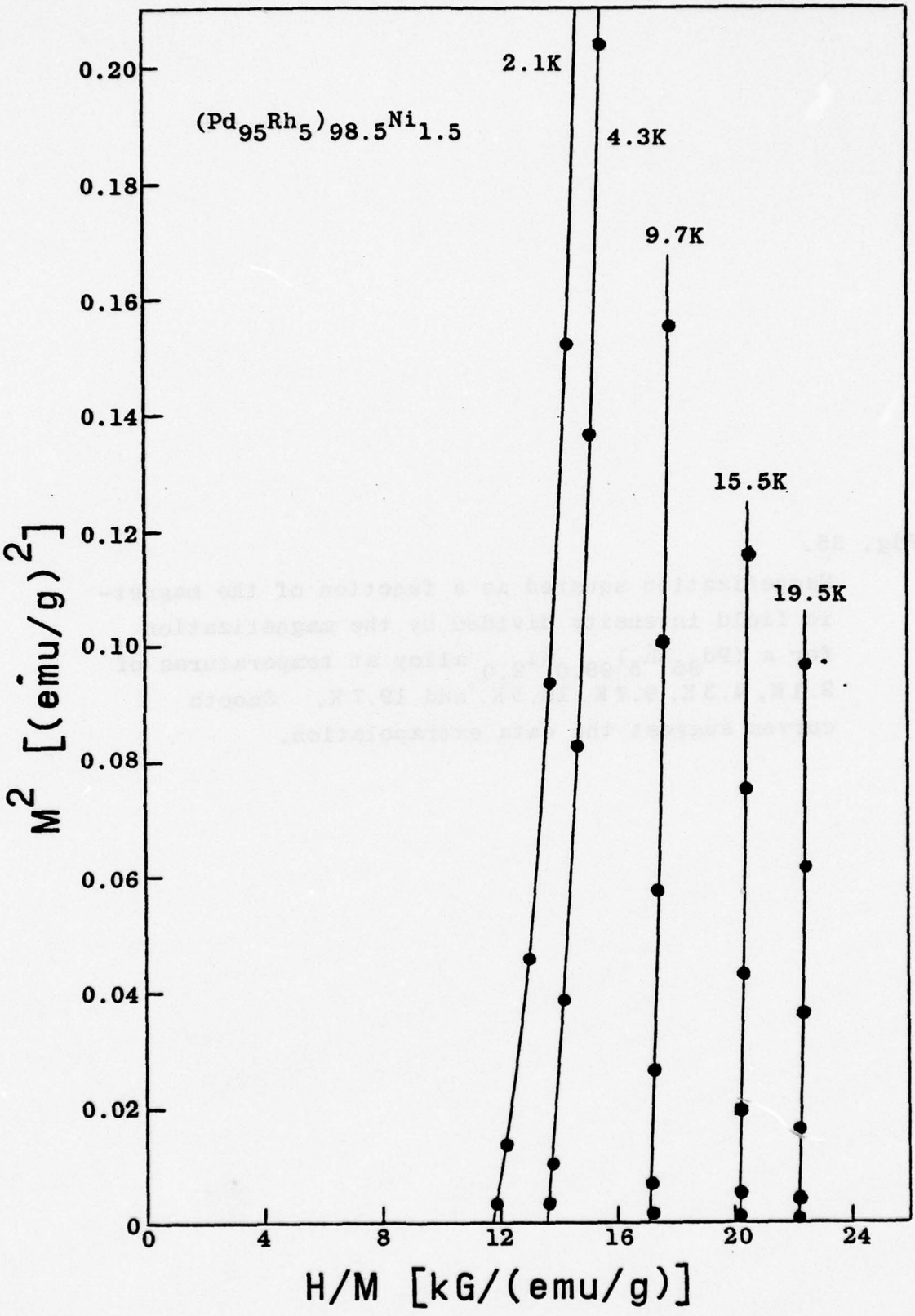

$(Pd_{95}Rh_5)_{98.5}Ni_{1.5}$
2.1K
4.3K
9.7K
15.5K
19.5K
M^2 [(emu/g)^2]
H/M [kG/(emu/g)]
0
0.02
0.04
0.06
0.08
0.10
0.12
0.14
0.16
0.18
0.20
0
4
8
12
16
20
24

Fig. 35.

Magnetization squared as a function of the magnetic field intensity divided by the magnetization for a $(Pd_{95}Rh_5)_{98.0}Ni_{2.0}$ alloy at temperatures of 2.1 K, 4.3 K, 9.7 K, 15.5 K, and 19.7 K. Smooth curves suggest the data extrapolation.

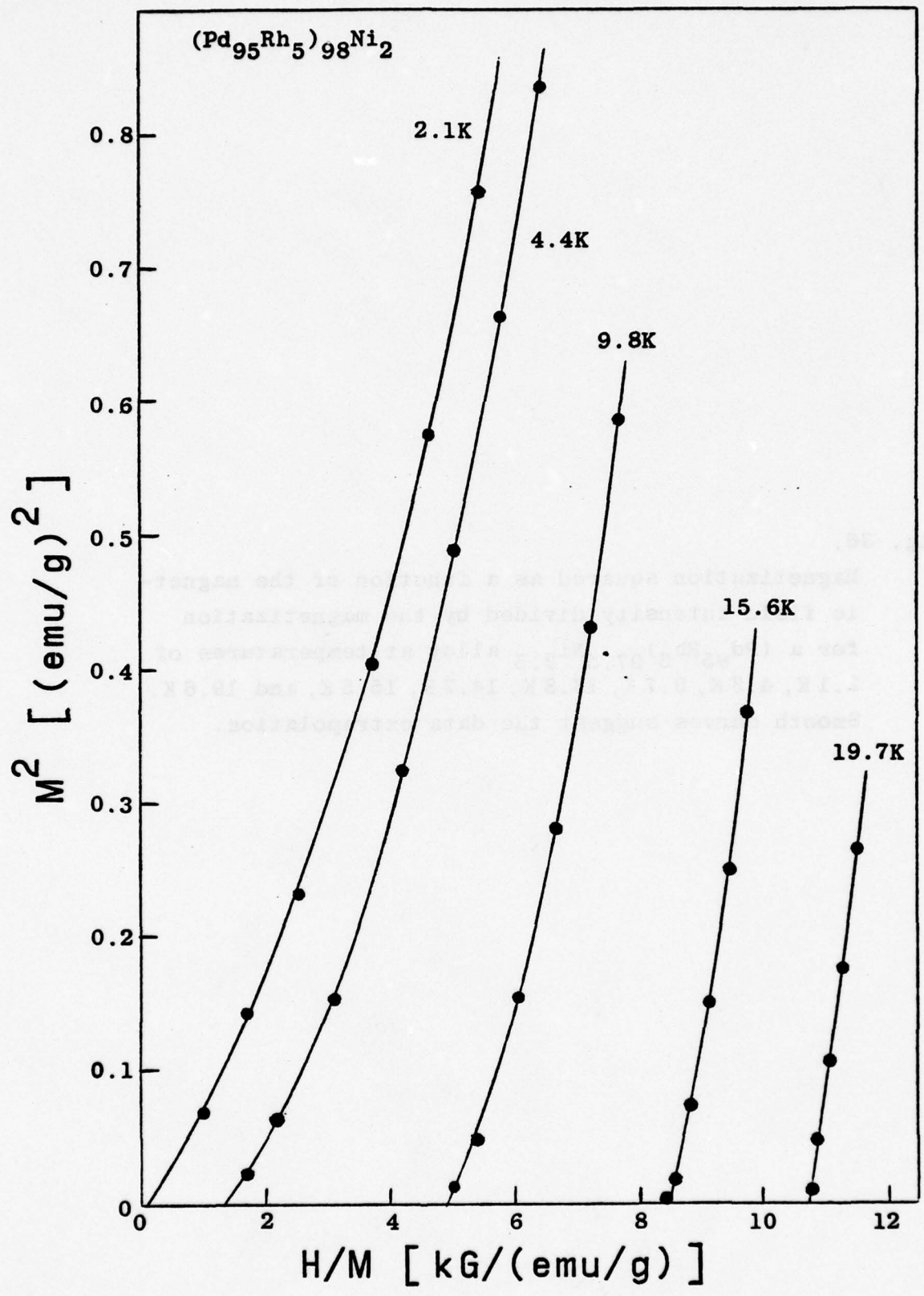

$(Pd_{95}Rh_5)_{98}Ni_2$
2.1K
4.4K
9.8K
15.6K
19.7K
M^2 [(emu/g)^2]
H/M [kG/(emu/g)]
0
0.1
0.2
0.3
0.4
0.5
0.6
0.7
0.8
2
4
6
8
10
12

Fig. 36.

Magnetization squared as a function of the magnetic field intensity divided by the magnetization for a $(Pd_{95}Rh_5)_{97.5}Ni_{2.5}$ alloy at temperatures of 2.1 K, 4.3 K, 9.7 K, 13.8 K, 14.7 K, 15.5 K, and 19.6 K. Smooth curves suggest the data extrapolation.

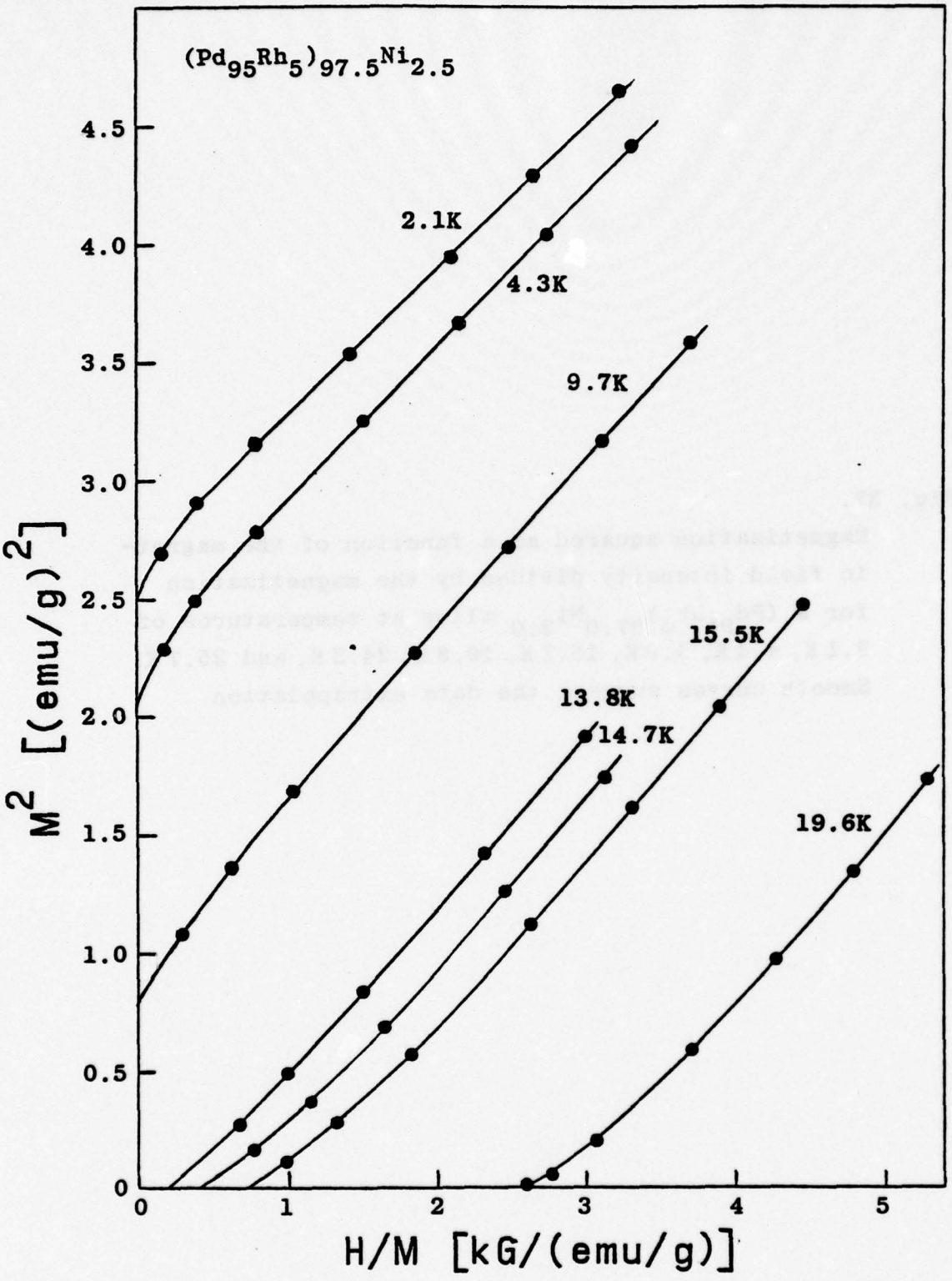

$(Pd_{95}Rh_5)_{97.5}Ni_{2.5}$
2.1K
4.3K
9.7K
15.5K
13.8K
14.7K
19.6K
M^2 [(emu/g)^2]
H/M [kG/(emu/g)]
0
0.5
1.0
1.5
2.0
2.5
3.0
3.5
4.0
4.5
1
2
3
4
5

Fig. 37.

Magnetization squared as a function of the magnetic field intensity divided by the magnetization for a $(Pd_{95}Rh_5)_{97.0}Ni_{3.0}$ alloy at temperatures of 2.1 K, 4.4 K, 9.9 K, 15.7 K, 19.8 K, 24.3 K, and 25.7 K. Smooth curves suggest the data extrapolation.

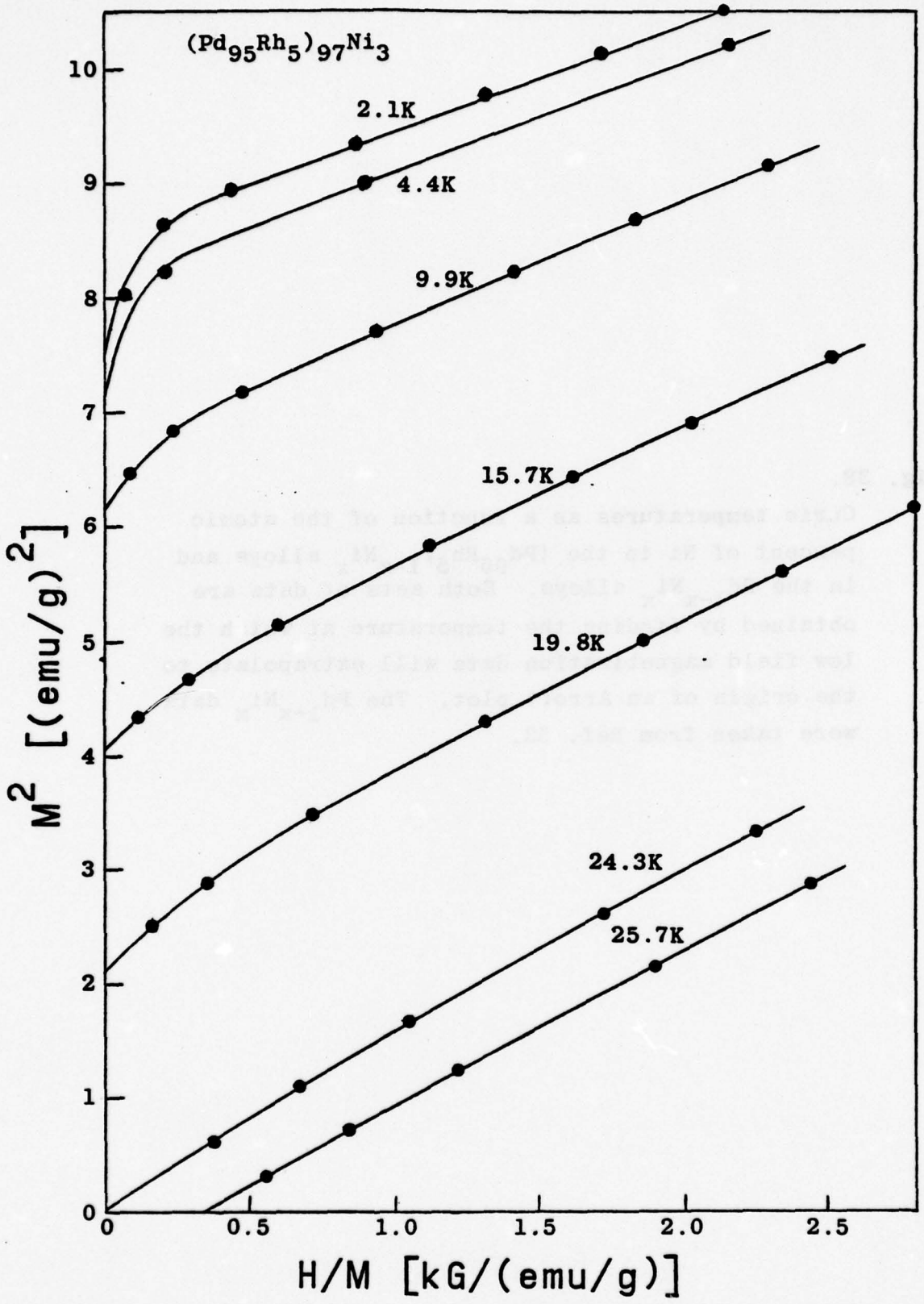
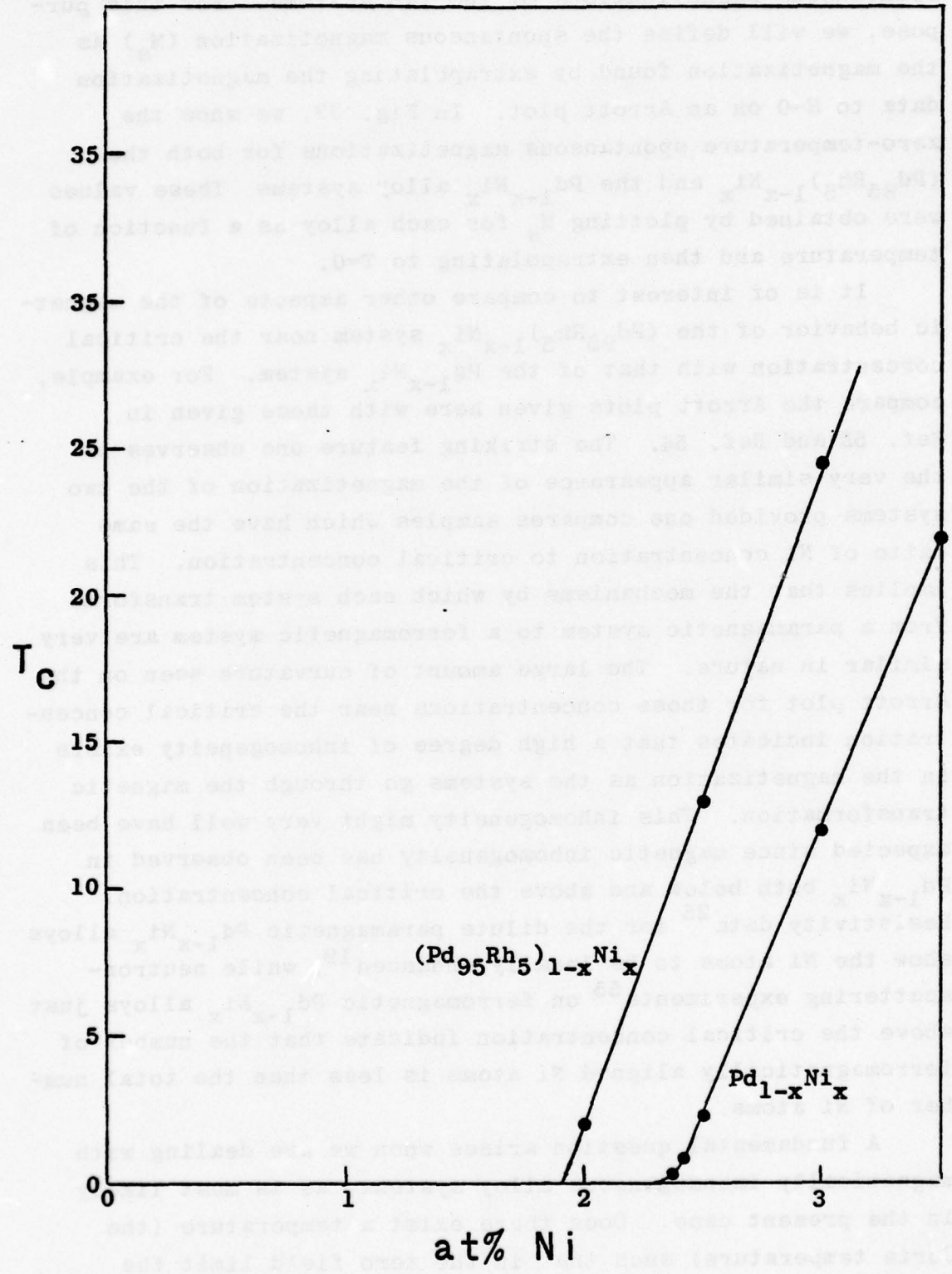

$(Pd_{95}Rh_5)_{97}Ni_3$
2.1K
4.4K
9.9K
15.7K
19.8K
24.3K
25.7K
M^2 [(emu/g)^2]
H/M [kG/(emu/g)]
0
1
2
3
4
5
6
7
8
9
10
0.5
1.0
1.5
2.0
2.5

Fig. 38.

Curie temperatures as a function of the atomic percent of Ni in the $(Pd_{95}Rh_5)_{1-x}Ni_x$ alloys and in the $Pd_{1-x}Ni_x$ alloys. Both sets of data are obtained by finding the temperature at which the low field magnetization data will extrapolate to the origin of an Arrott plot. The $Pd_{1-x}Ni_x$ data were taken from Ref. 53.


35
35
25
20
15
10
5
0
T_c
0
1
2
3
at% Ni
$(Pd_{95}Rh_5)_{1-x}Ni_x$
$Pd_{1-x}Ni_x$

We can also make use of the Arrott plot to compare the spontaneous magnetizations of the two systems. For this purpose, we will define the spontaneous magnetization (M_s) as the magnetization found by extrapolating the magnetization data to H=0 on an Arrott plot. In Fig. 39, we show the zero-temperature spontaneous magnetizations for both the $(Pd_{95}Rh_5)_{1-x}Ni_x$ and the $Pd_{1-x}Ni_x$ alloy systems These values were obtained by plotting M_s for each alloy as a function of temperature and then extrapolating to T=0.

It is of interest to compare other aspects of the magnetic behavior of the $(Pd_{95}Rh_5)_{1-x}Ni_x$ system near the critical concentration with that of the $Pd_{1-x}Ni_x$ system. For example, compare the Arrott plots given here with those given in Ref. 53 and Ref. 54. The striking feature one observes is the very similar appearance of the magnetization of the two systems provided one compares samples which have the same ratio of Ni concentration to critical concentration. This implies that the mechanisms by which each system transforms from a paramagnetic system to a ferromagnetic system are very similar in nature. The large amount of curvature seen on the Arrott plot for those concentrations near the critical concentration indicates that a high degree of inhomogeneity exists in the magnetization as the systems go through the magnetic transformation. This inhomogeneity might very well have been expected since magnetic inhomogeneity has been observed in $Pd_{1-x}Ni_x$ both below and above the critical concentration. Resistivity data[25] for the dilute paramagnetic $Pd_{1-x}Ni_x$ alloys show the Ni atoms to be locally enhanced[19], while neutron-scattering experiments[55] on ferromagnetic $Pd_{1-x}Ni_x$ alloys just above the critical concentration indicate that the number of ferromagnetically aligned Ni atoms is less than the total number of Ni atoms.

A fundamental question arises when we are dealing with magnetically inhomogeneous alloy systems, as is most likely in the present case. Does there exist a temperature (the Curie temperature) such that in the zero field limit the

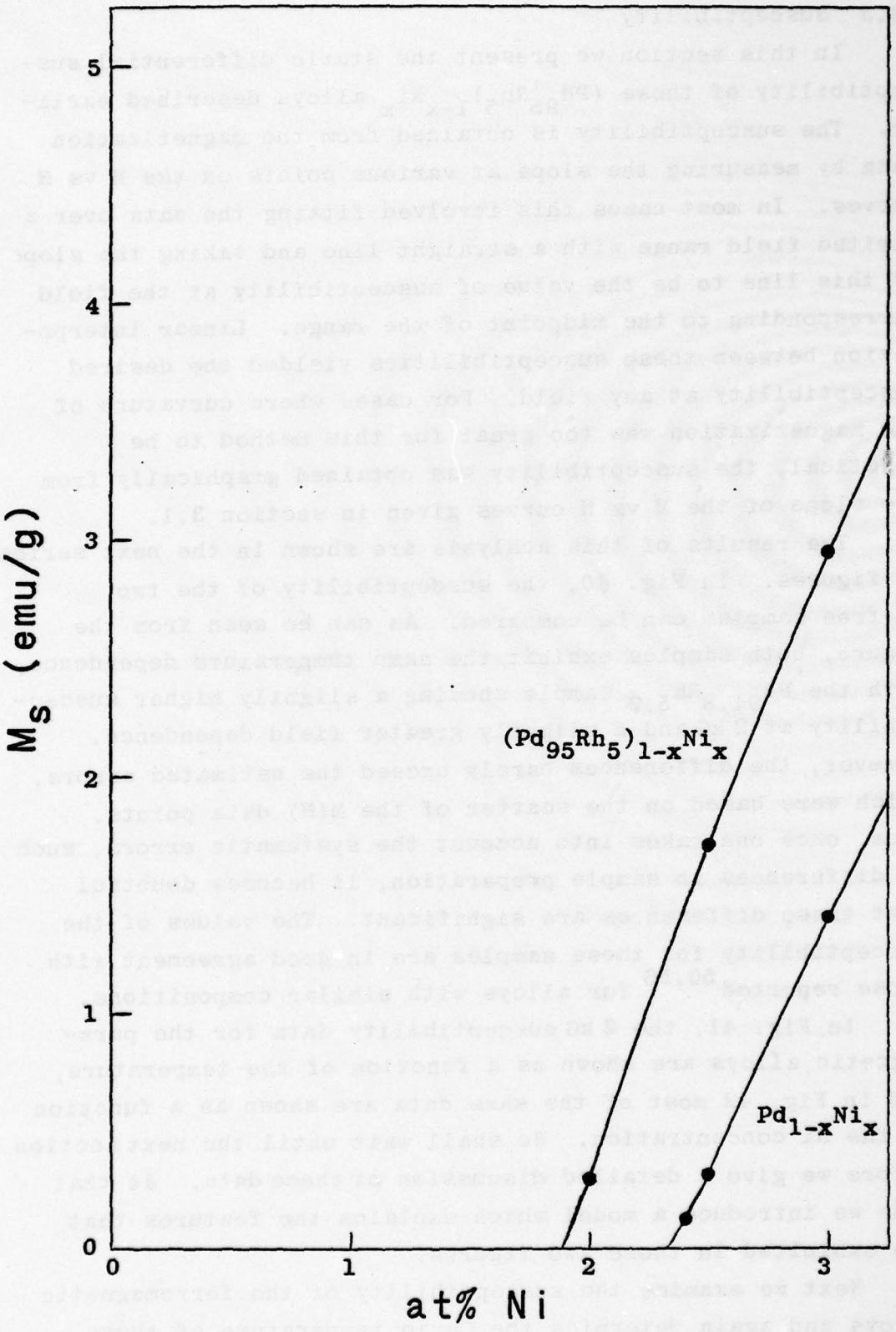
average magnetization at any given point is zero for temperatures above this temperature and nonzero for temperatures below this temperature? An example of a system without a fixed Curie temperature would be a system which formed a mixed state with both paramagnetic and ferromagnetic phases. One can also find an example of a inhomogeneous system with a well defined Curie temperature. Suppose for example, one had a locally enhanced system in which the amount of enhancement at a given site depended only on the type of atom at the site and on the average enhancement of the alloy. In this case, because the enhancement depends on the type of atom and not on the configuration of the atoms, once a spontaneous moment forms on one atom, it will, because of the identical nature of the atoms, exist on all the atoms of this species. If the concentration is high enough such that all the moments interact once formed, then the system will have well defined Curie temperature.

It should be clear that, if the Curie temperature exists, the Arrott plot will yield this temperature. However, for the inhomogeneous system, where one no longer expects the zero field extrapolations to be straight lines on the Arrott plot, the extrapolations become more difficult, and as a consequence, the Curie temperatures become more uncertain.

For systems which form mixed phase regions and therefore lack a Curie temperature, one may wish to generalize the definition of the Curie temperature so as to include these systems. In the next section we will use a generalized definition for the Curie temperature which is based on susceptibility rather than the magnetization of the sample. At that time, we will discuss the relation between the Arrott criteria and this generalized Curie temperature. We will also reexamine the data to see whether or not the Curie temperatures based on this new definition differ significantly from those determined on the basis of the Arrott method.

Fig. 39.

Spontaneous magnetization at T=0 as a function of the atomic percent of Ni in $(Pd_{95}Rh_5)_{1-x}Ni_x$ and $Pd_{1-x}Ni_x$ alloys. The spontaneous magnetization, defined as the magnetization, was obtained by extrapolating the magnetization data to zero field on an Arrott plot. The $Pd_{1-x}Ni_x$ data were taken from Ref. 53.


5
4
3
2
1
0
M_S (emu/g)
$(Pd_{95}Rh_5)_{1-x}Ni_x$
$Pd_{1-x}Ni_x$
0
1
2
3
at% Ni

3.3 Susceptibility

In this section we present the static differential susceptibility of those $(Pd_{95}Rh_5)_{1-x}Ni_x$ alloys described earlier. The susceptibility is obtained from the magnetization data by measuring the slope at various points on the M vs H curves. In most cases this involved fitting the data over a limited field range with a straight line and taking the slope of this line to be the value of susceptibility at the field corresponding to the midpoint of the range. Linear interpolation between these susceptibilities yielded the desired susceptibility at any field. For cases where curvature of the magnetization was too great for this method to be practical, the susceptibility was obtained graphically from the slope of the M vs H curves given in section 3.1.

The results of this analysis are shown in the next series of figures. In Fig. 40, the susceptibility of the two Ni-free samples can be compared. As can be seen from the figure, both samples exhibit the same temperature dependence, with the $Pd_{94.8}Rh_{5.2}$ sample showing a slightly higher susceptibility at 2 kG and a slightly greater field dependence. However, the differences barely exceed the estimated errors, which were based on the scatter of the M(H) data points. Thus, once one takes into account the systematic errors, such as differences in sample preparation, it becomes doubtful that these differences are significant. The values of the susceptibility for these samples are in good agreement with those reported[50,56] for alloys with similar compositions.

In Fig. 41, the 2 kG susceptibility data for the paramagnetic alloys are shown as a function of the temperature, and in Fig. 42 most of the same data are shown as a function of the Ni concentration. We shall wait until the next section before we give a detailed discussion of these data. At that time we introduce a model which explains the features that are exhibited in these two figures.

Next we examine the susceptibility of the ferromagnetic alloys and again determine the Curie temperature of these

alloys. It is useful in this case to define the "Curie" temperature as the temperature at which the initial susceptibility (dM/dH as H→0) is a maximum. For systems with a well defined Curie temperature (see definition given in previous section), this new definition is equivalent to the previous definition, since the susceptibility diverges at the Curie temperature for these systems. The new definition is useful because it extends the definition of a Curie temperature to those systems which form mixed phase regions and thus greatly increases the number of systems which can be compared using this parameter. In this new generalized sense, the Curie temperature is the temperature at which in the limit of a vanishingly small field the alloy exhibits the greatest response to the field.

It should be clear from the above definitions that the Curie temperatures obtained from an Arrott plot analysis may differ from those based on a susceptibility analysis. Take for example a system which is in a paramagnetic phase, but as the temperature is lowered a mixed phase region forms. As soon as any amount of the ferromagnetic phase is formed, the magnetization of the sample is no longer zero and the Arrott relation will imply that the Curie temperature has been reached, whereas the maximum response to an applied field may not occur until a much lower temperature. However, the exact difference between these two Curie temperatures will depend on the width of the two-phase region, the details of the Arrott extrapolation, and the sensitivity of the measurement.

We have found the Curie temperatures for the ferromagnetic alloys by closely examining the slopes of the M vs H curves given in section 3.1. First we extrapolate these slopes to zero field to obtain the zero field susceptibility, and then we find the temperature at which this susceptibility is a maximum. Within the errors of this procedure we find no detectable difference between these Curie temperatures and

(text continues on p. 184)

Fig. 40.

Differential susceptibility at 2 kG as a function of sample temperature for both $Pd_{94.8}Rh_{5.2}$ and $Pd_{95.0}Rh_{5.0}$. Also shown is the differential susceptibility at 50 kG for both alloys at a temperature of 4.3 K.

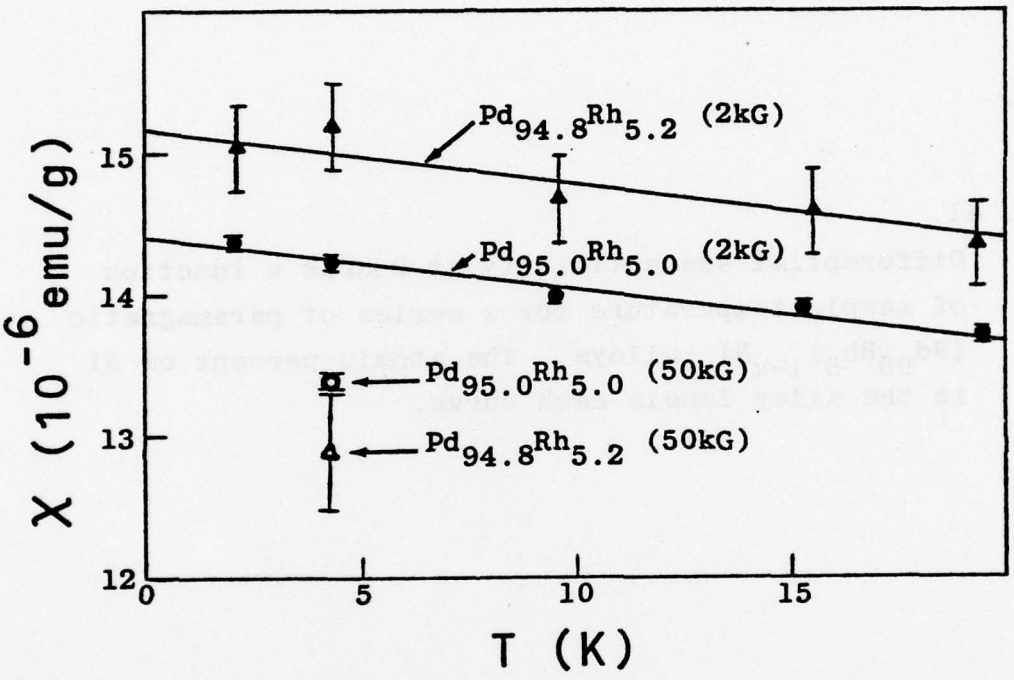

$Pd_{94.8}Rh_{5.2}$ (2kG)
$Pd_{95.0}Rh_{5.0}$ (2kG)
$Pd_{95.0}Rh_{5.0}$ (50kG)
$Pd_{94.8}Rh_{5.2}$ (50kG)
χ (10^{-6} emu/g)
15
14
13
12
0
5
10
15
T (K)

Fig. 41.

Differential susceptibility at 2 kG as a function of sample temperature for a series of paramagnetic $(Pd_{95}Rh_5)_{1-x}Ni_x$ alloys. The atomic percent of Ni in the alloy labels each curve.

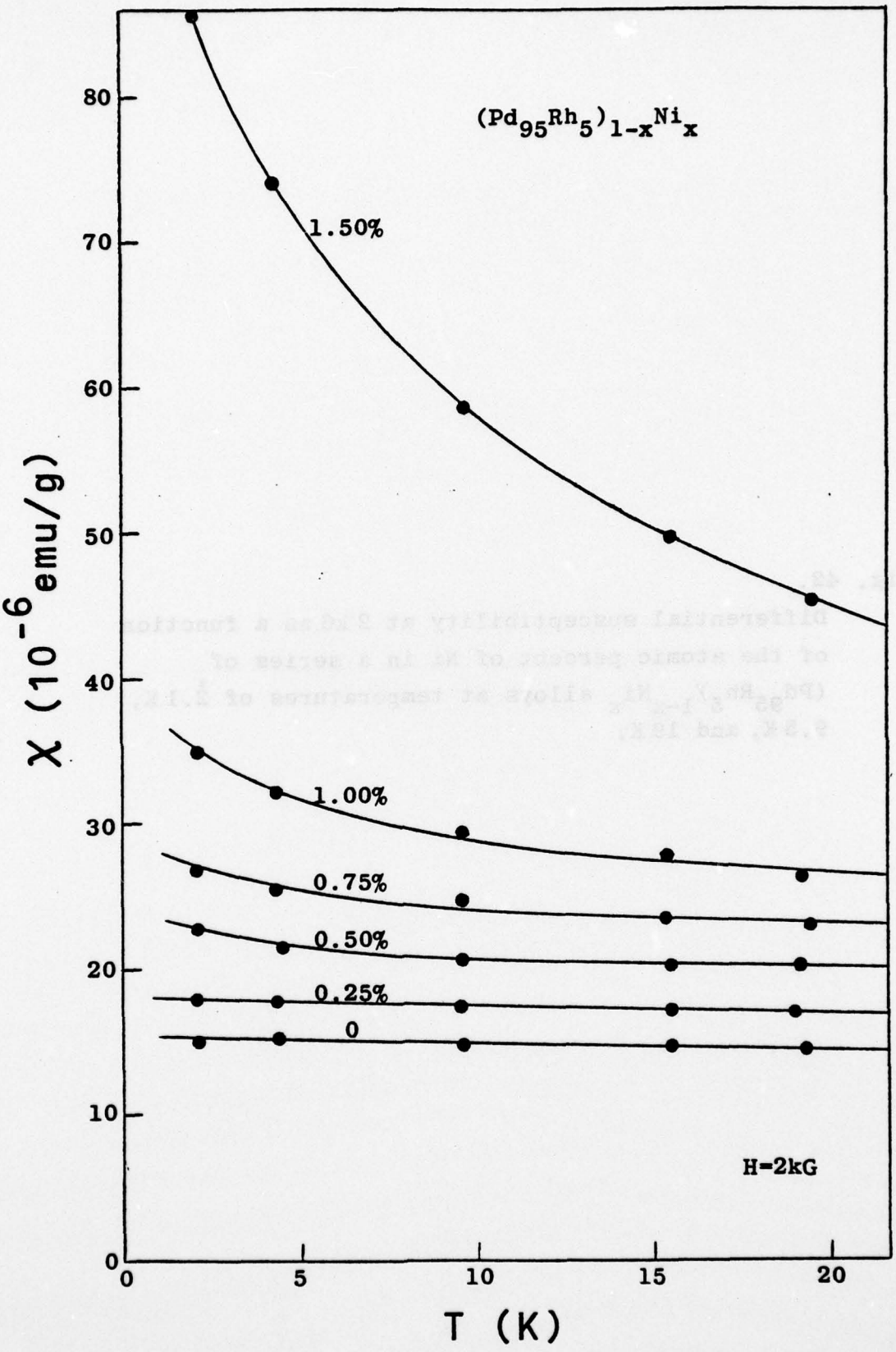

$(Pd_{95}Rh_5)_{1-x}Ni_x$
1.50%
1.00%
0.75%
0.50%
0.25%
0
H=2kG
χ (10^{-6} emu/g)
T (K)
0
10
20
30
40
50
60
70
80
0
5
10
15
20



Fig. 42.

Differential susceptibility at 2 kG as a function of the atomic percent of Ni in a series of $(Pd_{95}Rh_5)_{1-x}Ni_x$ alloys at temperatures of 2.1 K, 9.5 K, and 19 K.

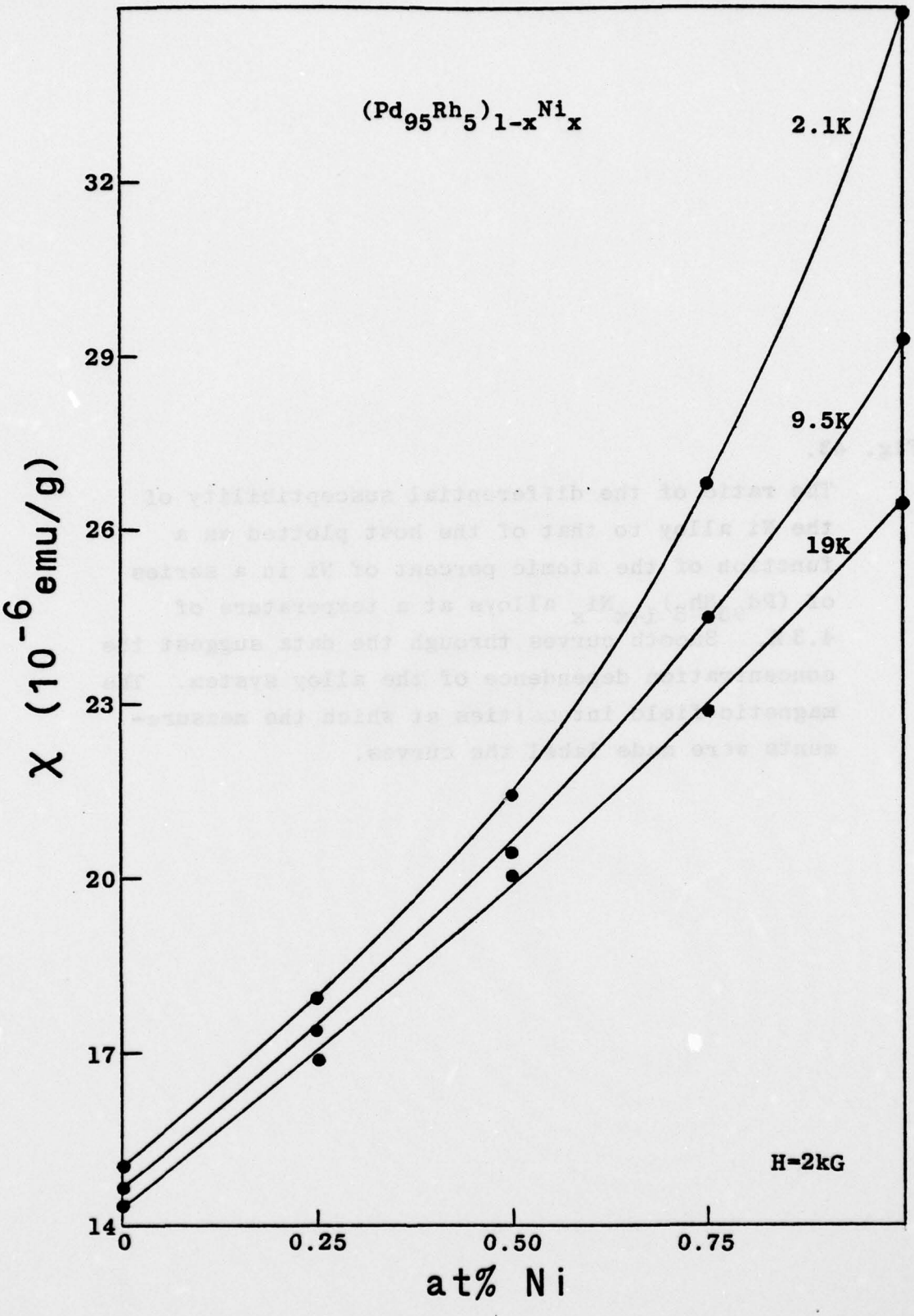
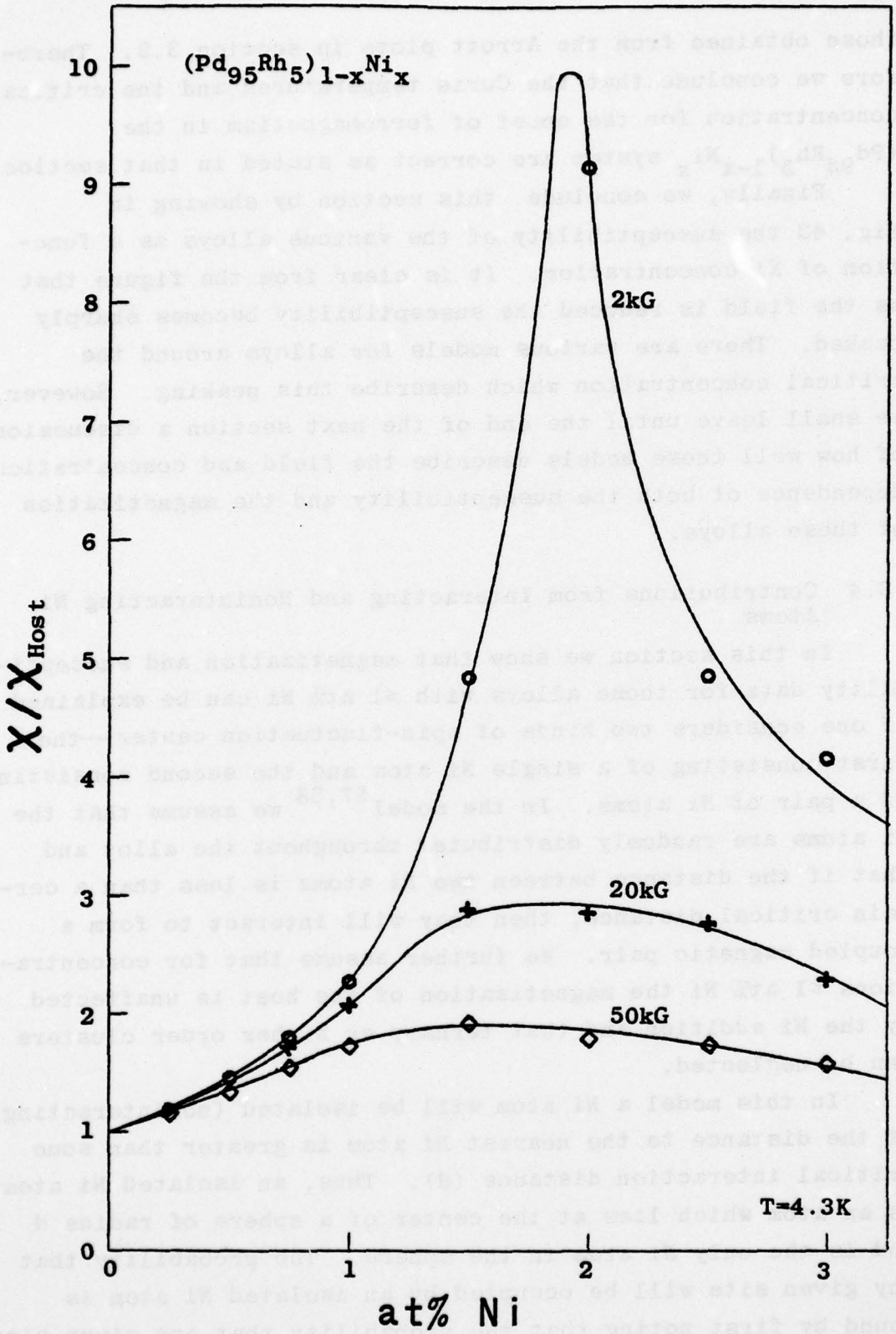

$(Pd_{95}Rh_5)_{1-x}Ni_x$
2.1K
9.5K
19K
H=2kG
χ (10^{-6} emu/g)
32
29
26
23
20
17
14
0
0.25
0.50
0.75
at% Ni

Fig. 43.

The ratio of the differential susceptibility of the Ni alloy to that of the host plotted as a function of the atomic percent of Ni in a series of $(Pd_{95}Rh_5)_{1-x}Ni_x$ alloys at a temperature of 4.3 K. Smooth curves through the data suggest the concentration dependence of the alloy system. The magnetic field intensities at which the measurements were made label the curves.


$(Pd_{95}Rh_5)_{1-x}Ni_x$
2kG
20kG
50kG
T=4.3K
χ/χ_{Host}
at% Ni
0
1
2
3
4
5
6
7
8
9
10

those obtained from the Arrott plots in section 3.2. Therefore we conclude that the Curie temperatures and the critical concentration for the onset of ferromagnetism in the $(Pd_{95}Rh_5)_{1-x}Ni_x$ system are correct as stated in that section.

Finally, we conclude this section by showing in Fig. 43 the susceptibility of the various alloys as a function of Ni concentration. It is clear from the figure that as the field is reduced the susceptibility becomes sharply peaked. There are various models for alloys around the critical concentration which describe this peaking. However, we shall leave until the end of the next section a discussion of how well these models describe the field and concentration dependence of both the susceptibility and the magnetization of these alloys.

3.4 Contributions from Interacting and Noninteracting Ni Atoms

In this section we show that magnetization and susceptibility data for those alloys with ≤1 at% Ni can be explained if one considers two kinds of spin-fluctuation center—the first consisting of a single Ni atom and the second consisting of a pair of Ni atoms. In the model[57,58] we assume that the Ni atoms are randomly distributed throughout the alloy and that if the distance between two Ni atoms is less than a certain critical distance, then they will interact to form a coupled magnetic pair. We further assume that for concentrations ≤1 at% Ni the magnetization of the host is unaffected by the Ni addition and that ternary or higher order clusters can be neglected.

In this model a Ni atom will be isolated (noninteracting) if the distance to the nearest Ni atom is greater than some critical interaction distance (d). Thus, an isolated Ni atom is an atom which lies at the center of a sphere of radius d and is the only Ni atom in the sphere. The probability that any given site will be occupied by an isolated Ni atom is found by first noting that the probability that any given site

will be occupied by a Ni atom is equal to the concentration of Ni atoms, c, and correspondingly the probability that any given site will be occupied by an atom other than Ni is equal to 1-c. Thus, the probability that the site is occupied by an isolated Ni atom is $c(1-c)^n$, where n is one less than the number of atoms within the interaction sphere mentioned above. The total number of isolated Ni atoms in a gram of alloy can be written as

$$N_1 = \frac{N_A}{W_M} c(1-c)^n , \qquad (3.4)$$

where the number of sites in a gram is Advogadro's number, N_A, divided by the molar weight of the alloy, W_M.

The probability that there will be a Ni atom at any given site and only one other Ni atom in the interaction sphere centered at the site is $nc^2(1-c)^{n-1}$. The factor n comes from the fact that there are n possible sites for the second Ni atom. The number of Ni atoms coupled to form pairs in a gram of alloy is

$$N_2 = \frac{N_A}{W_M} nc^2(1-c)^{n-1} . \qquad (3.5)$$

The number of Ni atoms remaining (coupled into clusters of three or more Ni atoms) in the gram is then

$$N_R = \frac{N_A}{W_A} c - N_1 - N_2 . \qquad (3.6)$$

For small concentrations of Ni atoms we can approximate N_1 and N_2 by keeping only the leading term in the concentration, yielding

$$N_1 \simeq \frac{N_A}{W_M} c , \qquad (3.7a)$$

and

$$N_2 \simeq \frac{N_A}{W_M} nc^2 . \qquad (3.7b)$$

Thus, we expect the contribution to the magnetization of isolated Ni atoms to be approximately proportional to c and

the contribution of Ni pairs to be approximately proportional to c^2. We write the total magnetization as

$$M = M_0 + M_1 c + M_2 c^2 \quad , \tag{3.8}$$

where M_0 is the magnetization of the host, M_1 is proportional to the magnetization of a single isolated Ni atom, and M_2 is proportional to the magnetization of an isolated pair of interacting Ni atoms.

Rewriting the above equation as

$$\frac{\Delta M}{c} = M_1 + M_2 c \tag{3.9}$$

yields an equation linear in c. In Fig. 44, we look for the above relation by plotting $\Delta M/c$ as a function of the atomic percent Ni in the alloys. Least squares fitting of this equation to the data yields M_1 and M_2 at the various fields. As can be seen from the figure, the above equation yields a good representation of the data.

In a similar manner, the contributions to the susceptibility from the isolated Ni atoms and the Ni atom pairs can be found by writing the total susceptibility as

$$\chi = \chi_0 + \chi_1 c + \chi_2 c^2 \quad , \tag{3.10}$$

where χ_0 is the susceptibility of the host, χ_1 is proportional to the susceptibility of an isolated Ni atom,and χ_2 is proportional to the susceptibility of an isolated pair of interacting Ni atoms. In Figs. 45 and 46, we show the fit of this equation to the data by plotting $\Delta\chi/c$ as a function of the atomic percent of Ni in the alloys.

In the above analysis the magnetization and susceptibility of each alloy host were determined in the following manner: Although only two host compositions ($Pd_{95.0}Rh_{5.0}$ and $Pd_{94.8}Rh_{5.2}$) were measured, the fact that the magnetic properties of these alloys[59,50] are relatively insensitive to the small variations in Rh content that occurred in the hosts (see table 1) made it easy to determine the appropriate values to use to represent any of the hosts. For the 2 kG data, where the differences between the susceptibility of

the two measured hosts slightly exceeds the estimated errors, we linearly interpolated to obtain the values for the other hosts. For the higher fields, where the measured differences were insignificant, we used the more accurate measurements of the $Pd_{95.0}Rh_{5.0}$ host to represent all the hosts.

In the next three figures we show the results of the analysis. In the upper half of Fig. 47 we show the temperature dependence of the susceptibility for the isolated Ni atoms, and in the lower graph of this figure we show the temperature dependence of the reciprocal of the susceptibility for the isolated Ni pairs. In contrast to the temperature independent susceptibility seen for the isolated Ni atom, the susceptibility of a Ni pair is seen to be strongly temperature dependent in the measured range. The straight line through the data in the lower graph shows that the susceptibility of a Ni pair is reasonably well described by Curie-Weiss behavior (χ_2^{-1} proportional to $T-\theta$) with $\theta \sim -4\frac{1}{2}$ K. The small magnitude of θ is an indication[58] of a local spin fluctuation with a low spin fluctuation temperature (see section 1.12 for a definition of the spin-fluctuation temperature). In contrast to the low spin-fluctuation temperature of a Ni pair, the temperature independence found for the susceptibility of the isolated Ni atoms indicates that these atoms have a much higher spin-fluctuation temperature. In a later section we will use the resistivity data to determine the spin-fluctuation temperature for both the isolated Ni atom and the isolated Ni pair.

In Fig. 48, we show the field dependence of the susceptibility for the isolated Ni atoms (upper graph) and the isolated Ni pairs (lower graph). The susceptibility of the Ni pair is found to be more field dependent than the isolated Ni atom. This is consistent with our previous conclusion that a Ni pair has a lower spin-fluctuation temperature.

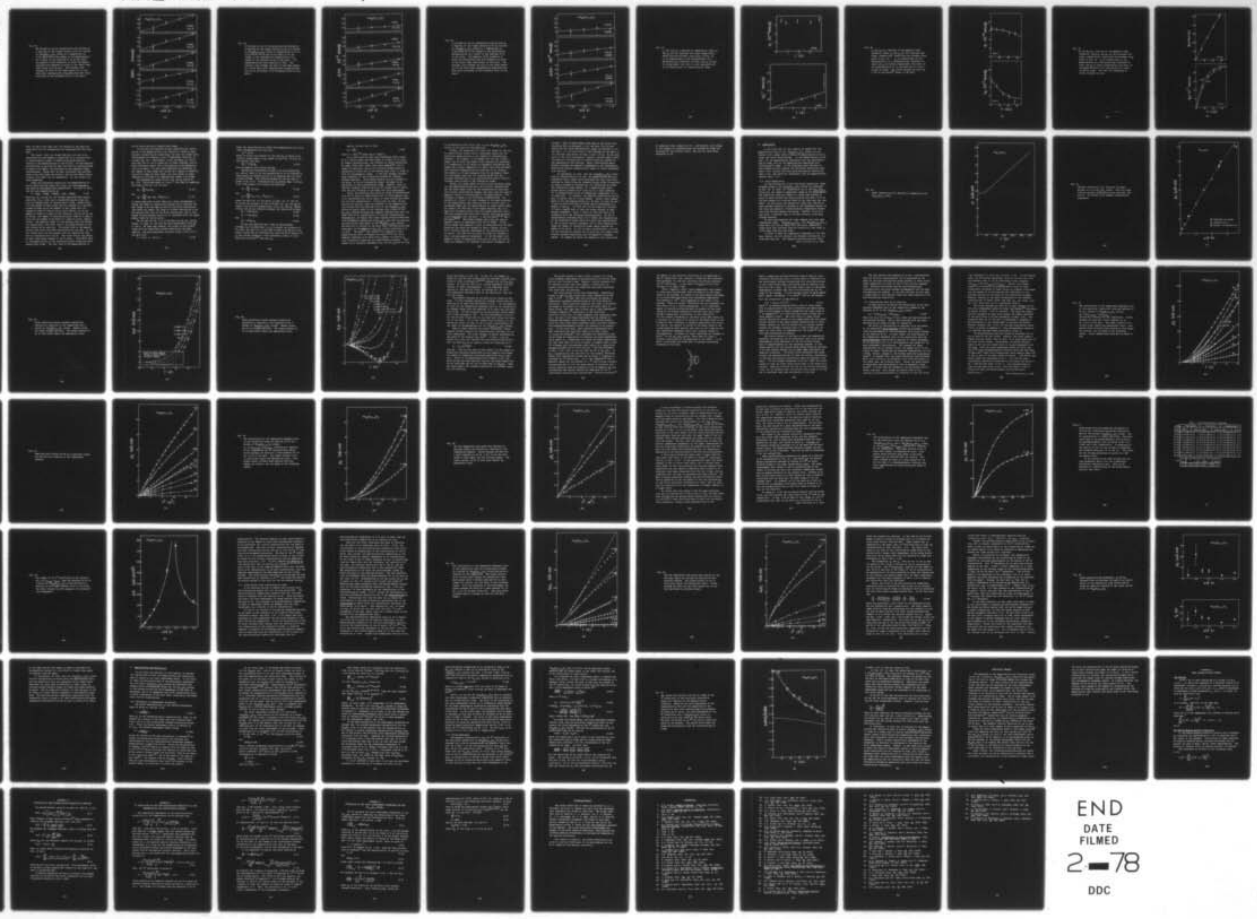
Schulz[60] has extended the local enhancement model of Lederer and Mills to include the field dependence of the

(text continues on p. 200)

AD-A049 154 NAVAL RESEARCH LAB WASHINGTON D C F/G 20/3
SPIN FLUCTUATIONS AND THE PARAMAGNETIC-FERROMAGNETIC TRANSITION--ETC(U)
OCT 77 D J GILLESPIE

UNCLASSIFIED NRL-MR-3630 SBIE-AD-E000 056 NL

3 OF 3
AD A049154



END
DATE FILMED
2-78
DDC

Fig. 44.

ΔM divided by the Ni concentration and plotted as a function of the atomic percent of Ni in a series of $(Pd_{95}Rh_5)_{1-x}Ni_x$ alloys at a temperature of 4.3 K, where ΔM is the change in the magnetization as a result of the addition of Ni to the alloy. The magnetic field intensity at which the magnetizations were measured is given in the lower right hand corner of each plot. The straight line through the data is the least square fit to the data after appropriately weighting each data point according to the estimated error in the point.

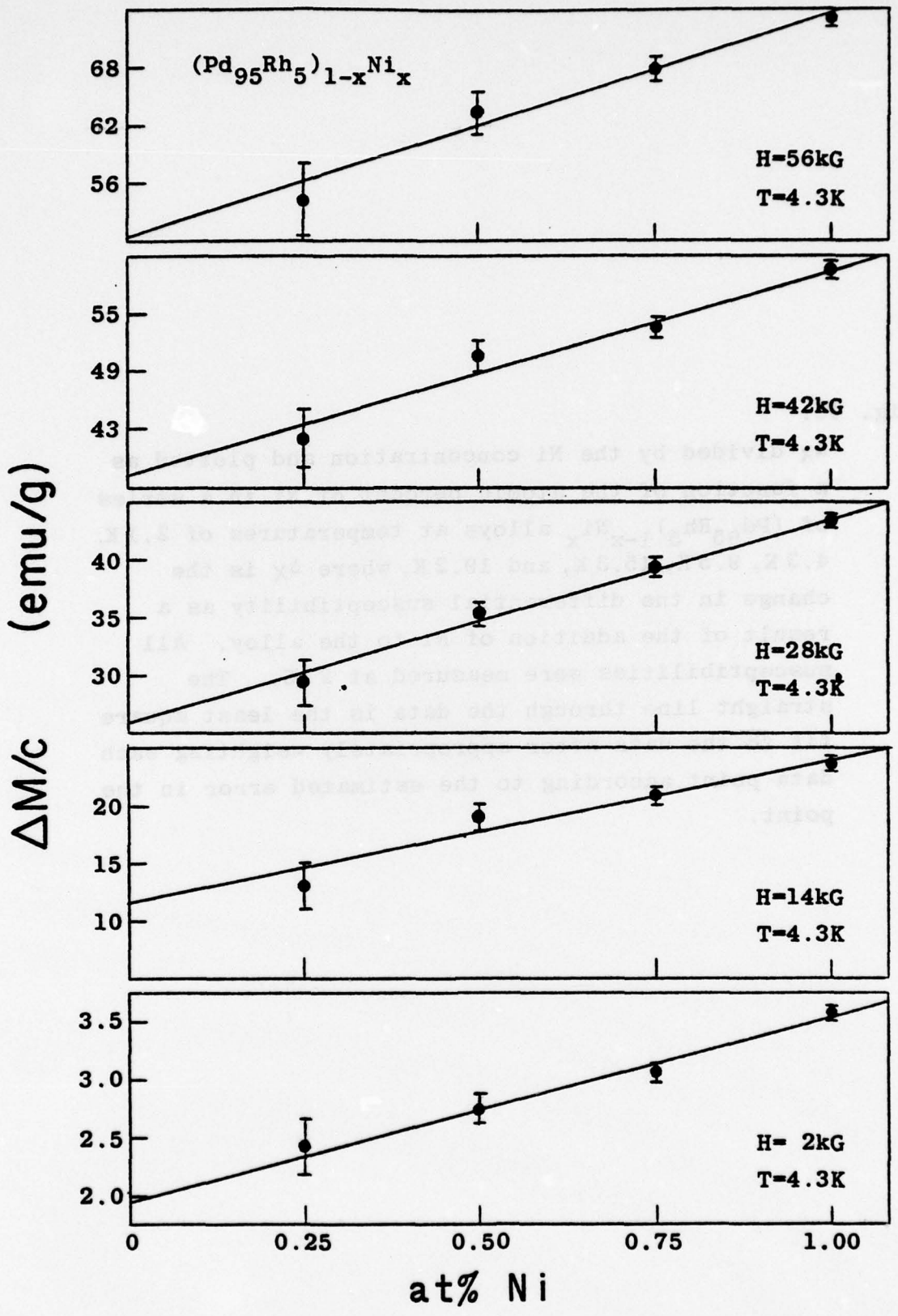

$(Pd_{95}Rh_5)_{1-x}Ni_x$
H=56kG
T=4.3K
H=42kG
T=4.3K
H=28kG
T=4.3K
H=14kG
T=4.3K
H= 2kG
T=4.3K
ΔM/c (emu/g)
at% Ni
68
62
56
55
49
43
40
35
30
20
15
10
3.5
3.0
2.5
2.0
0
0.25
0.50
0.75
1.00

Fig. 45.

$\Delta\chi$ divided by the Ni concentration and plotted as a function of the atomic percent of Ni in a series of $(Pd_{95}Rh_5)_{1-x}Ni_x$ alloys at temperatures of 2.1 K, 4.3 K, 9.5 K, 15.3 K, and 19.2 K, where $\Delta\chi$ is the change in the differential susceptibility as a result of the addition of Ni to the alloy. All susceptibilities were measured at 2 kG. The straight line through the data is the least square fit to the data after appropriately weighting each data point according to the estimated error in the point.

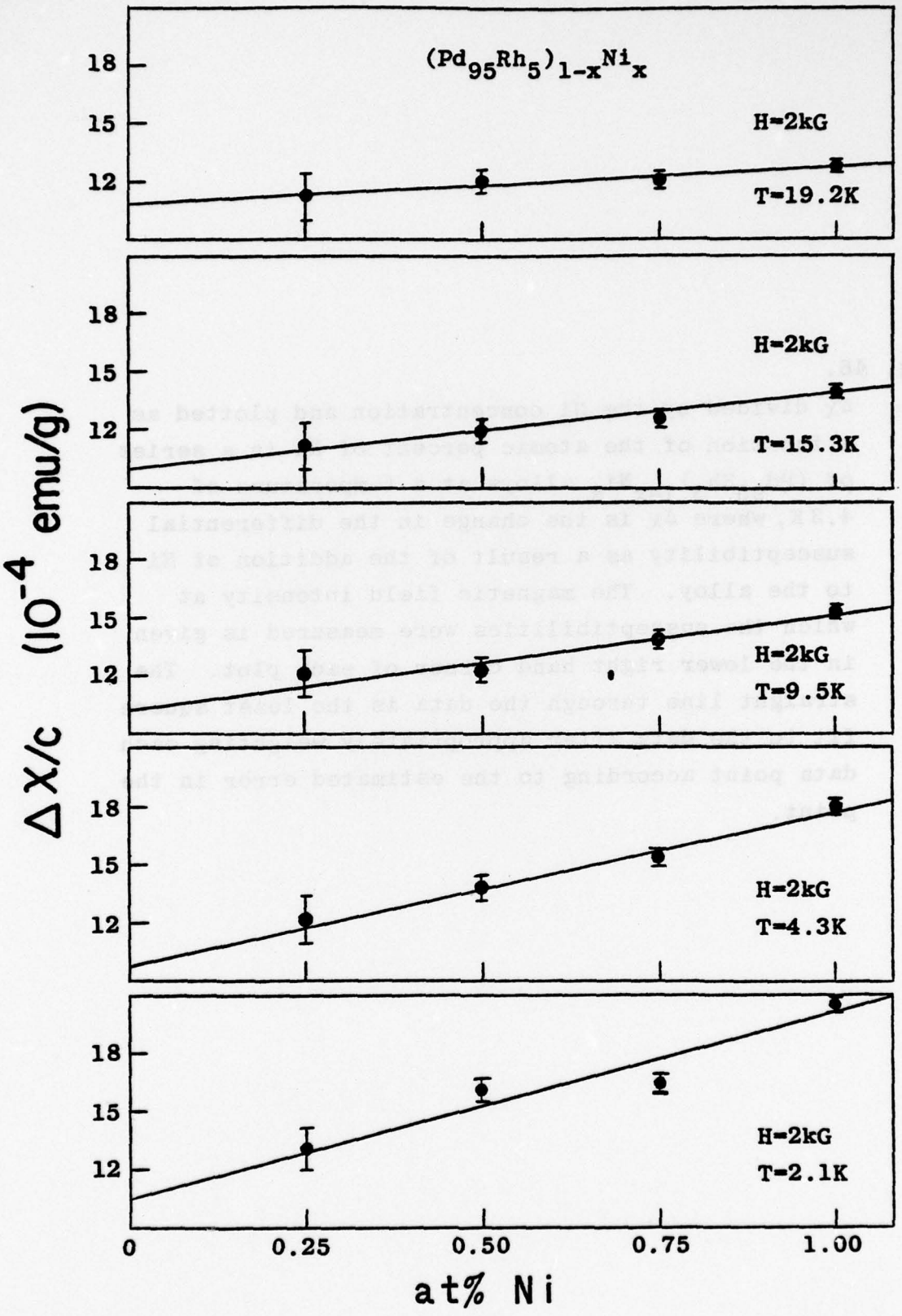

$(Pd_{95}Rh_5)_{1-x}Ni_x$
H=2kG
T=19.2K
H=2kG
T=15.3K
H=2kG
T=9.5K
H=2kG
T=4.3K
H=2kG
T=2.1K
18
15
12
0
0.25
0.50
0.75
1.00
at% Ni
$\Delta\chi/c$ $(10^{-4}$ emu/g)

Fig. 46.

$\Delta\chi$ divided by the Ni concentration and plotted as a function of the atomic percent of Ni in a series of $(Pd_{95}Rh_5)_{1-x}Ni_x$ alloys at a temperature of 4.3 K, where $\Delta\chi$ is the change in the differential susceptibility as a result of the addition of Ni to the alloy. The magnetic field intensity at which the susceptibilities were measured is given in the lower right hand corner of each plot. The straight line through the data is the least square fit to the data after appropriately weighting each data point according to the estimated error in the point.

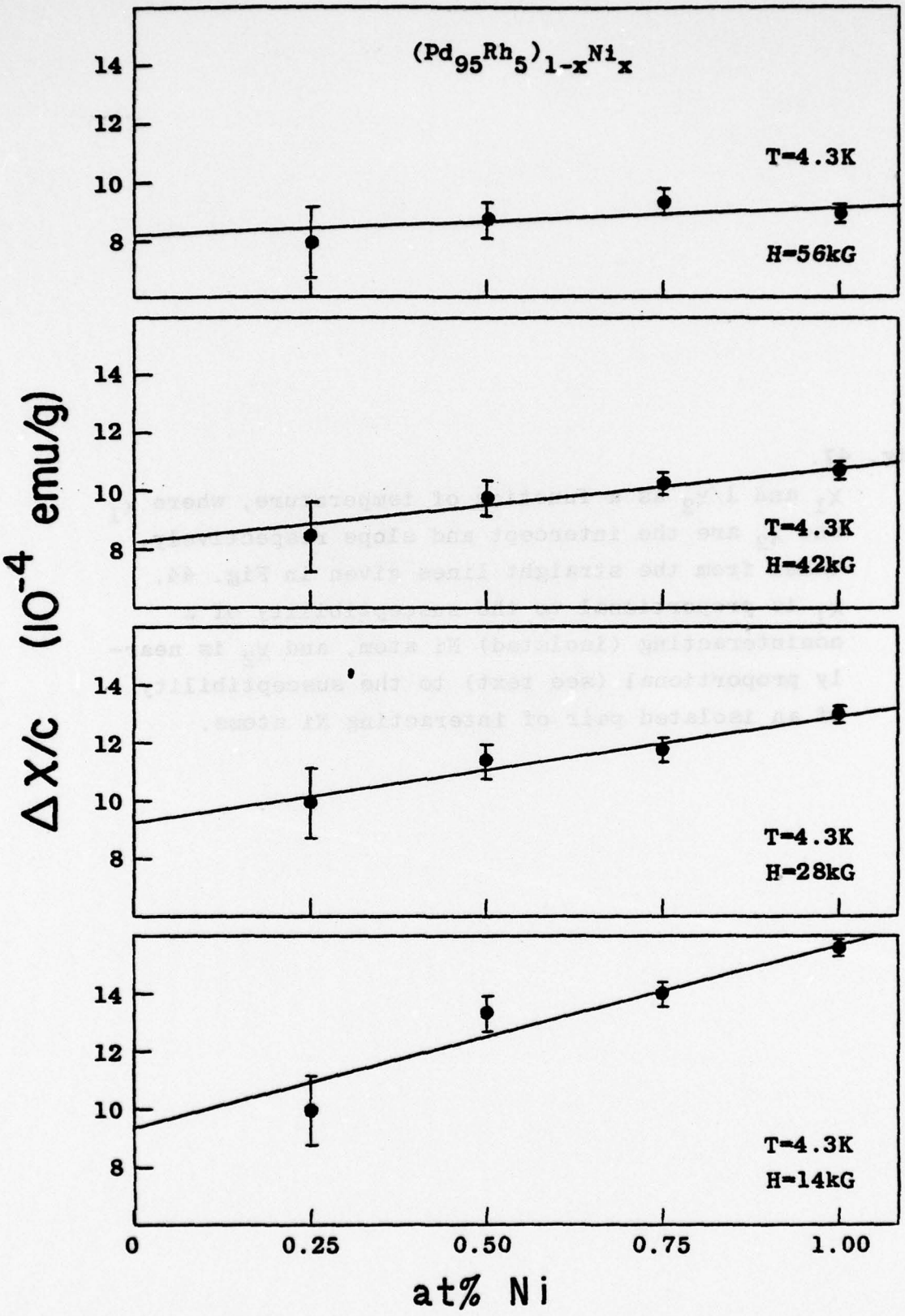
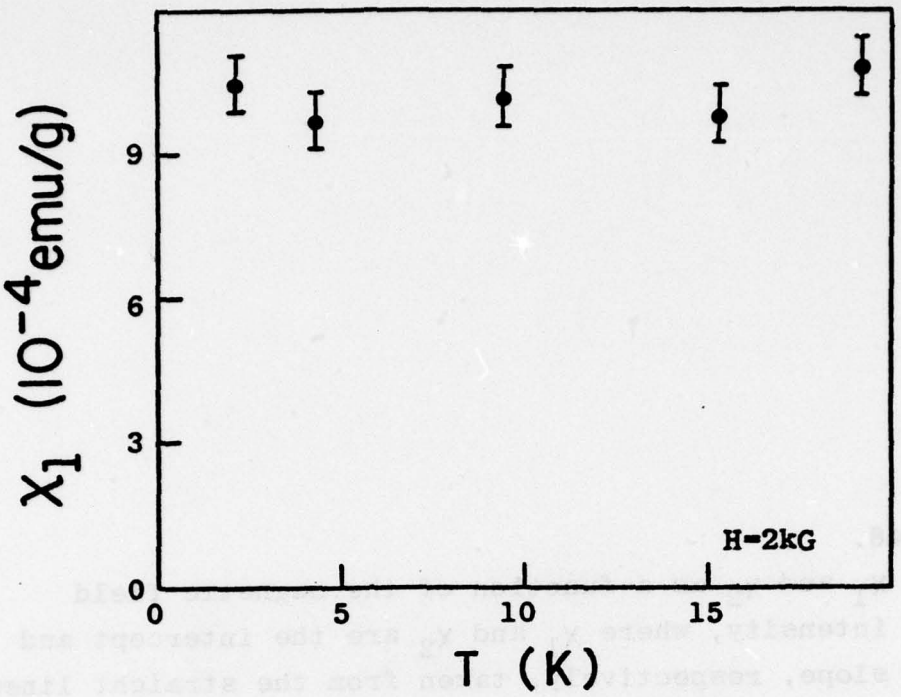

$(Pd_{95}Rh_5)_{1-x}Ni_x$
T=4.3K
H=56kG
T=4.3K
H=42kG
T=4.3K
H=28kG
T=4.3K
H=14kG
$\Delta\chi/c$ (10^{-4} emu/g)
14
12
10
8
0
0.25
0.50
0.75
1.00
at% Ni

Fig. 47.

χ_1 and $1/\chi_2$ as a function of temperature, where χ_1 and χ_2 are the intercept and slope respectively, taken from the straight lines given in Fig. 44. χ_1 is proportional to the susceptibility of a noninteracting (isolated) Ni atom, and χ_2 is nearly proportional (see text) to the susceptibility of an isolated pair of interacting Ni atoms.


χ_1 (10^{-4}emu/g)
9
6
3
0
0
5
10
15
T (K)
H=2kG

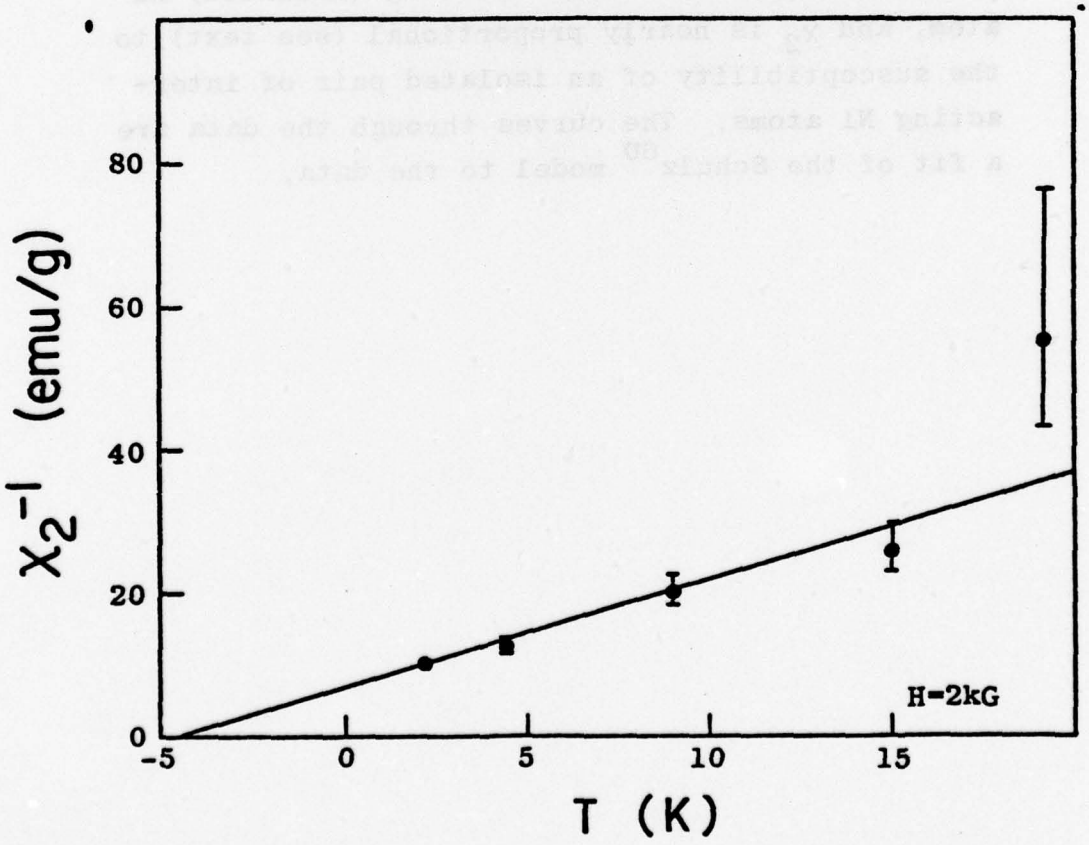

χ_2^{-1} (emu/g)
80
60
40
20
0
-5
0
5
10
15
T (K)
H=2kG

Fig. 48.

χ_1 and χ_2 as a function of the magnetic field intensity, where χ_1 and χ_2 are the intercept and slope, respectively, taken from the straight lines given in Fig. 45. χ_1 is proportional to the susceptibility of a noninteracting (isolated) Ni atom, and χ_2 is nearly proportional (see text) to the susceptibility of an isolated pair of interacting Ni atoms. The curves through the data are a fit of the Schulz[60] model to the data.

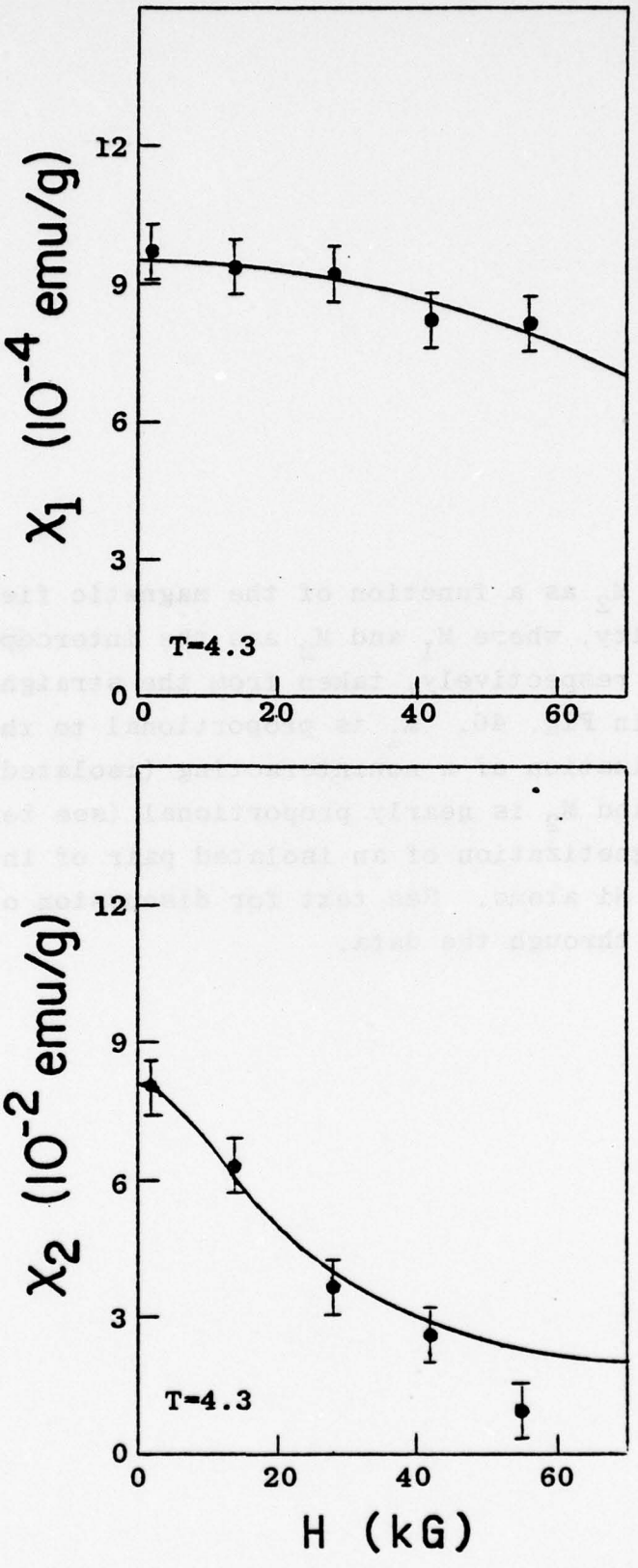
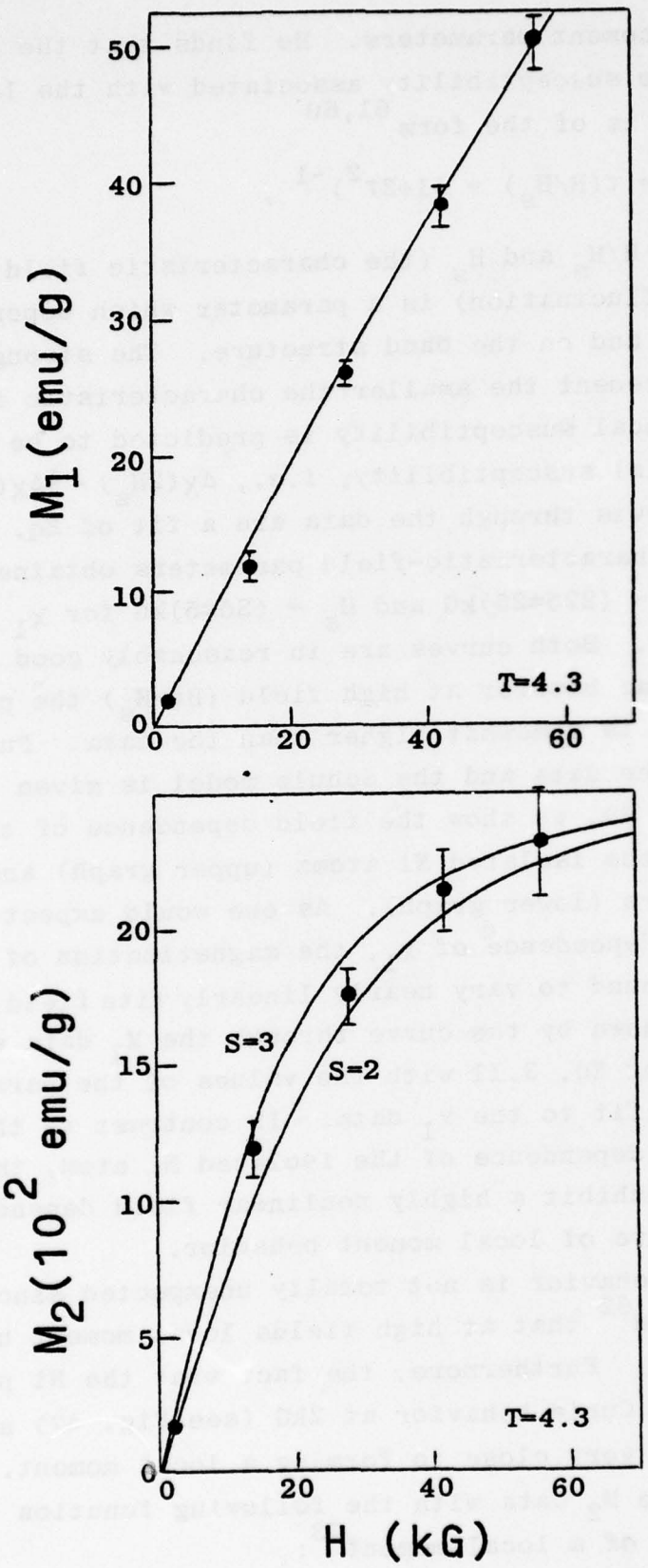

12
9
6
3
0
χ_1 (10^{-4} emu/g)
T=4.3
0
20
40
60
12
9
6
3
0
χ_2 (10^{-2} emu/g)
T=4.3
0
20
40
60
H (kG)

Fig. 49.

M_1 and M_2 as a function of the magnetic field intensity, where M_1 and M_2 are the intercept and slope, respectively, taken from the straight lines given in Fig. 46. M_1 is proportional to the magnetization of a noninteracting (isolated) Ni atom, and M_2 is nearly proportional (see text) to the magnetization of an isolated pair of interacting Ni atoms. See text for discussion of curves through the data.


50
40
30
20
10
0
M_1(emu/g)
T=4.3
0
20
40
60
20
15
10
5
0
$M_2(10^2$ emu/g)
S=3
S=2
T=4.3
0
20
40
60
H (kG)

local enhancement parameters. He finds that the field dependence of the susceptibility associated with the local enhancement is of the form[61,60]

$$\frac{\Delta\chi(H)}{\Delta\chi(0)} = f(H/H_s) = (1+3\tau^2)^{-1} , \qquad (3.11)$$

where $\tau+\tau^3 = H/H_s$ and H_s (the characteristic field of the local spin fluctuation) is a parameter which depends on the enhancement and on the band structure. The stronger the local enhancement the smaller the characteristic field. When $H=2H_s$ the local susceptibility is predicted to be $\frac{1}{4}$ as large as the initial susceptibility, i.e., $\Delta\chi(2H_s) = \frac{1}{4}\Delta\chi(0)$.

The curves through the data are a fit of Eq. 3.11 to the data. The characteristic-field parameters obtained from the fits are H_s = (225±25)kG and H_s = (35±5)kG for χ_1 and χ_2, respectively. Both curves are in reasonably good agreement with the data; however at high field ($H>>H_s$) the prediction of the model is somewhat higher than the data. Further discussion of the data and the Schulz model is given in Sect. 3.9.

In Fig. 49, we show the field dependence of the magnetization for the isolated Ni atoms (upper graph) and the isolated Ni pairs (lower graph). As one would expect from the small field dependence of χ_1, the magnetization of an isolated Ni atom is found to vary nearly linearly with field. The field dependence shown by the curve through the M_1 data was obtained by integrating Eq. 3.11 with the values of the parameters given by the fit to the χ_1 data. In contrast to this nearly-linear field dependence of the isolated Ni atom, the Ni pair is found to exhibit a highly nonlinear field dependence, somewhat suggestive of local moment behavior.

Such a behavior is not totally unexpected since it has been suggested[62] that at high fields local moment behavior will be found. Furthermore, the fact that the Ni pairs display nearly a Curie behavior at 2kG (see Fig. 47) suggests that they are very close to forming a local moment. Thus, we try to fit the M_2 data with the following function for the magnetization of a local moment[63]:

$$M_2 c^2 = \tfrac{1}{2} N_2 g S \mu_B B_S(x) \ ,$$

where (3.12)

$$x = g S \mu_B H / k_B T \ ,$$

where $\frac{1}{2}N_2$ is the number of Ni pairs per gram, g is the Lande' g factor, S is the effective spin, μ_B is the Bohr magneton, $B_S(x)$ is the Brillouin function, and k_B is Boltzmann's constant.

In fitting the data we use Eq. 3.7b for N_2 and take g=2. The fitting parameters are then S and n. We start by choosing 2500 emu/g for the saturation value of M_2. Thus,

$$\frac{N_A}{W_M} n S \mu_B = 2500 \ , \text{ or } nS = 47. \qquad (3.13a)$$

Since S will be largest at saturation, this equation sets an upper limit on S. A similar expression which sets a lower limit on S can be found by expanding $B_S(x)$ in Eq. 3.12 to first order in x and by evaluating the expression for M_2 at H=2 kG and at T=4.3 K. Then,

$$\frac{2N_A n S(S+1)\mu_B^2}{3W_M k_B} = 0.34 \ , \text{ or } nS(S+1) = 140. \qquad (3.13b)$$

Combining Eqs. 3.13a and 3.13b yields S>2 and n<24. For a Ni atom to be isolated, at least the nearest neighbors must all be host atoms; thus for face centered cubic systems, such as we have here, n>12. So finally,

$$S = 2\tfrac{1}{2} \pm \tfrac{1}{2} \ ; \quad n = 18 \pm 6 \ . \qquad (3.14)$$

It is of interest to note that since there are a total of 18 nearest and next-nearest neighbors in a f.c.c. system, n~18 implies that the two Ni atoms interact to form a coupled pair if they are either nearest or next-nearest neighbors. For the interaction to extend to third-nearest neighbors requires n=42.

In the lower half of Fig. 49, we show the fit to the data for S=2 and S=3. We find that S=$2\frac{1}{2}$ and n=18 give the best fit to the data and that the fit is reasonably good. However, before we can say the model is consistent with the

data, we must first show that the results of the model are consistent with the assumptions and approximations that were made.

The result (that the values $S=2\frac{1}{2}$ and n=18 are to be associated with the magnetic properties of an isolated pair of interacting Ni atoms) is based on M_2 being directly related to the magnetization of the Ni pair. We had expected contributions to M_2 from the host and from the noninteracting Ni atoms to be small, and therefore we had neglected these contributions. Using n=18, we have calculated the contributions to M_2 from these two sources, and we find these contributions to be small but not negligible. We now correct for these omissions.

Since the calculated results for the magnetization of the Ni pairs and the values of S and n are interdependent, they must be determined self-consistently. We start by writing the total magnetization as

$$M = N_0M_0' - nN_1M_0' - an'N_2M_0' + N_1M_1' + \tfrac{1}{2}N_2M_2' , \qquad (3.15)$$

where M_0', M_1', and M_2' are the average magnetizations associated with a host atom, with a noninteracting Ni atom, and with an isolated pair of interacting Ni atoms, respectively; n' is the number of host atoms that are coupled to a noninteracting Ni atom, an' is the number of host atoms that are coupled to each Ni atom in the Ni pair ($\frac{1}{2}<a<1$), N_0 is the number of atoms in a gram of host material, and N_1 and N_2 are, as before, the number of noninteracting Ni atoms in a gram of alloy and the number of Ni pairs in a gram of alloy, respectively. The separate terms in this equation have the following significance: The first term is the magnetization of the host before the Ni addition. The second term is the magnetization that would have been associated with the host if the host atoms which are now coupled with the isolated Ni atom had not interacted with the Ni. The third term is the result of host atoms being coupled to the Ni pairs. The fourth term is the magnetization of the noninteracting Ni atoms and their coupled host atoms. The last term is the magnetization of

the Ni pairs and their coupled host atoms.

In writing this equation we have neglected any contribution to the magnetization from clusters of three or more mutually interacting Ni atoms since the data for alloys with ≤1% Ni showed no evidence of any c^3 dependence (see Fig. 44 through Fig. 46). Furthermore, using the model, we calculate that ≤1% of the Ni atoms are in these clusters, and we would therefore expect their contribution to the magnetization to be small. We have also neglected the reduction in the number of host atoms that occurs as a result of substitution of Ni atoms for host atoms, but this effect is small compared to the effect of coupling host atoms to Ni atoms.

By expanding N_1 (given by Eq. 3.4) and N_2 (given by Eq. 3.5), collecting terms in c and c^2, and then by comparing the result with Eq. 3.8, we find

$$M_1' = \frac{W_M}{N_A}(M_1+nM_0) \quad , \tag{3.16}$$

and

$$M_2' = \frac{2W_M}{nN_A}\{M_2 + nM_1 - n^2M_0(2-a)\} \quad . \tag{3.17}$$

In these equations we have taken n′=n, which corresponds to taking the range of interaction between the Ni atom and the host atoms to be the same as that of the Ni-Ni interaction. (One would not expect the range of Ni-host interaction to be any greater than that of the Ni-Ni interaction, and it also cannot be much smaller and still be consistent with the large moment found for the Ni pair).

We can now fit Eq. 3.17 to the data for M_0, M_1, and M_2 (given in Figs. 17 and 49) and self-consistently find M_2', S, and n. We take $a=\frac{3}{4}$; however, any value in the allowed range ($\frac{1}{2}<a<1$) would have yielded essentially the same results. The self-consistent analysis yields a best fit to the data with

$$S = 2 \pm \tfrac{1}{2}; \quad n = 30 \pm 12 \quad , \tag{3.18}$$

where the uncertainties in these two parameters are not to be taken independently but such that

$$nS = 60 \pm 5.$$

Since to within the accuracy of the data M_2' is found to be directly proportional to M_2 (shown in Fig. 49), we will not plot M_2' but note that

$$M_2' \simeq (8/N_A)M_2 \qquad (3.19)$$

and is slightly less curved than M_2.

Having self-consistently found n, we can evaluate M_1', χ_1', and χ_2', where χ_1' is the susceptibility of an isolated Ni atom and χ_2' the susceptibility of an isolated pair of interacting Ni atoms. The relation between M_1' and the data is given in Eq. 3.16. Differentiating M_1' and M_2' (Eqs. 3.16 and 3.17) with respect to H yields the relations

$$\chi_1' = \frac{W_M}{N_A}(\chi_1 + n\chi_0) \ , \qquad (3.20)$$

and

$$\chi_2' = \frac{2W_M}{nN_A}\{\chi_2 + n\chi_1 - n^2\chi_0(2-a)\} \ , \qquad (3.21)$$

where the data for χ's are given in Figs. 40, 47, and 48. To within the accuracy of the 4.2 K data, M_1', χ_1', and χ_2' are found to be directly proportional to M_1, χ_1, and χ_2, respectively, and we can therefore express the results as follows:

$$M_1' = (150/N_A)M_1 \ , \qquad (3.22)$$

$$\chi_1' = (150/N_A)\chi_1 \ , \qquad (3.23)$$

and

$$\chi_2' \simeq (8/N_A)\chi_2 \ . \qquad (3.24)$$

In the last equation the $\simeq$ sign is used because, although χ_2' is proportional to χ_2 to within the accuracy of the data, the best fit to the data yielded a χ_2' which at the higher fields did not decrease with field quite as rapidly as χ_2 and thereby displays a field dependence closer to that predicted by Schulz[60] than does χ_2.

Lastly, we note that at 2 kG

$$\chi_2' = \frac{C}{T-\theta} \quad , \tag{3.25}$$

where $C = \sim 5 \times 10^{-24}$ emu-K and $\theta = -5\frac{1}{2} \pm 1$ K.

Up to this point we have been discussing those alloys with ≤1 at% Ni, where the above model is likely to be valid. At higher concentrations, the clusters of three interacting Ni atoms, which most likely form local moments[58], can no longer be neglected, and as the critical concentration is approached at least one of two effects must occur in order to form the ferromagnetic phase: 1) the host becomes increasingly enhanced, 2) the interaction between Ni clusters becomes important. Since these effects are not included in the model, we do not necessarily expect the model to be applicable in this concentration range. However, there is indirect evidence from the data on the alloys with >1 at% Ni that the main features of the model are still applicable.

First, the effective spin which we found to be associated with the Ni pairs in those alloys with ≤1 at% Ni appears also to be associated with the Ni pairs in those alloys just above the critical concentration. To see this, we note, as was pointed out earlier, that the increase in the magnetization that occurs with the addition of Ni in the $(Pd_{95}Rh_5)_{1-x}Ni_x$ system is nearly equal to the increase that occurs in the $Pd_{1-x}Ni_x$ system—provided one compares samples which have the same ratio of Ni concentration to critical concentration. Consequently, we expect that those results which are concerned with the magnetic properties of $Pd_{1-x}Ni_x$ near the critical concentration will also apply to the $(Pd_{95}Rh_5)_{1-x}Ni_x$ system. One such set of results is the data from a neutron-scattering experiment on ferromagnetic $Pd_{1-x}Ni_x$ alloys containing 3 to 5 at% Ni. The data[55] were found to be consistent with a magnetization which is largely the result[64] of the ferromagnetic ordering of Ni pairs with a moment of $4.6 \pm 1.6\ \mu_B$ (the isolated Ni atoms are not significantly ordered). This number is in excellent agreement with the $5 \pm 1\ \mu_B$ which we find

to be associated with the Ni pair in the $(Pd_{95}Rh_5)_{1-x}Ni_x$ alloys at the lower Ni concentrations.

Second, the parameters (S~2 and n~30) found for the low Ni concentration alloys yield a reasonable result for the saturation magnetization at the highest Ni concentration measured. For example, if we assume that for the 3 at% Ni sample the Ni pairs and higher order clusters are saturated at a temperature of 2 K (which is reasonable considering the sample has a Curie temperature of ~25 K), then from the model the saturation magnetization is predicted to be ~2 emu/g. This number is in good agreement with the M_s~3 emu/g found for this sample (see Fig. 39) considering we have not included contributions to M_s from band splitting or from an internal field acting on the isolated Ni atoms.

Lastly, the large amount of Arrott plot curvature found for the magnetization data near the critical concentration and the broad peaks found for the susceptibility data near the critical concentration suggest that more than one type of magnetic center is contributing to the magnetization. This statement is based on the following considerations. We pointed out in Sect. 3.2 that, because of the high curvature of the magnetization data when plotted on a Arrott plot, a successful model for the magnetization of these alloys could not neglect the $\nabla^2 M$ term in the Landau equation (Eq. 3.1). There are two models which solve the Landau equation with a $\nabla^2 M$ term included and which yield results that are in qualitative agreement with the data: a lattice model[64,65] and a CPA model[66,67]. Each model assumes that only one type of magnetic center is associated with the Ni atoms. In the lattice model this magnetic center is associated with Ni atom pairs, and the pairs are assumed to form a regular lattice with a lattice constant determined by the concentration of the pairs. The host and the other Ni atoms are assumed to form a uniform magnetic background. In the CPA model this magnetic center is associated with each Ni atom, and the Ni atoms are assumed to be randomly distributed throughout the

lattice. Both of these models show some of the Arrott plot curvature that is necessary to fit the data, but in both models the low field susceptibility peaks too sharply to fit the data, i.e. the half width at half maximum is too small to fit the data (see curves in Figs. 3 and 5 of Ref. 66 and data given in Fig. 43 of this report). However, neither model treats the case of a distribution of cluster sizes as proposed in the beginning of this section. Such a distribution would greatly increase the magnetic inhomogeneity and consequently would yield broader susceptibility peaks in closer agreeement with the data.

In conclusion, we find that for $(Pd_{95}Rh_5)_{1-x}Ni_x$ alloys with Ni concentration of ≤ 1 at% the magnetization data are consistent with a model which describes the local spin fluctuations in these alloys as centered around either an isolated Ni atom or around an isolated pair of interacting Ni atoms. The isolated Ni atoms exhibit (1) a magnetization which varies nearly linearly with field up to at least 56 kG and (2) a susceptibility which is temperature independent up to at least 20 K. In contrast, the behavior exhibited by the Ni pair is nearly that of a local moment. Using a local moment model to fit the magnetization of a Ni pair, we find the pair to have an effective spin of $S=2\pm\frac{1}{2}$ (which corresponds to a moment of $5\pm1\,\mu_B$). We find that two Ni atoms will interact to form a coupled pair if they are either nearest or next-nearest neighbors. Above 1 at% Ni, we find the data to be consistent with the following generalizations: As the Ni concentration increases from 1 to 3 at% Ni, the concentration of the isolated Ni atoms levels off while the concentration of the Ni pairs rapidly increases, but in this concentration range the number of isolated Ni atoms always exceeds the number of Ni pairs. At the critical concentration (~1.9 at% Ni) the interaction between the Ni pairs and the higher order clusters becomes significant and ferromagnetic alignment begins. At roughly $2\frac{1}{2}$ at% Ni, the moments on the interacting

Ni atoms are fully ordered at 4 K. And finally, even though at the highest Ni concentrations the isolated Ni atoms are polarized by the internal field, they are far from being saturated at 4 K.

B. Resistivity

In the first part of this chapter we showed that the magnetization data of the $(Pd_{95}Rh_5)_{1-x}Ni_x$ alloys are consistent with a model which divided the magnetization of each alloy into three contributions: (1) the magnetization of the host, (2) the magnetization associated with the noninteracting Ni atoms, and (3) the magnetization associated with interacting Ni atoms. In the following three sections of this chapter we will present the electrical resistivity data (Sect. 3.5), extract the local spin-fluctuation resistivity (Sect. 3.6), and check for consistency with the magnetization results (Sect. 3.7).

3.5 Total Resistivity

In this section all of the electrical resistivity measurements taken on the $(Pd_{95}Rh_5)_{1-x}Ni_x$ alloys are presented. In Fig. 50, we show the resistivity (ρ) of the $Pd_{95.0}Rh_{5.0}$ alloy over the complete temperature range of the measurements. The resistivity data are shown by a solid line instead of point by point because the high precision (see Sect. 2.4) of the data results in a scatter which is far less than the line width. On this scale the resistivity looks very typical—a high residual resistivity because of the disordered nature of the alloy and possibly a Bloch-Gruneisen temperature dependence from electron-phonon scattering. However, as we will see later, a detailed look at the data reveals a much more complex behavior.

We have also measured two other samples over this same temperature range: $(Pd_{95}Rh_5)_{99.9}Ni_{0.1}$ and $(Pd_{95}Rh_5)_{99.8}Ni_{0.2}$. These data will not be shown over the entire temperature range since they differed from the resistivity just shown by little more than the line width.

In order to show the temperature dependence of the data more clearly, we will subtract the residual resistivity (ρ_o) from each data set. The residual resistivities have been

(text continues on p. 220)

Fig. 50.

Total resistivity as a function of temperature for $Pd_{95.0}Rh_{5.0}$ alloy.

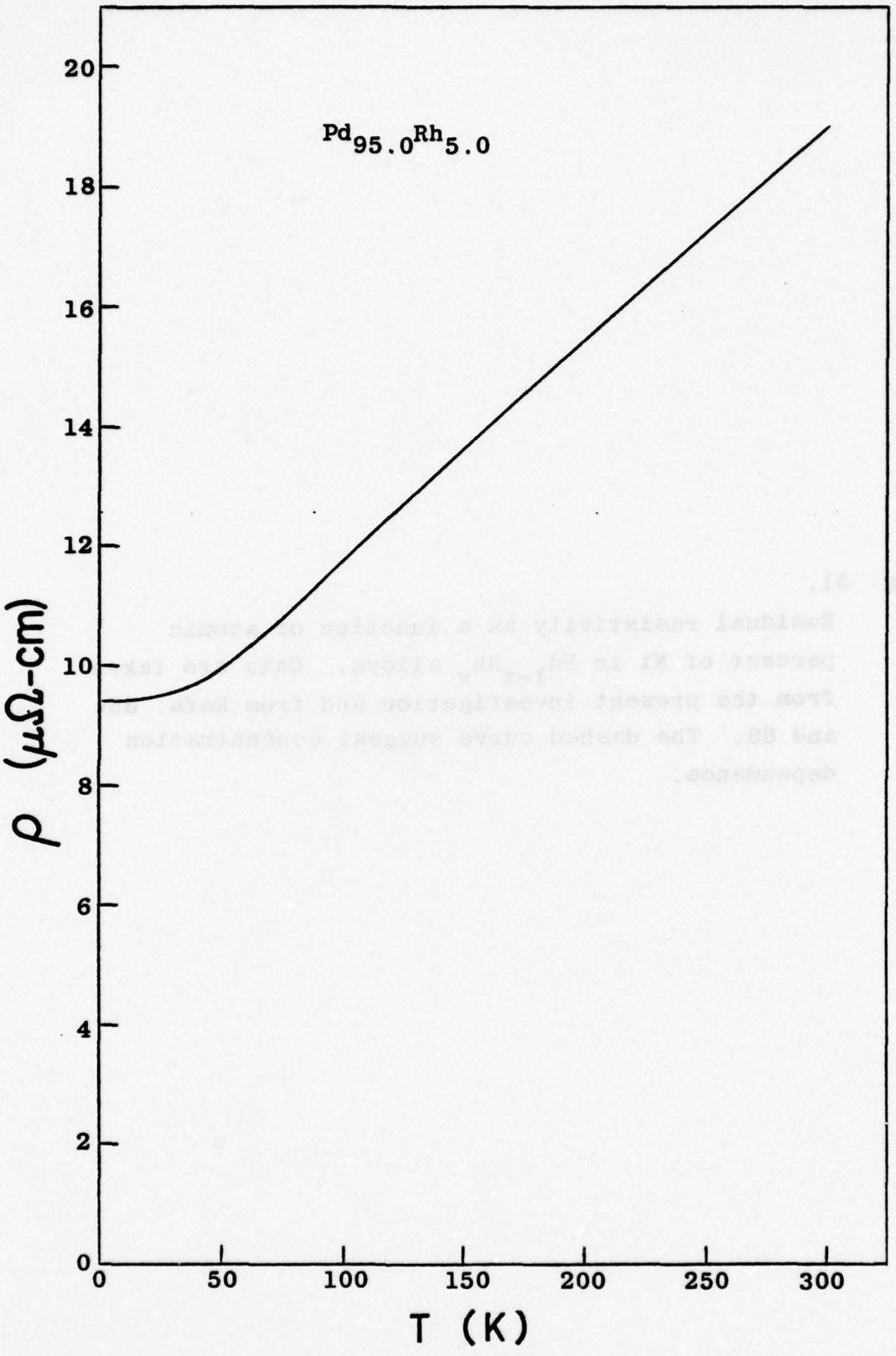

$Pd_{95.0}Rh_{5.0}$
ρ (μΩ-cm)
T (K)
0
2
4
6
8
10
12
14
16
18
20
0
50
100
150
200
250
300

Fig. 51.

Residual resistivity as a function of atomic percent of Ni in $Pd_{1-x}Rh_x$ alloys. Data are taken from the present investigation and from Refs. 68 and 69. The dashed curve suggest concentration dependence.

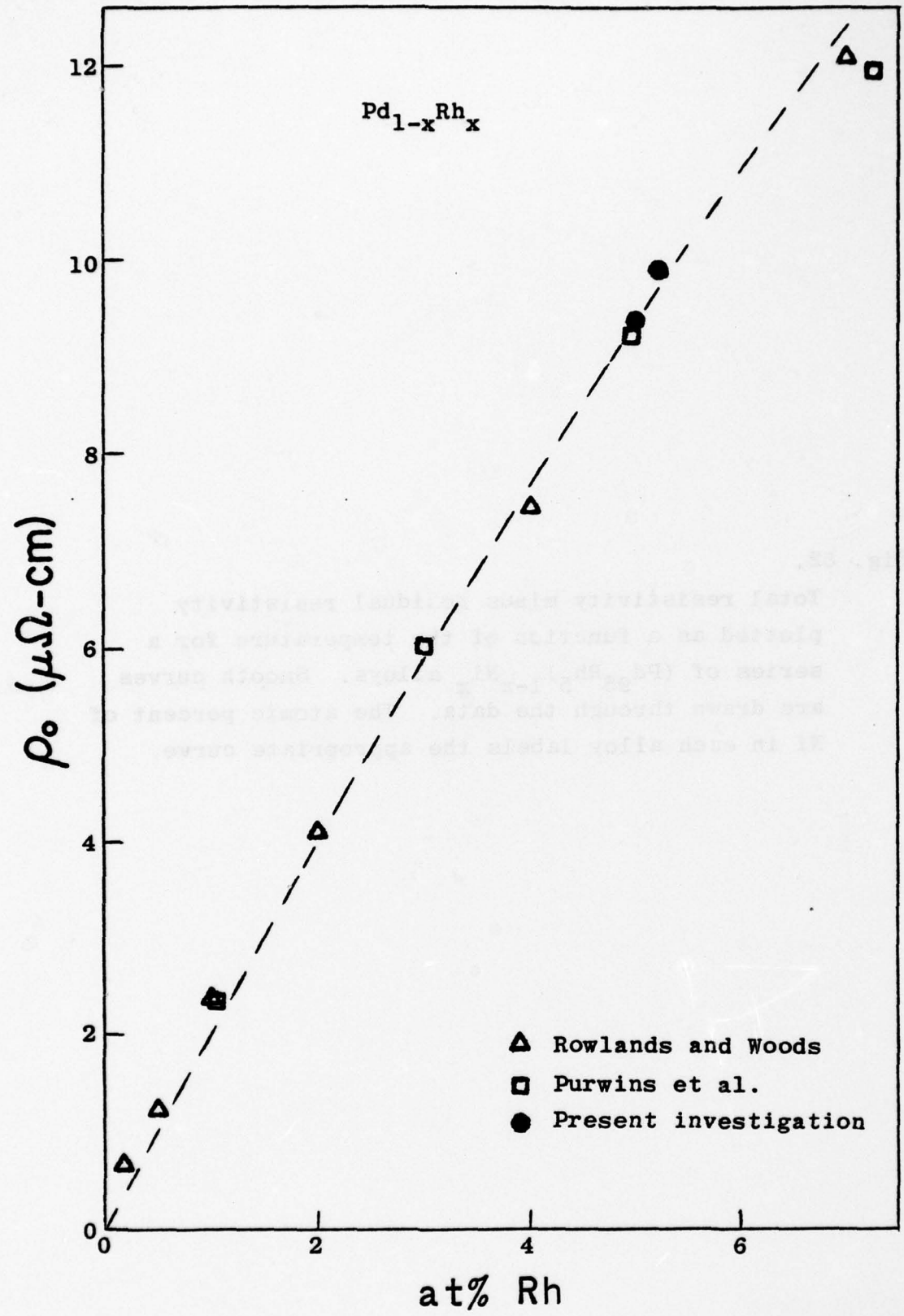
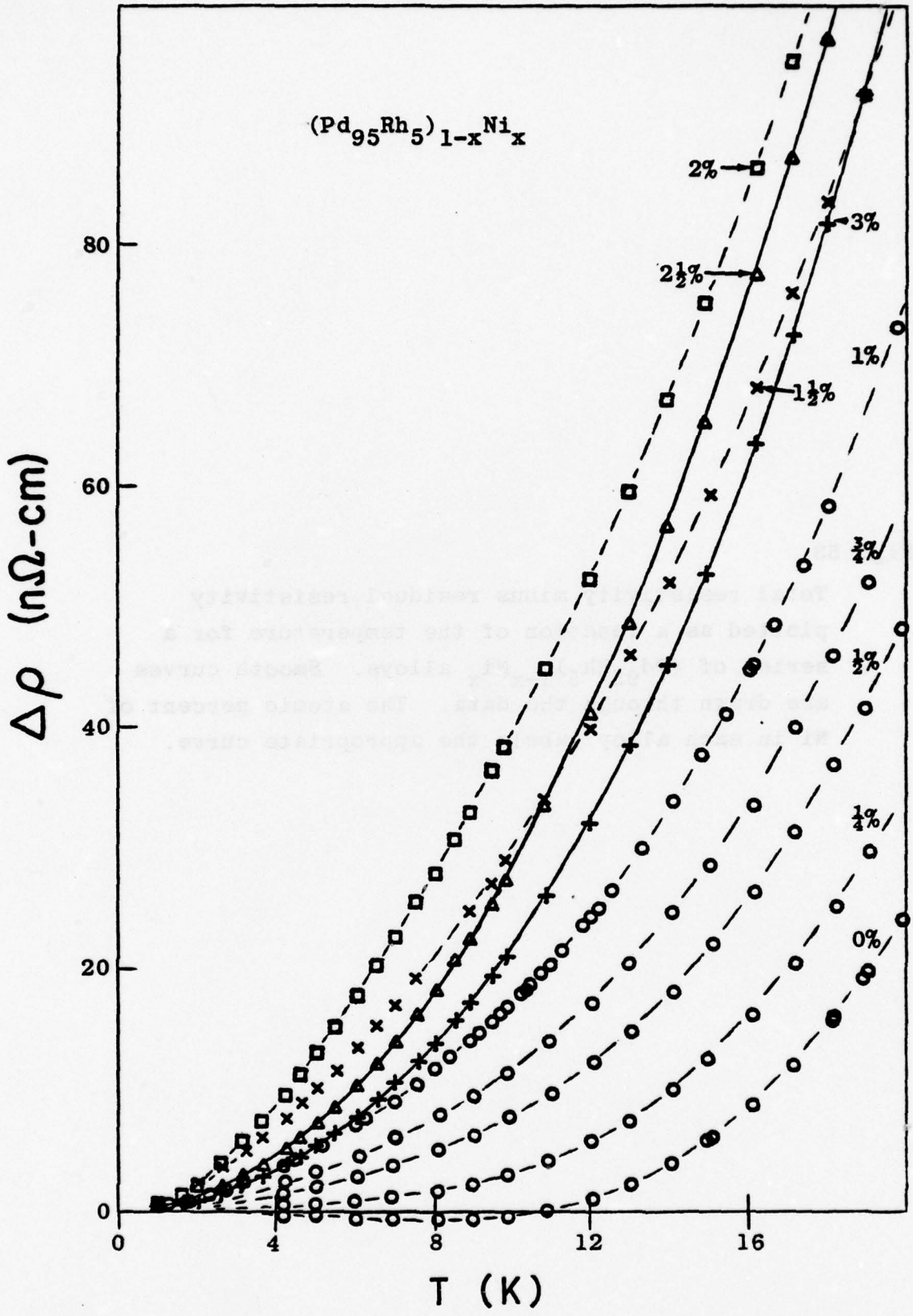

$Pd_{1-x}Rh_x$
ρ_o ($\mu\Omega$-cm)
at% Rh
0
2
4
6
8
10
12
Rowlands and Woods
Purwins et al.
Present investigation

Fig. 52.

Total resistivity minus residual resistivity plotted as a function of the temperature for a series of $(Pd_{95}Rh_5)_{1-x}Ni_x$ alloys. Smooth curves are drawn through the data. The atomic percent of Ni in each alloy labels the appropriate curve.


$(Pd_{95}Rh_5)_{1-x}Ni_x$
2%
3%
2½%
1%
1½%
¾%
½%
¼%
0%
Δρ (nΩ-cm)
T (K)
0
20
40
60
80
0
4
8
12
16

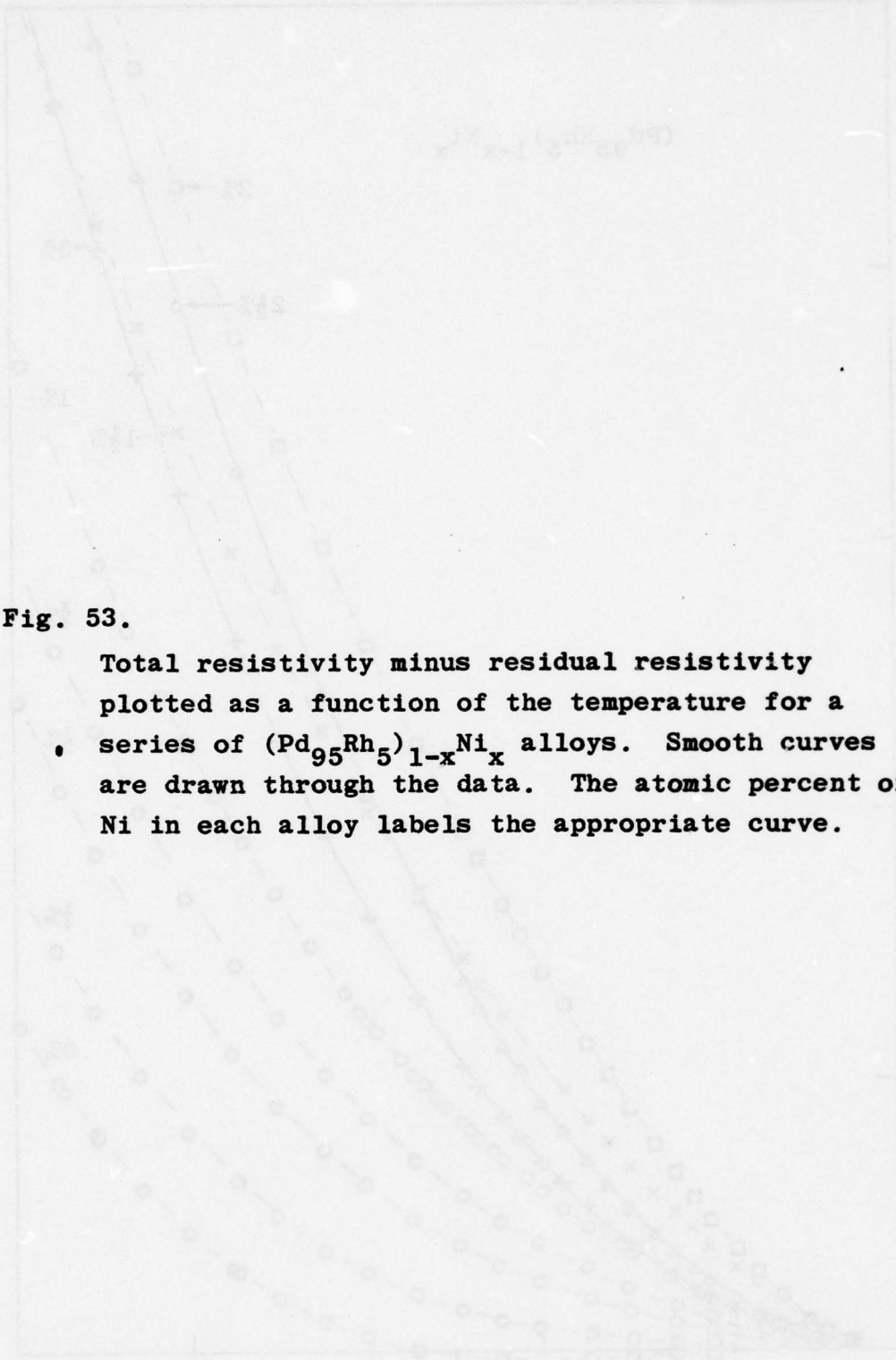


Fig. 53.

Total resistivity minus residual resistivity plotted as a function of the temperature for a series of $(Pd_{95}Rh_5)_{1-x}Ni_x$ alloys. Smooth curves are drawn through the data. The atomic percent of Ni in each alloy labels the appropriate curve.

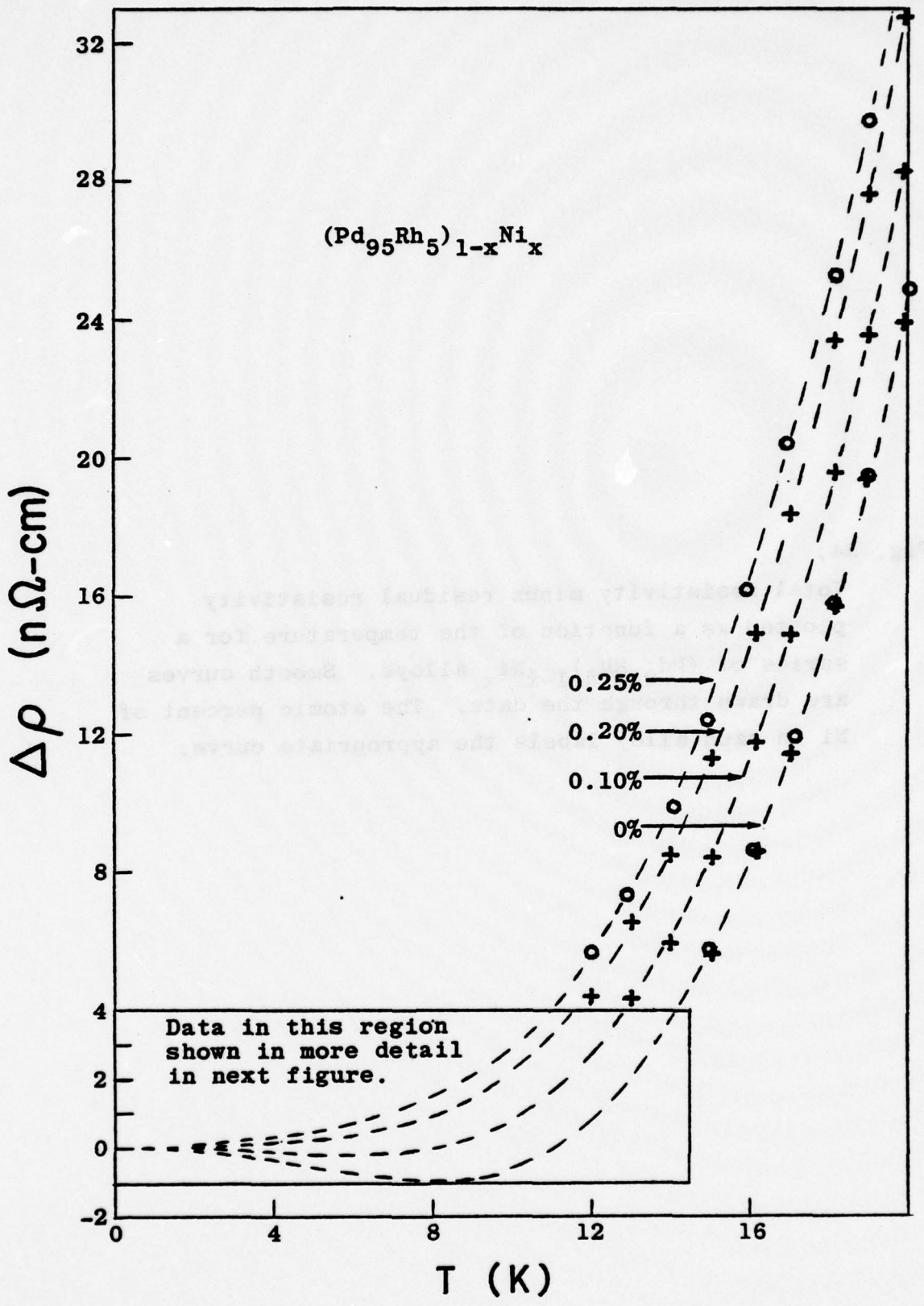
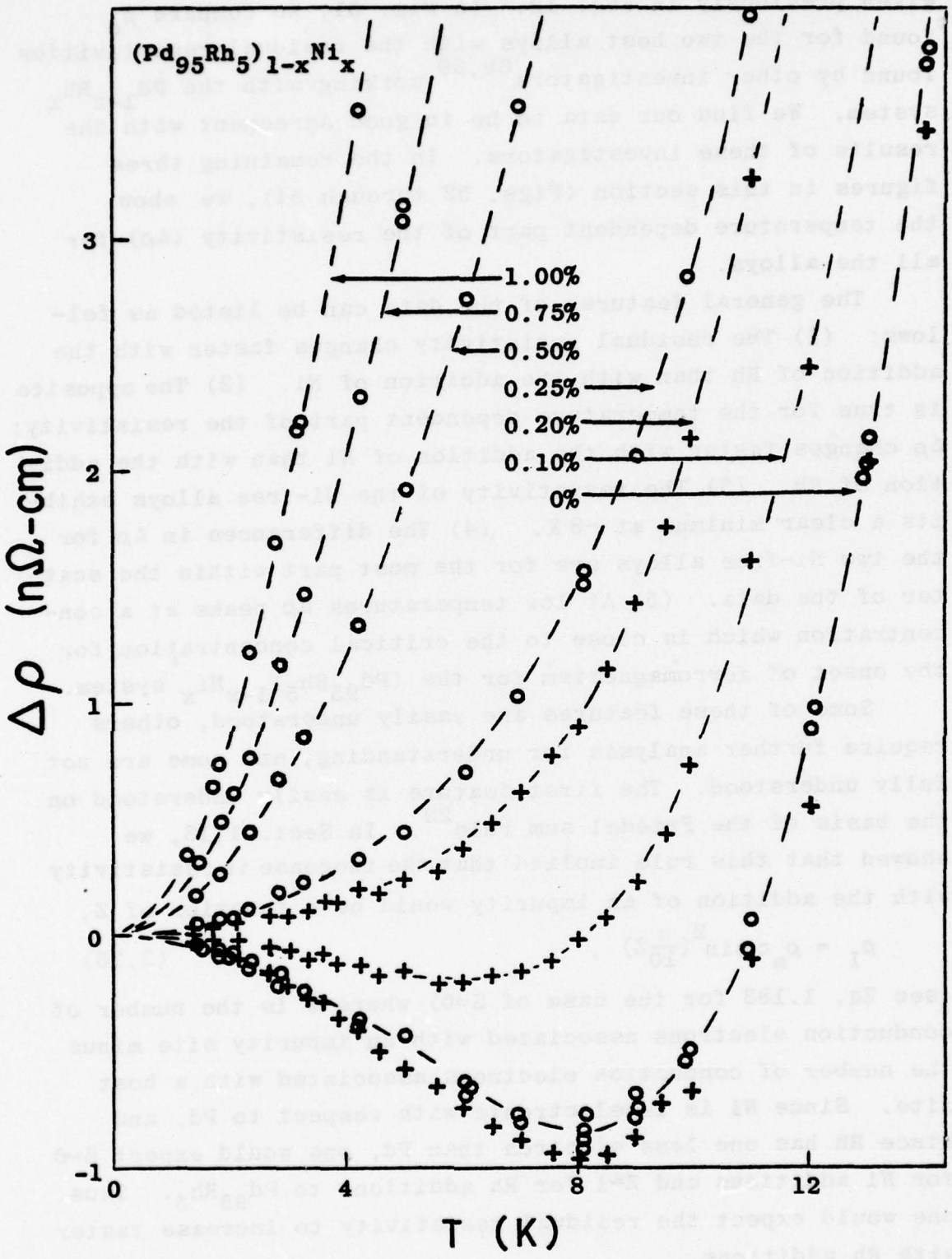

$(Pd_{95}Rh_5)_{1-x}Ni_x$
0.25%
0.20%
0.10%
0%
Data in this region shown in more detail in next figure.
Δρ (nΩ-cm)
T (K)
32
28
24
20
16
12
8
4
2
0
-2
0
4
8
12
16

Fig. 54.

Total resistivity minus residual resistivity plotted as a function of the temperature for a series of $(Pd_{95}Rh_5)_{1-x}Ni_x$ alloys. Smooth curves are drawn through the data. The atomic percent of Ni in each alloy labels the appropriate curve.


$(Pd_{95}Rh_5)_{1-x}Ni_x$
1.00%
0.75%
0.50%
0.25%
0.20%
0.10%
0%
Δρ (nΩ-cm)
T (K)
3
2
1
0
-1
0
4
8
12

given previously in Fig. 12. In Fig. 51, we compare ρ_o found for the two host alloys with the residual resistivities found by other investigators[68,69] working with the $Pd_{1-x}Rh_x$ system. We find our data to be in good agreement with the results of these investigators. In the remaining three figures in this section (Figs. 52 through 54), we show the temperature dependent part of the resistivity ($\Delta\rho$) for all the alloys.

The general features of the data can be listed as follows: (1) The residual resistivity changes faster with the addition of Rh than with the addition of Ni. (2) The opposite is true for the temperature dependent part of the resistivity: $\Delta\rho$ changes faster with the addition of Ni than with the addition of Rh. (3) The resistivity of the Ni-free alloys exhibits a clear minimum at ~8 K. (4) The differences in $\Delta\rho$ for the two Ni-free alloys are for the most part within the scatter of the data. (5) At low temperatures $\Delta\rho$ peaks at a concentration which is close to the critical concentration for the onset of ferromagnetism for the $(Pd_{95}Rh_5)_{1-x}Ni_x$ system.

Some of these features are easily understood, others require further analysis for understanding, and some are not fully understood. The first feature is easily understood on the basis of the Friedel sum rule[22]. In Sect. 1.13, we showed that this rule implied that the increase in resistivity with the addition of an impurity would be a function of Z,

$$\rho_I = \rho_m c \sin^2(\tfrac{\pi}{10}Z) \ , \qquad (3.26)$$

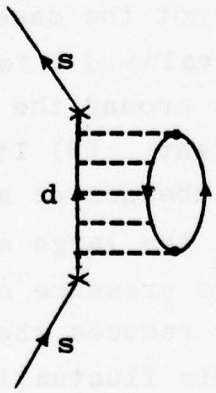
(see Eq. 1.183 for the case of S=0) where Z is the number of conduction electrons associated with an impurity site minus the number of conduction electrons associated with a host site. Since Ni is isoelectronic with respect to Pd, and since Rh has one less electron than Pd, one would expect Z≃0 for Ni additions and Z≃1 for Rh additions to $Pd_{95}Rh_5$. Thus, one would expect the residual resistivity to increase faster with Rh additions.

The second feature is most likely a result of a large local exchange enhancement being associated with the Ni atoms and not with the host atoms. However, further analysis will be required to show that this change in resistivity is, indeed, associated with the conduction electrons scattering from local spin fluctuations.

The third feature is not well understood. Resistivity minima in the $Pd_{1-x}Rh_x$ alloys were first discovered by Rowland et al.[68] . At that time they attributed the minima to temperature dependent modifications of the inter-band s-d scattering. Using electronic specific heat data to determine the shape of the density of states at the Fermi level of these alloys, they were able to show that a rigid band model[70] yielded a negative T^2 coefficient in the electrical resistivity which was in close agreement with experiment. However, the use of the rigid band model and the neglect of exchange-enhancement effects makes the calculation suspect since the rigid band model frequently gives incorrect results and exchange-enhancement effects are expected to be significant. On the other hand, other possible explanations have been considered and have been found to be less likely: (1) Greig and Rowlands[71] have discussed the possibility that the Rh atoms are displaying the behavior of a spin-compensated local moment at a temperature far below the Kondo temperature, but they find there is little evidence to support such a view. (2) Although spin fluctuations could result in a resistivity minimum provided $5/2 < Z < 15/2$ (see Eq. 1.183 and discussion in Sect. 1.13), this is not the case for Rh in $Pd_{1-x}Rh_x$. In fact, because of the low value of Z for this system, one would expect spin fluctuations around the Rh atoms to increase, not decrease, the T^2 coefficient. (3) It was suggested[56] that a possible reason for the absence of a T^2 term arising from spin fluctuations may be that the large amount of potential scattering resulting from the presence of the Rh dampens the spin fluctuations and thereby reduces the magnitude of the T^2 contribution from the spin fluctuations. We have calculated[72]

the effect of the potential scattering on the magnitude of the T^2 coefficient, and, contrary to what may have generally been presumed, we find that potential scattering increases the T^2 coefficient. In the case of $Pd_{95}Rh_5$ we find this increase to be small (~2%).

Since a magnetic effect (spin-compensated local moment or local spin fluctuations) does not seem to be the likely cause of the minimum, we return to the band effect (a decrease in s-d inter-band scattering with increasing temperature) that Rowland et al.[68] have suggested as the cause of the minimum. There are several conditions that are necessary for this effect to be a viable explanation: (1) A sufficient amount of electron scattering must be present so that scattering of the s-band conduction electrons into the d band yields a significant contribution to the resistivity. (2) The thermal broadening of the Fermi level must result in a decrease in the density of states at the Fermi level of the d band so that a decrease in residual resistivity will occur. (3) Lastly, the density of states at the Fermi level of the d band should be much greater than that of the s band so that the temperature dependent effect has a greater chance of being observed. Although all these conditions are thought to exist[71] in the $Pd_{1-x}Rh_x$ system, there does not exist a reliable calculation of the magnitude of the effect. To do such a calculation one would have to consider scattering processes of the form:



where a conduction electron scatters from an impurity atom (potential scattering) into a d state where it interacts via the intra-atomic Coulomb interactions with spin-fluctuations in the d band before again scattering from an impurity atom back into the s band. On the other hand, there is additional experimental evidence that this s-d scattering may be the cause of the minimum. In such diverse alloys as Pd-Rh, Pd-Ru, Pd-Cr, Pd-Pt, and Pd-Ag, it is found[71] that at low temperature the resistivity is described by

$$\rho(T) \simeq \rho(0)\{1-(T/T^*)^2\} , \qquad (3.27)$$

where T^* is between 200 K and 500 K in each of these cases. This is qualitatively the type of behavior one would expect from s-d scattering in these systems, and the large value of T^* is suggestive[71] of a band structure effect rather than a local magnetic effect. The first three of these alloys exhibit resistivity minima at low temperatures and for dilute solutes because of the high residual resistivities in these alloys, whereas the last two alloys fail to exhibit minima because the residual resistivities in these alloys are too small for this effect to compensate for the large T^2 term from spin-fluctuation scattering.

The fourth feature of the data is that the temperature dependent contribution to the resistivity ($\Delta\rho$) is, to within experimental error, identical for the two Ni-free alloys. This is understandable for the following reasons: (1) The phonon spectra for the various Pd-Rh alloys would be expected to be very similar because of the small mass difference and identical structure. (2) Since little difference was found between the susceptibilities of these two alloys, differences in the spin-fluctuation contribution would be expected to be small. (3) The largest difference in $\Delta\rho$ for these two alloys should be from the effect which gives rise to the resistivity minimum. Using Eq. 3.27 and the $\rho(0)$ of the two Ni-free alloys (Fig. 12), we estimate that this effect will change $\Delta\rho$ by $\leq 5\%$, and is therefore less than the scatter in the data.

The last feature (the peaking of $\Delta\rho$ for a concentration near the critical concentration) can be explained on the basis of the spin-fluctuations being greatest in those alloys whose composition is close to that of the critical composition. Electron scattering from the spin-fluctuations increases until the alloy becomes ferromagnetic and the spin-fluctuations are reduced. In the next section, we will take a closer look at this feature along with other aspects of the spin-fluctuation resistivity.

3.6 Contribution from the Ni Addition

In this section, we obtain the contribution to the temperature dependent part of the resistivity caused by the addition of Ni to the $(Pd_{95}Rh_5)_{1-x}Ni_x$ alloys,

$$\rho_I \equiv (\rho-\rho_o)_{alloy} - (\rho-\rho_o)_{host} , \qquad (3.28)$$

where the data for $\Delta\rho\equiv\rho-\rho_o$ of the alloys and host are given in the previous section. The ρ_I data obtained from the above subtraction are shown in Figs. 55 through 59.

The total ρ_I contribution is expected to be the result of the additional <u>spin-dependent</u> scattering processes (electron-paramagnon or electron-magnon) that occurs because of the addition of Ni. In other words, the contribution to the temperature dependent part of the resistivity from the <u>spin-independent</u> scattering is expected to remain unchanged by the addition of Ni (i.e. Matthiessen's rule holds for the spin-independent contribution). The reasons for these expectations are as follows: First, the amount of Ni in the alloys is small ($\leq$3 at%),and the measured temperatures are low ($\leq$20 K). Second, changes in the average mass upon alloying are known[73] to produce only very small deviations from Matthiessen's rule ($\leq$1 % of ρ_I is estimated to be from this source in the worst case, the 3 at% Ni alloy). Third, the major source of deviations from Matthiessen's rule is generally recognized[73] to arise from the changes in the electronic distribution function. This change can easily occur if the dominant scattering mechanism is different in the two alloys

(see discussion in first part of Sect. 1.11). In the present case, the scattering mechanisms found in the host are still the dominant ones in the Ni-containing alloys (compare $\rho(T)_{host}$ with $\rho(T)_{alloy}-\rho(T)_{host}$). Lastly, the largest source of a deviation from Matthiessen's rule for spin-independent processes in these alloys is probably from changing the amount of s-d scattering (see discussion in the previous section of the cause of the resistivity minimum). However, because of the small differences in the residual resistivities of these alloys (see Fig. 12), one finds, from Eq. 3.27, that this too is a negligible effect.

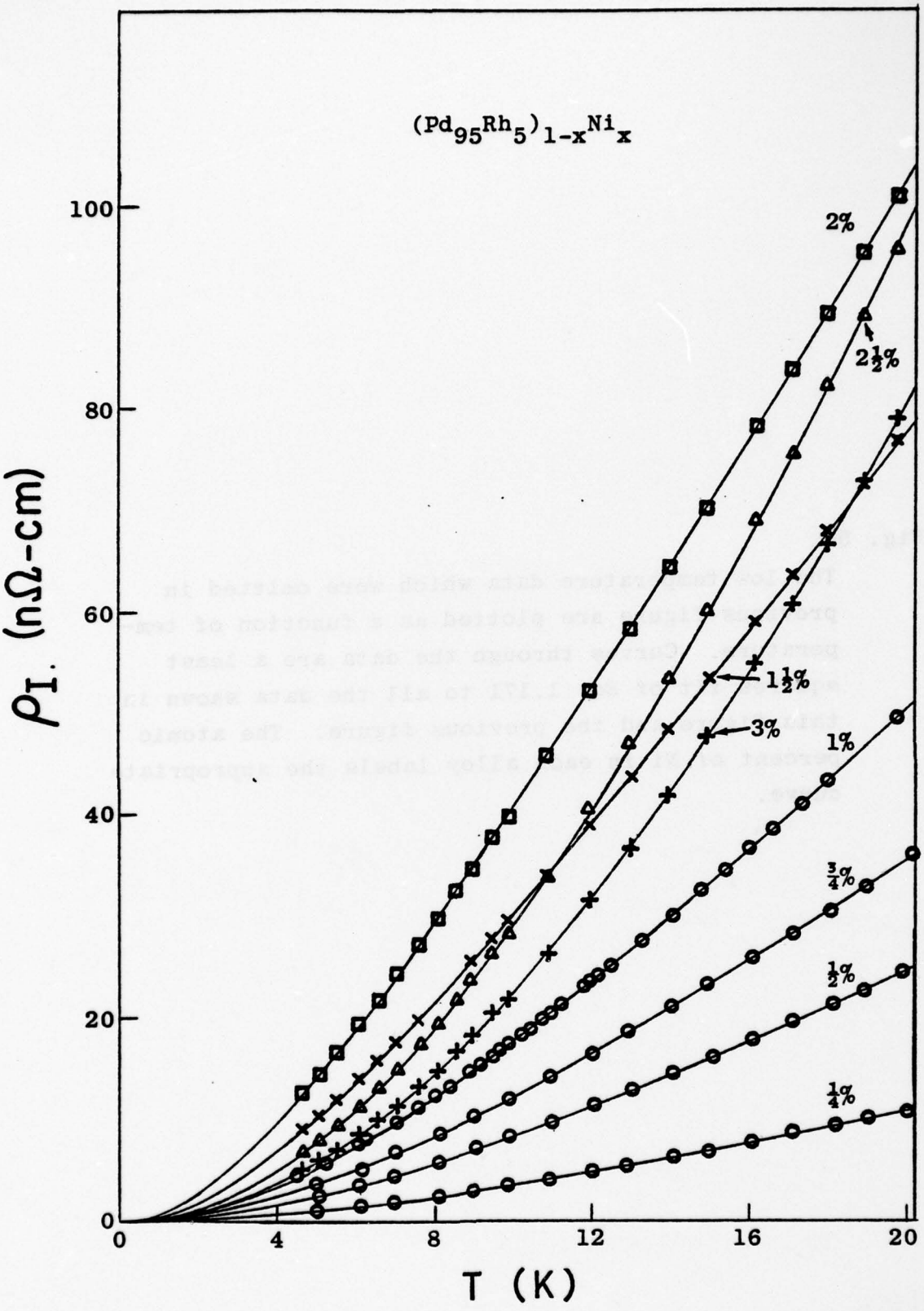
The curves through the data are a least squares fit of the local enhancement model of Kaiser and Doniach[38] (discussed in detail in Sect. 1.12) to the data. The data were appropriately weighted to take into account the higher precision of the data below 4.2 K (see discussion in Sect. 2.4). The procedure used to fit the data is presented in appendix A, and discussion of the method used to evaluate the Kaiser-Doniach integral (Eq. 1.171) for the spin-fluctuation resistivity is given in appendix B. This two-parameter resistivity function has been shown previously in Fig. 6.

The Kaiser-Doniach function yields an excellent fit to the ρ_I data of all the alloys. However, one would expect a single particle model, such as this, to be applicable only to the more dilute alloys. Furthermore, the Kaiser-Doniach model is not the only model which is in good agreement with the data. Both the local enhancement model of Rivier and Zlatic[44] and a phenomenological function which has been used to describe[19] local spin fluctuations yield equally good fits to the ρ_I data of the more dilute Ni alloys. (The Rivier and Zlatic model was discussed in Sect. 1.13, and the spin-fluctuation resistivity predicted by this model was given in Eq. 1.188 and was shown in Fig. 8. The phenomenological function has been given in Eq. 1.191 and shown in Fig. 9 along with both the Kaiser-Doniach and Rivier-Zlatic predictions.)

(text continues on p. 236)

Fig. 55.

The contribution to the temperature dependent part of the electrical resistivity from the addition of Ni to a series of $(Pd_{95}Rh_5)_{1-x}Ni_x$ alloys, $\rho_I \equiv (\rho-\rho_o)_{alloy} - (\rho-\rho_o)_{host}$, plotted as a function of the temperature. Curves through the data are a least squares fit of Eq. 1.171 to the data. The atomic percent of Ni in each alloy labels the appropriate curve. Data points below 4.3 K have been omitted in this figure for clarity, but are shown in the following figure. Alloy compositions below ¼% are shown in Fig.


$(Pd_{95}Rh_5)_{1-x}Ni_x$
ρ_I (nΩ-cm)
T (K)
0
20
40
60
80
100
0
4
8
12
16
20
2%
2½%
1½%
3%
1%
¾%
½%
¼%

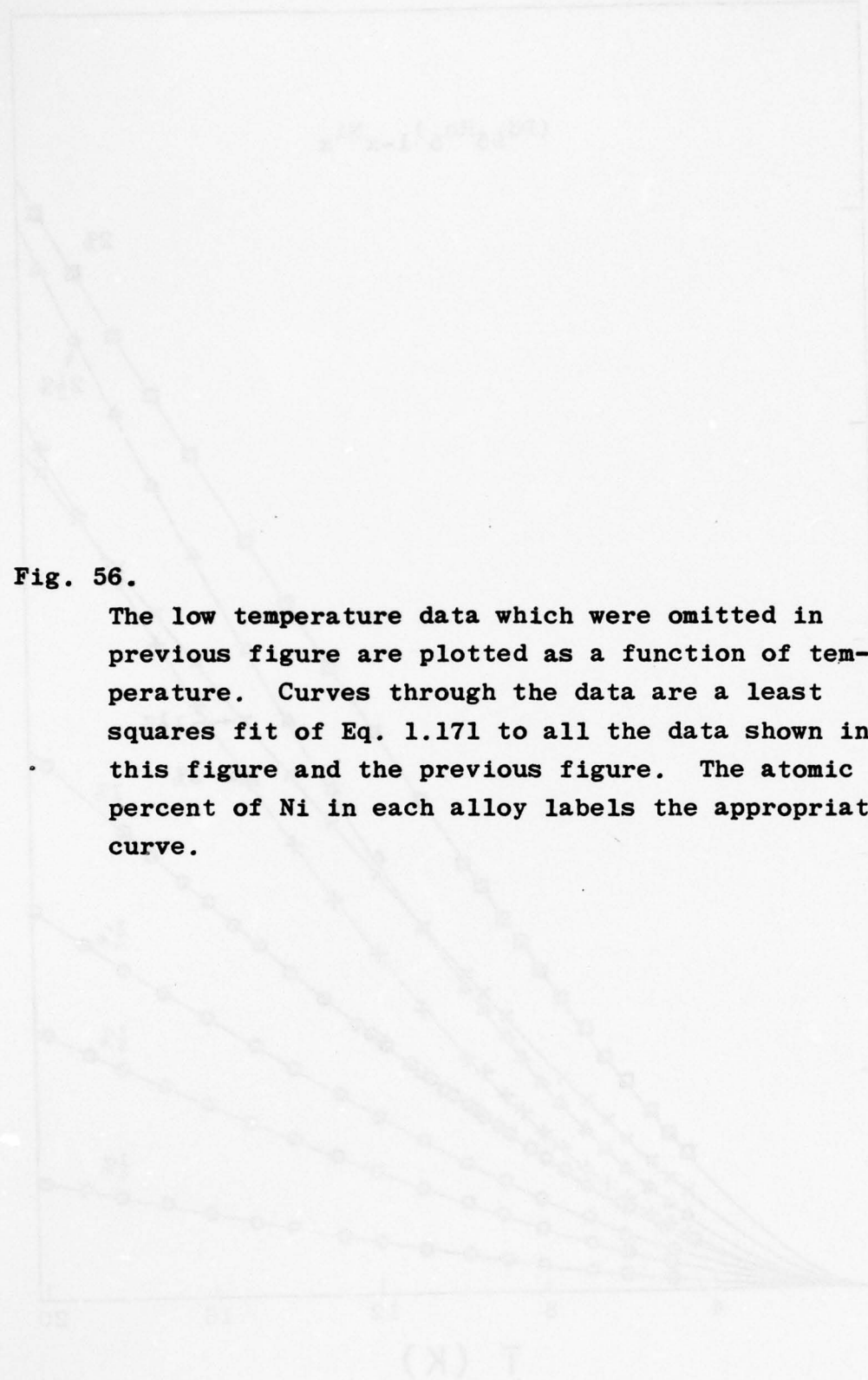
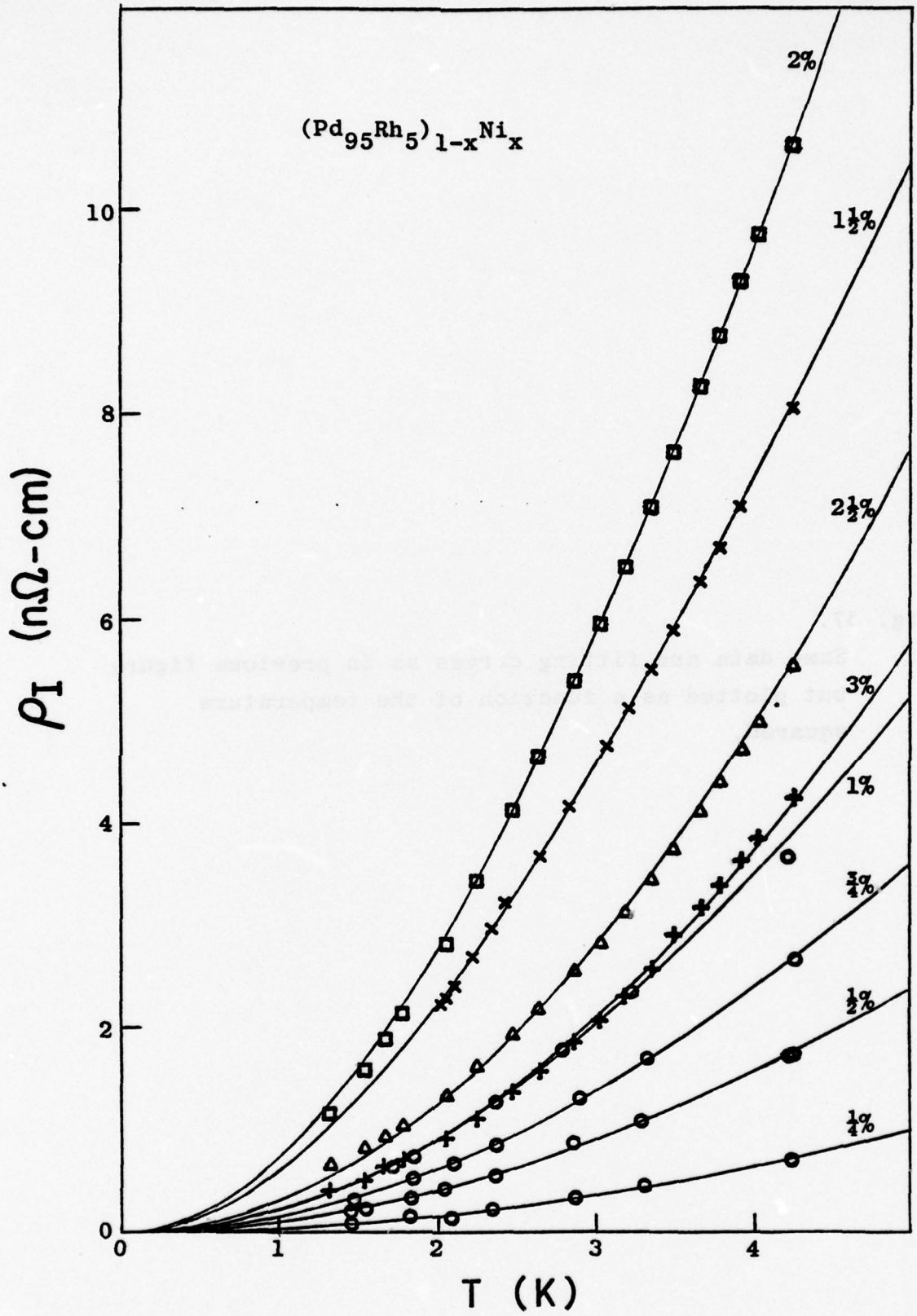


Fig. 56.

The low temperature data which were omitted in previous figure are plotted as a function of temperature. Curves through the data are a least squares fit of Eq. 1.171 to all the data shown in this figure and the previous figure. The atomic percent of Ni in each alloy labels the appropriate curve.


$(Pd_{95}Rh_5)_{1-x}Ni_x$
2%
1½%
2½%
3%
1%
¾%
½%
¼%
ρ_I (nΩ-cm)
T (K)
0
2
4
6
8
10
0
1
2
3
4

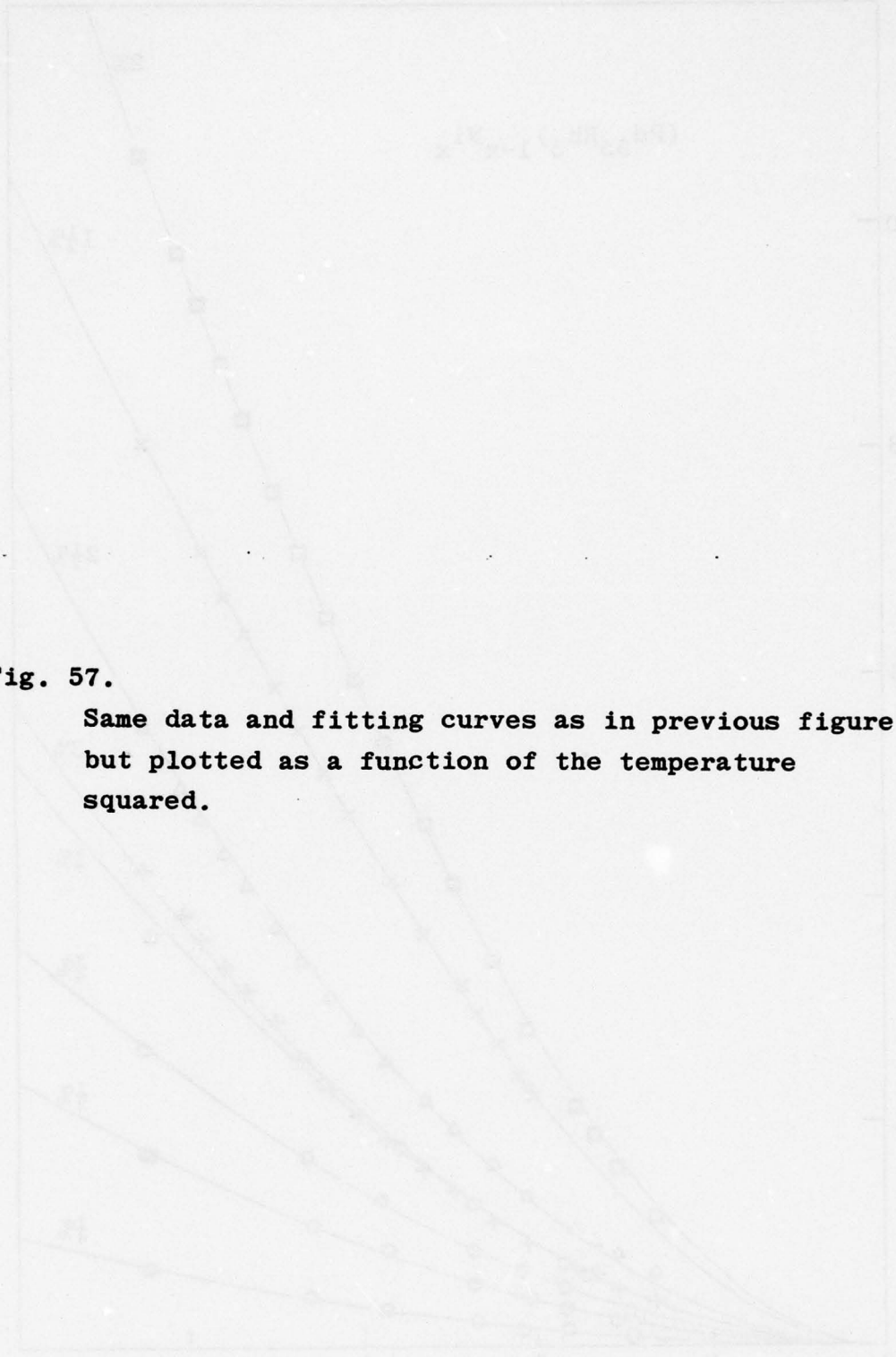


Fig. 57.

Same data and fitting curves as in previous figure but plotted as a function of the temperature squared.

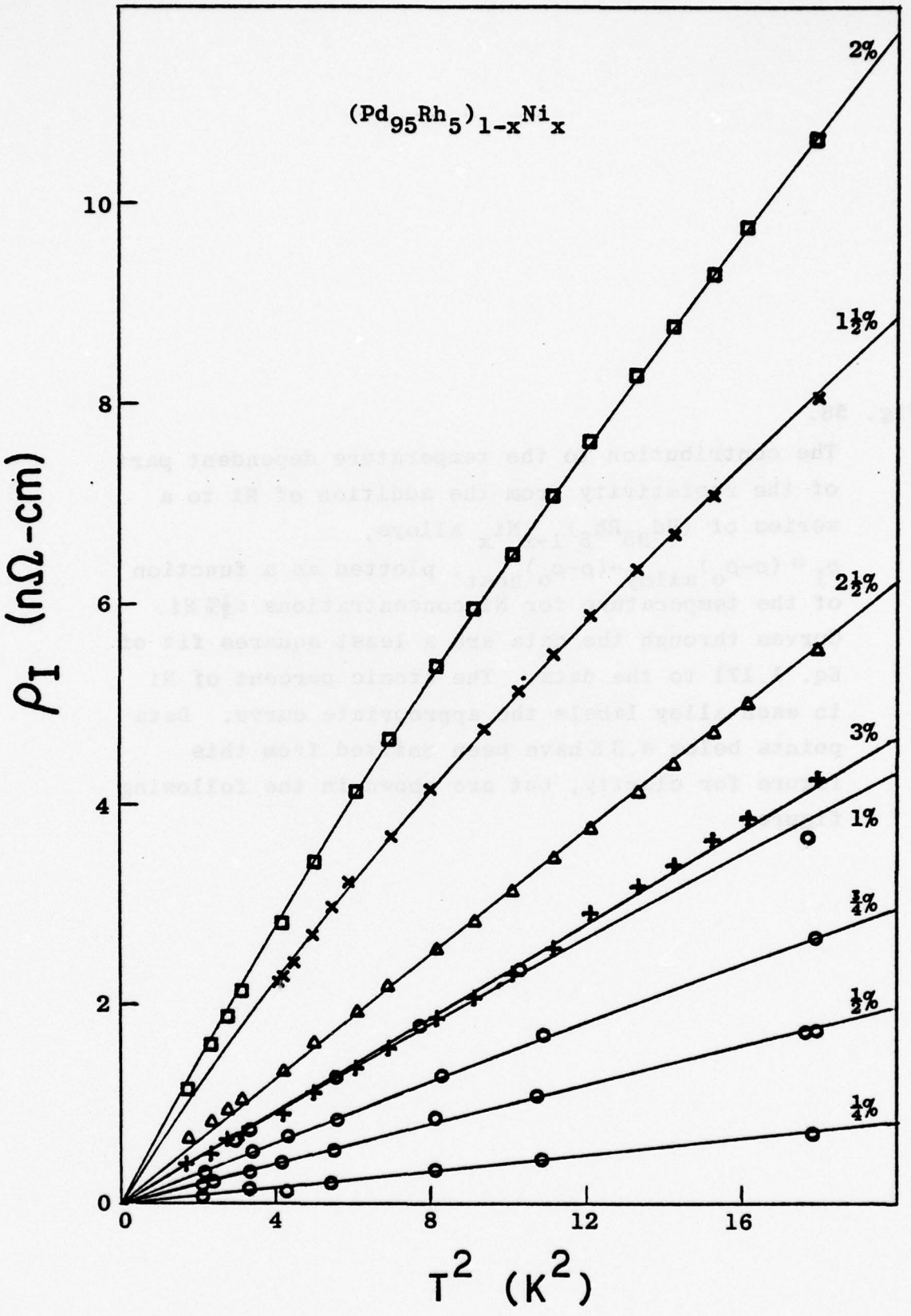

$(Pd_{95}Rh_5)_{1-x}Ni_x$
2%
1½%
2½%
3%
1%
¾%
½%
¼%
ρ_I (nΩ-cm)
T^2 (K^2)
0
2
4
6
8
10
0
4
8
12
16

Fig. 58.

The contribution to the temperature dependent part of the resistivity from the addition of Ni to a series of $(Pd_{95}Rh_5)_{1-x}Ni_x$ alloys, $\rho_I \equiv (\rho-\rho_o)_{alloy}-(\rho-\rho_o)_{host}$, plotted as a function of the temperature for Ni concentrations $\leq \frac{1}{4}\%$ Ni. Curves through the data are a least squares fit of Eq. 1.171 to the data. The atomic percent of Ni in each alloy labels the appropriate curve. Data points below 4.3 K have been omitted from this figure for clarity, but are shown in the following figure.

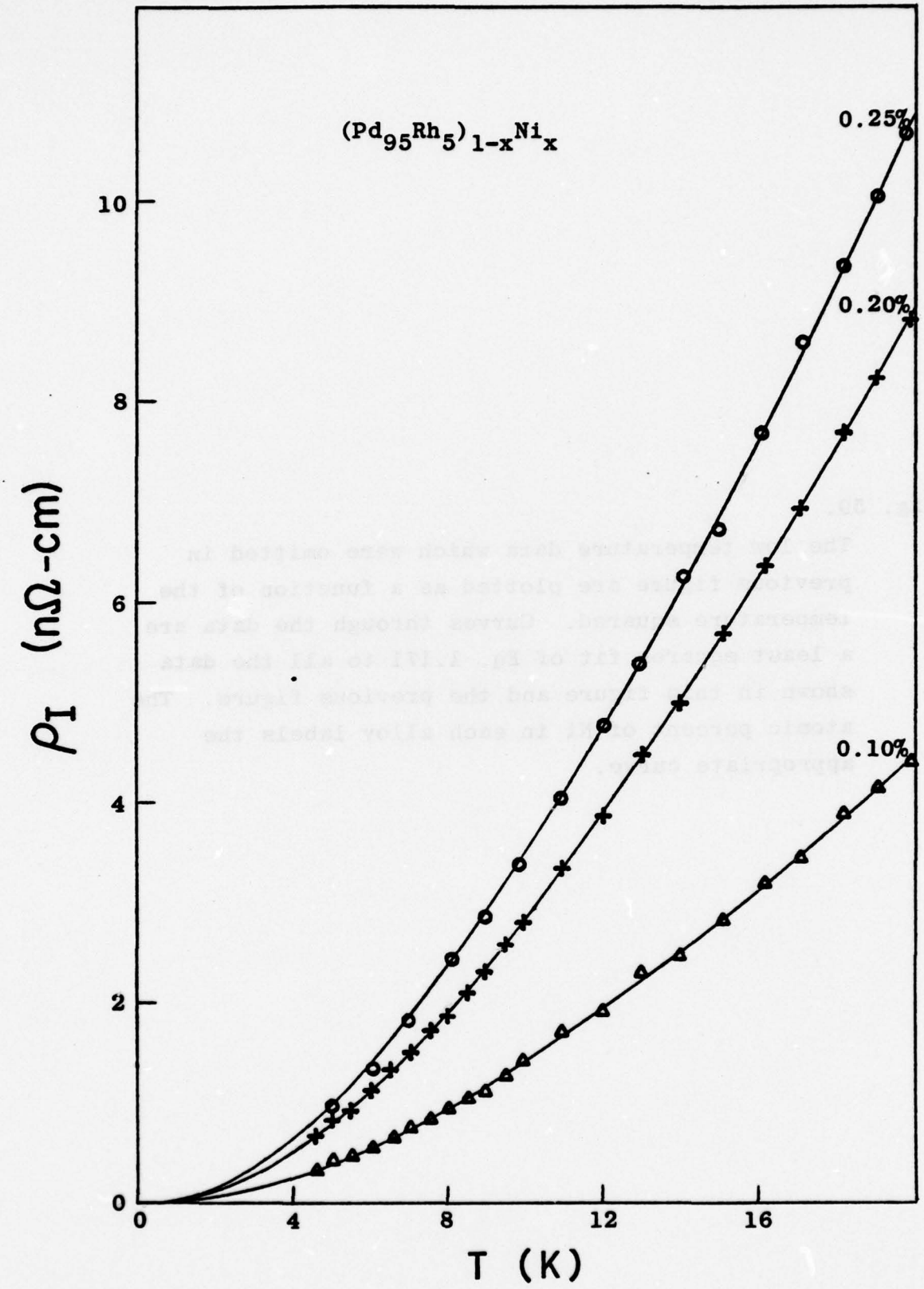
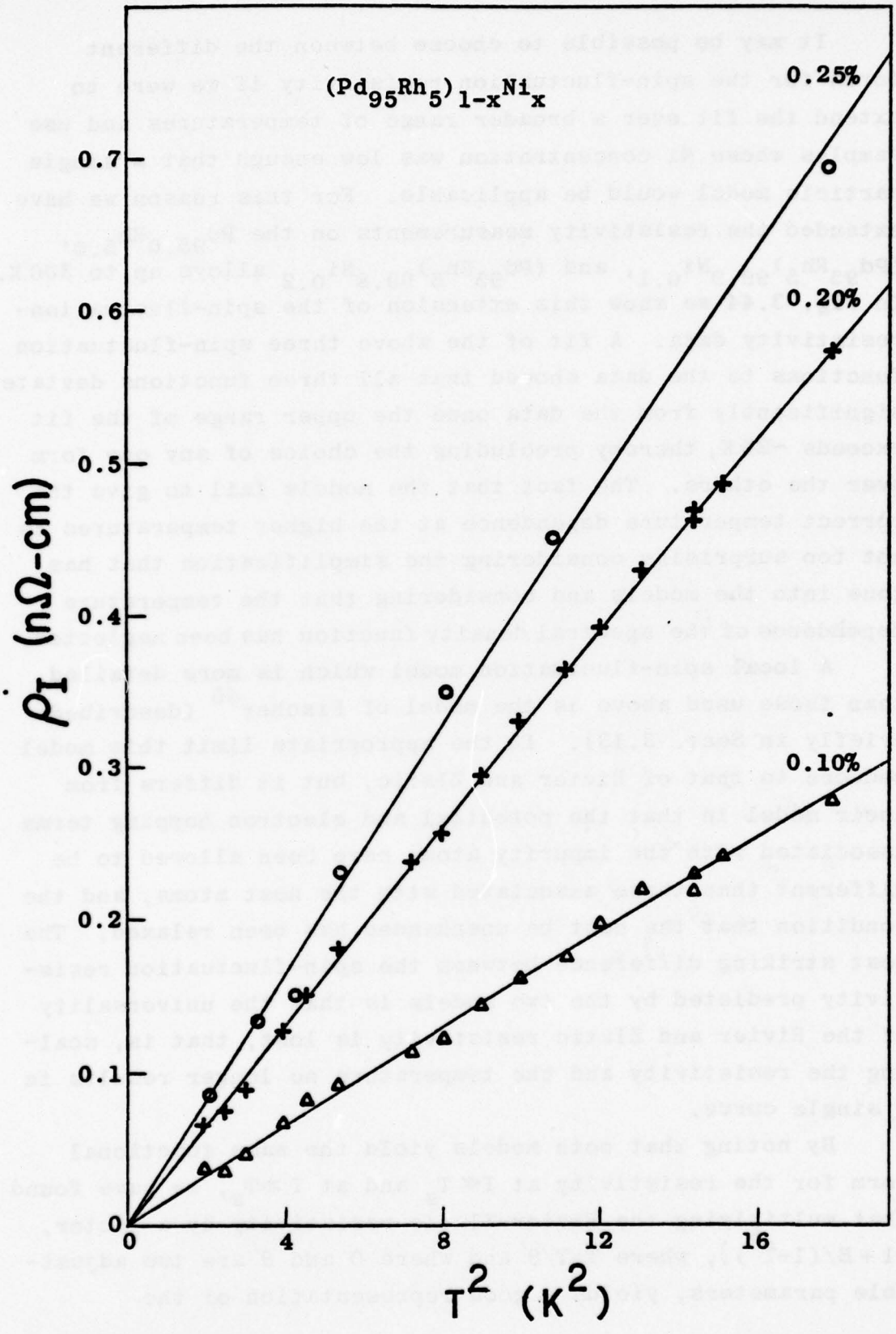

$(Pd_{95}Rh_5)_{1-x}Ni_x$
0.25%
0.20%
0.10%
ρ_I (nΩ-cm)
T (K)
0
2
4
6
8
10
0
4
8
12
16

Fig. 59.

The low temperature data which were omitted in previous figure are plotted as a function of the temperature squared. Curves through the data are a least squares fit of Eq. 1.171 to all the data shown in this figure and the previous figure. The atomic percent of Ni in each alloy labels the appropriate curve.


$(Pd_{95}Rh_5)_{1-x}Ni_x$
0.25%
0.20%
0.10%
0.7
0.6
0.5
0.4
0.3
0.2
0.1
0
ρ_I (nΩ-cm)
0
4
8
12
16
T^2 (K^2)

It may be possible to choose between the different forms for the spin-fluctuation resistivity if we were to extend the fit over a broader range of temperatures and use samples whose Ni concentration was low enough that a single particle model would be applicable. For this reason we have extended the resistivity measurements on the $Pd_{95.0}Rh_{5.0}$, $(Pd_{95}Rh_5)_{99.9}Ni_{0.1}$, and $(Pd_{95}Rh_5)_{99.8}Ni_{0.2}$ alloys up to 300 K. In Fig. 3.44 we show this extension of the spin-fluctuation-resistivity data. A fit of the above three spin-fluctuation functions to the data showed that all three functions deviate significantly from the data once the upper range of the fit exceeds ~25 K, thereby precluding the choice of any one form over the others. The fact that the models fail to give the correct temperature dependence at the higher temperatures is not too surprising considering the simplification that has gone into the models and considering that the temperature dependence of the spectral density function has been neglected.

A local spin-fluctuation model which is more detailed than those used above is the model of Fischer[45] (described briefly in Sect. 3.13). In the appropriate limit this model reduces to that of Rivier and Zlatic, but it differs from their model in that the potential and electron hopping terms associated with the impurity atoms have been allowed to be different than those associated with the host atoms, and the condition that the host be unenhanced has been relaxed. The most striking difference between the spin-fluctuation resistivity predicted by the two models is that the universality of the Rivier and Zlatic resistivity is lost, that is, scaling the resistivity and the temperature no longer results in a single curve.

By noting that both models yield the same functional form for the resistivity at $T \ll T_s$ and at $T \gg T_s$, we have found that multiplying the Rivier-Zlatic resistivity by a factor, $\{1 + B/(1+\bar{T}^2)\}$, where $\bar{T} \equiv T/\theta'$ and where B and θ' are two adjustable parameters, yields a good representation of the

resistivity predicted by Fischer. Using this representation we were able to obtain an excellent fit to the data over the entire temperature range as shown by the curves through the data in Fig. 60. However, since the Fischer model neglects the temperature dependence of the spectral density function and since four adjustable parameters were used to fit the data, the value of such a fit is questionable. On the other hand, the data should be a good representation of the spin-fluctuation resistivity resulting from the local enhancement of the noninteracting (isolated) Ni atoms.

The values of the various resistivity parameters along with the errors (90% confidence level) and the standard deviations (σ), all of which were determined from the least squares fit of data, are listed in Table 2. Although all the models yielded an excellent fit to the data for the more dilute alloys, the Kaiser-Doniach function yielded the best overall fit to the 1-20 K data. This can be seen by examining σ for the various fits.

These Kaiser-Doniach parameters are shown as a function of Ni concentration in Fig. 61. Also shown are the Kaiser-Doniach parameters obtained by Purwins et al.[69] on three Pd-Rh-Ni alloys in the same concentration range. The large disagreement that occurs at low Ni concentrations is the result of fitting the data over different temperature ranges and the higher precision of the present data. Purwins et al. have fitted their data up to 35 K, whereas we find systematic deviations from the data once the upper range of the fit exceeds ~25 K. If, however, we fit the data up to 35 K, we find we are in agreement with values found by Purwins et al., but the standard deviation is then five times as large as that of the 1-20 K fit.

By using Eq. 1.173 and the Kaiser-Doniach fitting parameters, one can evaluate the coefficient of the T^2 term in the resistivity. In Fig. 3.46 we show ΔA (the change in this T^2 coefficient over that of the host) as a function of the Ni

(text continues on p. 246)

Fig. 60.

The contribution to the temperature dependent part of the resistivity from the addition of Ni to a $(Pd_{95}Rh_5)_{99.8}Ni_{0.2}$ and a $(Pd_{95}Rh_5)_{99.9}Ni_{0.1}$ alloy, $\rho_I \equiv (\rho-\rho_o)_{alloy}-(\rho-\rho_o)_{host}$ plotted as a function of the temperature. The atomic percent of Ni in each alloy labels the appropriate curve. Data points below 20 K have been shown in previous figures and are omitted here for clarity. The curve through the data is a least square fit of all the data to a phenomenological function (see text) representing the spin-fluctuation model of Fischer[45].

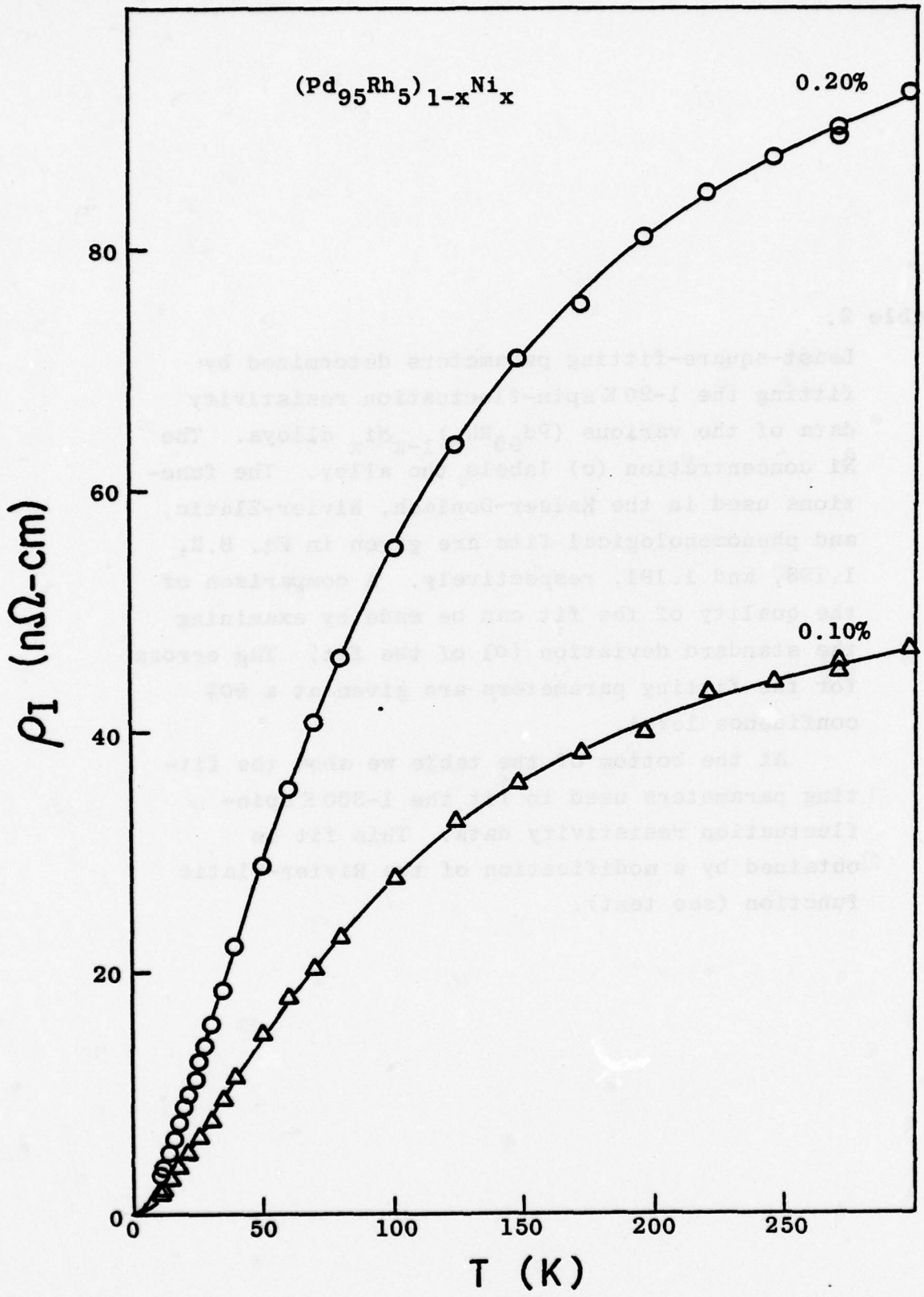

$(Pd_{95}Rh_5)_{1-x}Ni_x$
0.20%
0.10%
80
60
40
20
0
0
50
100
150
200
250
ρ_I (nΩ-cm)
T (K)

Table 2.

Least-square-fitting parameters determined by fitting the 1-20 K spin-fluctuation resistivity data of the various $(Pd_{95}Rh_5)_{1-x}Ni_x$ alloys. The Ni concentration (c) labels the alloy. The functions used in the Kaiser-Doniach, Rivier-Zlatic, and phenomenological fits are given in Eq. B.2, 1.188, and 1.191, respectively. A comparison of the quality of the fit can be made by examining the standard deviation (σ) of the fit. The errors for the fitting parameters are given at a 90% confidence level.

At the bottom of the table we show the fitting parameters used to fit the 1-300 K spin-fluctuation resistivity data. This fit is obtained by a modification of the Rivier-Zlatic function (see text).

TABLE 2: SPIN-FLUCTUATION RESISTIVITY PARAMETERS

1-20K	Kaiser-Doniach			Rivier-Zlatic			Phenomenological		
c (at%)	ρ_s ($\mu\Omega$-cm)	T_s (K)	σ (pΩ-cm)	ρ_s ($\mu\Omega$-cm)	T_s (K)	σ (pΩ-cm)	ρ'_s ($\mu\Omega$-cm)	θ (K)	σ (pΩ-cm)
0.10	16.7±1.8	57.8±3.8	11	25.8±1.7	90.6±3.8	11	13.6±0.9	21.0±0.9	11
0.20	15.7±0.6	55.7±1.3	8	25.1±1.0	89.0±1.1	13	13.2±0.5	20.6±0.5	13
0.25	14.3±1.7	53.1±4.0	32	24.0±1.9	87.5±4.6	36	12.6±1.0	20.2±1.1	36
0.50	11.7±0.4	42.8±0.9	22	22.2±1.1	75.8±2.5	56	11.6±0.6	17.5±0.6	55
0.75	9.5±0.4	38.0±1.0	42	19.8±1.1	71.7±2.7	111	10.3±0.6	16.5±0.6	109
1.00	9.1±0.2	35.3±0.7	70	20.4±0.8	70.4±2.1	222	10.6±0.4	16.2±0.5	214
1.50	4.8±0.2	21.3±0.7	95	15.1±1.0	53.8±3.0	382	7.6±0.5	12.1±0.5	360
2.00	4.0±0.1	18.7±0.2	49	13.4±0.8	49.1±2.4	540	6.7±0.4	11.0±0.5	497
2.50	25.1±1.5	80.7±2.7	97	32.1±0.6	113±1	48	16.9±0.3	26.1±0.3	46
3.00	31.9±2.1	116±4	63	35.7±2.2	151±5	74	18.7±1.2	34.7±1.2	76

1-300K	c (at%)	B	θ' (K)	ρ_s ($\mu\Omega$-cm)	T_s (K)	σ (pΩ-cm)
	0.01	1.19±0.14	26±4	59.5±0.7	207±8	95
	0.02	1.15±0.08	24±2	58.8±0.3	202±4	101

Fig. 61.

Least-square-fitting parameters, ρ_s and T_s, obtained from the previous fitting are shown as a function of the atomic percent Ni in $(Pd_{95}Rh_5)_{1-x}Ni_x$. The solid circles (●) correspond to the parameters obtained when fitting the present data between temperatures of 1 K and 20 K. The crosses (X) correspond to the parameters obtained by Purwins et al.[69] when fitting their data between 1 K and 35 K. The open circles (○) correspond to the parameters obtained when fitting the present data between 1 K and 35 K.

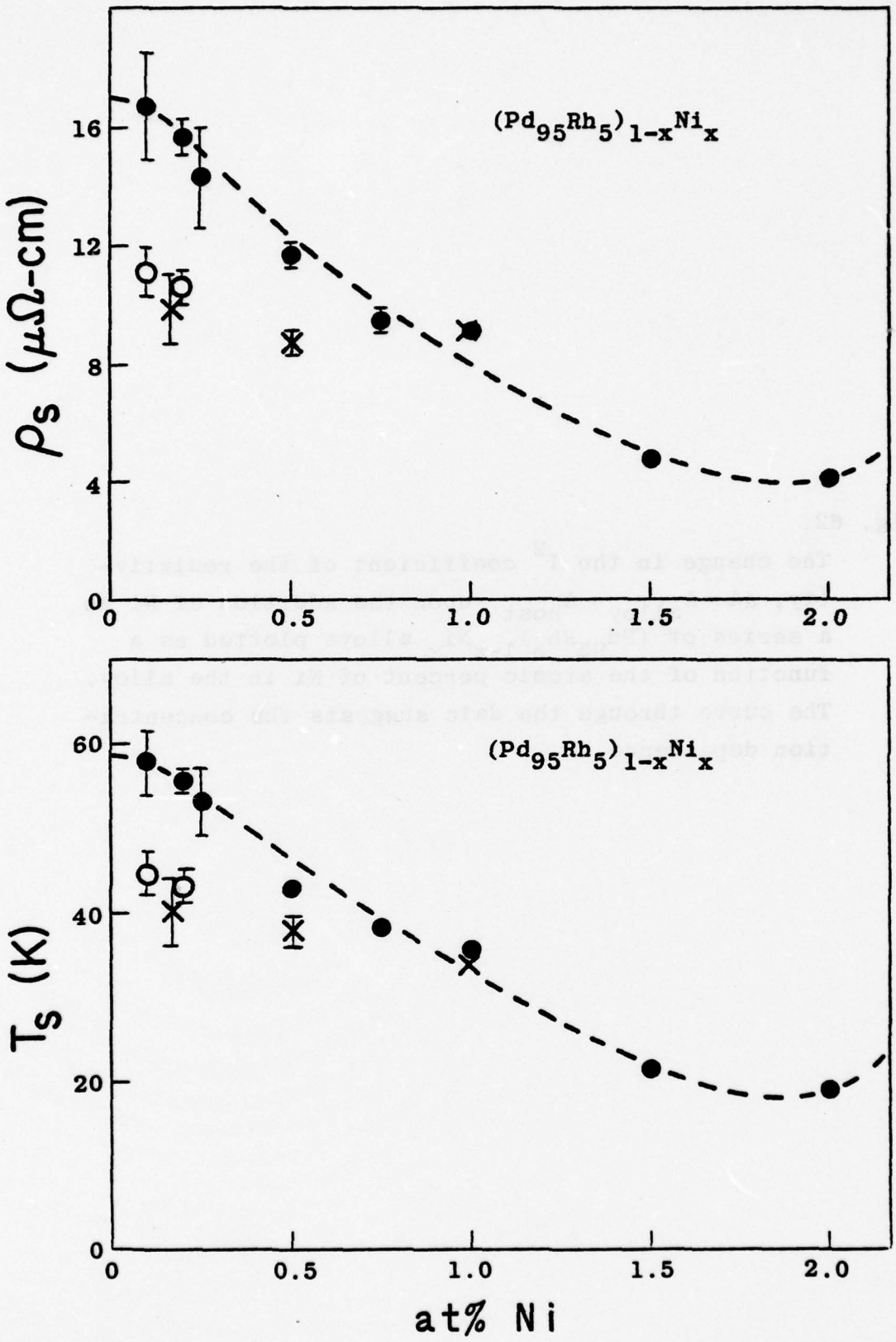
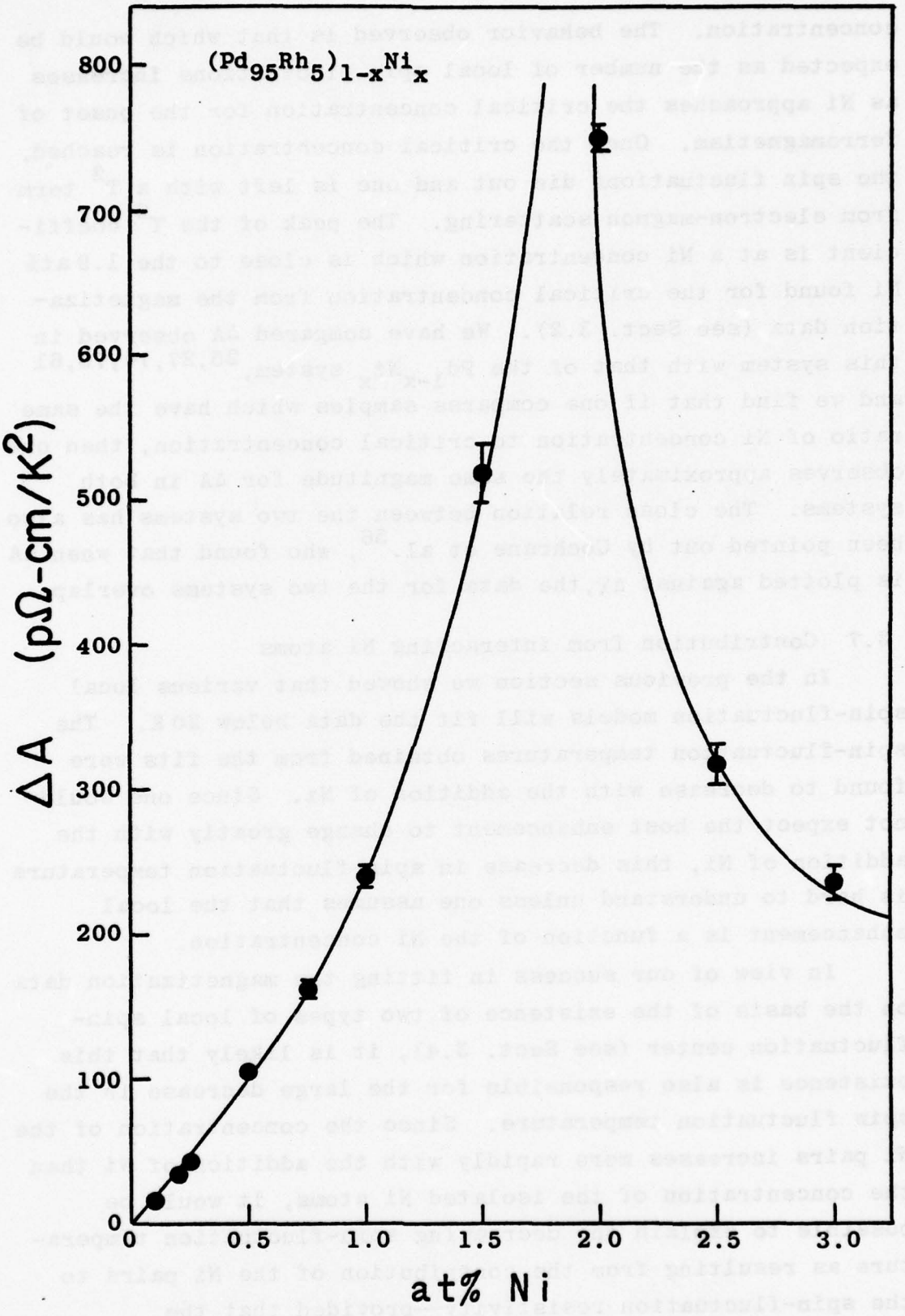

$(Pd_{95}Rh_5)_{1-x}Ni_x$
ρ_s ($\mu\Omega$-cm)
16
12
8
4
0
0
0.5
1.0
1.5
2.0
$(Pd_{95}Rh_5)_{1-x}Ni_x$
T_s (K)
60
40
20
0
0
0.5
1.0
1.5
2.0
at% Ni

Fig. 62.

The change in the T^2 coefficient of the resistivity, $\Delta A = A_{alloy} - A_{host}$, upon the addition of Ni to a series of $(Pd_{95}Rh_5)_{1-x}Ni_x$ alloys plotted as a function of the atomic percent of Ni in the alloy. The curve through the data suggests the concentration dependence.


$(Pd_{95}Rh_5)_{1-x}Ni_x$
ΔA (pΩ-cm/K²)
800
700
600
500
400
300
200
100
0
0
0.5
1.0
1.5
2.0
2.5
3.0
at% Ni

concentration. The behavior observed is that which would be expected as the number of local spin fluctuations increases as Ni approaches the critical concentration for the onset of ferromagnetism. Once the critical concentration is reached, the spin fluctuations die out and one is left with a T^2 term from electron-magnon scattering. The peak of the T^2 coefficient is at a Ni concentration which is close to the 1.9 at% Ni found for the critical concentration from the magnetization data (see Sect. 3.2). We have compared ΔA observed in this system with that of the $Pd_{1-x}Ni_x$ system,[25,27,74,75,61] and we find that if one compares samples which have the same ratio of Ni concentration to critical concentration, then one observes approximately the same magnitude for ΔA in both systems. The close relation between the two systems has also been pointed out by Cochrane et al.[56], who found that when ΔA is plotted against $\Delta\chi$, the data for the two systems overlap.

3.7 Contribution from interacting Ni atoms

In the previous section we showed that various local spin-fluctuation models will fit the data below 20 K. The spin-fluctuation temperatures obtained from the fits were found to decrease with the addition of Ni. Since one would not expect the host enhancement to change greatly with the addition of Ni, this decrease in spin-fluctuation temperature is hard to understand unless one assumes that the local enhancement is a function of the Ni concentration.

In view of our success in fitting the magnetization data on the basis of the existence of two types of local spin-fluctuation center (see Sect. 3.4), it is likely that this existence is also responsible for the large decrease in the spin fluctuation temperature. Since the concentration of the Ni pairs increases more rapidly with the addition of Ni than the concentration of the isolated Ni atoms, it would be possible to explain the decreasing spin-fluctuation temperature as resulting from the contribution of the Ni pairs to the spin-fluctuation resistivity—provided that the

spin-fluctuation temperature of a Ni pair is lower than the spin-fluctuation temperature of an isolated Ni atom.

There are two other conditions that must be fulfilled for the model to be consistent with the data. First, the contribution to the spin-fluctuation resistivity from the Ni pairs should be proportional to the concentration of the Ni pairs, and, second, the spin-fluctuation temperature of the Ni pairs should be roughly independent of Ni concentration. We can check to see if these condtions are met by subtracting from the resistivity data the following: the resistivity of the host, the residual resistivity due to the Ni, and the spin-fluctuation resistivity due to the isolated Ni atoms. The subtraction of the first two contributions yields ρ_I, which was given in the previous section. The last contribution is determined from the Kaiser-Doniach fit to the data in the limit of $c \to 0$. Extrapolating to $c=0$ the curves for ρ_s and T_s given in Fig. 61 yields $\rho_s = 17.0\ \mu\Omega$-cm and $T_s = 58.6$ K. Substituting these parameters into the Kaiser-Doniach expression for the spin-fluctuation resistivity (Eq. 1.171) and replacing c in this expression by the concentration of the noninteracting Ni atoms, $c(1-c)^n$, yields the contribution to the spin-fluctuation resistivity due to the noninteracting Ni atoms. Subtracting this from the data for ρ_I yields the contribution to the spin-fluctuation resistivity due to the interacting Ni atoms, which for concentration $\leq 1\frac{1}{2}$ at% Ni consists mostly of Ni pairs. This resistivity, $\Delta\rho_I$, is shown in Figs. 63 and 64 for the case n=18 (see Sect. 3.4 for a discussion of the most likely value for n which would be consistent with the magnetization data).

The spin-fluctuation temperature which is to be associated with the Ni pairs can be found by replacing c in the Kaiser-Doniach expression for the spin-fluctuation resistivity with the concentration of the Ni pairs, $nc^2(1-c)^{n-1}$ for n=18, and fitting this expression to the $\Delta\rho_I$ data. With the exception of the 2 at% Ni sample, a good fit to the data was obtained up to ~10 K. Beyond this temperature the data falls

Fig. 63.

The contribution to the temperature dependent part of the resistivity from the interacting Ni atoms in a series of $(Pd_{95}Rh_5)_{1-x}Ni_x$ alloys plotted as a function of the temperature. The atomic percent of Ni in each alloy labels the appropriate curve. Data points below 4.3 K have been omitted in this figure for clarity, but are shown in the following figure. With the exception of the 2% Ni sample the curves through the data are a least squares fit of Eq. 1.171 to the data below 10 K. Only data below 6.5 K was used in fitting the data for the 2% Ni sample.

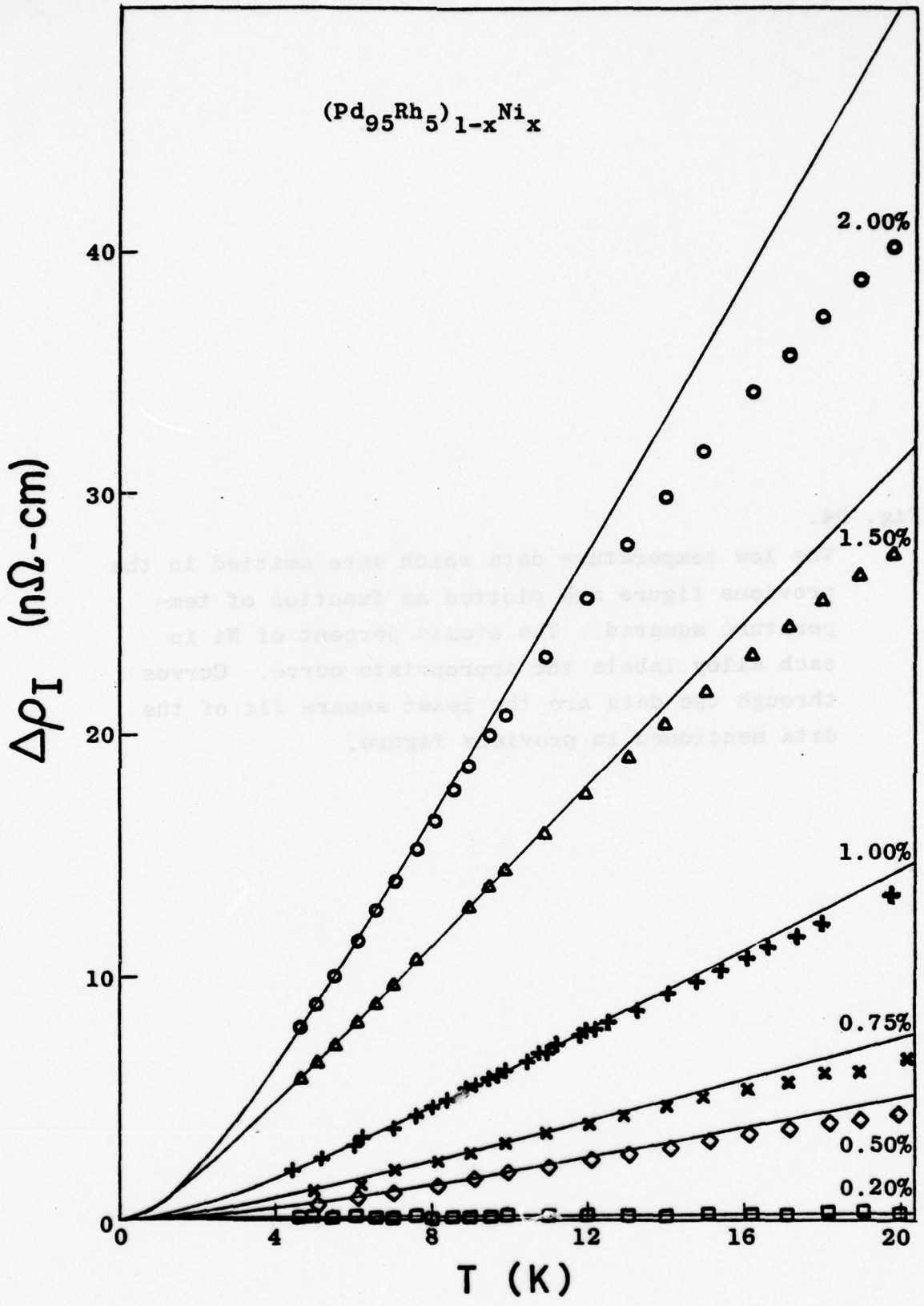
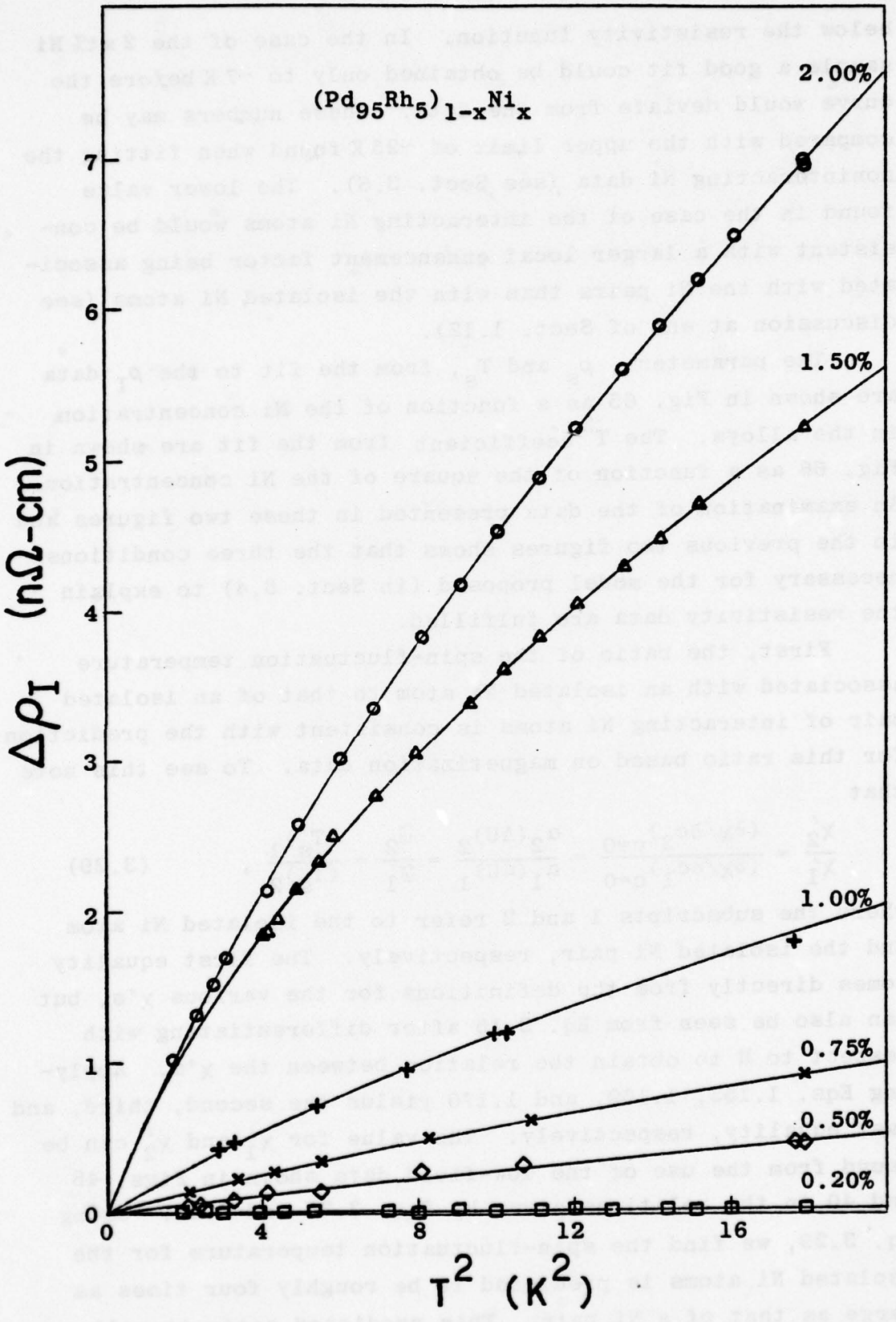

$(Pd_{95}Rh_5)_{1-x}Ni_x$
2.00%
1.50%
1.00%
0.75%
0.50%
0.20%
$\Delta\rho_I$ (nΩ-cm)
T (K)
0
10
20
30
40
0
4
8
12
16
20

Fig. 64.

The low temperature data which were omitted in the previous figure are plotted as function of temperature squared. The atomic percent of Ni in each alloy labels the appropriate curve. Curves through the data are the least square fit of the data mentioned in previous figure.


$(Pd_{95}Rh_5)_{1-x}Ni_x$
2.00%
1.50%
1.00%
0.75%
0.50%
0.20%
$\Delta\rho_I$ (nΩ-cm)
T^2 (K^2)
0
1
2
3
4
5
6
7
0
4
8
12
16

below the resistivity function. In the case of the 2 at% Ni sample a good fit could be obtained only to ~7 K before the curve would deviate from the data. These numbers may be compared with the upper limit of ~25 K found when fitting the noninteracting Ni data (see Sect. 3.6). The lower value found in the case of the interacting Ni atoms would be consistent with a larger local enhancement factor being associated with the Ni pairs than with the isolated Ni atoms (see discussion at end of Sect. 1.12).

The parameters, ρ_s and T_s, from the fit to the ρ_I data are shown in Fig. 65 as a function of the Ni concentration in the alloys. The T^2 coefficient from the fit are shown in Fig. 66 as a function of the square of the Ni concentration. An examination of the data presented in these two figures and in the previous two figures shows that the three conditions necessary for the model proposed (in Sect. 3.4) to explain the resistivity data are fulfilled.

First, the ratio of the spin-fluctuation temperature associated with an isolated Ni atom to that of an isolated pair of interacting Ni atoms is consistent with the prediction for this ratio based on magnetization data. To see this note that

$$\frac{\chi_2'}{\chi_1'} = \frac{(\partial\chi/\partial c_2)_{c=0}}{(\partial\chi/\partial c_1)_{c=0}} = \frac{\alpha_2(\Delta U)_2}{\alpha_1(\Delta U)_1} = \frac{\tilde{\omega}_2}{\tilde{\omega}_1} = \frac{(T_s)_1}{(T_s)_2} , \qquad (3.29)$$

where the subscripts 1 and 2 refer to the isolated Ni atom and the isolated Ni pair, respectively. The first equality comes directly from the definitions for the various χ's, but can also be seen from Eq. 3.15 after differentiating with respect to H to obtain the relation between the χ's. Applying Eqs. 1.153, 1.169, and 1.170 yields the second, third, and last equality, respectively. The value for χ_1' and χ_2' can be found from the use of the low-field data shown in Figs. 48 and 40 in the relations given by Eqs. 3.20 and 3.21. Using Eq. 3.29, we find the spin-fluctuation temperature for the isolated Ni atoms is predicted to be roughly four times as large as that of a Ni pair. This predicted ratio is well

within that which is experimentally observed from the resistivity data: $(T_s)_1 = 59\,K \pm 4\,K$, and $(T_s)_2 = 18\,K \pm 8\,K$.

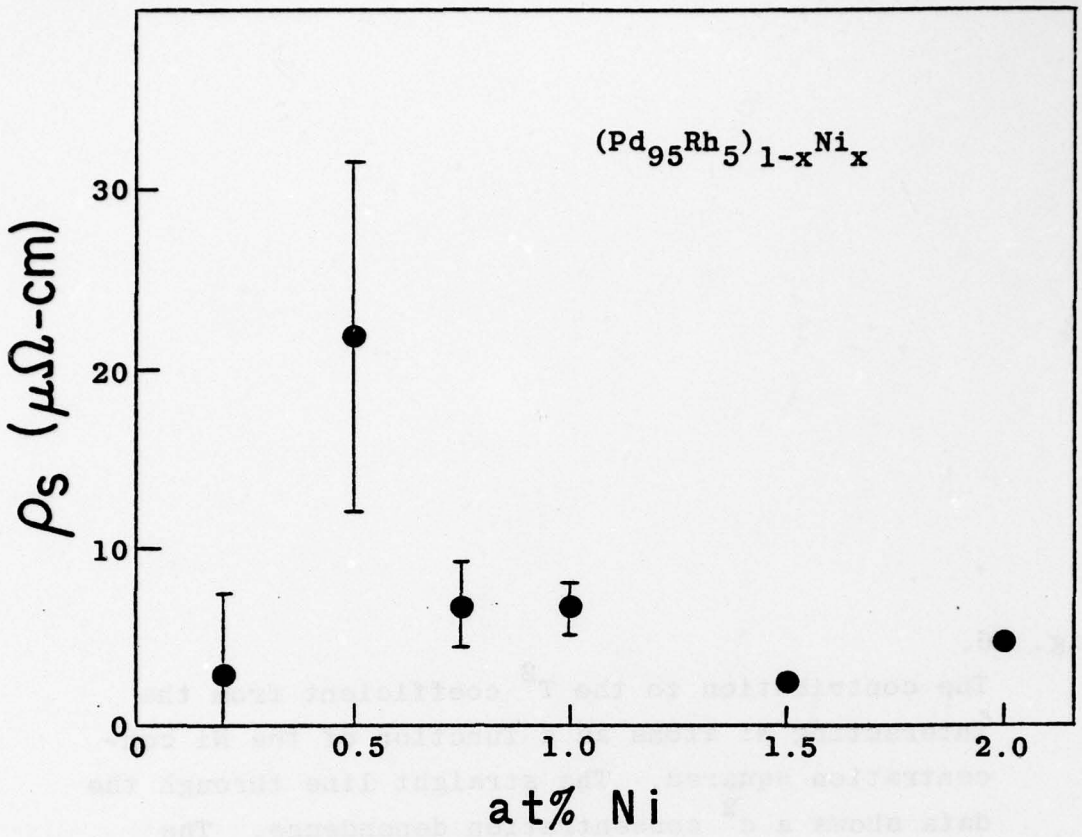
Second, the spin-fluctuation temperature of the Ni pairs (Fig. 65) is roughly independent of the Ni concentration, which is what we would expect if the interacting Ni atoms are to consist mostly of Ni pairs as indicated by magnetization results for those alloys with $< 1\frac{1}{2}$ at% Ni.

Lastly, as predicted by the model, the temperature-dependent contribution of the interacting Ni atoms to the resistivity increases approximately as the square of the Ni concentration. This c^2 dependence can be seen from various aspects of the data. First, a direct comparison at a fixed temperature of the various values of the resistivities given in Figs. 63 and 64 shows the c^2 dependence. (The 2 at% Ni sample is an exception to this statement, but it is ferromagnetic and would therefore not be expected to be consistent with the model.) Second, the fact that ρ_s (Fig. 65) is roughly independent of Ni concentration implies that the resistivity, $\Delta\rho_I$, is proportional to c^2. (Recall that, to fit the data, c in Eq. 1.171 was replaced by the concentration of Ni pairs.) Third, the fact that the contribution to the T^2 coefficient from the interacting Ni atoms is proportional to c^2 (see Fig. 66) shows that the resistivity in the T^2 region has a c^2 dependence.

In the above analysis, we have taken n=18 which is equal to the total number of nearest and next-nearest neighbors in the system and which implies that the two Ni atoms interact to form a coupled pair if they are either nearest or next-nearest neighbors (see Sect. 3.4). We have also tried to fit the data with n ranging from n=12 to n=42, which corresponds to the number of nearest neighbors and the total number of near neighbors up to and including third-nearest neighbors, respectively. Within the errors of the experiment both magnetization and the resistivity data remain consistent with the model for this range of n. As n increases from 12 to 42, the average value of T_s increases from ~15 K to ~25 K; however,

Fig. 65.

Least-square-fitting parameters, ρ_s and T_s, obtained from the previous fitting of the contribution to the resistivity from interacting Ni atoms are shown as function of the atomic percent of Ni in $(Pd_{95}Rh_5)_{1-x}Ni_x$.


$(Pd_{95}Rh_5)_{1-x}Ni_x$
ρ_S ($\mu\Omega$-cm)
30
20
10
0
0
0.5
1.0
1.5
2.0
at% Ni

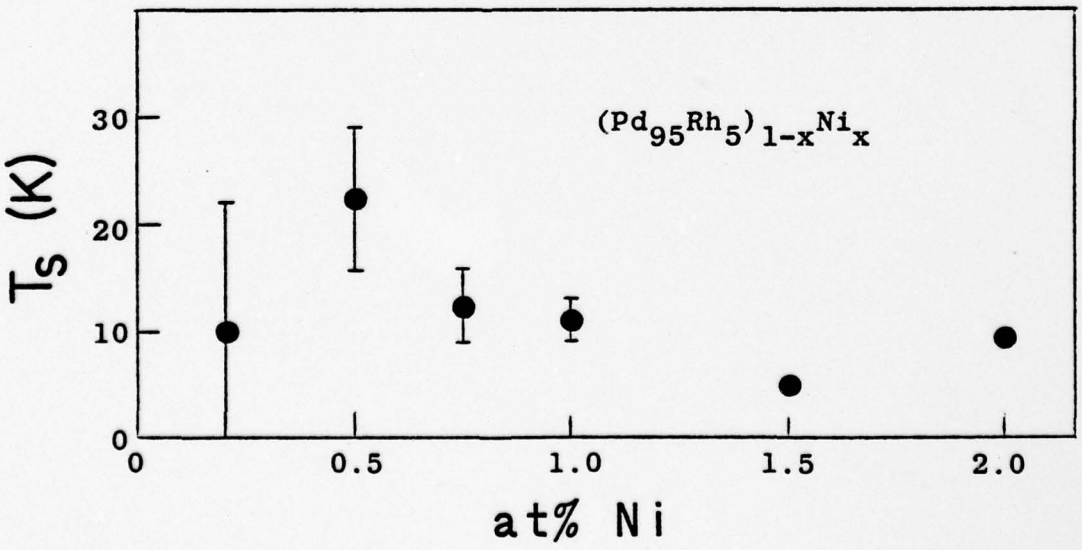
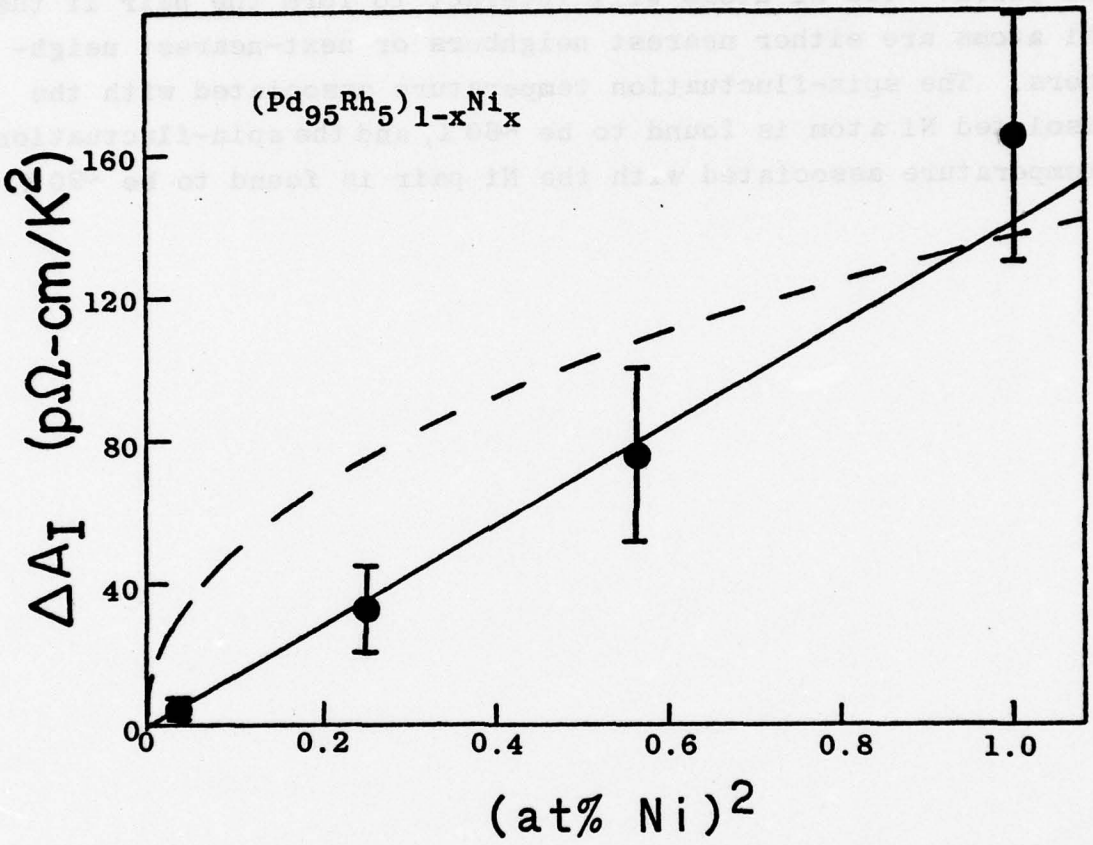

$(Pd_{95}Rh_5)_{1-x}Ni_x$
T_S (K)
30
20
10
0
0
0.5
1.0
1.5
2.0
at% Ni

Fig. 66.

The contribution to the T^2 coefficient from the interacting Ni atoms as a function of the Ni concentration squared. The straight line through the data shows a c^2 concentration dependence. The dash line shows the concentration dependence of the contribution *from the noninteracting* Ni atoms to the T^2 coefficient.


$(Pd_{95}Rh_5)_{1-x}Ni_x$
ΔA_I (pΩ-cm/K^2)
160
120
80
40
0
0
0.2
0.4
0.6
0.8
1.0
(at% Ni)^2

at the upper end of this range T_s tends to decrease with increasing Ni content at a rate which is faster than would be expected from the model.

In conclusion, we find, that for $(Pd_{95}Rh_5)_{1-x}Ni_x$ alloys with Ni concentration of $\leq$1 at%, both the magnetization data and the resistivity data are consistent with a model which describes the local spin fluctuations in these alloys as centered around isolated single Ni atoms and around isolated Ni pairs. Two Ni atoms will interact to form the pair if the Ni atoms are either nearest neighbors or next-nearest neighbors. The spin-fluctuation temperature associated with the isolated Ni atom is found to be ~60 K, and the spin-fluctuation temperature associated with the Ni pair is found to be ~20 K.

C. Magnetization and Resistivity

In the final two sections of this chapter, we discuss the implications of both the magnetization and resistivity data in regard to the local enhancement model. In the first of these two sections, values of the enhancement parameters for the dilute $(Pd_{95}Rh_5)_{1-x}Ni_x$ system are determined and compared with corresponding values for the $Pd_{1-x}Ni_x$ system. In the second section the field dependence of the data is discussed, and it is suggested that Ni-Ni interactions yield a better explanation of the data than a shifting of the Fermi level with Ni concentration.

3.8 Estimation of Enhancement Parameters

The static susceptibility in the uniform enhancement model is given by (see Eq. 1.94)

$$\chi = \frac{\chi_o}{1-UN(E_F)} , \qquad (3.30a)$$

where χ_o is the unenhanced Pauli susceptibility, $N(E_F)$ is the density of d states at the Fermi level per atom per spin-state, and U is the intra-atomic Coulomb interaction parameter. Since the Stoner enhancement factor is defined by $S \equiv \chi/\chi_o$, the uniform enhancement model yields

$$S = \frac{1}{1-UN(E_F)} . \qquad (3.30b)$$

Using the results of the band calculation of Andersen[76] to obtain the unenhanced susceptibility and dividing this susceptibility into the experimentally determined enhanced susceptibility yields S~10 for Pd. Since the susceptibility of $Pd_{95}Rh_5$ ($\sim 14\times10^{-6}$ emu/g) is roughly twice as large as that of Pd ($\sim 7\times10^{-6}$ emu/g) and since the density of states does not differ greatly between these two materials (~10% on the basis of the rigid band model[76]; ~5% on the basis of the specific heat data[77]), one expects S~20 for $Pd_{95}Rh_5$. Such a factor does not seem unreasonable since only a 5% increase in the product $UN(E_F)$ is sufficient to yield this result.

On the other hand, if we assume that S=20 is correct for the $Pd_{95}Rh_5$ host, then we are unable within the error of the experimental data to fit the local enhancement model to both the magnetization and resistivity data. This failure of the model to fit the data is most likely the result of the assumption that the $Pd_{95}Rh_5$ host could be treated as a uniformly enhanced material. Experimental data[78] and theoretical calculations[79,80] indicate that the Rh atom exhibits a much larger susceptibility enhancement than the Pd atom. If we assume the susceptibility of the $Pd_{95}Rh_5$ alloy consists of (1) a uniformly enhanced susceptibility associated with the background and (2) a locally enhanced susceptibility associated with the Rh atoms, then we can fit the local enhancement model to the $(Pd_{95}Rh_5)_{1-x}Ni_x$ data. Thus, it appears that $Pd_{95}Rh_5$ has a uniform enhancement which, although greater than Pd, is not as large as first thought.

The local enhancement parameters for the dilute $(Pd_{95}Rh_5)_{1-x}Ni_x$ alloy system can be estimated in a manner analogous to that given in Appendix D for the dilute $Pd_{1-x}Ni_x$ system. We assume a uniform background susceptibility in the $Pd_{95}Rh_5$ host to be 25% greater than that of pure Pd; the remaining part of the susceptibility of the host is assumed to arise from the local enhancement of the Rh atoms. These assumptions are in agreement with the CPA calculations of J. van der Rest et al.[80] for the $Pd_{95}Rh_5$ alloy and yield

$$S=12\tfrac{1}{2} \ , \tag{3.31}$$

and

$$UN(E_F)=0.92 \ . \tag{3.32}$$

With a uniform background susceptibility of $\chi_U=8\tfrac{3}{4}\times10^{-6}$ emu/g and with the data yielding (see Figs. 45 and 47) $d\chi/dc = (1020\pm50)\times10^{-6}$ emu/g, we have $\chi_U^{-1}\, d\chi/dc = 117\pm6$. Proceeding as in Appendix D yields

$$\frac{\Delta U}{U} = 0.33 \ , \tag{3.33}$$

$$\alpha = 30\pm2 \ , \tag{3.34}$$

and $\bar{\chi}(0)/N(E_F) = 3.1$.

That these values are consistent with the resistivity data can be seen as follows. Plotting $\Delta A/c$ as a function of c and taking the limit as $c \to 0$, we have

$$\left.\frac{dA}{dc}\right|_{c=0} = (150\pm5)\times10^{-10}\ \Omega\text{-cm/K}^2 \qquad (3.35)$$

for the $(Pd_{95}Rh_5)_{1-x}Ni_x$ system and

$$\left.\frac{dA}{dc}\right|_{c=0} = (120\pm15)\times10^{-10}\ \Omega\text{-cm/K}^2 \qquad (3.36)$$

for the $Pd_{1-x}Ni_x$ system.[25,27,60,61] From the local enhancement model (see Eq. C7 in Appendix C),

$$\left.\frac{dA}{dc}\right|_{c=0} = b\left[\alpha\,\frac{\Delta U}{U}\,SUN(E_F)\right]^2 , \qquad (3.37)$$

where, to first order, b is independent of the enhancement parameters. We find b for the $Pd_{1-x}Ni_x$ system by using the results from the data (Eq. 3.36) and the enhancement parameters in Appendix D. Assuming b to be equal in the two systems and using the enhancement parameters given above yield a prediction of $(167\pm40)\times10^{-10}\Omega$-cm/K^2 for dA/dc in good agreement with the expermental result (Eq. 3.35).

In the above estimation of the enhancement parameters we assumed that the uniform background susceptibility for the $Pd_{95}Rh_5$ alloy to be 25% greater than the susceptibility of Pd; however a uniform background susceptibility ranging from 20% to 50% greater than Pd would yield enhancement parameters consistent with the data. Assuming the uniform susceptibility increases from a value 20% greater than that of Pd to a value 50% greater than that of Pd, we find the data yields the following range for the enhancement parameters: S increases from 12 to 15, $UN(E_F)$ increases from 0.92 to 0.93, $\Delta U/U$ decreases from 0.34 to 0.31, α decreases from 33 to 23, and U at the Ni site, U_{Ni}, changes such that $U_{Ni}N(E_F)$ decreases from 1.23 (which is the same value of $U_{Ni}N(E_F)$ estimated for $Pd_{1-x}Ni_x$ system) to 1.22.

It is of interest to note that, if we use the procedures discussed in this section to estimate the ratio of the

spin-fluctuation temperature of an isolated Ni atom in the $Pd_{1-x}Ni_x$ system to that of an isolated Ni atom in the $(Pd_{95}Rh_5)_{1-x}Ni_x$ system (see Eqs. 1.170 and 1.169), then we find that the spin-fluctuation temperature associated with an isolated Ni atom in the $Pd_{1-x}Ni_x$ system is predicted to be

$$(T_s)_{Pd_{1-x}Ni_x} = 74 \pm 12\,K\ , \qquad (3.38)$$

which is in good agreement with the value of 76 found by Kaiser and Doniach[38] after fitting the data of Schindler and Rice[25].

Lastly, we can use the $(Pd_{95}Rh_5)_{1-x}Ni_x$ data to evaluate the local enhancement parameters associated with an isolated pair of interacting Ni atoms. The error in the evaluation of the local enhancement factor α_2 is necessarily large because of the large experimental uncertainty associated with the contribution of the Ni pair to the susceptibility and resistivity data. On the other hand, the parameter $\Delta U/U$ is known to increase by less than 5% since an increase of 5% is sufficient to make α diverge. The ratio of the local enhancement factor of the Ni pair to that of the isolated Ni atom can be evaluated by using the susceptibility data and Eq. 3.29, by using the spin-fluctuation temperatures and Eq. 3.29, or by using the T^2 coefficients and Eq. 3.37. We find α_2/α_1 to be between 3 & 8, 2 & 6, and 2 & 4, respectively.

3.9 Field Dependence

The magnetic susceptibility and the T^2 coefficient in the electrical resistivity of $(Pd_{95}Rh_5)_{1-x}Ni_x$ alloys vary strongly both with Ni concentration and magnetic field (see Fig. 43 in Sect. 3.3 for the susceptibility data and see Ref. 69 for the resistivity data). Purwins et al.[61] have shown that for $Pd_{1-x}Ni_x$ alloys ($x \lesssim 0.01$) this strong dependence on the Ni concentration can be explained if the Schulz[60] model is generalized to include a Fermi level shift which depends on the Ni concentration as well as the magnetic field. In this section we show that the field dependence of the

$(Pd_{95}Rh_5)_{1-x}Ni_x$ data ($x \leq 0.01$) can be explained without generalizing the Schulz model if one takes into account the Ni-Ni interactions in these alloys.

By extending the local enhancement model of Lederer and Mills (see Sects. 1.10 and 1.12) to include the presence of a magnetic field, Schulz was able to show that the change in the T^2 coefficient, ΔA, which occurs with the addition of Ni, has a field dependence which is given by[61]

$$\frac{\Delta A(H)}{\Delta A(0)} = \frac{1}{3(1+3\tau^2)^2} + \frac{2}{3(1+\tau^2)^2} , \tag{3.39}$$

where $\tau+\tau^3 = H/H_s$,

$$H_s = \left[(1-J)\tau_o(\lambda/\delta J)^3\mu_B^2\sigma\right]^{-\frac{1}{2}} , \tag{3.40}$$

$J=UN(E_F)$, $\delta J=\Delta U\, N(E_F)$, $\tau_o=(J+\delta J)/\delta J$, $\lambda=\chi^{-1}\, d\chi/dc$,

$$\sigma = -\frac{1}{6}\left\{\frac{N''(E_F)}{N(E_F)} - \frac{3}{2}\left[\frac{N'(E_F)}{N(E_F)}\right]^2\right\} , \tag{3.41}$$

$N'(E_F) = dN(E_F)/dE$, and $N''(E_F) = d^2N(E_F)/dE^2$.

By using the Schulz model, the field dependence susceptibility data, and the zero-field resistivity data, we can predict the field dependence of the T^2 coefficient for $(Pd_{95}Rh_5)_{1-x}Ni_x$ alloys. Writing the contribution to the T^2 coefficient from the Ni atom as

$$\Delta A(H) = A_1(H) + A_2(H) , \tag{3.42}$$

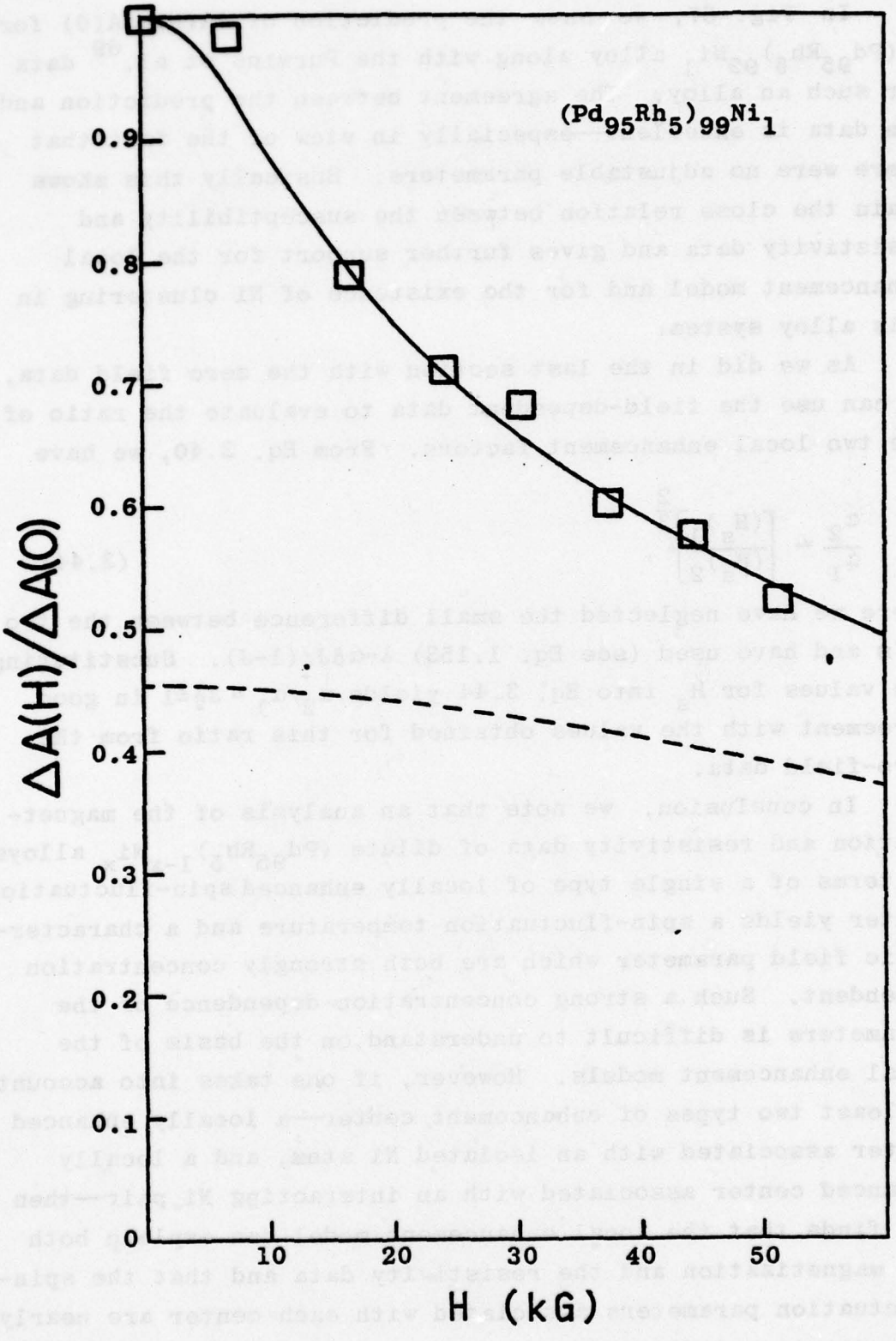
where the subscripts 1 and 2 refer to the contribution from the noninteracting Ni atoms and the interacting Ni atoms, respectively (see Sect. 3.4 for a discussion of the two classes of Ni atom), we then have

$$\frac{\Delta A(H)}{\Delta A(0)} = \frac{A_1(0)}{\Delta A(0)}\frac{A_1(H)}{A_1(0)} + \frac{A_2(0)}{\Delta A(0)}\frac{A_2(H)}{A_2(0)} . \tag{3.43}$$

All the quantities on the right side of the equation are known. The ratios $A_i(0)/\Delta A(0)$, $i=1,2$, can be determined from the data in Fig. 66, and the field-dependent ratios $A_i(H)/A_i(0)$, $i=1,2$, can be determined from Eq. 3.39 after one uses the values for H_s (see discussion concerning Fig. 48

Fig. 67.

The scaled contribution from the Ni atoms to the T^2 coefficient of the electrical resistivity shown as a function of the magnetic field intensity. Based on the field dependence of the susceptibility data and the separation of the resistivity data into contributions from isolated Ni atoms and Ni pairs, the field dependence of the T^2 coefficient for a $(Pd_{95}Rh_5)_{99}Ni_1$ alloy is predicted to be that shown by the solid curve. The data of Purwins et al.[69] for such an alloy are shown by the squares. The dashed curve shows the predicted contribution from the noninteracting Ni atoms.


$(Pd_{95}Rh_5)_{99}Ni_1$
$\Delta A(H)/\Delta A(0)$
0
0.1
0.2
0.3
0.4
0.5
0.6
0.7
0.8
0.9
10
20
30
40
50
H (kG)

in Sect. 3.4) to find the values of $T(H)$.

In Fig. 67, we show the prediction of $\Delta A(H)/\Delta A(0)$ for a $(Pd_{95}Rh_5)_{99}Ni_1$ alloy along with the Purwins et al.[69] data for such an alloy. The agreement between the prediction and the data is excellent—especially in view of the fact that there were no adjustable parameters. Basically this shows again the close relation between the susceptibility and resistivity data and gives further support for the local enhancement model and for the existence of Ni clustering in this alloy system.

As we did in the last section with the zero field data, we can use the field-dependent data to evaluate the ratio of the two local enhancement factors. From Eq. 3.40, we have

$$\frac{\alpha_2}{\alpha_1} \simeq \left[\frac{(H_s)_1}{(H_s)_2}\right]^{\frac{2}{3}}, \qquad (3.44)$$

where we have neglected the small difference between the two δJ's and have used (see Eq. 1.153) $\lambda = \alpha\delta J/(1-J)$. Substituting the values for H_s into Eq. 3.44 yields $\alpha_2/\alpha_1 = 3\frac{1}{2}\pm 1$ in good agreement with the values obtained for this ratio from the zero-field data.

In conclusion, we note that an analysis of the magnetization and resistivity data of dilute $(Pd_{95}Rh_5)_{1-x}Ni_x$ alloys in terms of a single type of locally enhanced spin-fluctuation center yields a spin-fluctuation temperature and a characteristic field parameter which are both strongly concentration dependent. Such a strong concentration dependence of the parameters is difficult to understand on the basis of the local enhancement models. However, if one takes into account at least two types of enhancement center—a locally enhanced center associated with an isolated Ni atom, and a locally enhanced center associated with an interacting Ni pair—then one finds that the local enhancement model can explain both the magnetization and the resistivity data and that the spin-fluctuation parameters associated with each center are nearly concentration independent.

CONCLUDING REMARKS

The measuring of the magnetization and electrical resistivity for a series of $(Pd_{95}Rh_5)_{1-x}Ni_x$ alloys and the analyzing of the data in terms of various models has yielded the following results. For those alloys with Ni concentrations ≤1 at%, the data can be explained by the local enhancement model provided one considers two types of local spin-fluctuation center in an enhanced host: the first type consists of an isolated Ni atom, and the second type consists of a pair of interacting Ni atoms. The Ni atoms appear to be randomly distributed throughout each alloy, and two Ni atoms are found to interact to form a coupled pair if they are either nearest or next-nearest neighbors. The local enhancement associated with the Ni pair is found to be roughly 3 or 4 times as large as that associated with the isolated Ni atom. The spin-fluctuation temperature[38] and the characteristic-field parameter[61] associated with the locally enhanced centers are, respectively, $T_s = 59 \pm 4$ K and $H_s = 225 \pm 25$ kG for the isolated Ni atom and $T_s = 18 \pm 8$ K and $H_s = 35 \pm 5$ kG for the isolated Ni pair. The magnetic behavior exhibited by the Ni pair is nearly that of a local moment having a magnitude of $5 \pm 1\ \mu_B$.

Using the local enhancement model in the single impurity limit and comparing the data for this system with that for the $Pd_{1-x}Ni_x$ system, we find 1) the local enhancement factor associated with the Ni impurity to be approximately equal in the two systems, 2) the Stoner enhancement factor for the $Pd_{95}Rh_5$ host to be roughly 25% greater than that for Pd, and 3) the increase in the density of states predicted by the rigid band model to be inconsistent with the data.

Above 1 at% Ni, the following generalizations are consistent with the data: As the Ni concentration increases from 1 to 3 at% Ni, the concentration of the isolated Ni atoms levels

off while the concentration of the Ni pairs rapidly increases, but in this concentration range the number of isolated Ni atoms always exceeds the number of Ni pairs. At the critical concentration (~1.9 at% Ni) the interaction between the Ni pairs and the higher order Ni clusters becomes significant and ferromagnetic alignment begins. At roughly 2½ at% Ni, the moments on the Ni pairs are fully ordered at 4 K. And finally, even though at the highest Ni concentrations the isolated Ni atoms are polarized by the internal field, the magnetization that results from these atoms is far from being saturated at 4 K.

APPENDIX A

LEAST SQUARE FITTING METHOD

The Problem

Given a set of data consisting of N values $Y_i = Y(x_i)$, $i=1,2,\ldots,N$, which were measured at N different values of an independent variable x, and given a fitting function $y(x,b)$ which has the value $y_i(\vec{b}) = y(x_i,\vec{b})$ at x_i, where $\vec{b}$ represents M independent fitting parameters b_j, $j=1,2,\ldots,M$ $(M<N)$, we wish to find $\vec{b}$ such that

$$\sigma = \sum_{i=1}^{N} \{y_i(\vec{b}) - Y_i\}^2$$

is a minimum. Such will be the case when

$$d\sigma = 2 \sum_{i=1}^{N} \sum_{j=1}^{M} \{y_i(\vec{b}) - Y_i\} \frac{\partial y_i(\vec{b})}{\partial b_j} db_j = 0 \ .$$

Since the b_j's are independent this reduces to solving the M equations,

$$\sum_{i=1}^{N} \{y_i(\vec{b}) - Y_i\} \frac{\partial y_i(\vec{b})}{\partial b_j} = 0 \ , \ j=1,2,\ldots,M \ ,$$

for $\vec{b}$.

The Newton-Raphson Method of Solution

In the Newton-Raphson method of solution the M independent equations are approximated by a set of equations which are linear in the unknowns. The solution of these equations is found by standard matrix inversion techniques and the results are used to make a better linear approximation. The process is repeated until the desired accuracy is obtained.

This procedure is outlined in the following steps:

1) Let

$$f_j(\vec{b}) \equiv \sum_{i=1}^{N} \{y_i(\vec{b}) - Y_i\} \frac{\partial y_i(\vec{b})}{\partial b_j} \ ;$$

then the problem is to find the $\vec{b}$ which satisfies the M equations

$$f_j(\vec{b}) = 0 \ , \ j=1,2,\ldots,M$$

and to approximate $f_j(\vec{b})$ with a first order Taylor expansion about an initial guess for $\vec{b}$, say $\vec{b}_o$, i.e.,

$$f_j(\vec{b}) \approx f_j(\vec{b}_o) + \nabla f_j(\vec{b})\Big|_{\vec{b}=\vec{b}_o} \Delta\vec{b} \ ,$$

where $\Delta\vec{b} \equiv \vec{b}-\vec{b}_o$ and

$$\nabla f_j(\vec{b})\Big|_{\vec{b}=\vec{b}_o} \equiv \left(\frac{\partial f_j(\vec{b})}{\partial b_1}\Big|_{\vec{b}=\vec{b}_o}, \frac{\partial f_j(\vec{b})}{\partial b_2}\Big|_{\vec{b}=\vec{b}_o}, \ \ldots, \frac{\partial f_j(\vec{b})}{\partial b_M}\Big|_{\vec{b}=\vec{b}_o} \right) .$$

2) Solve for the root $\vec{b}$ of the approximated functions (now linear in $\vec{b}$), i.e., find $\vec{b}$ such that

$$f_j(\vec{b}_o) + \nabla f_j(\vec{b})\Big|_{\vec{b}=\vec{b}_o} \Delta\vec{b} = 0 \ , \ j=1,2,\ldots,M \ .$$

3) Use the $\vec{b}$ found in step 2 as a new guess for the root $\vec{b}$. Repeat step 1 to find a better approximation for $f_j(\vec{b})$ and repeat step 2 to find the new root, $\vec{b}$.

4) Repeat steps 1, 2, and 3 until $\Delta\vec{b}/\vec{b}$ meets the accuracy required.

The equations given in step 2 can be written out more explicitly by noting that

$$\frac{\partial f_j(\vec{b})}{\partial b_k} = \sum_{i=1}^{N} \frac{\partial y_i(\vec{b})}{\partial b_k} \frac{\partial y_i(\vec{b})}{\partial b_j} + \sum_{i=1}^{N} \{y_i(\vec{b}) - Y_i\} \frac{\partial^2 y_i(\vec{b})}{\partial b_k \, \partial b_j} \ .$$

Then the equation of step 2 becomes

$$\sum_{i=1}^{N} \{y_i(\vec{b}_o) - Y_i\} \frac{\partial y_i(\vec{b})}{\partial b_j}\Big|_{\vec{b}=\vec{b}_o}$$

$$+ \sum_{k=1}^{M} \sum_{i=1}^{N} \left[\frac{\partial y_i(\vec{b})}{\partial b_k} \frac{\partial y_i(\vec{b})}{\partial b_j} + \{y_i(\vec{b}) - Y_i\} \frac{\partial^2 y_i(\vec{b})}{\partial b_k \, \partial b_j} \right]_{\vec{b}=\vec{b}_o} \Delta b_k = 0$$

We can write this as the matrix equation

$$\mathbf{G}\Delta\vec{b} = \vec{R} \ ,$$

where the matrix elements of $\mathbf{G}$ are

$$G_{jk} = \sum_{i=1}^{N}\left[\frac{\partial y_i(\vec{b})}{\partial b_j}\frac{\partial y_i(\vec{b})}{\partial b_k} + \{y_i(\vec{b}) - Y_i\}\frac{\partial^2 y_i(\vec{b})}{\partial b_k\,\partial b_j}\right]_{\vec{b}=\vec{b}_o}$$

and the vector components of $\vec{R}$ are

$$R_j = \sum_{i=1}^{N}\{Y_i - y_i(\vec{b}_o)\}\frac{\partial y_i(\vec{b})}{\partial b_j}\Big|_{\vec{b}=\vec{b}_o} .$$

Solving this matrix equation yields the change in $\vec{b}_o$ necessary to arrive at the first approximation for $\vec{b}$.

There are two observations we would like to make. First, whenever $y_i(\vec{b})$ is linear in the b_j's, the first order Taylor expansion is exact, and therefore only one iteration is needed, i.e., if

$$y_i(\vec{b}) = c_{1i}b_1 + c_{2i}b_2 + \ldots + c_{Mi}b_M \ ,$$

then

$$f_j(\vec{b}) = \sum_{i=1}^{N}\{y_i(b_o) - Y_i\}c_{ji} + \sum_{i=1}^{N}\sum_{k=1}^{M}c_{ji}c_{ki}\Delta b_k$$

is exact, and $f_j(\vec{b}) = 0$, $j=1,2,\ldots,M$, can be solved for $\vec{b}$ directly. Second, for most cases of interest the term

$$\sum_{i=1}^{N}\{y_i(\vec{b}) - Y_i\}\frac{\partial^2 y_i(\vec{b})}{\partial b_k\,\partial b_j}$$

in G_{jk} can be neglected. The reason for this is that in a good fit $y_i(\vec{b}) - Y_i$ will have an approximately random scattering of positive and negative values about zero, whereas the partial derivative will generally be found to be a slowly varying function of x. Thus, the sum over i will tend to have canceling terms. (In the linear case, mentioned above, only the first partial derivatives are non-zero and therefore the above mentioned term is identically zero.)

APPENDIX B

EVALUATION OF THE KAISER-DONIACH RESISTIVITY FUNCTION

The Kaiser-Doniach function is given by (see Eq. 1.171)

$$\tilde{\rho}(\tilde{T}) = \frac{1}{\tilde{T}} \int_{-\infty}^{\infty} \frac{d\tilde{\omega}\ \tilde{\omega}^2}{(e^{\tilde{\omega}/\tilde{T}}-1)(1-e^{-\tilde{\omega}/\tilde{T}})(1-\tilde{\omega}^2)} \ . \tag{B.1}$$

This integral is most easily evaluated[38] when expressed in terms of the trigamma function, $\psi(x)$, for then

$$\tilde{\rho}(\tilde{T}) = \frac{\pi\tilde{T}}{2} - \frac{1}{2} + \frac{1}{4\pi\tilde{T}}\psi\left(1+\frac{1}{2\pi\tilde{T}}\right) \ . \tag{B.2}$$

We evaluate the trigamma function, first, by noting that for $x>1$,

$$\psi(x) = \frac{1}{x} + \frac{1}{2x^2} + \sum_{n=1}^{\infty} \frac{B_{2n}}{x^{2n+1}} \ , \tag{B.3}$$

where B_{2n} are the Bernoulli numbers and, second, by noting

$$\psi(x) = \psi(x+1) + \frac{1}{x^2} \ . \tag{B.4}$$

Then, by using these recursion and expansion relations for $\psi(x)$, we have

$$\psi(x) \simeq \sum_{n=0}^{9} \frac{1}{(x+n)^2} + \frac{1}{x+10} + \frac{1}{2(x+10)^2} + \sum_{n=1}^{3} \frac{B_{2n}}{(x+10)^{2n+1}} \ , \tag{B.5}$$

where $B_2=1/6$, $B_4=-1/30$, and $B_6=1/42$. This expression, which is accurate to nine significant figures in the range $x>1$, was used in evaluating $\tilde{\rho}(\tilde{T})$.

A similar expression was used to evaluate the digamma function in the Rivier and Zlatic expression for the spin-fluctuation resistivity (Eq. 1.188).

APPENDIX C

T^2 COEFFICIENT OF THE SPIN-FLUCTUATION RESISTIVITY IN THE LEDERER-MILLS AND KAISER-DONIACH MODELS

The temperature dependence of the spin-fluctuation resistivity at low temperatures can be obtained from

$$\rho = \frac{b_o N(E_F)\beta}{\chi_o k_F^4} \int_0^\infty d\omega \int_0^{2k_F} dq\, q^3 \frac{\omega A(q,\omega)}{(e^{\beta\omega}-1)(1-e^{-\beta\omega})} \qquad (C.1)$$

(see Eqs. 1.161 and 1.163 is Sect. 1.12) as follows. First, note that as ω becomes larger than the thermal energy $k_B T$, the Bose factor, $(e^{\beta\omega}-1)^{-1}$, approaches zero exponentially, and, as a result, the spectral density function need be considered only for values of ω which are $\lesssim k_B T$. For small values of ω, the spectral density function divided by ω is independent of ω; thus for low temperatures the integration can be performed without any further knowledge of the functional form of the spectral density function. After integrating over ω, one finds that the low-temperature resistivity is given by

$$\rho = \left[\frac{\pi^2 b_o N(E_F) k_B^2}{3\chi_o k_F^4} \int_0^{2k_F} dq\, q^3 \frac{A(q,\omega)}{\omega}\right] T^2 \quad , \text{ as } T\to 0, \text{ and } \omega\to 0 \; . \qquad (C.2)$$

Thus, the T^2 coefficient is given by

$$A = \frac{\pi^2 b_o N(E_F) k_B^2}{3\chi_o k_F^4} \int_0^{2k_F} dq\, q^3 \frac{A(q,\omega)}{\omega} \quad , \; \omega\to 0 \; . \qquad (C.3)$$

(There should be no confusion between the two A's since the spectral density function is always written as a function of q,ω). The change in A arising from the addition of Ni is

$$\Delta A = \frac{2b_o N(E_F) k_B^2}{3\chi_o k_F^4} \int_0^{2k_F} dq\, q^3 \frac{A_I(q,\omega)}{\omega} \quad , \quad \omega \to 0 \qquad (C.4)$$

(see Eqs. 1.164 through 1.166). For a large local enhancement and small ω the spectral density function, $A_I(q,\omega)$, given in Eq. 1.166 can be approximated[19] as

$$A_I(q,\omega) = \frac{2cN(E_F)}{\chi_o |F(q)|^2} \{\Delta U\alpha\}^2 \{\mathrm{Re}\,\chi(q,0)\}^2 \mathrm{Im}\{\bar{\chi}(\omega)\} \quad . \qquad (C.5)$$

By combining Eqs. C.4 and C.5, we have the desired result

$$\frac{\Delta A}{c} = \frac{2\pi^2 b_o k_B^2}{3k_F^4} \frac{\{N(E_F)\Delta U\alpha\}^2}{\chi_o^2} \left.\frac{\mathrm{Im}\{\bar{\chi}(\omega)\}}{\omega}\right|_{\omega\to 0} \int_0^{2k_F} dq\, q^3 \left[\frac{\mathrm{Re}\,\chi(q,0)}{|F(q)|}\right]^2 , \qquad (C.6)$$

which gives the change in the T^2 coefficient divided by the Ni concentration as a function of 1) the dynamic susceptibility of the host, 2) the change of the intra-atomic Coulomb interaction at the impurity site over that of the host, 3) the local enhancement, and 4) band parameters of the host.

It is convenient to rewrite the above equation as

$$\frac{\Delta A}{c} = b\{\alpha \frac{\Delta U}{U} SUN(E_F)\}^2 \quad , \qquad (C.7)$$

where

$$b = \frac{2\pi^2 b_o k_B^2}{3k_F^4} \left.\frac{\mathrm{Im}\{\bar{\chi}(\omega)\}}{\omega}\right|_{\omega\to 0} \int_0^{2k_F} dq\, q^3 \left[\frac{\mathrm{Re}\,\chi(q,0)}{S\chi_o |F(q)|^2}\right]^2 |F(q)|^2 \quad . \qquad (C.8)$$

We evaluate the integral by using Eqs. 1.92 and 1.89, by using the approximation for F(q) given by Schriempf et al.[27] for Pd, and by taking $2k_F = q_F$. The values of $\bar{\chi}(\omega)$ are found in the manner described in Appendix D. As S becomes greater the increase in $\mathrm{Im}\,\chi(\omega)/\omega$ is nearly offset by the decrease in the integral, so that the product of these two terms is largely independent of S. Thus, the coefficient C is, to first order, independent of the enhancement parameters.

APPENDIX D

ESTIMATION OF THE LOCAL ENHANCEMENT PARAMETERS FOR THE $Pd_{1-x}Ni_x$ SYSTEM

We can estimate the local enhancement parameters in the $Pd_{1-x}Ni_x$ system by comparing the predictions of the local enhancement model with the susceptibility data. From the model (see Sect. 1.10 and Eq. 1.153)

$$\frac{1}{\chi}\frac{d\chi_A}{dc}\bigg|_{c\to 0} = \alpha\frac{\Delta U}{U}SUN(E_F) \ , \tag{D.1}$$

where χ_A is the susceptibility of the alloy, χ is the susceptibility of the Pd host, ΔU is the value of U at the Ni site minus the value of U at the Pd site, S is the Stoner enhancement factor, $N(E_F)$ the density of states at the Fermi level, and α is the local enhancement factor, which is given by

$$\alpha = \{1-\Delta U\bar{\chi}(0)\}^{-1} \ , \tag{D.2}$$

where $\bar{\chi}(\omega)$ is defined by Eq. 1.143. From the band calculation of Andersen[76] and the susceptibility of pure Pd, we have

$$S = 10 \tag{D.3}$$

and

$$UN(E_F) = 0.9 \ . \tag{D.4}$$

Using these values and combining Eqs. D.1 and D.2 yields

$$\frac{1}{\chi}\frac{d\chi_A}{dc}\bigg|_{c\to 0} = \left[1 - 0.9\frac{\Delta U}{U}\frac{\bar{\chi}(0)}{N(E_F)}\right]^{-1} 9\,\frac{\Delta U}{U} \tag{D.5}$$

By changing the sum to an integral in Eg. 1.143, we have

$$\frac{\bar{\chi}(0)}{N(E_F)} = \frac{3}{q_z^3}\int_0^{q_z} dq\, q^2 \frac{\chi(q,0)}{\chi_o |F(q)|^2} \ , \tag{D.6}$$

where q_z is the radius of the Brillouin zone boundary (assumed spherical). After taking $q_z = 2q_F$, using the

approximation for $|F(q)|$ given in Ref. 27, using Eq. 1.92 to evaluate $\chi(q,0)$, and evaluating the above integral, we find

$$\bar{\chi}(0)/N(E_F) = 2.9 \ . \qquad (D.7)$$

Then by using the experimental values for $\chi^{-1}d\chi/dc$, which range from 87 to 115 for $Pd_{1-x}Ni_x$ alloys[25,81,82], we can solve Eq. D.5 for $\Delta U/U$. We find

$$\frac{\Delta U}{U} = 0.37 \ , \qquad (D.8)$$

$$\alpha = 29 \pm 4 \ . \qquad (D.9)$$

Lastly, we find from Eqs. D.4 and D.8

$$U_{Ni}N(E_F) = 1.23 \ , \qquad (D.10)$$

where U_{Ni} is the value of U at the Ni site.

ACKNOWLEDGEMENTS

The author would like to thank his advisors Dr. A. I. Schindler and Prof. R. Segnan for their help and encouragement throughout the course of this work. The author would also like to thank Dr. C. A. Mackliet, Dr. A. C. Ehrlich, Dr. J. T. Schriempf, Dr. C. F. Egan, and Dr. N. C. Koon for helpful discussions throughout the course of this work. Special thanks are due Dr. N. C. Koon for the use of the magnetometer and Mr. S. Cress for the spectrographic analysis of the samples. The author gratefully acknowledges the support of the Naval Research Laboratory, which granted him an Edison Memorial Scholarship to continue his education at The American University.

This report is based on the thesis submitted by the author in partial fulfillment of the requirements for the Ph.D. degree at The American University.

REFERENCES

1. A.H. Wilson, Theory of Metals, (Cambridge University Press, London, 1958), 2nd ed., p. 151.
2. R.M. White, Quantum Theory of Magnetism, (McGraw-Hill, New York, 1970), p. 77.
3. Ibid. p. 69.
4. E.C. Stoner, Proc. Roy. Soc. (London) A165; 372 (1938), A169, 339 (1939).
5. J. Hubbard, Proc. Roy. Soc. Ser. A 276, 238 (1963).
6. A.L. Fetter and J.D. Walecka, Quantum Theory of Many-Particle Systems, (McGraw-Hill, New York, 1971), p. 299.
7. Ibid. p. 66.
8. Ibid. p. 83.
9. Ibid. p. 67.
10. G.C. Wick, Phys. Rev. 80, 268 (1950).
11. J. Goldstone, Proc. Roy. Soc. (London) A239, 267 (1957).
12. A.L. Fetter and J.D. Walecka, op. cit., p. 174.
13. J. Lindhard, Kgl. Danske Videnskab, Selskab, Mat.-Fys. Medd. 28, No. 8 (1954).
14. T. Izuyama, D-J. Kim, and R. Kubo, J. Phys. Soc. Japan 18, 1025 (1963).
15. A.M. Clogston, Phys. Rev. Lett. 19, 583 (1967).
16. R.M. White, op. cit., p. 20.
17. S. Doniach, Proc. Phys. Soc. 91, 86 (1967).
18. P.A. Wolff, Phys. Rev. 124, 1030 (1961).
19. P. Lederer and D.L. Mills, Phys. Rev. 165, 837 (1968).
20. D.L. Mills, M.T. Beal-Monod, and P. Lederer, Magnetism V (Academic Press, New York and London, 1973), p. 89.
21. P. Lederer and D.L. Mills, Solid State Comm. 5, 131 (1967).
22. J. Friedel, Phil. Mag. 43, 153 (1952).
23. N. Berk and J.R. Schrieffer, Phys. Rev. Lett. 17, 433 (1966).
24. S. Doniach and S. Engelsberg, Phys. Rev. Lett. 17, 750 (1966).
25. A.I. Schindler and M.J. Rice, Phys. Rev. 164, 759 (1967).

26. M.J. Rice, Phys. Lett. A26, 86 (1967).

27. J.T. Schriempf, A.I. Schindler, and D.L. Mills, Phys. Rev. 187, 959 (1969).

28. J. Mathon, Proc. Roy. Soc. A306, 355 (1969).

29. R. Harris and M.J. Zuckermann, J. Phys. F2, 1151 (1972).

30. D.L. Mills, J. Phys. Chem. Solids 34, 679 (1973).

31. R. Jullien, M.T. Beal-Monod, and B. Cogblin, Phys. Rev. B9, 1441 (1974).

32. W.G. Baber, Proc. Roy. Soc. Ser. A 153, 699 (1936).

33. E.D. Thompson, Ann. Phys. 22, 309 (1963).

34. A.L. Fetter and J.D. Walecka, op. cit., p. 188.

35. D.L. Mills and P. Lederer, J. Phys. Chem. Solids 27, 1805 (1966).

36. P.F. de Chatel and E.P. Wohlfarth, Comments on Solid State Phys. 5, 133 (1973).

37. R.J. Trainor, M.B. Brodsky, and H.V. Culbert, Phys. Rev. Lett. 34, 1019 (1975).

38. A.B. Kaiser and S. Doniach, Int. J. Magn. 1, 11 (1970).

39. J.M. Ziman, Electrons and Phonons (Clarendon Press, Oxford, 1960), Ch. 7.

40. J.W. Loram, R.J. White, and A.D.C. Grassie, Phys. Rev. B5, 3659 (1972).

41. H. Nagasawa, Solid State Comm. 10, 33 (1972).

42. J. Souletie, J. Low Temp. Phys. 7, 141 (1972).

43. E. Daniel, J. Phys. Chem. Solids 23, 975 (1962).

44. N. Rivier, and V. Zlatic, J. Phys. F2, L99 (1972).

45. K. Fischer, J. Low Temp. Phys. 17, 87 (1974).

46. N.F. Mott and H. Jones, The Theory of the Properties of Metals and Alloys (Dover Publications, Inc., New York, 1958), p. 262.

47. J.W. Garland, K.H. Bennemann, A. Ron, and A.S. Edelstein, J. Appl. Phys. 41, 1148 (1970).

48. E. Raub, H. Beeskow, and D. Menzel, Z. Metallk, 50, 428 (1959).

49. L.R. Bidwell and R. Speiser, Acta Cryst. 17, 1473 (1964).

50. A.J. Manuel and J.M.P. St. Quinton, Proc. Roy. Soc. A273, 412 (1963).

51. A. Arrott, Phys. Rev. 108, 1394 (1957).

52. L.D. Landau and E.M. Lifshitz, Statistical Physics (London, Pergamon Press, 1958), Chap. 14.

53. A.P. Murani, A. Tari, and B.R. Coles, J. Phys. F4, 1769 (1974).

54. J. Beille, D. Bloch, and M.J. Besnus, J. Phys. F4, 1275 (1974).

55. A.T. Aldred, B.D. Rainford, and M.W. Stringfellow, Phys. Rev. Lett. 24, 897 (1970).

56. R.W. Cochrane, R.T. Hedgcock, J.P. Tidman, and M.J. Zuckermann, Can, J. Phys. 53, 145 (1975).

57. E. Boucai, B. Lecoanet, J. Pilon, J.L. Tholence, and R. Tournier, Phys. Rev. B3, 3834 (1971).

58. G. Chouteau, R. Tournier, and P. Mollard, J. de Physique 35, C4-185 (1974).

59. R. Doclo and S. Foner, J. Appl. Phys. 40, 1206 (1969).

60. H. Schulz, Z. Phys. 242, 381 (1971).

61. H.-G. Purwins, H. Schulz, and J. Sierro, Int. J. Magn. 2, 153 (1972).

62. J.L. Genicon, F. Lapierre, and J. Souletie, Phys. Rev. B10, 3976 (1974).

63. C. Kittel, Introduction to Solid State Physics, (John Wiley & Sons, Ins. New York, 1966), p. 435.

64. D.M. Edwards, J. Mathon, and E.P. Wohlfarth, J. Phys. F5, 1619 (1975).

65. D.M. Edwards, J. Mathon, and E.P. Wohlfarth, J. Phys. F3, 161 (1973).

66. T. Kato and J. Mathon, J. Phys. F6, 1341 (1976).

67. T. Kato and J. Mathon, J. Phys. F6, 221 (1976).

68. J.A. Rowlands, D. Greig, and P. Blood, J. Phys. F1, L29 (1971).

69. H.-G. Purwins, Y. Talmor, J. Sierro and F.T. Hedgcock, Solid State Commun. 11, 361 (1972).

70. B.R. Coles and J.C. Taylor, Proc. R. Soc. A267, 139 (1962).

71. D. Greig and J.A. Rowlands, J. Phys. F4, 536 (1974).

72. D.J. Gillespie, Phys. Rev. B14, 4021 (1976).

73. J. Bass, Adv. Phys. 21, 431 (1972).

74. A.I. Schindler and B.C. LaRoy, Solid State Comm. 9, 1817 (1971).

75. M.G. Leger and W.B. Muir, Phys. Stat. Sol. (b) 49, 659 (1972).

76. O.K. Andersen, Phys. Rev. B2, 883 (1970).

77. D.W. Budworth, F.E. Hoare, and J. Preston, Proc. Roy. Soc. A257, 250 (1960).

78. A. Narath and H.T. Weaver, J. Appl. Phys. 41, 1077 (1970).

79. K. Levin, R. Bass, and K.H. Bennemann, Phys. Rev. B6, 1865 (1972).

80. J. van der Rest, F. Gautier, and F. Brouers, J. Phys. F5, 995 (1975).

81. D. Shaltiel, J.H. Wernick, and H.J. Williams, Phys. Rev. 135, 1346 (1964).

82. G. Chouteau, R. Fourneaux, K. Gobrecht, and R. Tournier, Phys. Rev. Lett. 20, 193 (1968).